



HAL
open science

Hydrophobic Porous Liquids: design, synthesis, and evaluation in metal extraction

Lorianne Ginot

► **To cite this version:**

Lorianne Ginot. Hydrophobic Porous Liquids: design, synthesis, and evaluation in metal extraction. Material chemistry. Université de Montpellier, 2024. English. NNT: . tel-04958012

HAL Id: tel-04958012

<https://theses.hal.science/tel-04958012v1>

Submitted on 20 Feb 2025

HAL is a multi-disciplinary open access archive for the deposit and dissemination of scientific research documents, whether they are published or not. The documents may come from teaching and research institutions in France or abroad, or from public or private research centers.

L'archive ouverte pluridisciplinaire **HAL**, est destinée au dépôt et à la diffusion de documents scientifiques de niveau recherche, publiés ou non, émanant des établissements d'enseignement et de recherche français ou étrangers, des laboratoires publics ou privés.

THÈSE POUR OBTENIR LE GRADE DE DOCTEUR DE L'UNIVERSITÉ DE MONTPELLIER

En chimie séparative, matériaux et procédés

École doctorale Chimie Balard – ED 459

Unité de recherche : Institut de Chimie Séparative de Marcoule – UMR 5257

Liquides poreux hydrophobes : conception, synthèse, et évaluation pour l'extraction de métaux

Présentée par Lorianne GINOT

Le 04 novembre 2024

Sous la direction de Sandrine DOURDAIN et Stéphane PELLET-ROSTAING

Devant le jury composé de

Corinne CHANEAC, Professeur, Sorbonne-Univ./CNRS/LCMCP

Hakima MENDIL-JAKANI, Ingénieur-chercheur, CEA/DRF/Symmes/STEP, Grenoble

Sheng DAI, Professor, ORNL & University of Tennessee, Knoxville (UTK), Etats-Unis

Corinne GERARDIN, Directrice de recherche, CNRS/ICG, Université de Montpellier

Margarida COSTA GOMES, Directrice de recherche, CNRS/ENS Lyon

Sandrine DOURDAIN, Ingénieur-chercheur, CEA/DRF/ISEC/ICSM, Marcoule

Stéphane PELLET-ROSTAING, Directeur de recherche, CNRS/ISEC/ICSM, Marcoule

Fabrice GIUSTI, Ingénieur de recherche, CNRS/ISEC/ICSM

Rapporteur

Rapporteur

Examineur

Examinatrice

Examinatrice

Co-directrice

Co-directeur

Co-encadrant



UNIVERSITÉ DE
MONTPELLIER

Lorsque vous avez une idée, vous devez la garder au fond de vous pour lui permettre de mûrir. Vous devez l'empêcher de sortir, vous devez la laisser grandir en vous jusqu'à ce que vous sentiez que c'est le moment.

Faire des idées... des illuminations.

Joël Dicker

Remerciements

Ce rapport de thèse n'aurait jamais pu voir le jour sans le support de nombreuses personnes que je souhaite vivement remercier ici.

Mes premières pensées vont à mes encadrants de thèse, qui grâce à leur bienveillance, et une entente chaleureuse, ont tant fait mûrir mon expérience. Ils m'ont tous les trois portée par des échanges scientifiques d'une grande qualité, dans la complémentarité de leurs domaines d'expertise. Merci à Stéphane PELLET-ROSTAING pour ses conseils précieux, la reconnaissance du travail effectué, le suivi attentif de l'avancée des recherches. Merci à Fabrice GIUSTI pour le soutien pratique à la paillassa, pour sa présence et sa disponibilité, et pour sa rigueur qui m'a guidée au cœur des méandres de la chimie organique. Merci à Sandrine DOURDAIN pour les encouragements à toute épreuve, pour sa gentillesse, pour la diversité des sujets de conversation : silice mésoporeuse, retraites religieuses, SAXS, psychanalyse, extraction liquide-liquide, cultures et société – j'emporte tout cela dans mon cœur.

Je remercie sincèrement Mesdames Corinne CHANEAC, Hakima MENDIL-JAKANI, Corinne GERARDIN, Margarida COSTA GOMES et Monsieur Sheng DAI, qui ont honoré mes travaux de thèse en acceptant de les relire et de les évaluer. Nos échanges à l'occasion de la soutenance résonnent comme un point d'orgue à la maturation de ce travail.

Je souhaite adresser ma gratitude à mes collègues de l'ICSM, et en particulier à Xavier LE GOFF et Joseph LAUTRU pour les séances d'imagerie électronique, à Matthieu VIROT pour les essais de réactions sous ultrasons, à Tony CHAVE pour les mesures COT. Merci à tous les permanents pour leur immense disponibilité et leur prévenance, qui crée un environnement de travail profondément agréable. Mentions spéciales pour l'Aisther, pour la cellule environnement (Guilhem Q., Diane, Rachel, Marielle, Véronique, Sandrine) et pour la team badminton ICSM (Guilhem A., Cyrielle, Rayan, Marie) qui m'ont permis un ancrage fort dans la vie de l'institut.

C'est bien sûr grâce au support de toute l'équipe du LTSM (Guilhem A., Béatrice, Stéphane, Fabrice, Sandrine, Elise, David, Baptiste, Marine, Evan, Clément, Chen, Claudine, Sahar) et à celui de son équipe sœur, le LNER (Cyrielle, Xavier, Jérémy, Guillaume, Pierre, Aya, Anna, Jun, Rayan, Hiba, Sylvain), que mon séjour à l'ICSM s'est révélé si plaisant : je m'y suis sentie accueillie dès mon arrivée. Merci tout spécialement à Cyrielle REY qui consacre beaucoup de temps à faire du laboratoire un espace de travail confortable, et à Guilhem ARRACHART qui m'a grandement aidée pour l'analyse des échantillons à Montpellier et dans l'élaboration des voies de synthèse.

Je voudrais remercier Justine BEN GHOZI BOUVRANDE qui a synthétisé l'amine EthA-92, et qui a conduit les expériences de perméabilité au synchrotron au cours de sa propre thèse ; ainsi qu'Amal EL BAKKOUCHE, qui a grandement contribué à la synthèse d'un liquide poreux fonctionnalisé au cours de son stage. Merci à Margarida COSTA GOMES de m'avoir accueillie dans son laboratoire pour des mesures complémentaires sur la balance de sorption, et à Cintia MARQUES CORREA qui a effectué les mesures. Merci également à Amine GENESTE pour les mesures DSC, ainsi qu'à Antoine LEYDIER pour les mesures BET de dépannage, et son intérêt porté à mes travaux : vive la porosité, et vive la silice ! Je n'oublie pas non plus les conseils pratiques d'Ahmad MEHDI, qui maîtrise la fabrication des particules de silice.

Si ce document contient des illustrations originales d'une grande finesse, c'est grâce au talent de ma sœur, Gwenaëlle GINOT, qui s'est proposée de surpasser les réalisations PowerPoint. Elle aura mis beaucoup de cœur à ajouter cette touche créative et personnelle, qui me rend encore plus fière d'éditer mon mémoire de thèse.

A mes amis d'Avignon, pour toutes les expériences que j'ai eu la chance de partager avec eux.

Pour une virée dans l'archipel suédois avec Elise et David à bord du bateau de Patrick. Pour les « Lorianne, tu viens manger ? » quotidiens de Baptiste. Pour les jeux de société et les jeudis gourmet avec Simon, Antoine, Gabriel, Vincent et Martin, et pour les repas avec Sergio. Pour les très belles discussions avec Pierre, et parce qu'on partage de nombreux centres d'intérêt.

A ceux dont j'ai croisé la route au badminton, à l'AFEV, à l'orchestre (merci Thibaud pour les covoit jusqu'aux lieux de concert), et à la chorale de St Agricol.

Aux « scouts de Marcoule » : Denis, Anne, Tojo, Agnès... qui m'ont ouvert grand leur porte.

A mes chères compagnes CVX (Emilie, Hélène, Dominique, Martine et Marie-Laure) et à Paco, car le mûrissement spirituel compte intensément dans le processus de construction d'une thèse.

Et aux amis d'ailleurs qui sont près de mon cœur.

J'aimerais exprimer toute ma reconnaissance à ma famille. Merci à mes parents qui m'ont transmis leur passion de la science et de la recherche. Ils savent ce qui se cache derrière le mot « thèse », et j'ai toujours pu compter sur eux. Merci à Gwen, Tim, Christelle et Séverine : on ne peut pas rêver meilleur·e·s frangin·e·s que vous.

Enfin, voici qu'une étoile s'est décrochée du ciel il y a deux ans, pour venir se déposer à mes pieds. Une étoile curieuse et passionnée de sciences ; une étoile attentionnée ; une étoile qui brille si fort qu'elle illumine toute ma vie. Lucas, cette aventure aurait été bien différente sans toi.

Et même si c'est tacitement contre-indiqué en sciences, je remercie le Ciel, pour toutes ces rencontres, et les échanges qui en ont découlé, qui n'ont eu de cesse d'exalter l'intelligence humaine.

Table of Contents

Résumé substantiel en français.....	9
Abbreviations.....	16
Nomenclature	17
General introduction	19
Chapter I Introduction to porous liquids and applications.....	21
1. History of porous liquids	21
1.1. Genesis	21
1.2. Classification of porous liquids.....	23
1.2.1. Historical classification: Type I to Type IV porous liquids	23
1.2.2. New classification: Class A to Class D porous liquids	29
1.3. Definition and frontiers	31
2. Porosity and permeability of porous liquids	33
2.1. Definition	33
2.2. Methods for porosity and permeability assessment.....	34
3. Comprehension of the liquid behavior.....	36
4. Applications of porous liquids	39
4.1. Current studies	39
4.2. Potential future applications.....	41
5. Potential and challenges for porous liquids in liquid-liquid extraction of metals.....	42
5.1. Introduction to techniques of metal extraction.....	42
5.1.1. Liquid-liquid extraction.....	42
5.1.2. Solid-liquid extraction	43
5.2. Porous liquids employed for liquid-liquid extraction of metals	44
Conclusion	46
Chapter II Synthesis and characterization of a new range of hydrophobic silica-based porous liquids	49
1. Synthesis strategy – from Nanoscale Ionic Materials (NIMs) to Porous Liquids (PLs)	50
1.1. From NIMs to ionic PLs: state-of-the-art.....	50
1.2. Synthesis tunability of silica-based ionic PLs.....	52
1.2.1. Nature of the silica core	52
1.2.2. Modulation of the organic grafting	55
1.3. From ionic PLs with amphiphilic canopy to neutral PLs with hydrophobic canopy	55
1.4. Synthetic table of the synthesized materials presented in this chapter.....	57
2. Synthesis and characterization of hollow silica particles	58
2.1. Synthesis method	58
2.2. Transmission electronic microscopy	59

2.3.	Small angle X-ray scattering	60
2.4.	Reproducibility	62
3.	Synthesis and characterization of porous liquids.....	64
3.1.	Ionic porous liquids with amphiphilic canopy: PL-EthAs.....	64
3.1.1.	Syntheses development	64
3.1.1.1.	A reference nanoscale ionic material: PL-SiNPs-EthAs	65
3.1.1.2.	PLs containing small hollow silica particles as hollow cores: PL-sHSPs-EthAs	66
3.1.1.3.	PLs containing big hollow silica particles as hollow cores: PL-bHSPs-EthAs	66
3.1.2.	Characterization: chemical composition, grafting assessment and stability	66
3.1.2.1.	PLs containing small hollow silica particles as hollow cores: PL-sHSPs-EthAs	67
3.1.2.2.	PLs containing big hollow silica particles as hollow cores: PL-bHSPs-EthAs	71
3.1.2.3.	Grafting yield and grafting density of sulfonated organosilicon (SIT).....	73
3.1.2.4.	Corona-canopy grafting ratio	75
3.1.2.5.	Stability and density of ionic PLs	75
3.2.	Neutral porous liquid with hydrophobic canopy: PL-sHSPs-PPG	76
3.2.1.	Synthesis development	76
3.2.1.1.	Step 1: Silanization of PPG	77
3.2.1.2.	Step 2: Covalent grafting.....	78
3.2.1.3.	Competitive reactions and synthesis conditions.....	80
3.2.2.	Characterization	81
3.2.2.1.	Homogeneity and stability of PL-sHSPs-PPG	81
3.2.2.2.	Characterization of the two liquid phases of PL-sHSPs-PPG	82
	Conclusion	86
Chapter III Studying and tuning the physicochemical properties of porous liquids		87
1.	Studying porosity and permeability	88
1.1.	Porosity of hollow silica particles	88
1.1.1.	Porosity characterization with N ₂ sorption	88
1.1.2.	Effect of reproducibility problems on porosity	91
1.1.3.	Impact of the template removal method on porosity	92
1.2.	Porosity and permeability of porous liquids	93
1.2.1.	Failure of conventional measurement techniques	93
1.2.2.	Permeability of a hydrophilic PL to polar liquids.....	94
2.	Tuning solid-to-liquid physical state and viscosity	97
2.1.	Influence of ionic interactions on the liquid behavior	99
2.2.	Influence of temperature on physical state and viscosity.....	100
2.3.	Influence of size and density of silica particles on physical state and viscosity	102
2.4.	Influence of organic:inorganic ratio on viscosity.....	104
3.	Tuning hydrophobicity	110
3.1.	Amphiphilic canopy-based ionic porous liquids: PL-EthAs.....	111
3.2.	A neutral single-component canopy-based porous liquid: PL-sHSPs-PPG-2000.....	112
	Conclusion	115

Chapter IV Porous liquids for liquid-liquid extraction of rare earth elements.....	117
1. Context	117
1.1. Rare Earth Elements (REEs) in Europe.....	117
1.2. Conventional techniques of REEs extraction.....	119
1.2.1. Selective precipitation.....	119
1.2.2. Solid-liquid extraction of REEs.....	120
1.2.3. Liquid-liquid extraction of REEs.....	121
1.2.4. Ion-exchange processes for high-grade REEs.....	122
1.3. Innovation for REEs extraction	123
1.3.1. Synergistic liquid-liquid extraction or solid-liquid extraction.....	123
1.3.2. Ionic liquids and deep eutectic solvents	123
1.3.3. Ion foam flotation.....	124
1.3.4. Porous liquids	125
2. Functionalization of a porous liquid	125
2.1. Methods for particles functionalization: state-of-the-art.....	125
2.1.1. Post-grafting	125
2.1.2. Co-condensation.....	126
2.2. A functional porous liquid for REEs extraction.....	127
2.2.1. Choice of the functional group.....	127
2.2.2. From functional silica particles to the first functional porous liquid	127
2.2.2.1. Functional hollow silica particles	128
2.2.2.2. Functional porous liquid based on an ionic amphiphilic canopy	128
2.2.2.3. Characterization	129
3. Extraction of REEs from permanent magnets with a functional porous liquid.....	132
3.1. Case study of permanent magnets.....	132
3.2. Extraction method.....	132
3.3. Preliminary results.....	133
3.3.1. Hollow silica particles	133
3.3.2. Ionic porous liquids	134
4. Optimization of extraction performances.....	135
4.1. Influence of pH on the extraction of neodymium.....	135
4.2. Effect of the grafting method on the extraction of neodymium.....	136
4.3. Effect of the size of hollow silica particles on the extraction of neodymium	139
5. Stability of porous liquids toward acid and metals	141
5.1. Hydrophobic ionic porous liquid: PL-sHSPs-EthA-11.....	141
5.2. Hydrophobic neutral porous liquid: PL-sHSPs-PPG-2000-fluid	143
6. Opening: extraction of a neutral hydrophobic and functional porous liquid	145
Conclusion	146
General conclusion and outlook.....	149
Appendix A Methods for the syntheses of hollow silica particles and porous liquids	157

Appendix B Techniques for Characterization of Materials	162
Appendix C Small Angle X-Ray Scattering (SAXS) and Small Angle Neutrons Scattering (SANS).....	165
Appendix D Nitrogen sorption experiments	175
Appendix E Grafting Yield and Grafting Density of SIT.....	179
Appendix F Supplementary material	183
Appendix G Stability and homogeneity study of PPG-based porous liquids (PL-sHSPs-PPG)	191
Appendix H Publications during the PhD	197
Lead Extraction in a Functionalized and Permeable Silica-Based Porous Liquid	197
Hydrophobic Porous Liquids with Controlled Cavity Size and Physico-Chemical Properties.....	214
References	235

Résumé substantiel en français

Le travail présenté dans ce rapport vise à explorer la possibilité d'utiliser des liquides poreux pour l'extraction liquide-liquide de métaux.

Dans le premier chapitre, les liquides poreux et leurs applications sont présentés en prenant appui sur un état de l'art issu de la littérature. Ce concept récent, introduit en 2007 par le Pr. Stuart James et son équipe, suggère que la porosité d'un matériau peut exister à l'état liquide. La publication décrit trois types de liquides poreux : le Type I regroupe les matériaux liquides composés d'hôtes poreux moléculaires et discrets, dont le point de fusion a été abaissé par une modification chimique. Le Type II consiste à dissoudre des hôtes moléculaires dans un solvant encombrant, incapable de pénétrer les pores. Enfin, les liquides poreux de Type III sont une suspension stable de micro-réseaux poreux dans un solvant encombrant, qui ne pénètre pas les pores. En 2021, un quatrième type a été ajouté, désignant des réseaux poreux dont la température de fusion a été abaissée pour les rendre liquides à basse température.

Si cette classification a permis de diversifier les études, en laissant libre cours à l'imagination des chercheurs pour jouer sur la nature des hôtes poreux et la façon de leur procurer un caractère liquide, une nouvelle classification est proposée dans ce chapitre, se voulant plus fidèle aux interactions en jeu conférant l'état liquide, et permettant d'élargir le concept à des matériaux encore non synthétisés. Ainsi, les liquides poreux de classe A désignent les hôtes poreux (moléculaires, supramoléculaires, ou des particules solides) dont le point de fusion est abaissé par modification chimique. La classe B contient les dispersions ou suspensions d'hôtes poreux dans un solvant qui ne pénètre pas les pores. La classe C est constituée de matériaux composites, où les solides poreux sont piégés dans une matrice faiblement réticulée et fluide. Dans la classe D, ce sont les hôtes poreux eux-mêmes qui sont connectés pour former un réseau poreux suffisamment désorganisé pour exister à l'état liquide.

Parmi ces différents types de liquides poreux, les liquides poreux à base de nanoparticules creuses de silice, ont été synthétisés pour la première fois en 2015 par le Pr. Sheng Dai et son équipe. Appartenant à la classe A, ils sont obtenus en greffant autour de chaque coquille, un système de couronne-canopée organique induisant un effet stérique capable d'empêcher la floculation des particules. Présentant l'avantage d'être sans solvant, ces liquides poreux possèdent des cavités nanométriques, accessibles par un réseau de micropores au sein de la coquille de silice entourant la cavité. La silice étant par ailleurs un matériau aisément fonctionnalisable, il a été alors envisagé de fabriquer de nouveaux liquides poreux aptes à l'extraction de métaux.

L'extraction liquide-liquide est un procédé largement employé dans l'industrie pour la séparation de métaux. Il consiste à mettre en contact une phase aqueuse contenant les métaux d'intérêt et les métaux compétiteurs, avec une phase organique extractante capable de collecter sélectivement les métaux cibles. L'immiscibilité des deux phases permet une séparation efficace. Cependant, cette technique repose essentiellement sur de larges volumes de solvants, volatiles et très souvent toxiques, induisant un fort impact sur l'environnement et une dépendance à l'approvisionnement. Par ailleurs, d'autres désavantages lourds peuvent apparaître, comme la présence d'une troisième phase à l'interface, riche en métaux, créant des complications dans la gestion des flux du procédé. D'autre part, l'extraction sur phase solide est une alternative intéressante puisqu'elle requiert une installation moins

volumineuse pour extraire une même quantité de métaux, et la préparation de colonnes ou de membranes régénérables facilite la mise en place de processus continus. Il est même parfois avancé que dans certains cas, la fixation de groupements chélatants sur support solide induit une plus forte sélectivité pour l'ion ciblé, augmentant ainsi fortement les gains de l'étape d'extraction. Néanmoins, l'exploitation de l'extraction solide-liquide à l'échelle industrielle n'est en pratique possible que pour le traitement de volumes modérés d'effluents.

Conciliant l'efficacité de l'extraction solide-liquide (notamment en terme de réduction des déchets) avec la facilité de transport et de stockage des liquides, le liquide poreux sans solvant s'impose en candidat de choix pour une phase extractante alternative. Dans la littérature, les liquides poreux à base de silice décrits étaient hydrophiles, et ils ont principalement été testés pour la sorption et la séparation de gaz. La première partie de ce travail a donc consisté à adapter la synthèse pour obtenir une nouvelle gamme de liquides poreux, dont l'affinité avec l'eau pouvait être facilement contrôlée. Par ailleurs, les supports solides généralement utilisés pour la séparation de métaux possèdent des pores suffisamment grands pour permettre d'une part leur fonctionnalisation, et d'autre part la correcte diffusion des espèces à extraire.

Ainsi, la synthèse et la caractérisation d'une nouvelle gamme de liquides poreux sont développées dans le chapitre II. En particulier, différents types de coquilles de silice et de greffage organique ont été employés pour la préparation des liquides poreux, afin d'obtenir des matériaux aux propriétés physicochimiques variables. Concernant les coquilles de silice, un premier type dénommé « sHSP » (*small hollow silica particle*), déjà utilisé dans la première étude du Pr. Sheng Dai, possède un diamètre d'environ 25 nm et une cavité creuse d'environ 15 nm de diamètre. Les pores de la coquille de silice ont une taille moyenne de 1.4 nm, comme déterminé par les isothermes de sorption d'azote à 77 K. Un second type, dénommé « bHSP » (*big hollow silica particle*) a également été synthétisé notamment dans le but d'accroître la capacité poreuse du liquide final. Ces sphères mesurent environ 240 nm de diamètre (avec une grande hétérogénéité en taille et en forme, due à l'utilisation d'un surfactant pour façonner la particule), et possèdent une cavité d'environ 200 nm de diamètre. Les pores de la coquille de silice ont une taille moyenne de 3.7 nm.

La première voie de synthèse explorée (**Figure R1**) consiste à adapter le système ionique de couronne-canopée introduit dans l'état de l'art, en greffant de manière covalente un organosilane sulfonaté à la surface des coquilles (sHSP ou bHSP). Dans un deuxième temps, une amine tertiaire amphiphile et protonable, constituée d'une chaîne carbonée en C₁₆₋₁₈, et de deux chaînes PEGylées symétriques de longueur variable, est ajoutée pour former la canopée sur la base d'interactions ioniques entre le sulfonate et l'amine. En faisant varier le nombre de motifs ethoxylés sur les chaînes PEGylées de l'amine, il est donc possible de conférer un caractère plus ou moins hydrophobe au matériau final. Dans ce travail, le nombre de motifs ethoxylés total des deux chaînes a été varié entre 5 et 92 (5, 11, 22, 50, 92), choisis en fonction des disponibilités des amines dans le commerce. Les amines ont été nommées EthA-X, où X est le nombre de motifs ethoxylés.

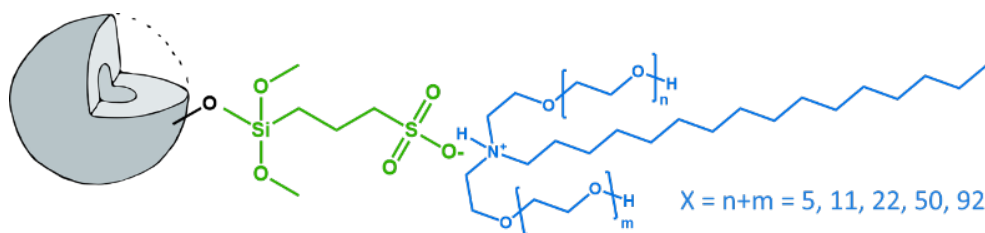


Figure R1. Greffage organique à la surface d'une nanocoquille de silice afin de former un liquide poreux ionique. Le greffage comprend une couronne sulfonatée (en vert) et une canopée amphiphile (en bleu) interagissant par liaisons ioniques. La canopée est constituée de molécules d'amines tertiaires (EthA) possédant une chaîne aliphatique (C_{16-18}) et deux chaînes PEGylées de longueur variable. Le nombre de motifs ethoxylés ($n+m$) total de ces deux chaînes varie entre 5 et 92.

La seconde voie de synthèse présentée dans ce rapport (**Figure R2**) vise à obtenir un liquide poreux sans interactions ioniques et purement hydrophobe. Dans la littérature, le polypropylène glycol (PPG) a déjà été utilisé pour liquéfier des nanocages et ainsi obtenir un liquide poreux de classe A. Ce polymère liquide (poids moléculaire 2000 g/mol) et hydrophobe a donc été silanisé afin de permettre son greffage covalent directement à la surface des nanocoquilles de silice. Il est apparu que l'optimisation de cette voie restait nécessaire, puisqu'elle n'a abouti qu'à un greffage hétérogène avec un faible rendement, probablement à cause de l'encombrement du polymère et de la difficulté à disperser les coquilles de silice. Le matériau obtenu, bien que liquide, forme deux à trois phases distinctes de densités différentes, avec des taux en silice également variables. Pour la caractérisation physicochimique en vue de l'application en extraction liquide-liquide, la phase la plus fluide a été prise comme modèle.

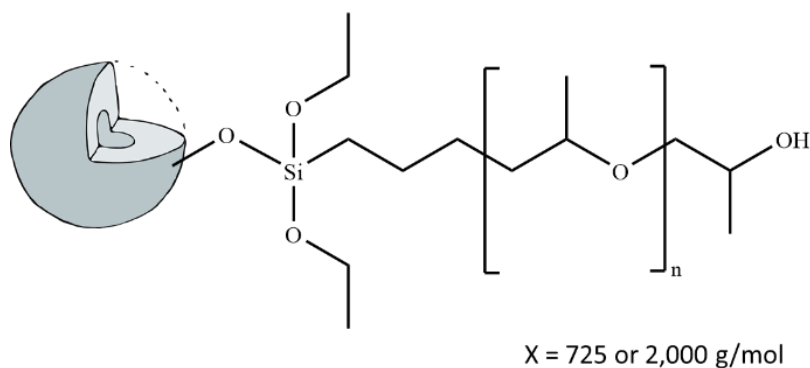


Figure R2. Greffage covalent d'un polymère hydrophobe (le PPG) à la surface d'une nanocoquille de silice afin de former un liquide poreux neutre.

Dans le troisième chapitre, la possibilité de moduler les propriétés des liquides poreux est analysée afin de concevoir le meilleur matériau pour l'extraction liquide-liquide. Un effort pour accroître les connaissances fondamentales à leur sujet, et en particulier pour comprendre l'origine de la fluidité, est également déployé dans ce chapitre.

En premier lieu, la modification du greffage organique a permis de confirmer que le caractère liquide découle d'un rapport massique organique/inorganique adéquat. En effet, de trop courtes chaînes organiques (par exemple l'amine EthA-5 ou un PPG de 725 g/mol) mènent à la synthèse de solides stables, se dégradant à des températures inférieures à leur température de fusion (**Figure R3**). A l'opposé, de longues chaînes PEGylées conduisent également à la fabrication de solides, mais

capables de fondre à des températures proches de celle de l'amine pure (40-50 °C). De fait, seules les amines EthA-11 et EthA-22, ainsi que le PPG₂₀₀₀ ont permis l'obtention de liquides à température ambiante. De manière intéressante, la viscosité des amines pures (EthA) évolue dans le sens inverse de la viscosité des liquides poreux correspondants : en terme de viscosité, on a : EthA-5 < EthA-11 < EthA-22 ; tandis que le liquide poreux PL-EthA-5 est solide, et que le PL-EthA-11 est plus visqueux que le PL-EthA-22. Cela ne vaut plus pour les amines longues, puisque la présence de particules solides devient « négligeable ». Enfin, si les liquides poreux ioniques synthétisés ont une viscosité relativement élevée (10⁴ Pa.s), l'élévation en température (50-60 °C) induit une diminution drastique de cette viscosité (de quatre ordres de grandeur). En outre, la présence d'interactions ioniques n'est pas nécessaire pour la synthèse de liquides poreux – bien qu'elle puisse avoir un impact sur la fenêtre de rapports organique/inorganique induisant le comportement liquide – puisque la phase fluide du liquide poreux à base de PPG (2000 g/mol) possède une viscosité bien plus faible que les liquides poreux ioniques.

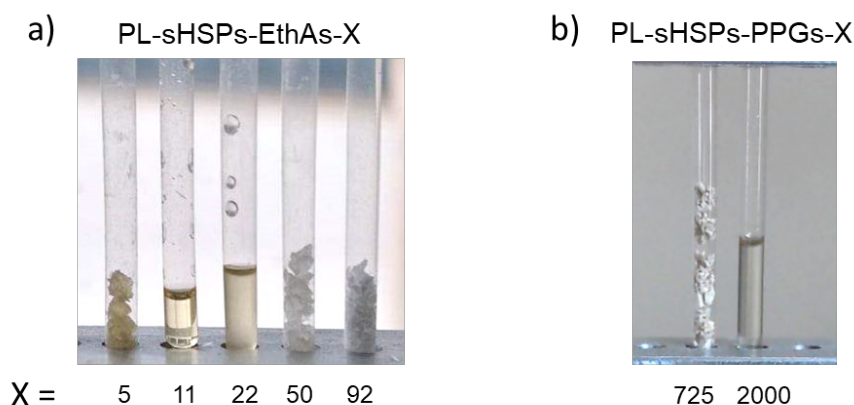


Figure R3. Photos de capillaires contenant différents matériaux poreux synthétisés : **a)** de type ionique (sulfonate/EthA) ; **b)** de type neutre (PPG). Le rapport organique/inorganique est un paramètre impactant fortement l'état physique du matériau final.

De manière générale, le caractère hydrophobe d'une phase organique se quantifie par la méthode du logP. Malheureusement, celui-ci ne peut pas être calculé pour des systèmes aussi complexes que les liquides poreux, contenant à la fois une part solide inorganique et un domaine organique plus fluide. L'affinité avec l'eau a donc été simplement vérifiée qualitativement, grâce à la mise en contact du liquide poreux avec l'eau. Dans le cas des liquides poreux ioniques (à base de sulfonate et d'amine), l'amine EthA-11 (plus hydrophobe que EthA-22 car possédant des chaînes PEGylées plus courtes), permet la séparation entre le liquide poreux correspondant et l'eau. En revanche, l'amine EthA-22 (plus longue) donne un liquide poreux complètement miscible à l'eau. En appliquant une force centrifuge importante, on assiste même à une précipitation des coquilles de silice (sulfonatées), tandis que l'amine reste solubilisée dans l'eau. Il existe donc un seuil à l'amphiphilie de l'amine au-delà duquel il n'est plus possible d'obtenir un liquide poreux hydrophobe.

Si la porosité des nanocoquilles de silice peut être très facilement quantifiée et analysée grâce aux mesures de sorption d'azote à 77 K, celle des liquides poreux est plus difficile à déterminer. En effet, à 77 K, les chaînes organiques (amines ou PPG) se solidifient et deviennent vitreuses, empêchant la diffusion du gaz dans le matériau. Par ailleurs, la problématique du dégazage (vidage de l'eau liée dans les pores de la silice) nécessaire à la mesure, est accentuée pour le liquide poreux. Plus que la porosité,

la propriété recherchée dans le cadre de l'extraction liquide-liquide est la perméabilité du liquide poreux à l'eau. Une méthode a donc été développée, fondée sur la diffusion des neutrons aux petits angles, pour affirmer la totale perméabilité d'un liquide poreux à base de silice aux liquides polaires (en particulier l'éthanol, car il était moins aisé d'interpréter les signaux obtenus avec l'eau). Les sources de neutrons n'étant pas facilement accessibles, une autre approche utilisant une microbalance et un système capable d'appliquer de grandes pressions de gaz est également envisagée comme une alternative possible pour quantifier le volume libre des liquides poreux obtenus lors de ces travaux de thèse.

Dans le quatrième et dernier chapitre, la question de la fonctionnalisation des liquides poreux est abordée. En effet, dans l'optique de proposer ces matériaux comme phase alternative extractante pour l'extraction liquide-liquide de métaux, il est nécessaire d'y introduire des groupements chélatants spécifiques des métaux ciblés. En l'occurrence, trois terres rares contenues dans les aimants permanents (notamment issus des disques durs et des batteries de véhicules électriques) sont difficiles à recycler de nos jours : le néodyme, le praséodyme et le dysprosium. Souvent trouvées avec de grandes quantités de fer, ces ions trivalents ont des propriétés proches, rendant difficile leur séparation. D'après la littérature, des agents solvatants tels que ceux appartenant à la famille des diglycolamides (DGA) ont été identifiés comme bons extractants pour les terres rares, permettant d'atteindre de bonnes sélectivités, notamment en extraction sur support solide. Cependant, ces DGA n'existent pas sous forme silylée dans le commerce. La première preuve de concept a donc été effectuée en utilisant un autre extractant affiné des terres rares, l'acide éthylène diamine tétraacétique (EDTA), dont la forme silylée était commerciale. Si l'EDTA est un échangeur de cation (et non un agent solvant) présentant une sélectivité intra-terres rares inférieure à celle permise par les DGA, il forme comme les DGA des complexes multidentés. Il est donc probable que l'optimisation de la fonctionnalisation conduite avec l'EDTA soit en majorité transférable aux DGA.

Dans le cadre de cette thèse a été fait le constat que les hôtes poreux (ici les nanocoquilles de silice) pouvaient également servir de support solide à l'extraction des terres rares. De ce fait, deux voies de fonctionnalisation des coquilles ont été étudiées : la co-condensation et le post-greffage. La co-condensation consiste à introduire l'EDTA silylé en co-précurseur de silice, lors de la formation de la coquille. Pour suivre cette méthode, il est donc nécessaire de maîtriser toutes les étapes de la synthèse de la nanocoquille de silice. Si la co-condensation permet théoriquement une insertion homogène du groupement complexant dans le réseau de silice, elle présente également le risque de l'exclusion de l'EDTA causé par l'encombrement plus important de ce motif. Le post-greffage est une voie alternative, qui implique la fixation covalente de l'EDTA silylé sur la surface de la coquille de silice déjà formée. Le facteur limitant dans ce cas est le risque d'obstruction des pores dont le diamètre est inférieur ou égal à la taille du greffon. Puisque cette méthode utilise les silanols de surface pour greffer les groupes complexants, ceux-ci seront également moins disponibles pour le greffage des composés organiques essentiels pour l'obtention de liquides poreux fonctionnels (sulfonate/EthA ou PPG). Il est finalement apparu que la formation des sHSP fonctionnalisées par co-condensation permettait l'ajout d'autant d'EDTA que le post-greffage. En revanche, le post-greffage des bHSP a permis d'augmenter significativement le nombre de groupes complexants par gramme de matériau.

Les premiers tests d'extraction ont été conduits avec un liquide poreux ionique hydrophobe contenant des sHSP fonctionnalisées par co-condensation (**Figure R4**). Ce matériau a été mis en contact avec une solution contenant du fer (1600 ppm), du néodyme (500 ppm), du praséodyme (68 ppm) et

du dysprosium (50 ppm) en milieu acide nitrique. La co-extraction des trois terres rares a été observée, à hauteur de 0.012 à 0.072 mmol/g, alors que l'extraction n'a pas eu lieu avec un liquide poreux non fonctionnalisé. En particulier, ces capacités (qui sont du même ordre de grandeur que d'autres adsorbants solides de la littérature) sont supérieures à celles des coquilles précurseurs des LP, utilisées en poudre, compte tenu du faible taux de coquilles présentes dans un liquide poreux (15% dans le cas présent). Malheureusement, le fer précipitait également dans la phase liquide poreux (sans toutefois saturer les sites chélatants), ce qui nécessiterait une optimisation dans le futur.

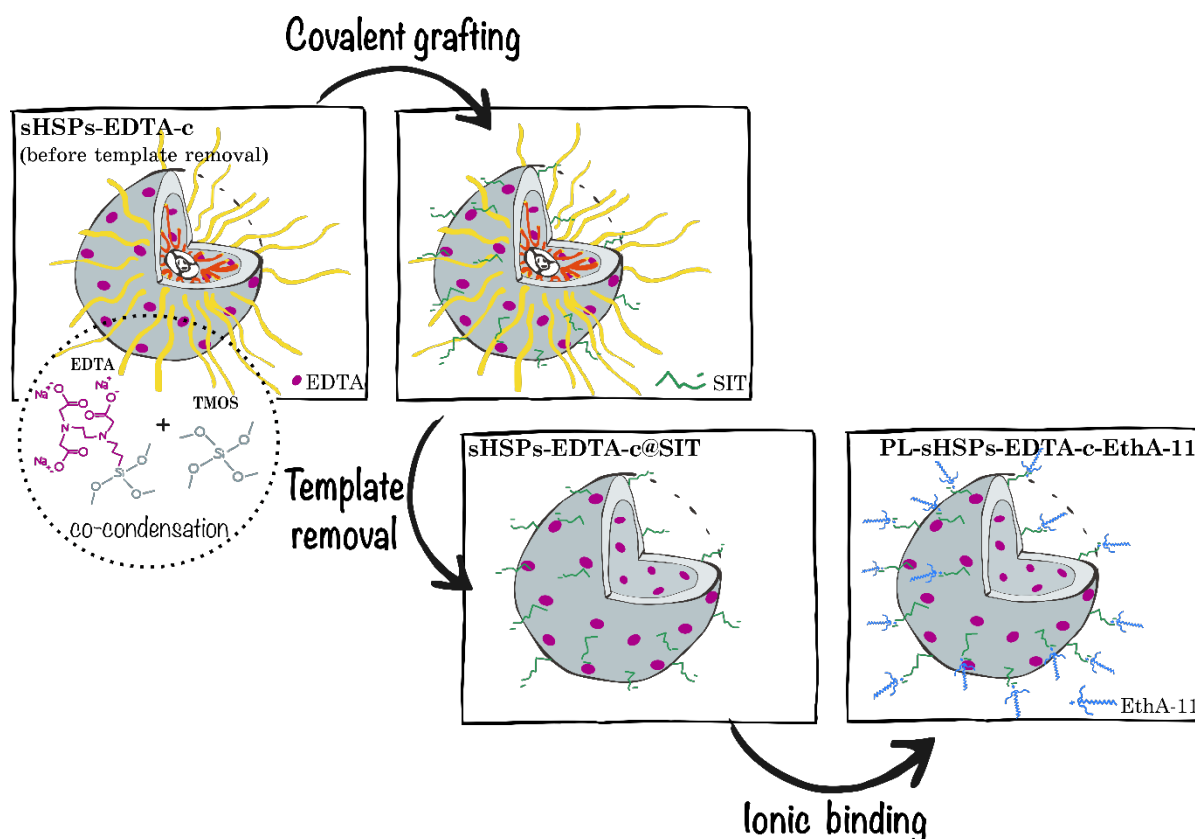


Figure R4. Synthèse d'un liquide poreux ionique hydrophobe et fonctionnalisé pour l'extraction de terres rares.

D'autres tests sur un système plus simple contenant uniquement du néodyme à 500 ppm ont été réalisés dans le but d'optimiser les performances d'extraction. Notamment, l'extraction atteinte avec les nanocoquilles sHSP fonctionnalisées par co-condensation ou par post-greffage sont similaires. En revanche, l'effet du pH sur la capacité des coquilles est important : à pH 6, l'extraction est 68 % plus importante qu'à pH 3. Enfin, les bHSP possédant plus d'EDTA que les sHSP, leur capacité d'extraction est également supérieure (+84 %). En résumé, la fenêtre de pH la plus adaptée pour l'extraction avec l'EDTA se situe entre 4,5 et 5. A ce jour, il n'a pas été possible de tester les voies d'optimisation étudiées sur les liquides poreux hydrophobes fonctionnels, qui n'ont pas pu être synthétisés en quantités suffisantes par manque de temps.

Bien que les liquides poreux employés soient hydrophobes et permettent une séparation de phase spontanée avec l'eau, leur stabilité en milieu acide et en présence de métaux restait à vérifier. Il a ainsi été constaté que le liquide poreux ionique à base d'amine EthA-11 n'était pas suffisamment stable, la solubilisation de l'amine en phase aqueuse étant facilitée par la présence de nitrates et de métaux. Si ce manque de stabilité n'impacte pas les capacités d'extraction du liquide poreux, la perte de son

intégrité est un désavantage pour son application en extraction liquide-liquide. En revanche, le liquide poreux à base de PPG s'est montré bien plus stable dans les mêmes conditions, malgré le greffage partiel du polymère.

La principale perspective envisagée consisterait à fonctionnaliser les bHSP par co-condensation, ce qui n'a pas pu être réalisé en raison d'une trop forte différence de réactivité entre les précurseurs de silice, qui nécessiterait une adaptation des conditions de synthèse (l'EDTA étant silylé sous forme méthoxy, tandis que le précurseur utilisé pour la synthèse des bHSP est le TEOS – *tetraethylorganosilicate*). Puis dans un second temps, il serait intéressant d'utiliser ces coquilles fonctionnelles pour la formation d'un liquide poreux à base de PPG (après optimisation de la méthode de greffage), avant de le tester pour l'extraction des terres rares. Une autre possibilité serait d'envisager un greffage ionique sulfonate/amine en utilisant une amine hydrophobe possédant une chaîne aliphatique et deux chaînes PPG. Ainsi, même en cas d'instabilité du liquide poreux en présence d'acide et de métaux, l'hydrophobie de l'amine permettrait de la collecter en fin de procédé pour reformer simplement le liquide poreux. Enfin, comme évoqué précédemment, la substitution de l'EDTA par des DGA silylées serait également utile pour augmenter la sélectivité du procédé. Une autre voie d'optimisation de la surface spécifique (et donc des performances d'extraction) pourrait consister à synthétiser des nanoparticules fortement poreuses sans cavité interne. De telles particules, une fois chargées en ions métalliques, deviendraient plus denses et entraîneraient possiblement la sédimentation rapide de la phase liquide poreux. Ce phénomène faciliterait ainsi la séparation des phases, pouvant éventuellement compenser les effets limitants liés à la viscosité de ce matériau innovant typiquement plus élevée que celle des phases extractantes conventionnelles.

D'autre part, les effets sur la stabilité et les capacités autorégénératives du liquide poreux après plusieurs contacts successifs, ainsi que les mécanismes entrant en jeu pendant l'extraction, pourraient être étudiés afin d'approcher la réalité de l'application en extraction liquide-liquide. Finalement, une analyse de cycle de vie d'un système liquide poreux extractant serait utile pour déterminer le bénéfice d'un tel procédé pour l'environnement.

Abbreviations

BET	Brunauer, Emmett, and Teller
bHSP	Big Hollow Silica Particle
BJH	Barrett, Joyner, and Halenda
CD	CycloDextrin
DFT	Density Functional Theory
DGA	DiGlycolAmide
DLVO	Derjaguin-Landau-Verwey-Overbeek theory
DSC	Differential scanning calorimetry
DTA	Differential Thermal Analysis
EDTA	EthyleneDiamineTetraAcetic acid
EG	Ethylene Glycol
EthA	Ethoxylated (tertiary) Amine
FTIR	Fourier-Transformed InfraRed spectroscopy
HLB	Hydrophilic Lipophilic Balance
HSP	Hollow Silica Particle
ICP	Inductively Coupled Plasma analysis
IL	Ionic Liquid
LLE	Liquid-Liquid Extraction
MOF	Metal Organic Framework
MS	Mass Spectrometry
NMR	Nuclear Magnetic Resonance spectroscopy
PALS	Positron Annihilation Lifetime Spectroscopy
PDMS	PolyDiMethylSiloxane
PEG/PEO	PolyEthylene Glycol/PolyEthylene Oxide
PG	Propylene Glycol
PL	Porous Liquid
POSS	Polyhedral OligoSilSesquioxanes
PPG/PPO	PolyPropylene Glycol/PolyPropylene Oxide
REE	Rare Earth Element
SANS	Small Angle Neutron Scattering
SAXS	Small Angle X-ray Scattering
sHSP	Small Hollow Silica Particle
SiEDTA	Silanized EthyleneDiamineTetraAcetic acid
SiNP	Silica NanoParticle
SIT	Sulfonated organosilicon
SLD	Scattering Length Density
SLE	Solid-Liquid Extraction
TEM	Transmission Electronic Microscopy
TEOS	TetraEthyl OrthoSilicate
TGA	ThermoGravimetric Analysis
THF	TetraHydroFurane
TMOS	TetraMethyl OrthoSilicate
TOC	Total Organic Carbon
USAXS	UltraSmall Angle X-ray Scattering

Nomenclature

bHSP	Big hollow silica particle
bHSP-EDTA-p	bHSP functionalized with EDTA by post-grafting
EthA-X	Ethoxylated tertiary amine with two PEG chains (total # of EG units X)
HSP	Hollow silica particle
mPPG-sHSPs	Mixture of sHSPs-2 and PPG ₂₀₀₀ without grafting
PL-bHSPs-EthAs	All porous liquids based on bHSPs and SIT/EthA canopy
PL-bHSPs-EthA-X	Porous liquid based on bHSPs and SIT/EthA canopy, with EthA-X
PL-EthAs	All porous liquids based on SIT/EthA canopy
PL-sHSPs	All porous liquids based on sHSPs
PL-sHSPs-EDTA-c-EthA-X	Porous liquid based on functional sHSPs and SIT/EthA canopy
PL-sHSPs-EthAs	All porous liquids based on sHSPs and SIT/EthA canopy
PL-sHSPs-EthA-X	Porous liquid based on sHSPs and SIT/EthA canopy, with EthA-X
PL-sHSPs-PPGs	All porous liquids based on sHSPs and PPG canopy
PL-sHSPs-PPG-X	Porous liquid based on sHSPs and PPG canopy, with PPG _x
PL-SiNP-EthA-X	Porous liquid based on SiNPs and SIT/EthA canopy, with EthA-X
PPG _x	Polypropylene glycol of molecular weight X g/mol
sHSP@SIT	sHSP after surface modification with SIT
sHSP-1	Set of sHSPs used to make all PL-sHSPs-EthAs
sHSP-2	Set of sHSPs used to make PL-sHSPs-PPGs, and for SIT grafting yield study
sHSP-3	Set of sHSPs before template removal (used as a reference)
sHSP-calci	sHSPs-2 after template removal by calcination
sHSP-EDTA-c	sHSPs functionalized with EDTA by co-condensation. Template removal was performed after SIT grafting, on sHSP-EDTA-c@SIT.
sHSP-EDTA-c@SIT	sHSPs functionalized with EDTA by co-condensation after surface modification with SIT
sHSP-EDTA-c-2	sHSPs functionalized with EDTA by co-condensation. Template removal was performed by soft ethanol washing.
sHSP-EDTA-p	sHSPs-1 functionalized with EDTA by post-grafting.
sHSP-wash	sHSPs-2 after template removal by soft ethanol washing
SiNP	Silica NanoParticle
SIT	Sulfonated organosilicon

General introduction

Porosity is a physical property generally associated with the porous state: the first example that springs to mind being the sponge. This important property, brought down to the micrometer or nanometer scale, is essential in many applications such as catalysis, gas capture, energy storage or molecular separation.¹ Confinement effect, pore structure and capillary condensation are all notions linked to porosity that are often exploited to succeed in the targeted application. Porosity means the presence of empty domains inside a material. It can be created either by porous molecules containing cavities (molecular porosity), by supramolecular hosts, by solids containing holes, or even by the non-efficient packing of non-porous moieties (molecules or assemblies) forming extrinsic porosity.

Presently, the types of porous materials described in literature are uncountable. They can be microporous (pore width below 2 nm), mesoporous, or macroporous (pore width over 50 nm), and complex materials sometimes contain interconnected pores of different sizes. To increase specific areas (*i.e.*, the interface between the solid phase and the surrounding fluid phase), hierarchical porosity is often targeted: this is the case of metal-organic frameworks, zeolites, graphene oxide or polymeric foams... In addition, this variety of porous solids can be processed into a wide range of shapes, such as powders, porous nanoparticles, nanosheets, nanotubes, membranes, resins, or monoliths.

In applications relying on porous solids, mechanical stress and aging are great disadvantages leading to increased costs of monitoring and maintenance.² Moreover, solids are not mobile as liquids are, and specific infrastructure have to be designed for them. In contrast, porosity exploited in the liquid state could bring the advantages of manipulating liquids, including pumping processes and compact storage. This is the promise of porous liquids, a recent concept that has become a reality in the mid-2010s.

If conventional liquids can be seen as sets of unorganized molecules, creating weak and short-time porosity by the inefficient packing which is intrinsic to the liquid state, porous liquids contain porous solid hosts that are brought to the liquid state by molecular engineering. Because different methods exist to obtain the liquid state, different types of porous liquids are now identified, and they display various properties.^{3,4} For instance, some porous liquids are solvent-free while others are stable suspensions. Some contain ångstrometric cavities while others can be qualified as nanoporous. Depending on these final properties, porous liquids become good candidates for many applications.

Among them, metal extraction and separation is a tedious topic owing to the current challenges of digital and energy system transformations. Because most metals are nowadays recognized as critical

resources by international agencies, more efficient and eco-friendly processes are urgently required for their extraction, purification and recycling.⁵ Indeed, conventional separation processes mainly rely on liquid-liquid extraction demanding high volumes of volatile (and potentially toxic) solvents, and producing many waste. If solid-liquid extraction would allow reducing the volume of the plant, and the amount of resources necessary to separate equivalent quantities of metal (by facilitating the material recycling),⁶ this alternative technique often displays lower efficiencies, and it needs new infrastructure to be implemented.

Therefore, combining the advantages of porous solids (reduced volumes, recyclability, stability) and liquids (easiness of manipulation, high efficiency and selectivity, compatible with current infrastructure), solvent-free porous liquids containing silica nanopores are herein proposed as an alternative extracting phase in liquid-liquid extraction of metals. In this thesis, the versatility of these materials is investigated and exploited to meet the application, while fundamental knowledge about this very young concept is improved.

In the first chapter, porous liquids and their applications will be introduced with the support of state-of-the-art literature. In the second chapter, the synthesis and characterization of a new range of silica-based porous liquids will be developed. In the third chapter, the tunability of the porous liquids will be investigated, so as to design the best material for liquid-liquid extraction. An effort to increase knowledge at a fundamental level, and in particular the origin of fluidity in porous liquids will also be part of this chapter. In the final chapter, functionalization of porous liquids and an application in rare earth elements extraction will be addressed.

Chapter I

Introduction to porous liquids and applications

Porous liquids associate porous properties – generally reserved to solids – with the fluidity of liquids. They are a very recent concept, born in 2007, which proves that the creation of holes inside matter is not restrained to organized molecular systems. In this chapter, the genesis and classification of porous liquids will be primarily detailed, before discussing their most important physical features: porosity and fluidity. Then, current studies and potential future applications will be introduced. Finally, the use of porous liquids for metal liquid-liquid extraction will be broached in terms of potential and challenges.

1. History of porous liquids

1.1. Genesis

Before the concept of porous liquid was first introduced in 2007, at least three of these original materials had been described in literature:

-In 1991, Cram *et al.* dissolved empty hemicarcerands in diphenyl ether, that was “too large to be incarcerated” (**Figure 1a**).^{7,8} In that case, heating for 5 days at 195°C was necessary to remove the guest (formamide) and let the cavity empty, as shown by ¹H-NMR.

-In 2002, Maitra and Wunder anchored oligomeric polyethylene oxide (PEO) onto polyhedral oligosilsesquioxanes (POSS) with the aim of increasing conductivity of PEO which served as an

electrolyte.⁹ Other studies have been published based on their method, with no consideration for the porosity of the materials.^{10–12}

-In 2003, Hsu *et al.* showed that a metallocube with small apertures (1.85 Å) could be prepared in the free-guest state and dissolved in a number of solvents (**Figure 1b**).¹³ This could be considered as an example of porous liquid with an inorganic host.

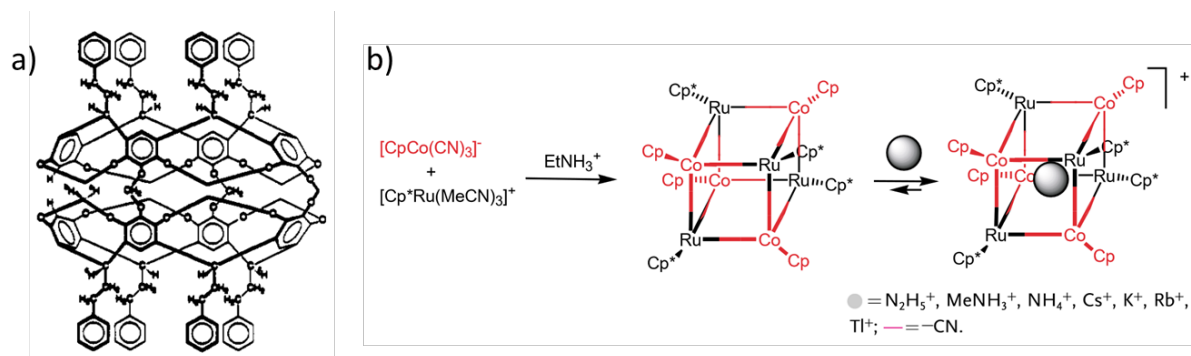


Figure 1. a) Hemicarcerand synthesized by Cram *et al.*,⁷ b) metallocube synthesized by Hsu *et al.*¹³

In 2007, based on the discoveries of Cram *et al.* and Hsu *et al.*, and few other publications, Pr. Stuart L. James and his co-workers described a new class of hybrid materials containing a permanent porosity while behaving as liquids at room (or a specified operating) temperature.³ The concept of porous liquid (PL) was given birth. Grounding on a large knowledge in the supramolecular chemistry field (especially the encapsulation of guests through non-covalent interactions), Chaffee *et al.* dissolved a cryptophane-111 cage in CDCl_3 in 2009, specifying that the solvent was too hindered to penetrate the internal cavity of the cryptophane. Even though it was not named a PL, dihydrogen was proven to be reversibly captured by the cages thanks to $^1\text{H-NMR}$ spectroscopy measurements.¹⁴ Between 2012 and 2014, the same group reported that the alkylation of imine cages could lead to meta-stable PLs by greatly lowering their melting point down to 40 °C.^{15,16} However, the penetration of alkyl chains was thermodynamically favorable, so that the porosity was not permanent.

In 2015, the synthesis of the first three permanent PLs with direct evidence of their porosity opened routes to a new field of research. On one hand, Pr. Sheng Dai and his team modified hollow silica nanospheres with an ionic grafting to create a neat liquid with permanent porosity.¹⁷ On the other hand, James and Cooper's group proposed the dispersion of molecular cages (crown-ether substituted imine cages or a mixture of cages called "scrambled cages") in hindered solvents such as 15-crown-5 or hexachloropropene (**Figure 2**).¹⁸ In both publications, gas sorption experiments were performed to evaluate the potential of these new materials in the fields of gas storage and gas separation.

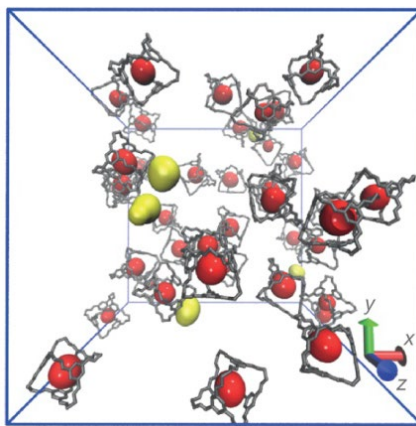


Figure 2. Molecular simulation for the PL made of imine cages in 15-crown-5 at 350 K (the solvent and the crown-ether substituents of the cages are not represented).¹⁸ Yellow and red surfaces indicate pores outside and inside the cages respectively.

1.2. Classification of porous liquids

1.2.1. Historical classification: Type I to Type IV porous liquids

In 2007, Pr. James *et al.* already proposed a standard classification of PLs in three categories.³ Type I PLs are neat liquids exclusively composed of host molecules containing an empty cavity. Type II PLs are host molecules dispersed in a sterically hindered solvent. Finally, Type III PLs are made of solid microporous framework materials dispersed in a sterically hindered solvent. In 2020, Ying Li further explains the difference between a Type II and a Type III PL in terms of molecular hosts dissolved in a bulky solvent for the former, and porous solid particles dispersed in a bulky solvent for the latter.² In 2021, Bennett *et al.* added a new category of PLs: Type IV PLs are neat liquids exclusively composed of host microporous frameworks (**Figure 3**).⁴


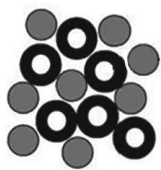

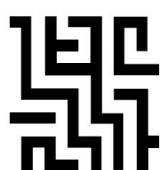
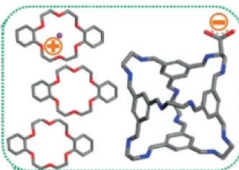
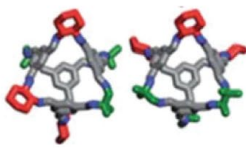
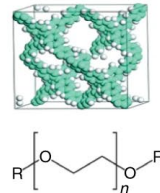
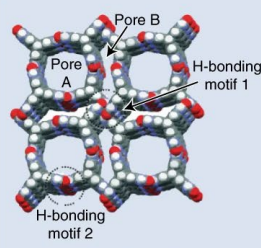
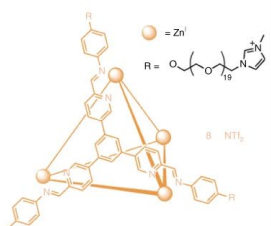
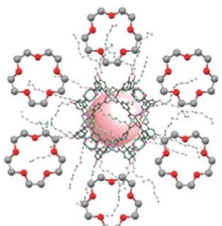
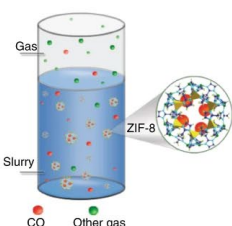
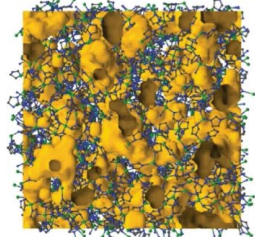
	Type			
	1	2	3	4
Inorganic	 <p>● Hollow SiO₂ — Organosilane — Poly(ethylene glycol) sulfonate</p> <p>Functionalized SiO₂</p>	 <p>Functionalized Mo₁₅₄ rings</p>	 <p>Hydrophobic hollow SiO₂ in water</p>	 <p>Mixed Si/Ge zeolites</p>
Organic	 <p>Crown ether anionic covalent cages</p>	 <p>Scrambled organic cages</p>	 <p>PAFs in oil</p>	 <p>Pore B Pore A H-bonding motif 1 H-bonding motif 2</p> <p>Triptycene trisbenzimidazolone (or other HOFs)</p>
Inorganic-organic	 <p>Functionalized metal-organic polyhedra</p>	 <p>Metal-organic polyhedra in crown ether</p>	 <p>Gas Slurry ZIF-8 CO Other gas</p> <p>ZIF-8 in glycol-2-methylimidazole</p>	 <p>Liquid ZIF-4</p>

Figure 3. Classification of PLs proposed by Bennett *et al.*⁴ Pictures/concepts origins: Inorganic 1 – ref¹⁷; Inorganic 2 – ref¹⁹; Inorganic 3 – ref²⁰; Inorganic 4 – ref²¹; Organic 1 – ref²²; Organic 2 – ref²³; Organic 3 – ref^{24,25}; Organic 4 – ref²⁶; Inorga-Orga 1 – ref²⁷; Inorga-orga 2 – ref²⁸; Inorga-orga 3 – ref²⁹; Inorga-orga 4 – ref³⁰.

To this date, **Type III** PLs are the most described in literature, benefitting from the easiness of their fabrication. The first published Type III PL could be the work of Liu *et al.* in 2014:²⁹ they reported a slurry made of zeolitic imidazolate framework-8 (ZIF-8) suspended in glycol-2-methylimidazole. CO₂ capture was possible, however neither any evidence of the porosity nor any information about the suspension stability were provided. In 2018, three studies reported Type III PLs based on suspension of ZIF-8 (or other microporous framework particles) in bulky ionic liquids (ILs): Costa Gomes *et al.*

dispersed 5% of ZIF-8 in a commercially available phosphonium-based IL (**Figure 4**).³¹ Shan *et al.* dispersed three types of hosts (ZIF-8, ZSM-5 and Silicalite-1) in a bulky IL ([DBU-PEG][NTf₂]).³² Liu *et al.* dispersed wet ZIF-8 in [BPy][NTf₂] (dipped in methanol): this strategy allowed to increase the interaction between the surface of the solid and the IL, thus greatly increasing the stability of the suspension overtime.³³

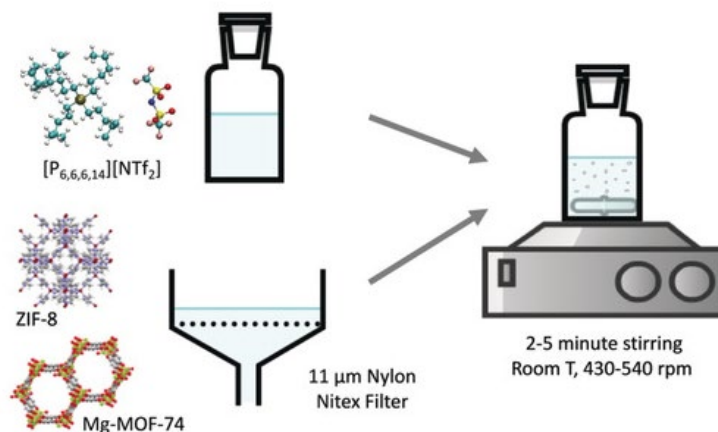


Figure 4. Mixture of ZIF-8 and a phosphonium-based IL forming a PL. Adapted from Ref ³¹.

In the following years, other Type III PLs have been reported, especially thanks to the fame of metalorganic frameworks (MOFs) and ILs.^{34,35} Indeed, ILs are non-volatile, tunable solvents with high structural organization, and ionic interactions are advantageous to play on steric and electrostatic repulsion for the suspension stability. Nowadays, designing a new Type III PL mainly consists in choosing a highly porous MOF with small pore apertures and a low-viscosity IL with large constituents to avoid the penetration of the solvent in the pores.³⁶ In parallel, linear polydimethylsiloxane (PDMS) has also been identified as a good bulky solvent for MOFs, allowing the introduction of mesoporosity in Type III PLs that were exclusively microporous so far.³⁵ More recently, the perspective of fabricating biocompatible PLs has become more palpable: Avila *et al.* reported PLs based on deep eutectic solvents³⁷ while Cahir *et al.* mixed CD-MOF-1 (a biocompatible MOF) in olive oil to find a suspension stable for one day.²⁵ In addition, a stable suspension of hydrophobic porous particles in water could make a very simple and “green” PL.²⁰

Very interestingly, macroporosity has been reported for the first time in a PL, by stabilizing very large cavities of 480 nm in PDMS through a previous non-covalent surface coating to induce particles stabilization.³⁸ Nevertheless, the pore aperture remain as small as 4 Å, thus excluding a number of possible application dealing with larger molecules than gas.

If **Type II** PLs were technically the first PLs to be synthesized,^{7,8,13,14} they generally encounter stability challenges. In addition, a very high solubility of host cages in the solvent is required (less than 20 molecules of solvent for each host molecule) otherwise their porosity are too low to be exploited.³⁹

As written above, organic cages were functionalized with crown-ether groups to better dissolve in the bulky 15-crown-5 ether solvent.¹⁸ Besides, an easiest synthesis route was proposed in the same study considering a mixture of cages made by a one-pot strategy and dissolved in hexachloropropene (**Figure 5**). Four years later, Kearsey *et al.* published a robotic workflow to identify the best cages-solvent combinations based on the same synthesis route with an increased concentration of cages.²³ They found out that halogenated aromatic solvents with molecular weight more than 100 g/mol were more likely to be good candidates. However, the reversibility of the imine bond formation was detected as a problem when using imine cages for gas sorption.⁴⁰

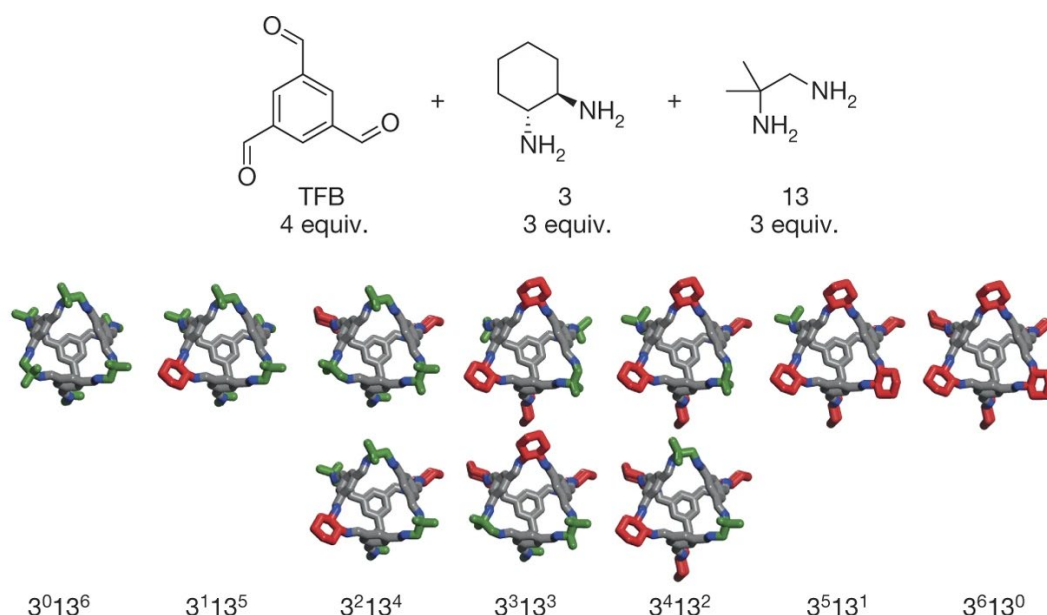


Figure 5. Synthesis of PLs based on « scrambled » cages in hexachloropropene.¹⁸

In 2020, Deng *et al.* proposed a Type II PL with a metal-organic polyhedra (MOP-18) in 15-crown-5 solvent.²⁸ Unlike MOFs, MOP-18 could be dissolved as individual cages (5 nm large, with an inner cavity of 1.4 nm) above 40 °C. Similarly, Jie *et al.* mixed an anionic porous organic cage (POC) with an excess of 15-crown-5 to obtain a PL.²² Other promising candidates to form Type II PLs would be cyclodextrins, cucurbiturils and pillararenes.⁴⁰

Type I PLs are the most complex to synthesize. First attempts used cyclodextrins or imine cages, modified with long alkane chains.^{15,16,41} However, they suffered from penetration of the organic

moieties inside the pores. A solution could be to use branched alkanes, but Pr. James' group also showed the counterintuitive result that terminal-branched alkanes were responsible for an increase in the melting point of the final material instead of lowering it. Alternatively, it seems that the covalent grafting of a neutral polymer (polypropylene glycol) to a 2 nm copper coordination nanocage through an "arm-first" approach prevented the penetration of the chains.⁴²

In 2015, Zhang *et al.* explored a new synthesis route based on ~20 nm large hollow silica particles (HSPs) undergoing a surface modification with a large cationic organosilicon (**Figure 6**).¹⁷ This grafter was not able to penetrate the large pore apertures of the HSP (1.9 nm). The addition of a sulfonated polyethylene glycol derivative bonded to the cation by the mean of ionic interactions conducted to the fabrication of a mesoporous ionic liquid. This strategy presents a great tunability, by playing on both the host nature (that can be organic or inorganic) and the organic moieties. For instance, Liu *et al.* proposed another porous ionic liquid with a surface modified silicalite as a host⁴³ while Kumar *et al.* invented the first anisotropic PL based on silica nanorods.⁴⁴ By changing the organic corona and canopy, new silica-based PLs were proposed for carbon capture.^{45,46}

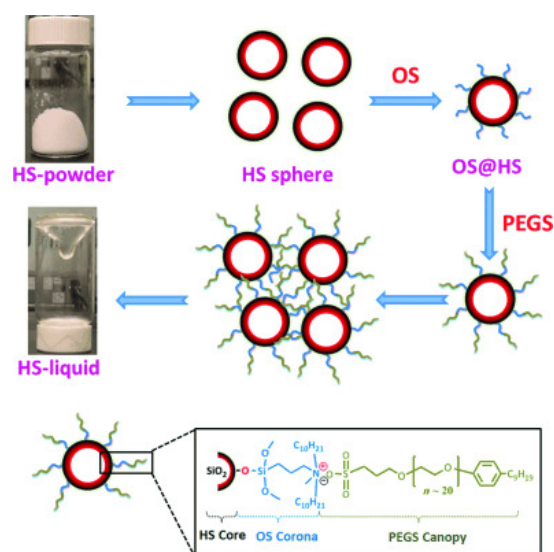


Figure 6. The first PL based on HSPs, modified by a hindered cationic corona and surrounded by a canopy formed by a sulfonated polyethylene glycol derivative.¹⁷

Two other examples of porous ionic liquids were reported by the same group: in 2017, hollow carbon particles were modified by the non-covalent anchoring of a polymerized ionic liquid at their surface.⁴⁷ In 2020, they made an IL made of a mixture of 18-crown-6/potassium cationic complex with anionic POCs (**Figure 7**).²² Their work attempted to generalize this supramolecular complexation strategy, but a 2:1 mixture of 15-crown-5 with POCs only resulted in a solid and it required an excess of solvent to form a Type II PL instead.

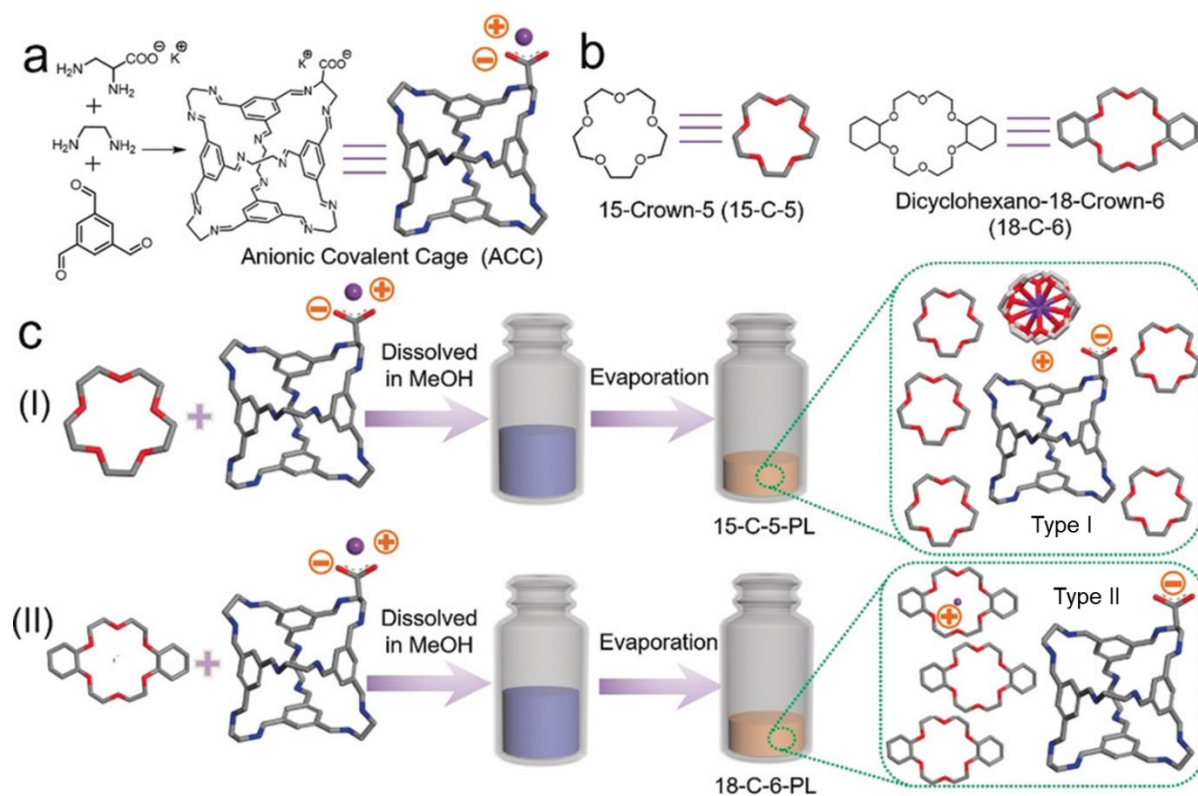


Figure 7. The synthesis of two PLs following a similar but different approach: (I) the salt made of an imine anionic cage with a complex cation led to the preparation of a Type I PL, (II) while the mixture of a similar salt changing the nature of the ligand necessitated an excess of this ligand acting as a solvent to obtain a Type II PL. Adapted from Ref ²².

Type IV PLs remain theoretical: they are based on a study showing the concept of liquid MOFs,³⁰ but at very high temperatures (over 1000 °C).

This historical classification displays several weaknesses. In fact, the difference between a Type II and Type III PL only relies on the contrast between dissolution and dispersion, when the concept is the same: introducing host particles inside a bulky solvent at the highest possible concentration. Of course, a soluble compound will not confer the same properties than an insoluble one,⁴⁸ but the classification was meant to rely only on conceptual notions.

More importantly, the silica-based PL synthesized by Pr. Dai and coworkers in 2015 (**Figure 6**)¹⁷ was claimed to be a neat Type I PL, although it is no salt like ILs. Instead, it could be seen as charged colloids in suspension in the anionic medium. This is even more possible when switching the nature of the interaction toward weaker ones. Only the comparison of the ionic strength with the energy required for molecular displacement could give the answer. Indeed, a simulation of similar systems has been performed⁴⁹ and it was found that linear canopies were strongly bonded to the corona (separated by a distance of 2.45 Å) with a small proportion of molecules being nearly twice more distant. However, the

result for branched canopy was far more unclear, with a very smooth peak in the radial density function at 2.61 Å and another large window between 3 and 5 Å, suggesting an increased freedom in the motion of the canopy likely due to steric hindrance.

Two carbon-based PLs have been reported so far.^{47,50} In the first case, hollow carbon particles were modified by a non-covalent π -cation interaction with an IL, followed by the replacement of the small anion by a bulky pegylated anion to ensure the liquid behavior. This material was labelled as a Type I PL (even though another publication mentioned it as a Type III PL instead²). In the second case, hollow carbon particles were mixed with a polymerized ionic liquid displaying similar surface interactions, but it was tagged as a Type III PL, probably owing to the synthesis route (mixture of a host and a solvent), rather than based on conceptual notions of the liquid behavior. They assume that the cationic head is orientated toward the particle surface, tacitly implicating a partial dissociation of the anion to make a layer of counter anions. With this model, the PL should be closer to a Type I PL.

Furthermore, the classification misses the possibility of obtaining a liquid matrix that would not be made of discrete solvent molecules but by a liquid network instead (*e.g.*, a partially cross-linked polymer). However, Bennett *et al.* introduced the concept of liquid porous networks and this is why they added the Type IV category, completely distinct from the Type I.⁴

1.2.2. New classification: Class A to Class D porous liquids

In this regard, a new classification could be suggested, intended to be more faithful to the interactions at play conferring the liquid state, and making it possible to extend the concept to as yet unsynthesized materials (**Figure 8**):

Class A: discrete hosts that are directly liquid at room temperature (or below 100 °C).

Class B: discrete hosts dissolved or dispersed in a solvent made of discrete molecules, which is not able to penetrate the pores of the hosts.

Class C: discrete hosts dispersed in a liquid network at room temperature (or below 100 °C).

Class D: porous network that is directly liquid at room temperature (or below 100 °C).

It should be noticed here that the terms “host” is deliberately vague; its definition is discussed in Section 1.3.

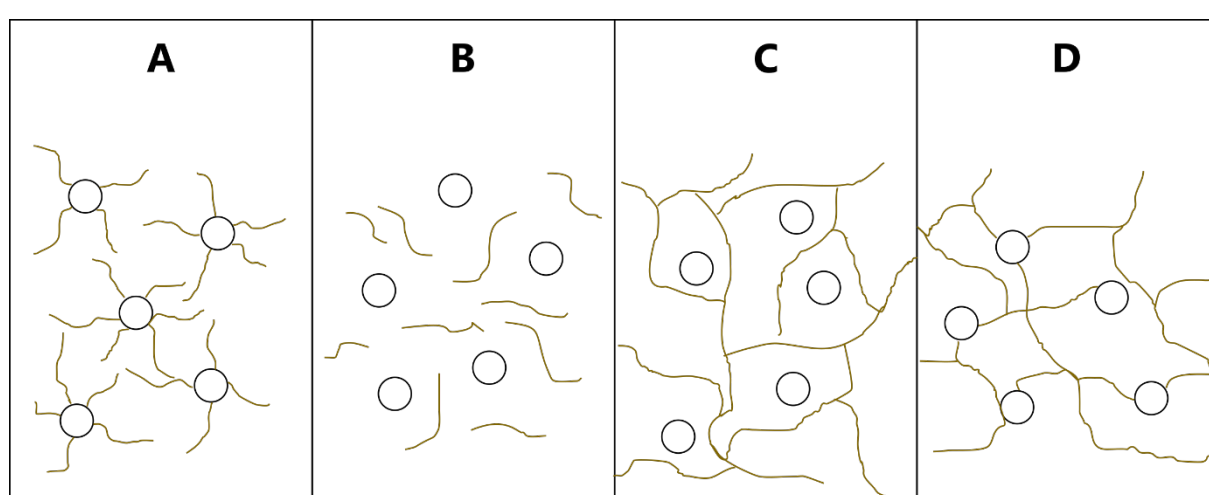


Figure 8. Four conceptual types of PLs ranged according to the origin of fluidity. Solid hosts (molecular, supramolecular, or particles) are represented by hollow circles; organic (or eventually inorganic?) moieties essential to bring fluidity are schemed by brown lines.

In particular, this new classification treats molecular cages and porous solid frameworks alike, given that they are seen as discrete molecules differing from each other by their size scale. In contrast, it focuses on the way used to obtain the liquid behavior, that could be:

- i) By lowering the melting point of a porous solid (Classes A and D). Porous ionic liquids or liquid alkylated cages have this common feature.
- ii) By the solvation of porous hosts (Classes B and C) to form stable enough solutions or suspensions. This process can be observed with discrete bulky solvent molecules (Class B) but also with liquid networks such as partially reticulated polymers trapping porous hosts (Class C).

Note that the hosts can be microporous, mesoporous or even macroporous (see the Section 2 for the definitions). In Class B, the solvent could also be aqueous, provided that hosts are hydrophobic enough to avoid water penetration. In Classes C and D, the network could be formed by chains entanglements or by partial cross-linking of polymers for instance.

Table 1. State-of-the-art of PLs allocated in the new classification.

Class A	Class B	Class C	Class D
Zhang <i>et al.</i> (2015) ¹⁷	Giri <i>et al.</i> (2015) ¹⁸	[MMMs like (first one in 1973) ⁵¹]	Cardoen and Coughlin (2004) ¹⁰
Li <i>et al.</i> (2017) ⁴⁷	Jie <i>et al.</i> (2020) ²²		
Shi <i>et al.</i> (2018) ⁴⁵	Costa Gomes <i>et al.</i> (2018) ³¹		Carne-Sanchez <i>et al.</i> (2018) (gel) ⁵²
Kumar <i>et al.</i> (2019) ⁴⁴	Liu <i>et al.</i> (2018) ³³		Gaillac <i>et al.</i> (2017) (high T°) ³⁰
Liu <i>et al.</i> (2019) ⁴³	Shan <i>et al.</i> (2018) ³²		
Jie <i>et al.</i> (2020) ²²	He <i>et al.</i> (2019) ³⁵		
Ma <i>et al.</i> (2020) ²⁷	Kearsey <i>et al.</i> (2019) ²³		Randriamahefa <i>et al.</i> (2009) ¹²
Ben Ghazi Bouvrande <i>et al.</i> (2021) ⁵⁴	Li <i>et al.</i> (2019) ³⁴		Wang <i>et al.</i> (2021) (glue) ⁵³
Wang <i>et al.</i> (2021) ^{53,55}	Cahir <i>et al.</i> (2020) ²⁵		
Sheng <i>et al.</i> (2022) ⁴⁶	Deng <i>et al.</i> (2020) ²⁸		
Lai <i>et al.</i> (2023) ⁴²	Avila <i>et al.</i> (2023) ³⁷		
Li <i>et al.</i> (2023) ^{56?}	Dinker <i>et al.</i> (2023) ⁴⁸		
Yang <i>et al.</i> (2023) ⁵⁷	Xin <i>et al.</i> (2023) ⁵⁸		
Ginot <i>et al.</i> (2024) ^{59,60}	Corsini <i>et al.</i> (2024) ³⁶		

Table 1 aims to summarize the state-of-the-art with the terms of the suggested classification. To date, only Class A PLs and Class B PLs were synthesized, while Class C PLs and Class D PLs mainly remain as concepts. Bennett *et al.* predicted that heating mixed matrix membranes (MMMs) could lead to the fabrication of PLs under certain conditions.⁴

Whatever the classification, the field of PLs would benefit from a strong definition with well-defined limits.

1.3. Definition and frontiers

Since PLs are a very recent concept, it is necessary to insert it inside the global context of research in material chemistry. For that, there are many frontiers to fix in the definition of a PL. For instance, the physical state (liquid), viscosity and melting temperature have to be well defined, as well as porosity. Speaking of suspensions and polymers, the notion of stability overtime is also essential.

The literature focused on three key notions that were essential for a liquid to be tagged as porous:¹

- The porosity must be permanent and open, so there is a way to experimentally prove it,
- The concentration of pores must be high enough to exhibit a significant gas uptake,
- The melting temperature must be below or close to the room temperature (or at a specified operating temperature).

For instance, Egleston *et al.* excludes solutions of fullerenes from the definition of PLs because these molecular compounds contain void but with no windows to access the cavity.¹ However, if proven, a close porosity should not be discarded from the definition of PLs at a fundamental level because it could confer other physicochemical properties to the material that do not meet straightforward applications. For this reason, the term “host” used in the literature, and in this report, may not be the most adequate to point a domain containing permanent pores.

The physical state of PLs must be liquid. This means that porous gels or glasses must be banished from the definition as well, in contradiction with a previous publication.² In this context, a PL must flow through the effect of gravity. This guideline seems reasonable especially for Class A PLs, Class C PLs, and Class D PLs because not all complex hybrid materials have obvious melting points. Following the definition of ILs or DES, it should be convenient to fix that the liquid behavior is to be obtained near the room temperature, or at least below 100 °C. Hence, the liquid MOF reported by Gaillac *et al.* in 2017³⁰ can hardly fit this characteristic. However, this does not exclude that other liquid MOFs or other organic or inorganic frameworks with very low melting point could be reported in the future, as predicted by Bennett *et al.* in 2021.⁴

The term “permanent porosity” is also confusing because it can never be. When considering porous suspensions or solutions, a notion of the stability overtime is required. For instance, the work of Liu *et al.* is often mentioned as a precursor of Type III PL, even if the material they report is a slurry, with no information about its stability.²⁹ As a benchmark, one could fix that a PL has to be stable on the shelf for a time fitting to the target application. If this feature is not respected, at least a notion of the suspension stability must be provided. This should also be applied to possibly metastable polymers undergoing very slow cross-linking, thus modifying the physical state from liquid to glass overtime, or to other complex systems whose viscosity increases overtime. In addition, pores initially empty might be slowly filled by the solvent or any surface chains grafted to make them liquid. Molecular dynamic can help predicting such a behavior: for instance, Giri *et al.* found no minimum of energy when the solvent is inside the imine cage, suggesting that the porosity will be permanent in this regard.¹⁸ Egleston *et al.* proposed that any gas uptake should be reversible to prove the permanent porosity of a PL.¹ In their regard, the free-guest state is essential to separate PLs from other dissolved coordination

cages used in many applications to this date.¹⁴ However, very hygroscopic materials such as porous silica particles might be very hard to empty once they are surrounded by an organic matrix. If so, a liquid might be more suitable to reversibly replace water than a gas. In addition, the liquid MOF reported in 2017 technically does not show permanent porosity but a transient one, because ligands are constantly moving when reassociating with the metal ions.³⁹

Therefore, it can be admitted that a PL should be liquid below 100 °C (it flows under gravity), and stable for at least six months (or a specified time duration). The presence of porosity should not be restrained to open pores existing in the free-guest state, because pores are just holes (absence of matter) in a solid structure (molecular, supramolecular, or particles), and the pores filling with a continuous fluid phase (gas or liquid) do not suppress this intrinsic porosity. In the case of solvent (or grafted organic moieties) penetration, porosity should be considered if it is still possible to chase them away from pores so other fluid guests can enter. For reader's attention, a finer definition of porosity and the difference with permeability are given in the following section.

2. Porosity and permeability of porous liquids

2.1. Definition

Porosity and permeability are notions generally associated to porous solids, which belong to "divided materials". Porosity is the volume ratio of pores over the total volume of the material, whereas permeability expresses the ability of the material to transmit fluids. A very porous solid like clay can show a low permeability because the pores are not well connected.

According to Rouquerol *et al.*,⁶¹ pores are channels or cavities contained in a material, which increase the interface between the porous matter and a surrounding fluid phase (gas or liquid). Their accessibility depends on their size. Pores are classified into three categories related to the size scale they belong to:

- Micropores have characteristic width below 2 nm,
- Mesopores range between 2 and 50 nm,
- Macropores are larger than 50 nm.

Among micropores, the ultramicropores are admitted to be pores less than three times larger than a molecule of nitrogen (or other probing gas). Additionally, pores may be accessible to guest molecules (open porosity) or not (close porosity).

In conventional liquids, transient cavities may be created by the mean of thermal motion: they are small and short-lived, explaining little gas uptake in some cases.⁶² This is why the introduction of a permanent porosity inside a liquid opens to very promising applications. However, the apprehension

of porosity in the liquid state might be slightly different from the one in the solid state.¹ Indeed, the solid state can host both extrinsic and intrinsic porosity due to non-efficient packing and internal cavities respectively, while a liquid's permanent porosity can be nothing but intrinsic.

The kinetics of diffusion of a fluid (gas or liquid) inside a porous material is related to the permeability of the latter. Among the different characterization methods mentioned below, some addresses more the question of porosity and others the permeability.

2.2. Methods for porosity and permeability assessment

Experimental methods were the first employed to assess the porosity of PLs. Stemming from the supramolecular coordination chemistry, ¹H-NMR has often been used to demonstrate the reversibility of host-guest interactions.^{7,13,14} This method shows the advantages of being quantitative and suitable for volatile PLs. However, all pores may not be accessible, depending on the guest size, and complex materials including the presence of long polymers can hardly be investigated.

The density of a PL could also be a good method to assess the presence of porosity,³¹ especially for Class B and C PLs when the concentration of hosts is well-known. To be accurate, this method requires to first ensuring that the PL is correctly emptied from any guest, as well as completely dried.

Positron annihilation lifetime spectroscopy (PALS) has raised as a method of choice to directly probe the porosity of a liquid material.^{1,18,22,27,32,33,43} Indeed, in the case of the first "Type II" PL (Class B PL) the resulting spectrum was found to be a linear combination of the pure solvent and the pure host taken separately. However, the technique is not widely spread, and the measure is performed under high vacuum, therefore not possible for PLs with any vapor pressure.

Nitrogen sorption measurements are the most famous method to quantify the porosity of solids. It is based on the assumption that nitrogen is small enough to access any open pore. However, when transferred to non-volatile PLs, the very low temperature imposed by the method (77 K) often leads to the blockage of the PLs' structure, thus creating an impermeable barrier.^{44,60} Thus, the mobility of hindered organic chains is essential to maintain a good permeability to nitrogen. In one case however, sorption results could be obtained with longer equilibration times (up to 120 s for each P/P_0 point), suggesting a very slow diffusion kinetics.⁴² In this regard, CO₂ sorption made at 0 °C has been used to prove that sorption was possible in a nanorods-based PL.⁴⁴ It was compared with the pure organic matrix so as to show a great increase (~20 times) in the sorbed volume of gas when introducing the nanorods as hosts. It was interesting to note that a limited pressure was required in this case ($P/P_0 = 0.03$ with $P_0 = 34.7$ bar). Increasing the pressure up to 5 bar could be realized with the use of an intelligent gravimetric analyzer consisting of a microbalance equipped with a hermetic chamber with a precise temperature and pressure control.⁶³ It was found that the quantity of gas adsorbed increased

linearly with the proportion of MOF within the IL, independently of the MOF type and the gas nature. A careful precaution is required when concluding on any permanent porosity based on gas uptake measurements. Indeed, a non-inert gas like quadrupolar CO₂ can have different affinities with the constituents of a mixture or hybrid material and the addition of a non-porous guest might also imply a great increase in gas uptake when compared to the solvent alone, just because of the addition of a new external surface.¹ Also, it is well-known that CO₂ displays a strong variation of solubility in non-porous ILs by only changing the water content.⁶⁴ In the case of Class D PLs, no comparison would be possible with any solvent or organic matrix as it can be considered for other PLs.

Small-angle X-ray scattering (SAXS) and small-angle neutron scattering (SANS) are the only techniques that can quantify close porosity. In fact, fitting SAXS or SANS curves give the scattering length density of the probed material, that is tightly linked to its porosity. In other words, the presence of pores, even inaccessible to external fluids, will significantly change the curve shape. If this technique can be used for volatile PLs, it is somehow restrained to a certain size scale (*i.e.* between 1 and 100 nm). Moreover, if the material contains both full and empty pores, the proportion can be hard to determine, and it would require an additional experiment varying the contrast between scattering length densities to “turn off” the signal of the porous host, and isolate the signal of the close porosity.

Very often, measurements of gas sorption are coupled with molecular dynamic simulations to better locate the porosity in the PL. For instance, Giri *et al.* show that no minimum of energy could be obtained when the solvent is inside the pores: thus, the penetration of the solvent within the cavity is not thermodynamically favorable.¹⁸ They also demonstrated by this method that the same organic cages grafted with long alkyl chains lead to a non-porous liquid because the alkyl chains were more able to penetrate the cavity. As a result, they claim that a well-designed “Type II” PL (Class B PL) is more likely to be a good PL than a comparable “Type I” PL (Class A PL). Li *et al.* used molecular simulation to show that the use of branched ILs helped the formation of PLs by preventing interpenetration.³⁴ Similarly, Corsini *et al.* predicted that a suspension of ZIF-8 in a deep eutectic solvent allowed the retention of porosity, not only thanks to Coulomb cohesion forces between ions (the hydrogen acceptor being a salt) but also for the low affinity of glycerol (the hydrogen donor) for ZIF-8 (considered as a hydrophobic MOF).³⁶ Intriguingly, the mobility of glycerol molecules in accessible pores was increased by the confinement effect.

Very recently, SANS could be employed as a technique to assess the permeability of a silica-based PL to polar liquids (see Chapter III, Section 1.2.2 for more details, and Appendix G).⁶⁰ This was invaluable to consider applications dealing with liquid diffusion inside a porous medium, like liquid-liquid extraction. While investigating gas sorption and selectivity, the question of permeability has also

been approached in a number of studies.^{28,42} For instance, the fabrication of PL-containing membranes of a defined thickness allows their characterization in terms of permeance for each gas (quantity of gas passing through the membrane per unit of time and surface of material), such that selectivity between two gases can easily be defined as the ratio of permeances. This principle may be applied for liquids as well: by measuring the conductivity of an ion-containing solution passing through the membrane, the diffusion of the liquid and the ions may be quantified.

Over the years, it has then appeared that porosity and permeability assessment of PLs – while indispensable – has to be chosen regarding the physicochemical properties of the PL (especially viscosity and vapor pressure, but also the size scale of porous items) and in coherence with the targeted application, when appropriate.

3. Comprehension of the liquid behavior

From the first syntheses of PLs, the desire to get more understanding about what causes the liquid behavior has been existing, especially concerning neat liquids. The first neat PL synthesized by Pr. James' group was only liquid when grafting sufficiently long alkyl chains at the surface of the molecular cages.^{15,16} Given that this strategy also increased the chance of interpenetration, they investigated the influence of branched alkanes. They found that terminal-branched alkanes raised the melting point of the PL, in a counterintuitive way. The same conclusion was drawn by molecular dynamics simulations performed on PLs made of hollow silica particles and ionic corona-canopy organic matrix.⁴⁹ The study even concludes that long and linear canopies must be adopted to both decrease the viscosity and the pore occupancy (setting a pore size of 2.4 nm which is quite large for such systems already tested experimentally and providing a value of 1.9 nm¹⁷). However, another study about a Class B PL made of a mixture of poly(dimethylsiloxane) and MOF reported that the use of a star polymer instead of its linear counterpart, lead to less viscous PLs.³⁵ In 2023, Lai *et al.* used a linear and neutral polymer but capable of hydrogen bonding, for covalent grafting onto nanocages.⁴² Based on distances calculations, they showed that the brushes did not penetrate the nanocage. Depending on the polymer length, they obtained either porous solids, glasses, gels or liquids.

Ionic interactions were also believed to open a path toward the liquid behavior. In 2015, Zhang *et al.* combined long organic moieties with ionic interactions.¹⁷ In 2020, Jie *et al.* demonstrated the feasibility of making a porous ionic liquid based on ionic interactions between an anionic molecular cage and a bulky cation (metal complex with crown-ether as ligand), with no long alkyl chains.²² It was classified as a Type I PL (and belongs to the Class A herein) because the porous molecular host was acting as the anionic part of an IL, such that no extra-solvent was required. Still, the similarity of this system with the one described by Giri *et al.* in 2015¹⁸ (a suspension made of imine cages solubilized in

a crown-ether solvent thanks to other crown-ether functionalization) raises more interrogation about the nature of interactions required for the liquid behavior. In this particular case, the presence of pair ions probably leads to a zero vapor pressure PL whereas the suspension in crown-ether undergoes degradation (crown-ether evaporates more easily since the melting temperature of 15-crown-5 is 96 °C, and a solid residue remains). The role of ionic strength was also studied on non-porous ionic systems based on silica nanoparticles (called NIMs, see Chapter II), and it was found that an isostearate canopy was less efficient in providing good fluidity to the system than a sulfonate.⁶⁵

Impressively, Li *et al.* recently reported a porous mixture made of a MOF in a stimuli-responsive IL (Figure 9). Shearing the liquid led to an organization of the molecules in the IL provoking precipitation, while heating the solid allowed reversibility toward the PL.⁶⁶

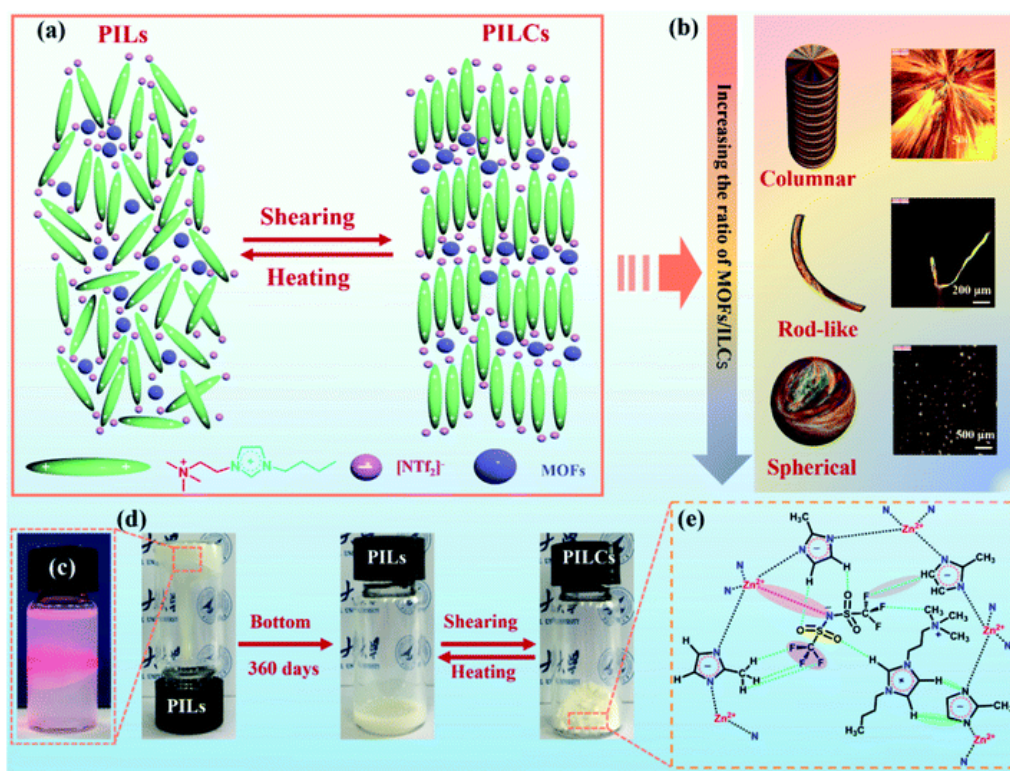


Figure 9. Dual-stimuli-responsive PL made of a mixture of MOFs in an IL.⁶⁶ A simple shearing of the suspension triggers the liquid-to-solid transition, which is reversible through moderate heating.

The reviewing article of Bennett *et al.* focuses the regards toward the solid-liquid transitions of complex materials.⁴ They observe that a supercooled PL could easily lead to a porous glass, especially when speaking of neat liquids. For this purpose, a reversible glass transition must be observed, while maintaining the porosity. They also regard porous solids as very organized materials, in which some disorder shall be introduced to transit their physical state toward glasses, gels and even liquids. If this is aligned with the publication of Li *et al.* above,⁶⁶ it may be in contradiction with the fact previously

discussed that branched alkanes are likely to increase the melting temperature with respect to their linear counterpart.

Besides, in the case of colloidal suspensions, the stability of PLs might be explained by the Derjaguin-Landau-Verwey-Overbeek (DLVO) theory in terms of attractive and repulsive forces. This theory is often applied to explain the stability of surface charged colloids in suspension. It accounts for both attractive Van Der Waals and repulsive Coulomb forces occurring from the electrical double-layer of interacting particles. However, it seems that there has not been used of this theory for porous suspensions until now.

Molecular dynamics can be judiciously employed to help bringing more fundamental comprehension of the liquid behavior. For an ionic PL made of hollow silica particles, Sheng *et al.* showed that a sufficient grafting density of surface silanol groups is necessary to prevent aggregation.⁶⁷ Indeed, the more polymeric chains are present, the higher the distance between two particles. This was consistent with experimental studies concerning polymeric brushes grafted at the surface of nanoparticles: the higher the grafting density, the more elongated the brushes.^{42,68} Also, it was shown that a larger pore apertures resulted in more viscous PLs assigned to strong interactions between the canopy and the pore channels.⁶⁹

All in all, empiric results and simulations both concede that the matrix:host weight ratio seems to significantly control the physical state of a porous hybrid material, be it a suspension or a neat system with no solvent. Very probably, the viscosity of PLs would decrease when *i)* increasing the free volume, and *ii)* increasing chains flexibility. Alike common salts, ionic interactions alone are not sufficient to bring the liquid state because they cannot avoid structural organization of short molecules. However, they might be able to reduce the matrix:host ratio necessary for obtaining a liquid. Even if this hypothesis is verified thereafter, it is most probable that very fluid porous ionic liquids with low viscosity would be harder to obtain (as it is the case for ILs). Although hydrogen bonding are not well studied yet, it would be interesting to apply the principle of deep eutectic solvents to PLs.³⁶ Finally, other considerations like the use of branched molecules deserve a careful attention especially when their role depends on the PL class (suspension or neat liquid).

It is believed that a better knowledge about specific features held by PLs (fluidity, porosity, permeability, among others) should orientate researchers toward suitable applications.

4. Applications of porous liquids

4.1. Current studies

Most of the studies cited before, in the wake of pioneers, evaluated the PLs as candidates for gas capture, storage and separation. The main applications have focused on CO₂ capture and N₂/CO₂ separation, because this acidic gas usually shows high interactions with liquids (**Figure 10**)^{17,25,32,43,45,48,53,55,58,70}. Again, molecular simulations can help understanding the thermodynamics and kinetics of gas diffusion and storage.⁷¹ Going further, the catalytic activity for CO₂ cycloaddition has also been reported.⁴⁸

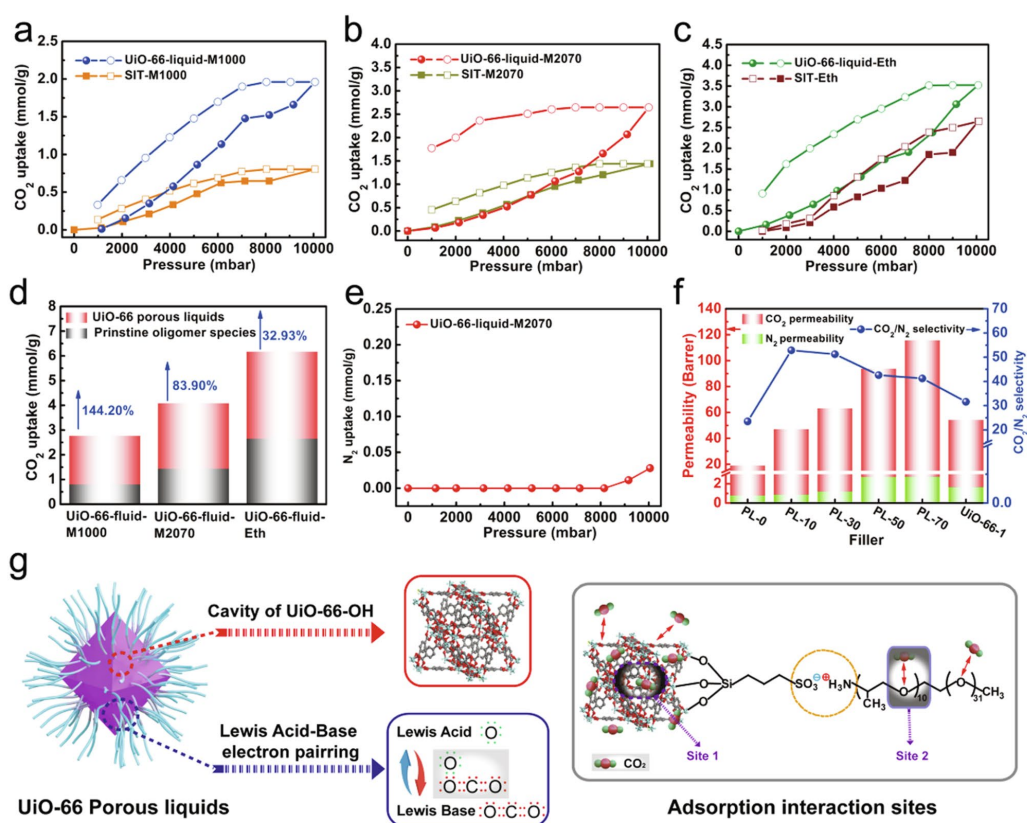


Figure 10. CO₂ adsorption-desorption behavior of a Class A PL. Reproduced from reference ⁵⁵.

Nevertheless, other gases were at the core of some works as well: Chaffee *et al.* studied the adsorption of hydrocarbon and other gases (including hydrogen, xenon and CO₂).¹⁴ They found that cryptophane-111 had a good affinity toward methane and smallest hydrocarbons, suggesting a good selectivity between the latter and bigger gas like ethylene or ethane. Giri *et al.* were also interested in methane, and supported their results with molecular simulations.¹⁸ Greenaway *et al.* measured the performance of similar PLs in xenon and SF₆ adsorption and found a very high pore occupancy (72% and 74%, respectively).⁷² Kearsley *et al.* considered releasing xenon from the PL thanks to thermal stimulation. They also suggested to store the gas by cooling the PL and forming a gel.²³ Cahir *et al.* used

Class B PLs for the gas separation of ethane and ethene.²⁵ They specified that no processes based on a liquid phase were currently available for such a separation because of the lack of a selective solvent. They also indicated that their biocompatible PLs could find applications in the medical field, with no further investigation.

To broaden the range of available solutions, several works proposed to make new membranes containing PLs and used them for gas separation.^{17,28,55,73} On the one hand, PLs can be directly anchored onto a support, such as polymeric membranes or nanoslits of graphene oxide. In this latter case, a great increase in gas permeability has been obtained thanks to the presence of the hollow cavities (**Figure 11**).²⁸ On the other hand, PLs can be used as homogeneous fillers for mixed matrix membranes (MMMs). This strategy consists in mixing the PL with a solution of a polymeric membrane, before drop-casting it to obtain a homogeneous membrane. It was shown that the use of a PL instead of the pure microporous solid as a filler avoided particle aggregation, increased the CO₂/N₂ selectivity and reduced MMM's swelling.^{55,73}

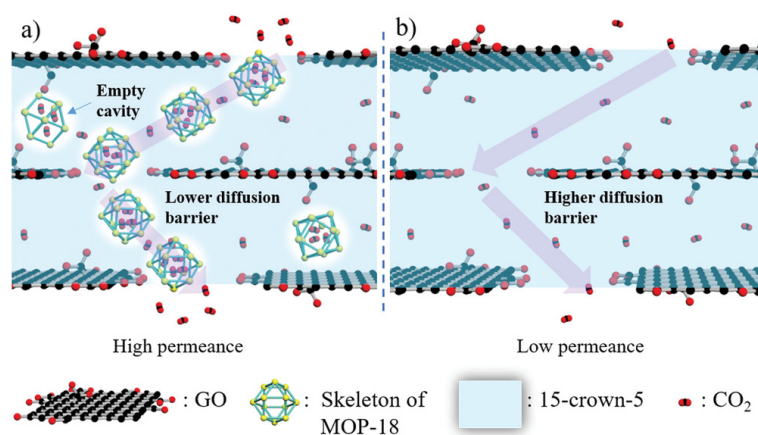


Figure 11. Scheme of CO₂ molecules passing through **a)** PL/graphene oxide (GO) membrane and **b)** 15-crown-5/graphene oxide membrane. The alkane chains in the nanocages are omitted for clarity. Reproduced from reference ²⁸.

In 2020, Ma *et al.* encapsulated small non-gaseous molecules into a porous ionic liquid based on tetrahedral coordination cages for the first time.²⁷ In 2019, Hemming *et al.* showed the possibility of encapsulating gold, platinum, and palladium nanoparticles inside silica-based PLs then acting as catalysts (**Figure 12**).^{74–76} Last year, two studies presented Class A PLs and Class B PLs applied to the desulfurization of fuel oil.^{77,78} In both cases, they evidenced the role of the quaternary ammonium in the extraction-adsorption process of sulfides.

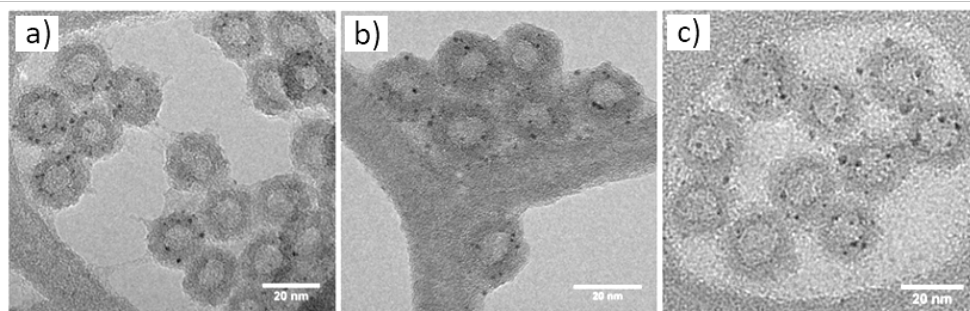


Figure 12. TEM images of a silica-based PL impregnated with **a) Au**, **b) Pt** and **c) Pd**. Reproduced from reference ⁷⁴.

More recently, the apparition of stimuli-responsive PLs proves the very fast achievements in the fields of PLs.⁶⁶ Dinker *et al.* published a simultaneously photo- and thermoresponsive Class B PL that could uptake and release CO₂ thanks to a reversible cis-trans isomerization of the azo-functionalized ligand used to make the nanocage.^{56,79}

4.2. Potential future applications

Obviously, the next step after CO₂ capture would be its exploitation through electrochemical reduction to making valuable molecules such as methane, ethylene, formic acid, and carbon monoxide.⁸⁰ Catalytic cycles should also be considered, based on already existing research in this field.^{48,81,82} Given that metallic nanoparticles had already been encapsulated in a PL, one could think of applying lab-in-shell chemistry in PLs for CO₂ processing as well as for all kind of molecular species.^{74,83}

Considering the numerous employments of hollow silica particles described in literature (often requiring a dispersing phase), it would be worthy to look into the potentiality of silica-based PLs in the same fields. Hence, the fabrication of functional superhydrophobic surfaces,^{84–86} stable antibacterial coatings,⁸⁷ smart inks and paints,^{88,89} and functional glasses, as well as cosmetics,⁹⁰ catalysis in hydrophilic or hydrophobic media,^{74,91,92} and solvent extraction are all applications for which these innovative liquid materials could be suitable, along with gas sorption, storage and separation.

Furthermore, PLs could meet applications in electrical energy storage, for instance benefitting from the properties of MOFs and ILs in this domain.⁹³ In Li-ion batteries, they could act as electrolytes or be supported onto an electrode. They might also be used as supercapacitors. Besides, they could also serve in drug delivery or other medical applications, on condition that more research is to be conducted about biocompatible PLs. As predicted by Bennett *et al.* in 2021, the extension of stimuli-responsive PLs might open route toward applications in sensing and information storage as well.⁴

5. Potential and challenges for porous liquids in liquid-liquid extraction of metals

5.1. Introduction to techniques of metal extraction

In 2021, 2.8 billion tons of metal have been extracted from the mine, including 2.6 billion tons of iron.⁹⁴ After ore processing, the metals are generally dissolved in aqueous solutions, from which the selected species will be extracted. For this, two types of processes for metal extraction are widely implemented in industry: liquid-liquid extraction (LLE) and solid-liquid extraction (SLE). As presented in this section, both techniques have advantages and drawbacks, and the choice will depend on the nature of the metal to extract, the purity to achieve, the competitive compounds that are present, and the medium in which they are contained.

5.1.1. Liquid-liquid extraction

Liquid-liquid extraction (LLE) is a widespread industrial technique used to separate metals or organic molecules from a bulk containing competitive molecules, ions or complexes. In general, it consists in contacting an organic phase containing extracting agents with an aqueous phase containing the targeted metal(s) or molecule(s) (**Figure 13**). In the particular case of metals, redox chemistry and pH-sensitive complexes usually get involved to enhance selectivity and efficiency.

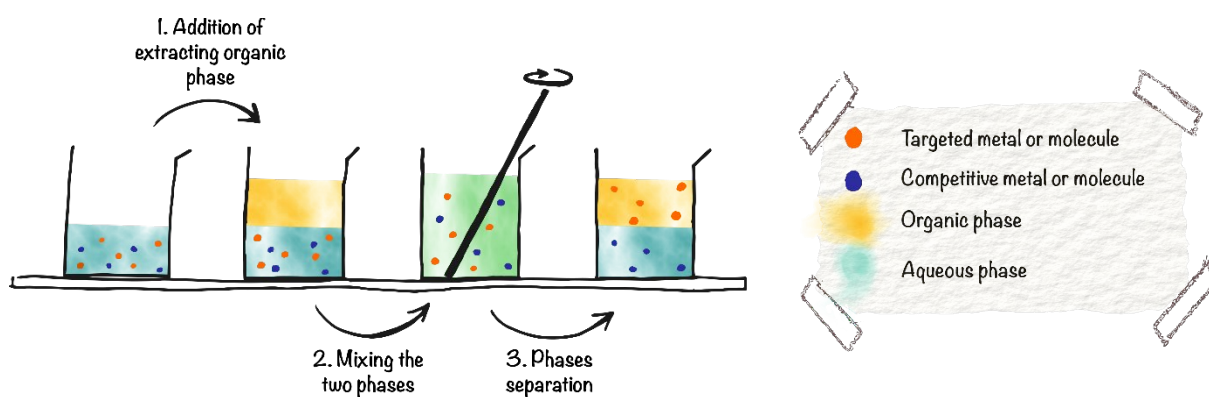
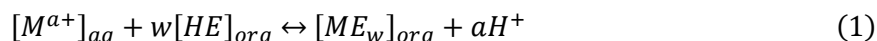


Figure 13. The principle of LLE.

However, the use of large volumes of organic solvents at industrial scales results in a high environmental impact due to their volatility and toxicity. In many cases, the formation of a third phase in the process forces the introduction of phase modifiers to avoid solid deposits and important losses. Another drawback lies in the potential dependence to supply. Moreover, in some cases like the separation of rare-earth elements, the selectivity of conventional LLE can be poor.

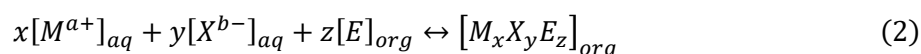
Two extraction mechanisms can take place during a LLE process: ionic exchange or solvation. In the case of metal extraction, ionic exchanges are often cationic (Chemical equation 1). They occur when

the ligands can easily lose protons, so the cationic metal will exchange with protons at the water/oil interface while establishing interactions with the deprotonated ligand.



where M^{a+} is a metal cation and E is a deprotonable organic extractant. For instance, 2-ethyl-hexyl phosphonic mono-2-ethyl-hexyl ester (PC 88A) is a phosphonic ester capable of a cationic exchange to extract neodymium.⁹⁵

Regarding solvation, the metal is transferred to the organic phase by ligand complexation, and the aqueous phase is simply depleted, according to the mechanism in Chemical equation 2. The electroneutrality is conserved thanks to the stoichiometric co-extraction of a counter-ion.



where M^{a+} is a metal cation, X^{b-} is an anionic counter-ion, and E is an organic extractant.

5.1.2. Solid-liquid extraction

On the opposite side, solid-liquid extraction (SLE) has been developed to reduce the required quantity of materials involved in the extraction process, as well as increasing their recyclability. Sorbents generally are porous inorganic or organic materials such as silica, carbon or polymers. They contain functional groups able to selectively chelate the targeted metals, and they can be settled in columns or membranes, so the process can be continuous.

Sorption mechanisms include adsorption, precipitation, and absorption. Adsorption refers to the fixation of fluid molecules at the surface of a solid. This can take place according to two distinct mechanisms which are: *i*) chemisorption, that implies the formation of chemical bonds, allowing poor reversibility because of the high strength of the interactions, and *ii*) physisorption relies on weaker interactions (electrostatic or Van Der Waals forces) without modification of the molecular structure of the solid, so this mechanism is prevalent in extraction because of its reversibility. Precipitation is the three-dimensional growth of a solid phase: it can be homogeneous (in the bulk), or heterogeneous (at the sorbent surface or in the pores). Absorption means the substitution of atoms within the structure of the sorbent, by atoms of the targeted element. It supposes similar ionic radii and charges between the two exchanged atoms.

As with LLE, the phenomenon of ion exchange can also take place in the solid phase and constitutes a sorption process. The extracted species is compensated by another species initially present in the system when the latter has functional groups on the surface. An ion exchanger is a solid, often a resin,

capable of exchanging ions with other ions from the aqueous solution in which it is immersed. In some cases, as well as being ion exchangers, resins have complexing functions in their matrix, and they are known as "chelating" resins. They are used, for example, in industry to obtain highly purified rare earth elements.⁹⁶

To quantify the extraction efficiency of a material to extract a metal, its loading capacity Q_M (mmol/g) is expressed as:

$$Q_M = \left[\frac{c_i^m \times V}{MW_M} - \frac{c_f^m \times V}{MW_M} \right] \times \frac{1}{m_{mat}} \quad (3)$$

Where c_i^m and c_f^m are the initial and final mass concentrations of metal respectively (mg/L), V the volume of solution in contact with the material (L), MW_M the molecular weight of the metal (g/mol), and m_{mat} the mass of material used for the extraction test (g).

Even if the fixation of the chelating agent on a support can allow reaching higher selectivity for a specific metal with respect to LLE, the mechanical aging of sorbents is often a brake for their industrial development. For these reasons, PLs could keep advantages from LLE and SLE, while setting the drawbacks aside.

5.2. Porous liquids employed for liquid-liquid extraction of metals

This thesis aims to defend the potential of PLs as a non-volatile alternative organic phase for LLE. Indeed, PLs can combine the high performances of porous solids with the ease of manipulation and storage of liquids. By contrast with conventional LLE, the absence of solvent in Class A PLs would imply neither possible third phase formation nor material losses due to volatility (**Figure 14**). Industrially, it would allow replacing conventional processes without changing infrastructure. In this context, it was necessary to synthesize functional hydrophobic PLs displaying high permeability and low viscosity.

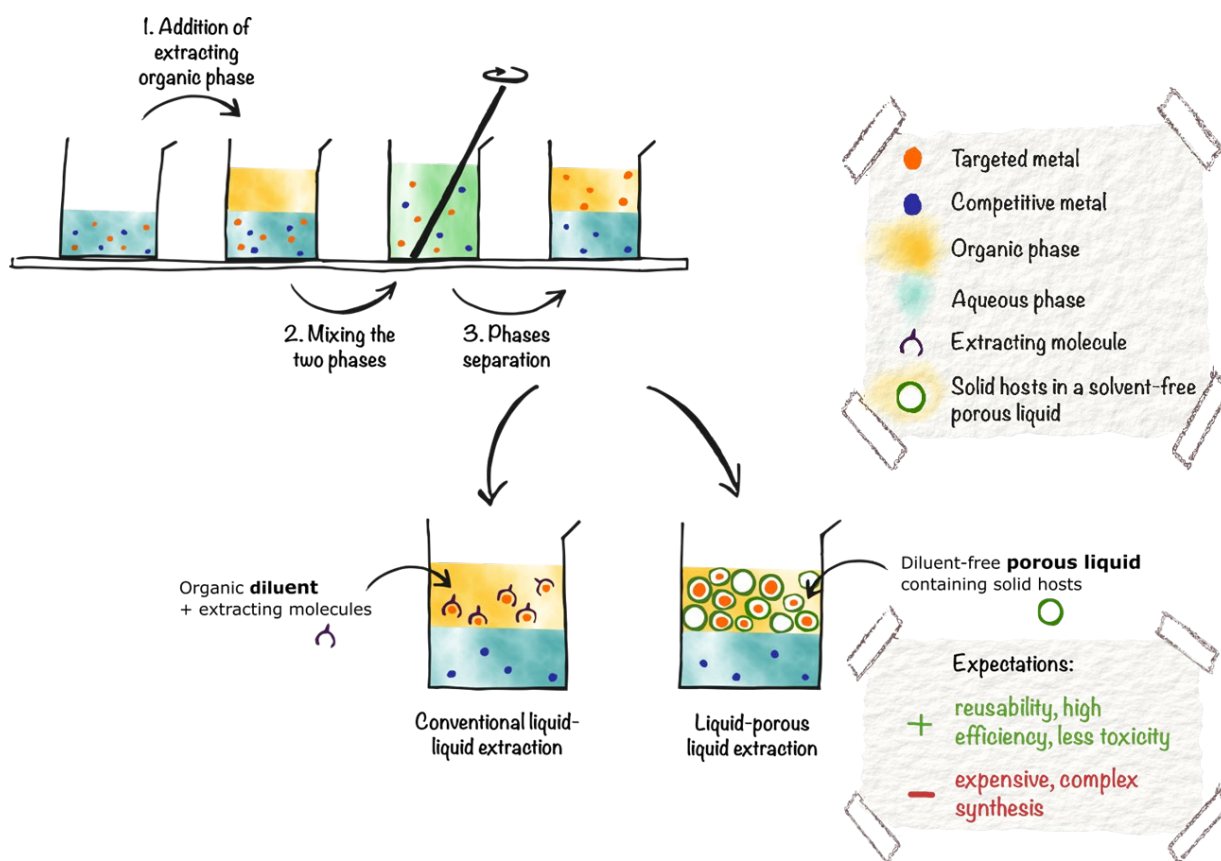


Figure 14. Comparison of conventional liquid-liquid extraction and liquid-porous liquid extraction.

Among the different types of PLs described previously, solvent-free PLs based on hollow silica particles are good candidates because of the nanometer size of their internal cavity, the high porosity of the silica shell and the tunability of the synthesis. Furthermore, silica can be easily functionalized by co-condensation or post-grafting (see Chapter IV, Section 2.1). In literature, most of the silica-based PLs are hydrophilic, following on from the study of Pr. Sheng Dai and coworkers.¹⁷ Therefore, this work was focused on developing new silica-based PLs adapted for LLE, with a hydrophobic behavior and functional moieties. In particular, it was centered on the extraction of rare earth elements (REEs) contained in permanent magnets, such as neodymium, praseodymium and dysprosium.

Even though silica-based PLs were often studied for gas sorption and separation, few investigations also took an interest in their interaction with metals. Hence, Hemming *et al.*⁷⁴ recently demonstrated the possibility of encapsulating nanoparticles of gold, platinum, and palladium inside the silica hollow cores during their synthesis, without significantly affecting the grafting steps forming the PL afterward. Furthermore, Yang *et al.* successfully separated heavy metals like lead and copper from a water phase by using a magnetic silica-based PL to make the collection possible (**Figure 15**).⁵⁷ In the course of this thesis, a study conducted in our group also showed the possible extraction of lead by a PL thanks to its

previous functionalization with thiols.⁶⁰ These two PLs being hydrophilic, they cannot be directly employed as organic phases in LLE yet. Regarding REEs, no research for their extraction has been conducted to date.

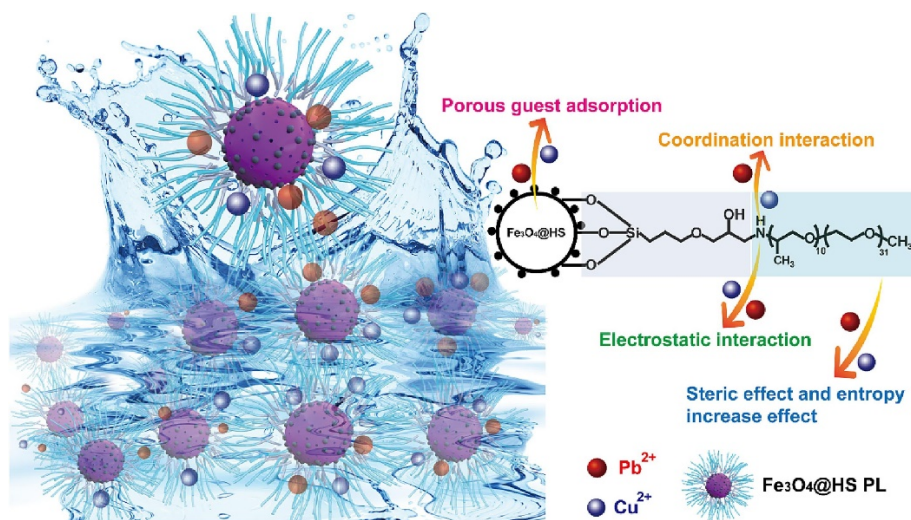


Figure 15. Mechanism of Cu(II) and Pb(II) adsorption by a magnetic PL based on hollow silica particles (HS stands for “hollow silica”).⁵⁷

Various challenges will be addressed in the following pages, like the synthesis optimization, the functionalization, the viscosity, the hydrophobicity and the extraction efficiency and selectivity. Specifically, the introduction of functional groups known for their affinity with REEs is expected to be essential to manage correct extraction of the metals. Porous structure and permeability of the PL to aqueous phases also deserve deep studies prior to choose the best system ensuring good diffusion of metal ions in the silica pores. Since PLs still are a young concept, there is a lack of knowledge about them in general. Therefore, this study also aspired to provide more fundamental information about the liquid behavior of these materials, depending on the nature of both organic and inorganic parts. Indeed, this could greatly help researchers designing PLs with low viscosity and specific features for various applications.

Conclusion

The heart of this chapter consisted in introducing the recent concept of porous liquids (PLs) as an innovative material with great potential. The genesis of PLs since the 2000s was reminded in the first place, along with the evolution of their classification. Literature nowadays proposes four conceptual types of PLs, but it was demonstrated how some confusions might be introduced in their definitions. In this thesis, a new classification has been presented, based on the origin of the liquid behavior: **Class A** gathers PLs made of discrete hosts that are directly liquid at room temperature (or below 100 °C). In **Class B**, PLs contain discrete hosts dissolved or dispersed in a sterically hindered solvent made of discrete molecules. **Class C** regroup PLs consisted of discrete hosts dispersed in a liquid network at

room temperature (or below 100 °C). **Class D** describes porous networks that are directly liquid at room temperature (or below 100 °C). In all cases, PLs are generally hybrid materials containing a solid host (organic or inorganic) either dissolved or dispersed in hindered organic solvents, physically treated, or chemically modified with organic moieties to be liquid at room temperature. Thanks to a careful screening of published works, it was finally found that Class A PLs and Class B PLs are the only kinds which are deeply studied, whereas Class C PLs and Class D PLs essentially remain at the conceptual level so far.

Whatever the category, PLs are porous materials before anything else, and their porosity must be accurately defined. In particular, it should not be limited to open pores existing in the free-guest state, because pores are just holes in a solid structure, increasing the interface area between matter and a surrounding fluid. Hence, the fact that pores are filled do not suppress this intrinsic porosity. In the case of solvent (or grafted organic moieties) penetration, the material is still porous if it is still possible to chase it away from pores so other fluid guests can enter. However, conventional techniques used for assessing porosity in porous solids cannot always be directly transferred to the characterization of PLs. For instance, nitrogen sorption at 77K is not efficient because the bulky organic moieties act as glasses at this temperature, blocking gas diffusion thus creating an impermeable barrier. Very long equilibration times must be respected to obtain an isotherm. Alternatively, changing the gas for CO₂ allows increasing the measurement temperature, but this gas is generally not inert.

Bringing porosity to the liquid state immediately raised more questions about the origin of the fluidity. For all types of PLs, it appeared that the weight ratio between organics (brought up for chemical modification or as bulky solvents) and solid hosts is crucial to obtain a liquid. The presence of ionic or hydrogen interactions can have an influence on the ratios window leading to liquids, but this hypothesis still needs to be verified.

Although most current studies focus their attention toward gas capture, storage and separation, the potential of PLs goes far beyond this field of application. If Class B PLs often contain only ångstrometric cavities, silica-based Class A PLs could be used as extractants for bigger organic molecules or metals thanks to their nanoporosity. Because of their high versatility, arising from their hybrid nature, it is easy to consider designing new PLs for a specific application. This would mean playing on the host nature as well as on the organic parts, so as to tune physicochemical properties (water affinity, viscosity, stability...), as well as adding task-specific groups to reach good performances. As an example, stimuli-responsive PLs have been recently reported, and they could act as “smart” materials in various applications.

To explore the possibility of using PLs for metal extraction, it has been decided to study silica-based Class A PLs in this thesis. Indeed, they have numerous advantages. The presence of porous silica shells as solid hosts allowed using the wide knowledge about silica treatment and functionalization. Since their synthesis is largely described in literature, it was also possible to change the size and porous profile of the silica shells employed as first building-blocks in the PL fabrication. Finally, the fact that Class A PLs were solvent-free brought a real benefit for the targeted liquid-liquid extraction process.

The investigation started with the synthesis and the characterization of the first hydrophobic Class A PLs based on two types of hollow silica particles. Porosity and permeability could be tuned by changing the nature of the silica particles, while viscosity, physical state, and affinity toward water could be modulated by varying the chain lengths and the nature of the organic moieties, so this versatility was deeply studied afterward. In the end, the functionalization of PLs and their application in extraction of rare earth elements completed the work.

Chapter II

Synthesis and characterization of a new range of hydrophobic silica-based porous liquids

As it has been discussed in the first chapter, silica-based porous liquids (PLs) might be good candidates to act as an extracting phase in liquid-liquid extraction (LLE) of metals. To achieve this goal, the first task consisted in adapting the state-of-the-art methods to synthesize hydrophobic and fluid porous materials. The strategy adopted in this work aimed to harness the tunability of silica-based PLs, by varying both the nature of the silica core (size, shell thickness, density, porosity) and the organic moieties (affinity toward water, ionic or neutral). The first section will describe the strategies chosen for the new synthesis methods and the publications from which they are inspired. The second and third sections will detail the synthesis and characterization of hollow silica particles (HSPs) and PLs, respectively.

1. Synthesis strategy – from Nanoscale Ionic Materials (NIMs) to Porous Liquids (PLs)

1.1. From NIMs to ionic PLs: state-of-the-art

The synthesis of the first PL based on HSPs was reported by Pr. Sheng Dai and his team in 2015.¹⁷ In all likelihood, the route they followed was inspired from different sources. Indeed, a new research field emerged in the 2000s, about solvent-free nanofluids called “nanoscale ionic materials” (NIMs).^{97,98} In particular, the work of Pr. Emmanuel P. Giannelis and coworkers^{65,99,100} consisted in functionalizing silica nanoparticles (SiNPs) by a two-steps procedure resulting in an ionic material that could be liquid at room temperature, depending on the grafting nature. As depicted in **Figure 16**, a first layer (corona) of an ionic organosilicon was covalently bonded at the surface of the SiNPs. Then, a second layer (canopy) of a large counter ion was formed by establishing ionic interactions with the corona.

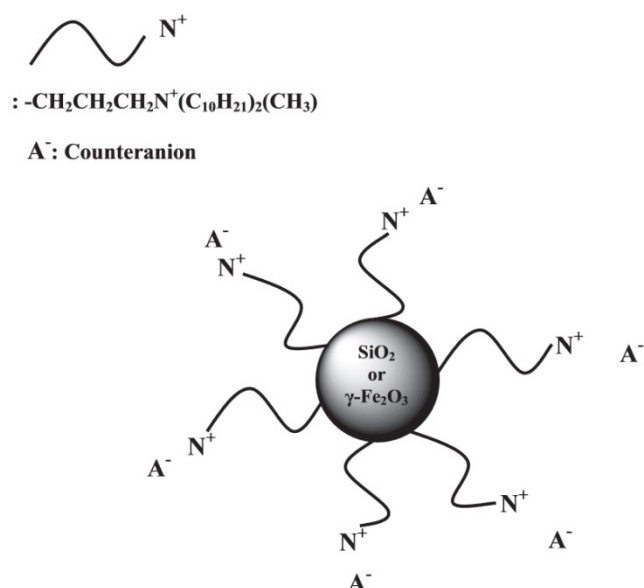


Figure 16. Scheme of the structure of a NIM based on an inorganic nanoparticle chemically modified by two layers of organic molecules interacting through electrostatic attraction. Reproduced from Reference ⁹⁸.

They found out that a long sulfonated poly(ethylene glycol) (PEG) as a canopy provided a liquid behavior to the final material. Therefore, Pr. Dai *et al.* used the same grafting on the surface of porous HSPs, giving birth to an ionic PL (**Figure 17**). The synthesis of HSPs was inspired from the works of Qiao *et al.*⁸³ and Li *et al.*¹⁰¹ It was also close to the synthesis route described by Liu *et al.*¹⁰² During the following years, a number of studies have used Pr. Dai’s synthesis route to explore potential applications to nanometric PLs.^{43,44,46} The nature of porous nano-objects was varied, with examples of

liquefied silica nanorods or zeolites, and the target application was most often CO₂ capture or gas separation.

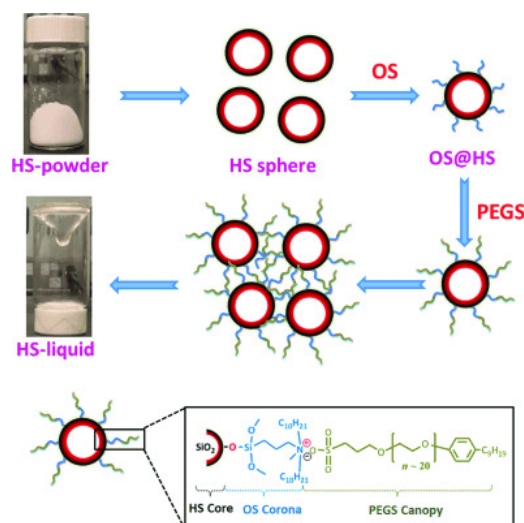


Figure 17. Scheme of the strategy pathway of the first silica-based ionic PL synthesized by Pr. Dai *et al.* Reproduced from Reference ¹⁷.

In the context of making hydrophobic PLs for LLE, another type of grafting was considered in this study. It derived from another NIM made by the team of Pr. Giannelis in 2008.^{99,100} The cationic organosilicon was replaced by a sulfonated one [3-(trihydroxysilyl)-1-propane sulfonic acid], named SIT, to form a corona covalently bonded to the surface of a SiNP (**Figure 18**). Then an amphiphilic tertiary amine (named EthA hereafter) was used in order to form the cationic canopy after protonation. This commercially available amine derived from tallow amines modified by PEGylation. It had one aliphatic chain (C₁₆-C₁₈) and two PEG chains (with a total number of ethylene glycol (EG) units of 25). Based on this work, it was presumed that tuning the hydrophilic-lipophilic balance (HLB) of the amine by varying the number of EG units would allow tailoring the hydrophobicity of the final material as well as its viscosity.

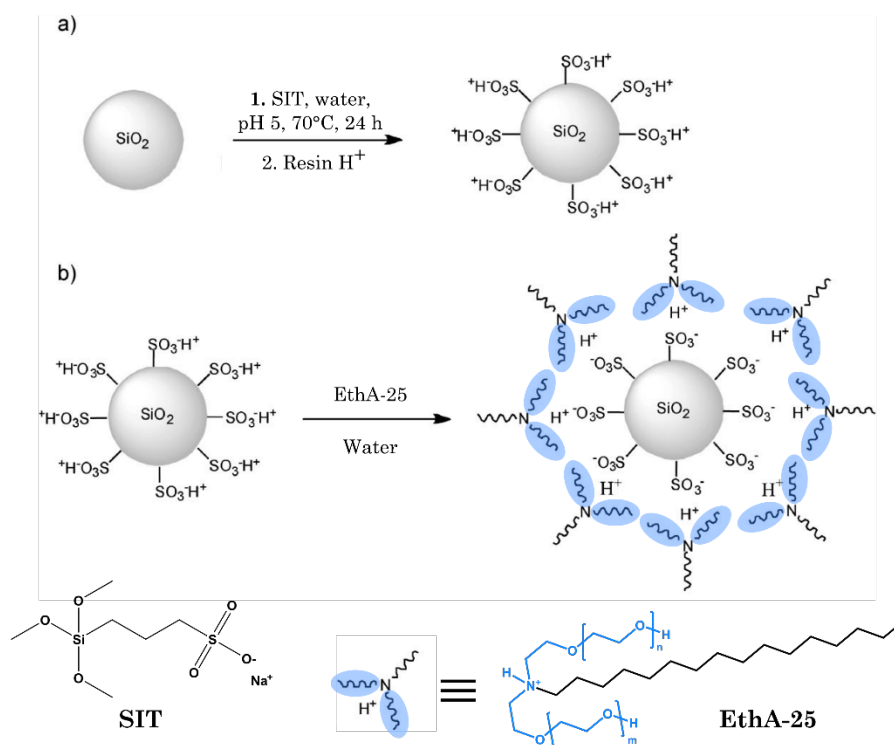


Figure 18. Scheme of the synthesis of a NIM with an amphiphilic canopy: **a)** sulfonation of the silica spheres is achieved by condensation with 3-(trihydroxysilyl)-1-propane sulfonic acid (SIT, 30-35% in water) followed by protonation with strong acid resin; **b)** neutralization with a PEGylated tallow amine ($n+m = 25$). The alkyl chain of the tertiary amine is represented as C_{16} , but the tallow amine derivative which was used had alkyl chains between C_{16} and C_{18} . Adapted from Reference ⁹⁹.

1.2. Synthesis tunability of silica-based ionic PLs

PLs based on HSPs can be viewed as hybrid organic-inorganic materials, and both organic and inorganic moieties can be tuned to change the physicochemical properties of the final material. In this regard, the nature of the silica core and the type of organic grafting were modified in this thesis.

1.2.1. Nature of the silica core

The nature of the silica core (shape, size, porosity and shell structure) might have a great influence on the fluidity and porosity of the PL. On the one hand, Pr. Dai *et al.* used around 30 nm large HSPs to make PLs¹⁷ and their fabrication followed quite similar route as the work of Liu *et al.* published in 2008.¹⁰² On another hand, the synthesis of larger HSPs (diameter over 100 nm) is extensively described in literature.^{85,103,104} Big HSPs also are good candidates for PLs because they usually display larger cavities and pore channels, thus allowing the inner diffusion of larger molecules or complexes.

In this study, two types of HSPs were synthesized: small HSPs (labeled sHSPs) following the method described by Pr. Dai *et al.*,¹⁷ and big HSPs (labeled bHSPs) according to the protocol of Teng *et al.*¹⁰⁴

Figure 19 shows how these two types HSPs were prepared and turned into ionic PLs. Details of the method are provided in Appendix A.

The fabrication of sHSPs (**Figure 19a**) consisted in forming large micelles of a triblock copolymer (Pluronic F127) in water thanks to the addition of a swelling agent (trimethylbenzene, TMB), in presence of potassium sulfate K_2SO_4 (to control the sol-gel kinetics in the next step). As a silica precursor, tetramethoxy orthosilicate (TMOS) was added to form a silica network around the hydrophilic arms of the polymer. After calcination, the template was removed, leaving a hollow mesoporous cavity and microporous pores inside the silica shell.

The method to synthesize bHSPs (**Figure 19b**) was derived from Stöber's,¹⁰⁵ *i.e.* achieving the condensation of tetraethoxy orthosilicate (TEOS) around an assembly made of cylindrical micelles of cetyltrimethylammonium bromide (CTAB), in a basic aqueous phase containing ethanol. An additional step of incubation into warm water allowed removing the less-condensed silica inside the core of the micelle assembly. The template was then softly removed by using acidic ethanol under reflux. By this way, a big silica shell surrounding a hollow cavity could be formed.

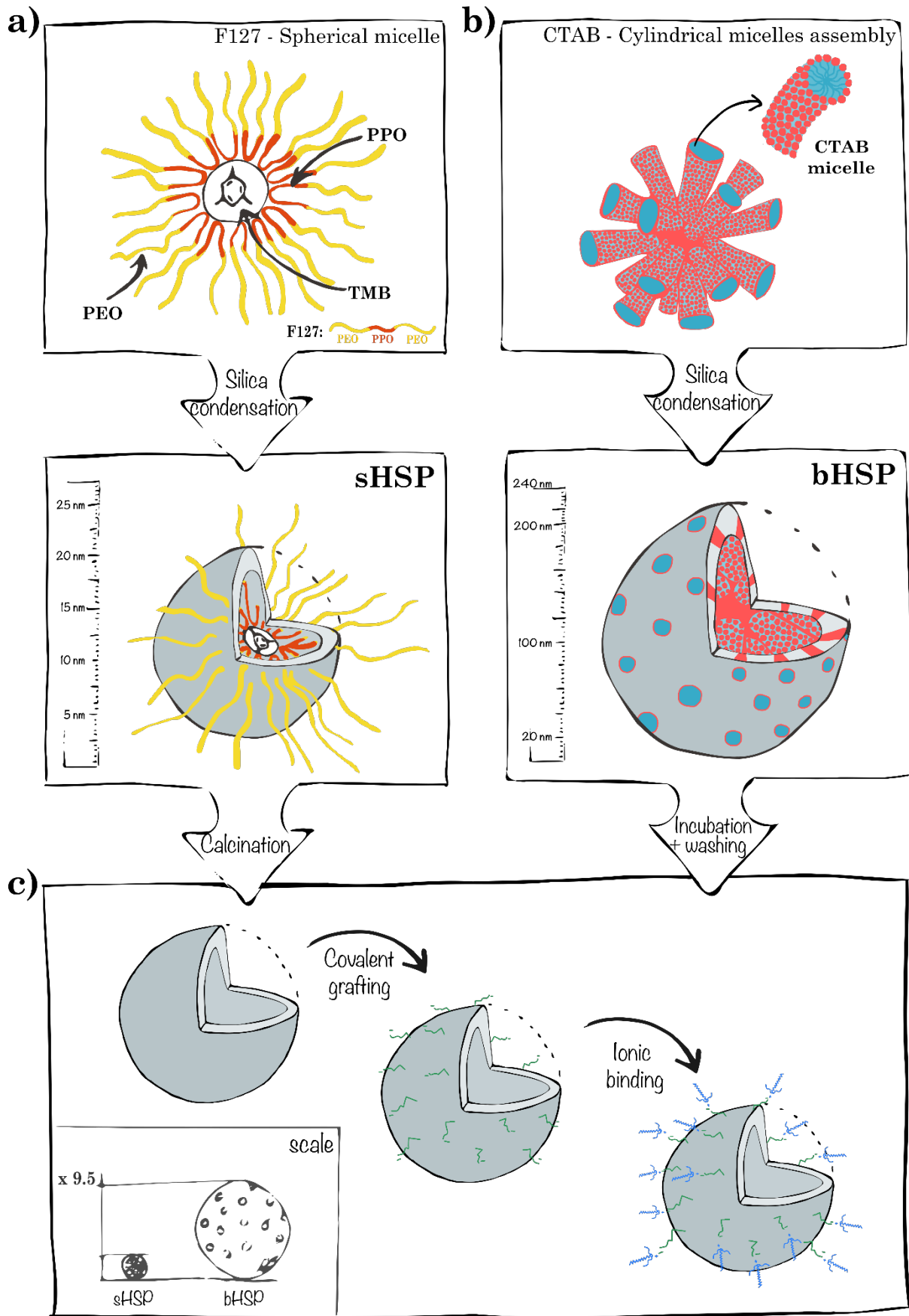


Figure 19. Scheme of the syntheses of a) sHSPs and b) bHSPs; c) HSPs are used to create an ionic PL.

1.2.2. Modulation of the organic grafting

To make them liquid, sHSPs and bHSPs were treated for surface modification with SIT.⁹⁹ Then, the neutralization of the modified HSPs with EthA, followed by the removal of water terminated the PL synthesis (**Figure 20**). Furthermore, the length of the PEG chains of the tertiary amine was varied to tune the hydrophobicity and the viscosity of the PL. Four commercially available EthAs and one made in the lab were included in the investigation. The total number of EG units ($n+m$) ranged from 5 to 92: the shorter the chains, the more hydrophobic the molecule. EthAs were referred to as EthA-X with X the number of EG units (5, 11, 22, 50, 92). EthA-5 to 22 were liquid, EthA-50 was a glassy solid and EthA-92 (made in the lab) was a powder. PL-sHSPs-EthA-X and PL-bHSPs-EthA-X stood for PLs containing sHSPs and bHSPs respectively, with a canopy made of EthA-X. In the aim to comparing with literature, the NIMs based on SiNPs were also synthesized and named PL-SiNPs-EthA-X even though they were not properly porous materials. More details about the method are in Appendix A.

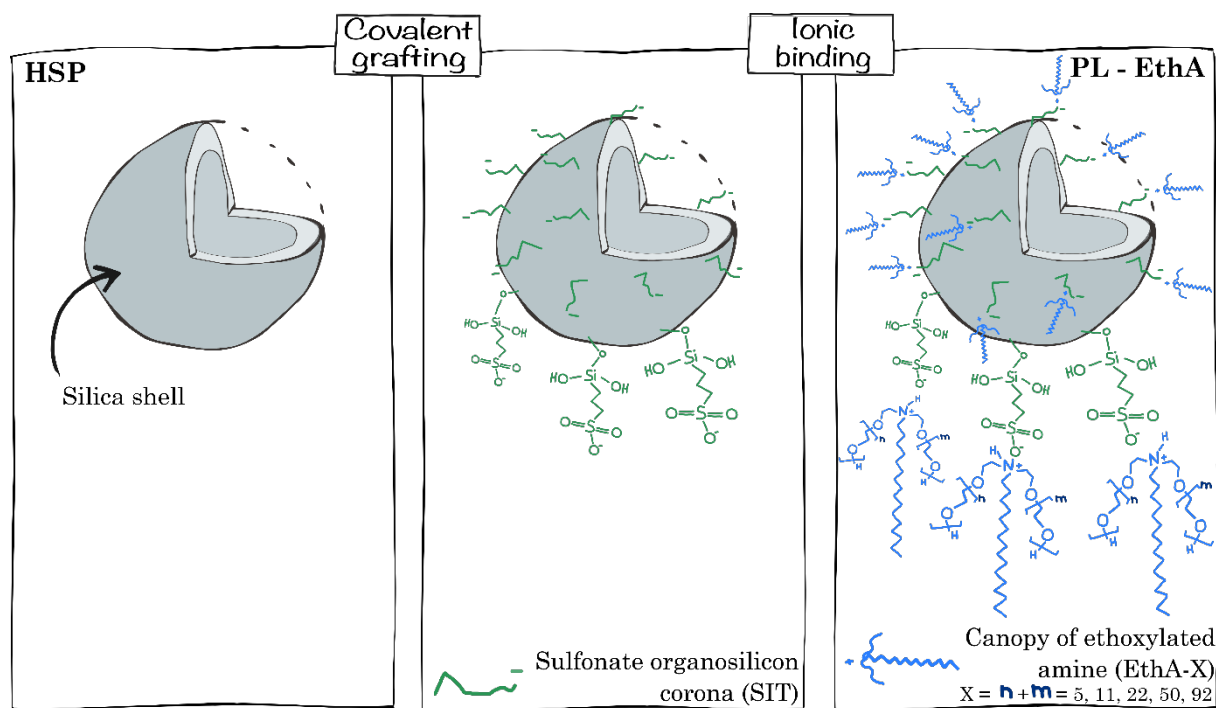


Figure 20. Scheme of the chemical grafting at the surface of the silica particle, applied to obtain a tunable ionic PL.

1.3. From ionic PLs with amphiphilic canopy to neutral PLs with hydrophobic canopy

In 2023, Pr. Panchao Yin and his team reported a non-ionic hydrophobic PL made of coordination nanocages decorated with poly(propylene glycol) (PPG) (**Figure 21**).⁴² By changing the molecular weight of the polymer, they obtained all the range of physical states, from the solid to the liquid, by way of gel-like materials. This study was only the second one to introduce a non-ionic PL based on nanocages, after the work of Wang *et al.* in 2021 concerning UiO-66.⁵³ Yet, before these studies, liquid

POSS-containing polymer composites were also described using PPG, but they were not recognized as PLs.¹² While designing new PLs for LLE, PPG was expected to provide a good hydrophobicity and a good stability against water.

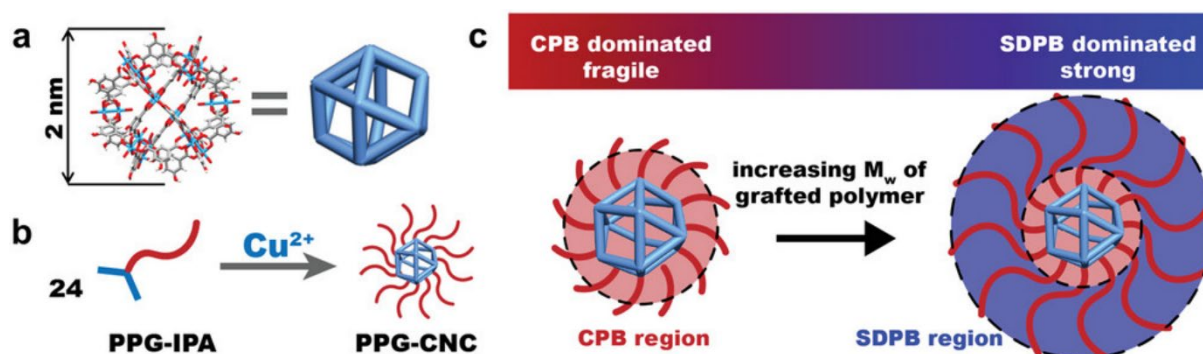


Figure 21. Scheme of the synthesis of a hydrophobic PL made of coordination nanocages (CNCs) and PPG brushes. Reproduced from Reference ⁴².

Therefore, inspired from the work of Randriamahefa *et al.*,¹² a new method has been developed in the present project to make a PL *via* the association of sHSPs with PPG. **Figure 22** shows a representation of the polymer grafted at the surface of a HSP. Two different lengths of polymeric chains were tested (PPG with a molecular weight (MW) of 725 g/mol (PPG₇₂₅) and 2,000 g/mol (PPG₂₀₀₀)).

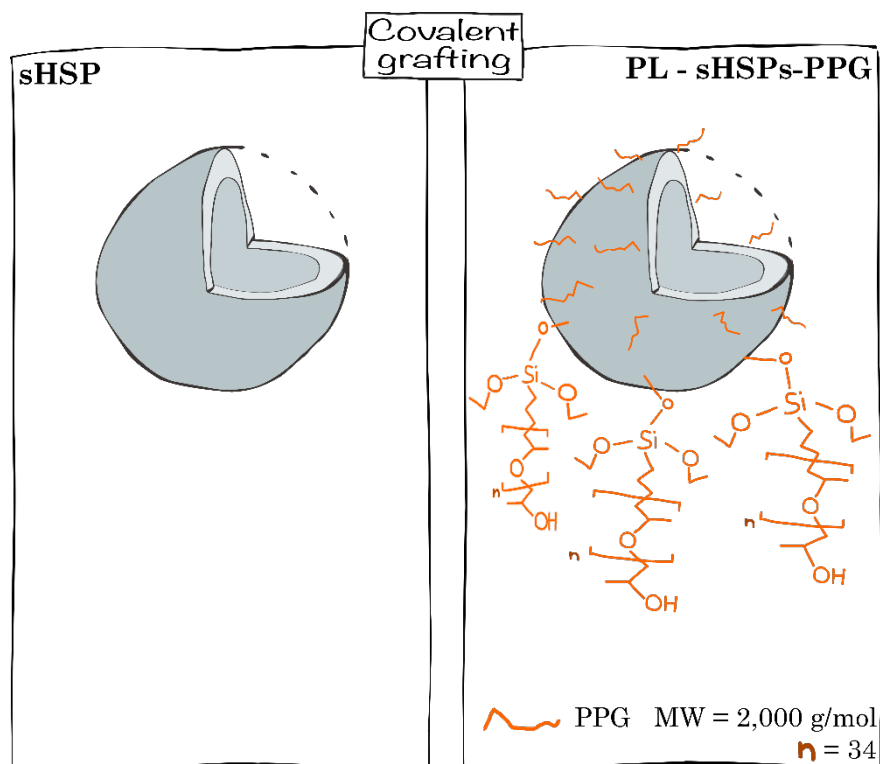


Figure 22. Scheme of the covalent grafting of PPG at the surface of a sHSP, leading to the PL-sHSPs-PPG.

As described in **Figure 23a**, either PPG₇₂₅ or PPG₂₀₀₀ was first silanized by forming the allyl intermediate and making it react with triethoxysilane in the presence of a platinum-based catalyst ($\text{Pt}_2[(\text{Me}_2\text{SiCH}=\text{CH}_2)_2\text{O}]_3$, Karstedt¹⁰⁶). Then it was grafted at the surface of sHSPs at room temperature under argon during one night to give PL-sHSPs-PPG (**Figure 23b**).

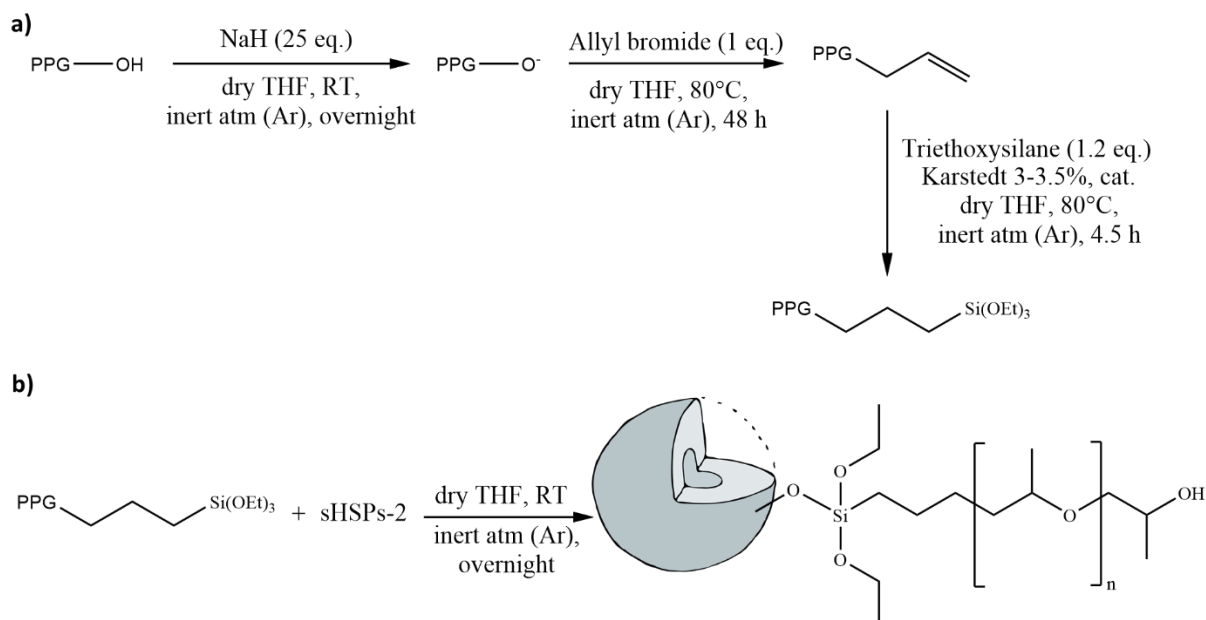


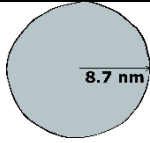
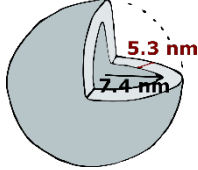
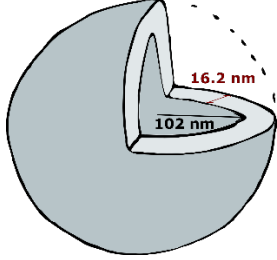
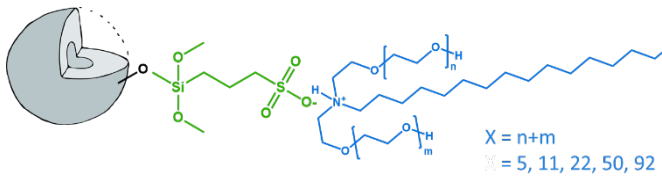
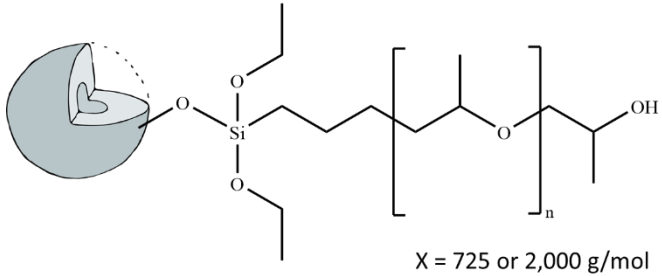
Figure 23. Synthesis of non-ionic single-component canopy-based PL (PL-sHSPs-PPG): **a)** Silanization of a commercially available PPG providing the expected PPGSi(OEt)₃ intermediate. Two different lengths of polymeric chains were tested (PPG with a molecular weight (MW) of 725 g/mol (PPG₇₂₅) and 2,000 g/mol (PPG₂₀₀₀); **b)** Scheme of the covalent grafting of PPG-(SiOEt)₃ at the surface of a sHSP, leading to the targeted PL-sHSPs-PPG.

Details of the method are provided in Appendix A. To optimize the synthesis, different parameters such as the temperature, the reaction time and the post-reaction treatment method have been varied, and this study will be presented in Section 3.2.

1.4. Synthetic table of the synthesized materials presented in this chapter

To guide the reader among the different materials mentioned in the following pages, schemes of the three types of silica nanoparticles (SiNPs, sHSPs, bHSPs), and their surface modification to obtain corresponding PLs have been compiled in **Table 2**. Note that functional materials will be presented in the last chapter, so they do not appear here.

Table 2. Synthetic table of the synthesized materials presented in this chapter. Functional materials discussed in Chapter IV do not appear here.

<i>Silica particles</i>		
SiNPs	Silica nanoparticles (Ludox)	
sHSPs	Small hollow silica particles	
bHSPs	Big hollow silica particles	
<i>Porous liquids</i>		
PL-sHSPs-EthA-X	PLs based on sHSPs and SIT-EthA corona-canopy	
PL-bHSPs-EthA-X	PLs based on bHSPs and SIT-EthA corona-canopy	
PL-sHSPs-PPG-X	Porous liquids based on sHSPs and PPG	

The following section will focus on the characterization of the size and shape of silica particles, while Section 3 will linger over the synthesis development and the characterization of PLs.

2. Synthesis and characterization of hollow silica particles

2.1. Synthesis method

Hollow silica particles (HSPs) of two different kinds were synthesized and used to make PLs (**Figure 19**, cf. bookmark No.2 and No.3): sHSPs were formed by condensation of TMOS around a soft template made of Pluronic F127 and TMB, whereas bHSPs were templated by self-assemblies of CTAB and the

hollow cavity was created afterward by incubation into warm water (see Section 1.2.1). Details of the methods are provided in Appendix A. In both cases, the particles were obtained with a quantitative yield (99.7% for sHSPs; 48.5% for bHSPs stemming from the deliberate release into the bulk of a large amount of non-condensed silica initially present in the core of the particle. This occurs during the incubation step and it allows creating the hollow core). Commercial silica nanoparticles (SiNPs) were also considered as a little porous reference, which had already been liquefied before, after endowing them with two ionic organic layers as reported in literature.⁹⁹

In the next section, some characterization methods are introduced and employed to provide information about the sizes and shape of the HSPs. The details about devices, methods and samples preparation are supplied in Appendix B.

2.2. Transmission electronic microscopy

Transmission electronic microscopy (TEM) was employed to image the three samples (**Figure 24**). First of all, sHSPs and bHSPs clearly show an inner cavity without silica, as indicated by the difference of contrast between the inside and the shell. As expected, SiNPs are dense with no contrast variation. It was interesting to note that some of the bHSPs present a non-perfect spherical shape, along with partial coalescence. This can be assigned to the use of a soft template for such big particles,⁸⁵ along with the different treatments that are applied to empty the particles which may lead to coalescence between the neighboring thin silica shells.

The internal and external diameters of the particles were statistically determined by using ImageJ software counting more than 200 spheres, and the size distributions of external diameters are supplied in **Figure 25**. For the counting of bHSPs, a mean diameter of mostly spherical particles was taken. Hence, SiNPs are 17.4 ± 2.8 nm large. sHSPs are in the same size range with an internal diameter of 14.8 ± 1.3 nm and an external diameter of 25.4 ± 1.4 nm. bHSPs are one order of magnitude bigger with mean internal and external diameters of 203.6 ± 58.8 nm and 236.0 ± 64.4 nm respectively. However, it was clear that two populations of spheres were present: around 40% had a diameter around 149 nm and 60% had a diameter around 278 nm. Such a heterogeneity was not mentioned in the original publication,¹⁰⁴ but it was not an issue in the next steps of the PL synthesis.

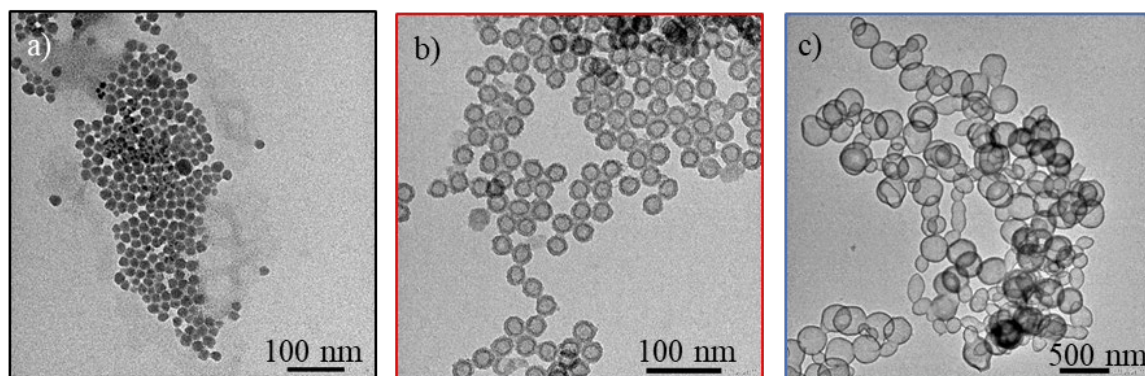


Figure 24. TEM images of **a)** SiNPs (x80k), **b)** sHSPs (x80k), and **c)** bHSPs (x10k). Reproduced from ⁵⁹.

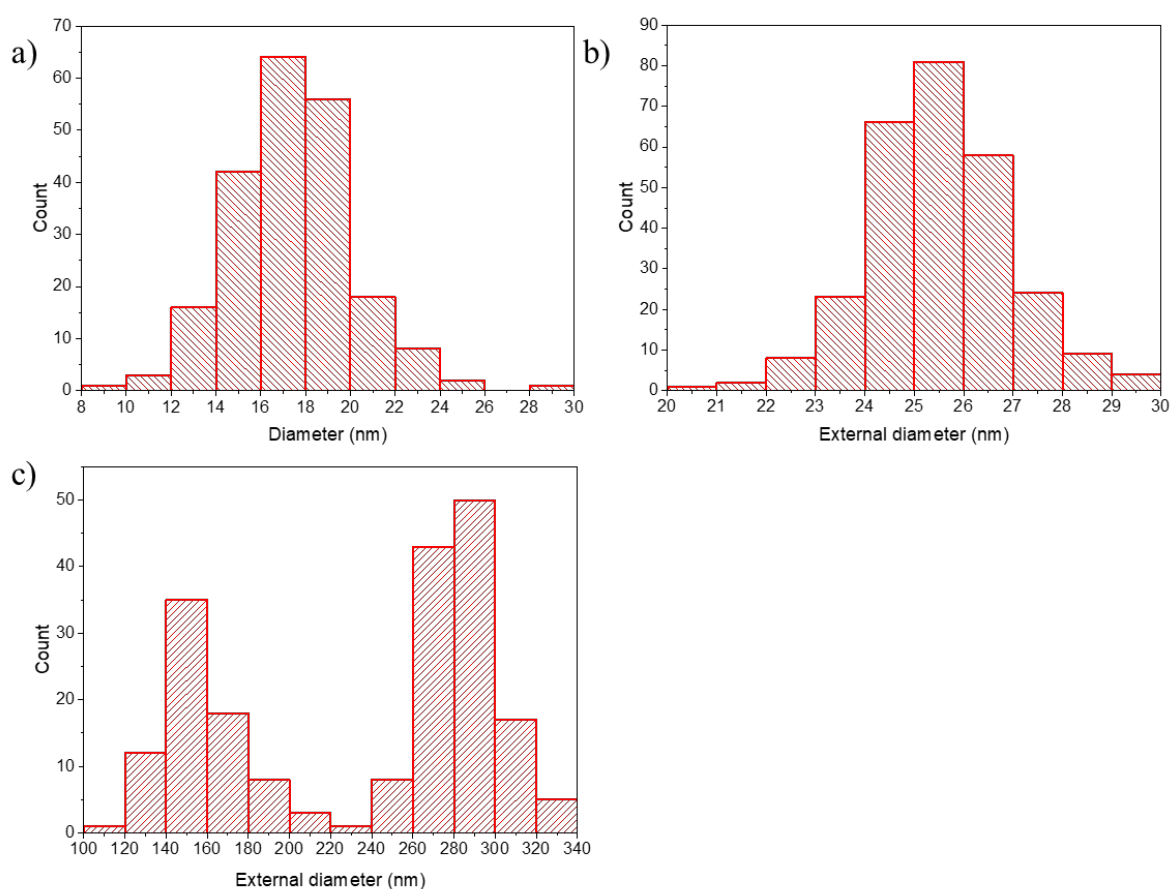


Figure 25. Statistical distribution ($\# > 200$) of external diameters deduced from TEM data analysis of **a)** SiNPs, **b)** sHSPs, **c)** bHSPs.

2.3. Small angle X-ray scattering

TEM results were correlated with the structural information deduced from small angle X-ray scattering (SAXS) and ultra-small angle X-ray scattering (USAXS) (**Figure 26**). Details about the theory of SAXS are supplied in Appendix C.

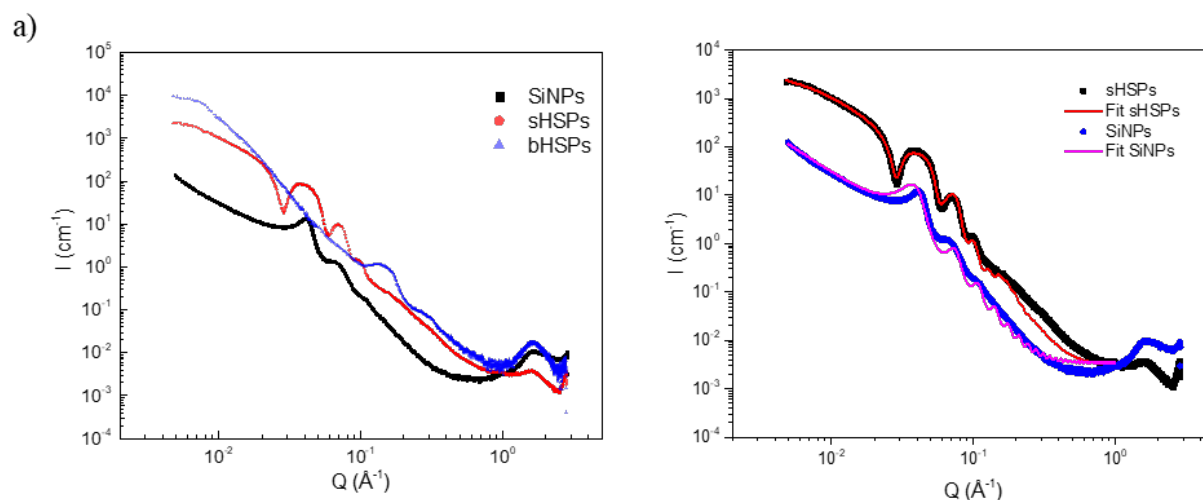


Figure 26. a) Comparison of the structural organization of SiNPs (black squares), sHSPs (red circles) and bHSPs (blue triangles) powders by SAXS; **b)** USAXS-SAXS signal of sHSPs (black squares) and SiNPs (blue circles) and the corresponding fitting curves (lines) obtained with the software SasView over the range $[0.00482;1.000]$ \AA^{-1} . The model used for fitting was a core-shell sphere structure with a sticky hardsphere behavior. The parameters and their value are listed in **Table 3**.

The spectra of the three powders (SiNPs, sHSPs, bHSPs) feature an increase in scattering intensity at low angles $[0.02 - 0.5 \text{ \AA}^{-1}]$, which is characteristic of nanospheres. Oscillations were fitted with SasView software for SiNPs and sHSPs (**Figure 26b**) and the fitting parameters are listed in **Table 3**. They are characteristic of monodisperse nanospheres and nanoshells respectively, with diameters consistent with the ones obtained from TEM images (**Table 4**). The less pronounced oscillations observable for SiNPs are consistent with a higher polydispersity for these particles. This polydispersity could not be well fitted because of the introduction of an additional structure factor in the model to account for the neat structure peak at 0.04 \AA^{-1} . This peak was characteristic of a distance of about 15 nm, being the distance between two SiNPs. bHSPs are found to be too big and polydisperse to provide any interpretable signal in this Q range. Theoretically, a plateau should be visible at low angles, before the first oscillation. In the cases of SiNPs and sHSPs, an increase in intensity was observable instead (below 0.02 \AA^{-1}), suggesting a high aggregation of the particles in the powder.

Table 3. Parameters for the fit of SiNPs and sHSPs in SasView using a sticky hardsphere model (core-shell for sHSPs) (see **Figure 26b**).

	SiNPs ^a	sHSPs
Internal radius (Å)	84	79.0
Shell thickness (Å)	-	51.0
Sld core ($10^{-6}/\text{Å}^2$)	19	0
Sld shell ($10^{-6}/\text{Å}^2$)	-	8.0
Sld solv ($10^{-6}/\text{Å}^2$)	0	0
Volume fraction	0.25	0.30
Perturbation	0.1	0.01
Stickiness	0.055	0.16
Radius polydispersity (ratio)	0.35	0.08
Thickness polydispersity (ratio)	-	0.19

^aFor the fitting of SiNPs, an additional structure factor was multiplied to the sticky hardsphere model to fit the structure peak at 0.04 Å^{-1} .

Table 4. Diameters and standard deviations of SiNPs, sHSPs and bHSPs deduced from TEM and SAXS measurements.

	External diameter (TEM) (nm)	Internal diameter (TEM) (nm)	External diameter (SAXS) (nm)	Internal diameter (SAXS) (nm)
SiNPs	17.4 ± 2.8	-	16.8 ± 1.5	-
sHSPs	25.4 ± 1.4	14.8 ± 1.3	26.0 ± 1.5	15.8 ± 1.5
bHSPs	201.6 ± 46.6	184.9 ± 50.3	-	-

2.4. Reproducibility

The influence of different synthesis parameters on the structure of sHSPs has already been studied in a previous work.⁵⁴ It was shown that a very fine control of each parameter (proportions, reaction and aging temperature, way of adding the chemicals, etc.) would be necessary to obtain a good reproducibility. During this work, two sets of sHSPs were synthesized and characterized prior to conversion into PLs, following the same method (Appendix A). However, their sizes appeared to be different, as shown by the shifted oscillation in the SAXS signal (**Figure 27**). The set described in the previous section was named sHSPs-1, one the second set was named sHSPs-2.

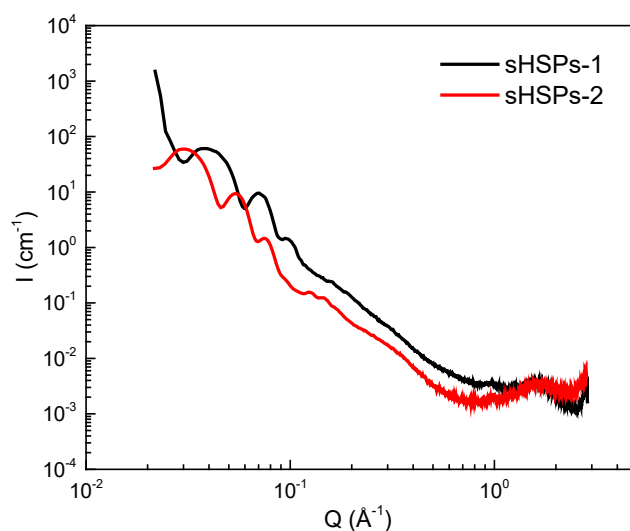


Figure 27. SAXS of two sets of sHSPs: sHSPs-1 corresponds to the set described in the previous sections. sHSPs-2 is a second set performed following the same method.

The statistical analysis of TEM images led to an internal diameter of 19.4 ± 2.5 nm and an external diameter of 37.3 ± 2.8 nm for sHSPs-2. As a result, a significant difference shall be expected in the porosity profiles of sHSPs-1 and sHSPs-2. This part will be further discussed in the following chapter (Section 1.1.2). sHSPs-1 were the set used to make all PL-sHSPs-EthAs, while sHSPs-2 were used for investigation about SIT grafting yield (Section 3.1.2.3), and to make PL-sHSPs-PPGs.

Regarding bHSPs, the reproducibility was even worse, because the reaction was performed at room temperature, and this parameter played an important role in the final size of the particles.¹⁰⁴ In one set, the size distribution was different, with half of the particles having a diameter of about 230 nm and the other half having diameters homogeneously ranging from 100 to 200 nm. In other sets, a various proportion of non-emptied particles could be observed on the TEM images (**Figure 28**).

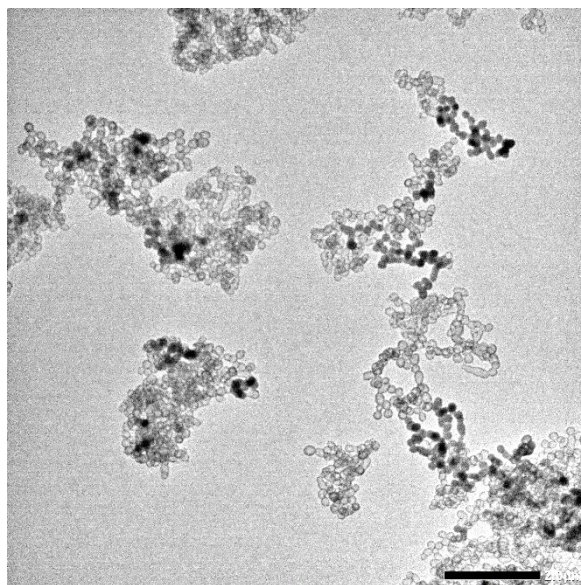


Figure 28. TEM image of a second set of bHSPs containing a proportion of non-emptied particles. Scale bar: 2 μm .

The PLs were made using the set of bHSPs presented in previous sections (**Table 4**), so that the size distribution was well known, and all the particles on the TEM grid were emptied.

3. Synthesis and characterization of porous liquids

Both sHSPs and bHSPs were used as inorganic building blocks to make PLs. A range of ionic PLs (PL-EthAs) was firstly synthesized by anchoring SIT molecules at the surface of HSPs, before adding a second layer (canopy) anchored through ionic interactions. A second synthesis route was then developed to turn sHSPs into a PL by the use of a neutral and hydrophobic polymer: the polypropylene glycol (leading to a PL-sHSPs-PPG). The chemical formula of grafting are reminded in **Table 2**, and in the bookmark (No.4 and No.5). In this section, the development of the PLs' syntheses and their characterization will be discussed.

3.1. Ionic porous liquids with amphiphilic canopy: PL-EthAs

3.1.1. Syntheses development

The synthesis of a range of PL-EthAs was developed during this project, by varying the nature of the HSPs and the length of the PEG chains contained in the amphiphilic canopy (EthA). The method is detailed in Appendix A. First of all, yields of the different syntheses steps have been estimated, and they are presented in **Table 5** for some PL-EthAs.

It appeared that SIT grafting and ion-exchange column were the most limiting steps. Overall, the yields of PL-sHSPs-EthAs and PL-bHSPs-EthAs lay between 6% and 7%.

Table 5. Detailed yields of some PL-EthAs syntheses.

	Yield of HSP synthesis	Yield of particles turned into liquids			Overall yield
		SIT grafting ^a	Column	EthA grafting ^b	
PL-SiNPs-EthA-11	-	100%	2.7%	85.5%	2.3%
PL-sHSPs-EthA-11	99.7%	6.2%	100%	95.3%	5.9%
PL-bHSPs-EthA-11	48.5% ^c	29.7%	30.9%	79.1%	7.2%

^a In terms of amount of spheres well grafted by SIT.

^b In terms of HSPs@SIT or SiNPs@SIT well grafted by EthA

^c half of the silica was washed out during the incubation, creating the hollow cavity.

To determine and explain these yields, some analyses were conducted at every step for each synthesis. They are detailed in the following sections for PL-SiNPs-EthAs, PL-sHSPs-EthAs, and PL-bHSPs-EthAs.

3.1.1.1. A reference nanoscale ionic material: PL-SiNPs-EthAs

The synthesis of PL-SiNPs-EthAs was achieved by following the method of Rodriguez *et al.*^{99,100} After SIT grafting in water at pH 5-6, a dialysis was performed in deionized water (Milli-Q), to remove the excess of NaOH and unreacted SIT (leading to the SiNPs@SIT intermediate) prior to elution through an ion-exchange column (Dowex 50W-X8) to protonate the sulfonate salts. The Total Organic Carbon (TOC) analysis of the dialysates allowed determining the amount of unreacted SIT (about 76%), hence a 2.1:1 mmol SIT:SiNPs grafting ratio.

Then, a diluted aqueous solution of *N,N*-polyethoxylated fatty amine (EthA) was prepared and added dropwise to the solution of grafted nanospheres. The addition, which was followed by pH measurement, could be stopped just after the equivalence point (**Figure 29**). It is useful to highlight that this equivalence point corresponded to only 0.09 mmol of tethered SIT, meaning that either the protonation in the column was not total, or the column retained product inside. The bulk *a priori* contained no free SIT molecules because they were eliminated during the dialysis.

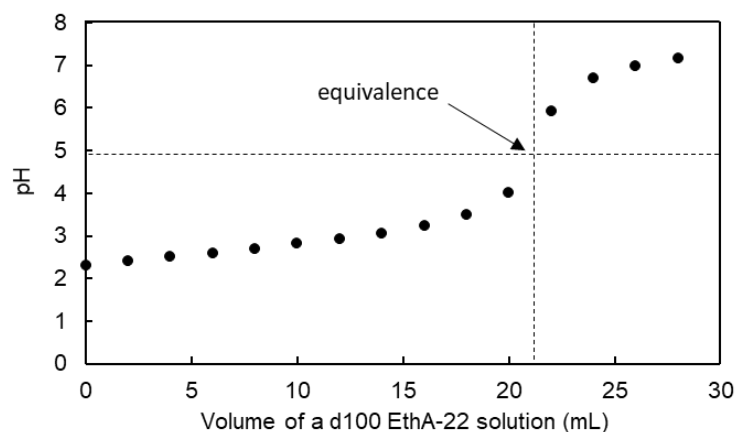


Figure 29. pH evolution of the bulk when adding a solution of EthA-22 (dilution factor 100) to an aqueous suspension of protonated SiNPs@SIT.

PL-SiNPs-EthA-X was recovered after drying under vacuum. As an example, the overall yield of PL-SiNPs-EthA-11 was only 2.3% (**Table 5**), when compared to the initial weight of SiNPs (1.14 g). This very low yield was not mentioned in literature,⁹⁹ but it was probably due to a high retention inside the column, and it may be improved by changing the column type.

3.1.1.2. PLs containing small hollow silica particles as hollow cores: PL-sHSPs-EthAs

Concerning PL-sHSPs-EthAs, the procedure was very similar, except that it was extremely difficult to disperse sHSPs powder in water, at any pH. It was chosen to use a high volume of deionized water (2 g of sHSPs in 325 mL of water) and to mix at 15,000 rpm with an Ultra-turrax rotor during 5 min. Then, the suspension was immersed in an ultrasonic bath for one minute in order to break aggregates. However, after performing SIT grafting at high dilution and at pH 5-6, it was observed that a large volume of powder remained undispersed (settling immediately when stopping the stirring). Hence, the solution recovered after the dialysis was centrifuged at 4000 g for 10 min, in order to eliminate this solid residue. A thermogravimetric analysis (TGA) indicated that this powder only contained 4% of SIT, suggesting that likely the lack of dispersion led to this low grafting ratio. These unreacted sHSPs accounted for almost 94% of the initial weight. On another hand, the TOC analysis of dialysis baths indicated that about 48% of the amount of SIT initially introduced passed through the membrane, ungrafted. This time, it seemed that no retention was observed in the column. In this regard, PL-sHSPs-EthA-11 was obtained with an overall yield of 5.9% of correctly grafted sHSPs (**Table 5**).

In an attempt to increase the yield, dispersion and SIT grafting were performed in a vessel equipped with an ultrasonic probe (20 kHz) at different times and temperatures (2 - 6 h; 30 - 60 °C). However, no significant improvement of the SIT grafting step yield was observed under these conditions.

3.1.1.3. PLs containing big hollow silica particles as hollow cores: PL-bHSPs-EthAs

PL-bHSPs-EthAs synthesis was achieved according to a similar procedure as described above. bHSPs were dispersed in deionized water and the resulting suspension was then added dropwise to an aqueous solution of SIT under vigorous stirring. Again, about 48% of the raw SIT passed through the membrane (according to the TOC measure), suggesting it did not react. In addition, a significant amount (70%) of residual powder was recovered by centrifugation (containing 12% of SIT). Subsequent treatments and procedures were applied following the same method as that described for PL-sHSPs. PL-bHSPs-EthA-11 was obtained in 7.2% overall yield (**Table 5**).

3.1.2. Characterization: chemical composition, grafting assessment and stability

The PL-EthAs consisted in a range of new ionic silica-based PLs, and their synthesis was adapted from different methods reported in literature. The first observation provided by TEM analyses was that the addition of the double layers (SIT/EthA) at the surface of silica particles did not alter their shape, their

size, nor their integrity. As an example, the TEM images of PL-SiNPs-EthA-11, PL-sHSPs-EthA-11, and PL-bHSPs-EthA-11 are supplied in **Figure 30**. In the case of sHSPs and bHSPs, the internal cavity is well conserved.

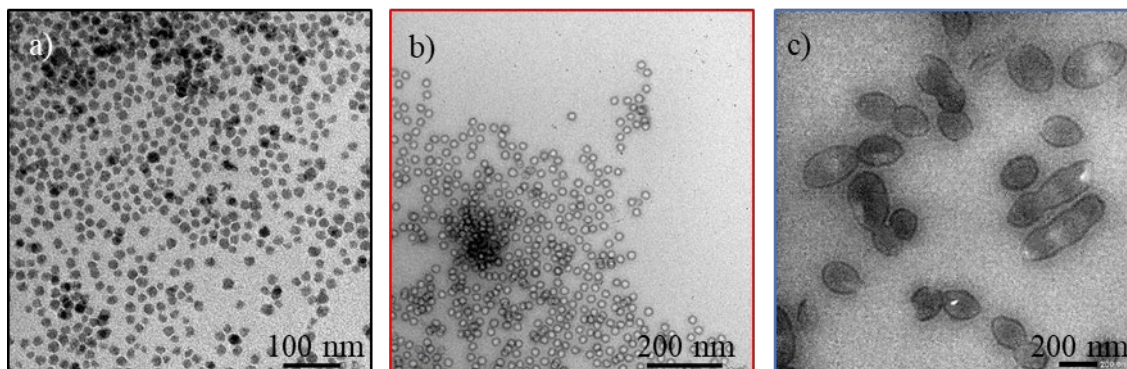


Figure 30. TEM analysis of **a)** PL-SiNPs-EthA-11 (x60k), **b)** PL-sHSPs-EthA-11 (x40k), and **c)** PL-bHSPs-EthA-11 (x20k).

Then, the synthesized materials were characterized in terms of grafting assessment, chemical composition, and stability.

3.1.2.1. PLs containing small hollow silica particles as hollow cores: PL-sHSPs-EthAs

The grafting efficiency was evaluated by thermogravimetric analysis (TGA), SAXS measurement and Fourier-transformed infrared (FTIR) spectroscopy. **Figure 31a** shows the thermal decomposition of PL-sHSPs-EthA-22 under air, at a rate of 5 °C/min. A comparison with the pure amine EthA-22 is also presented in **Figure 31b**.

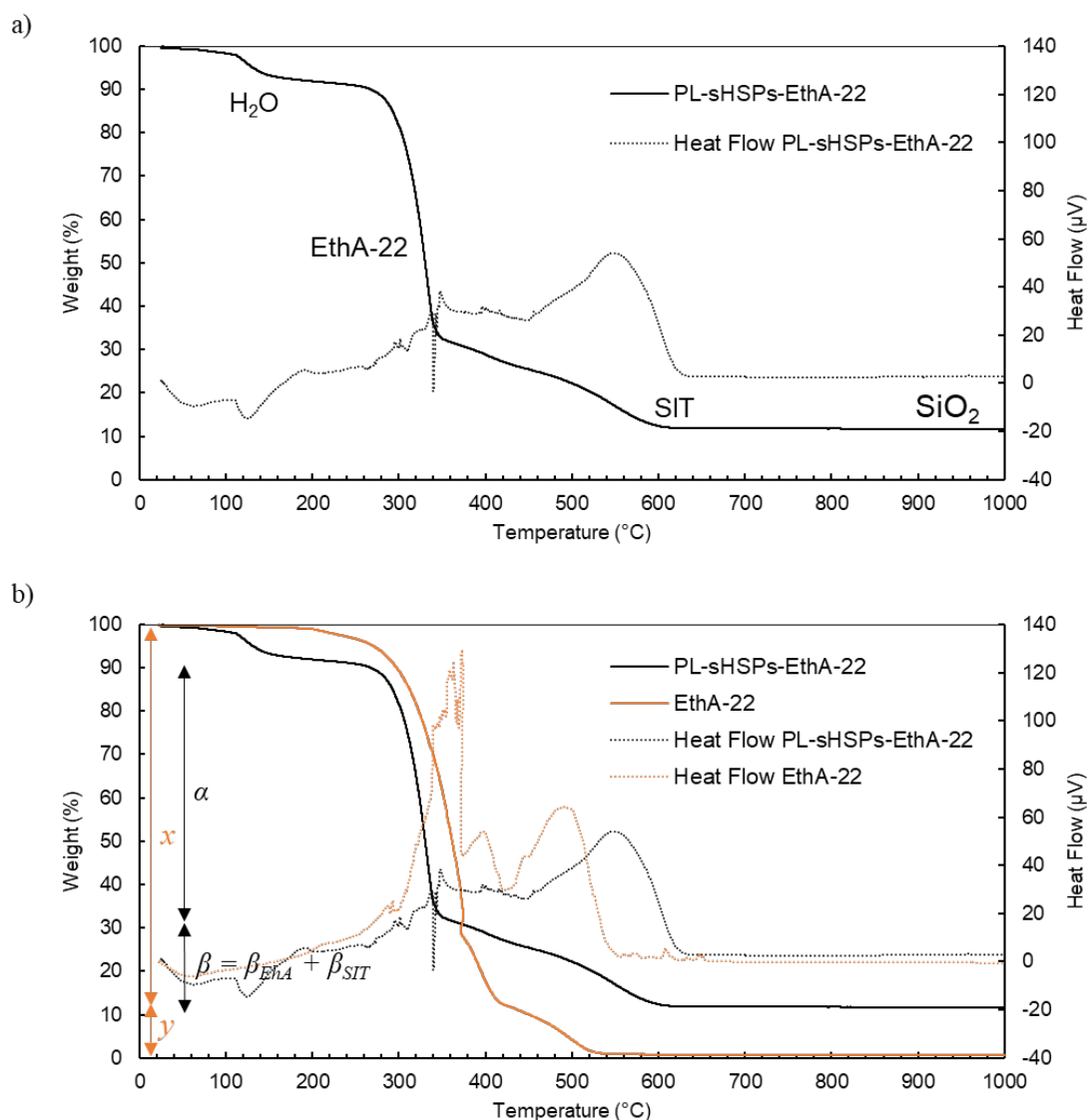


Figure 31. **a)** Thermal decomposition of PL-sHSPs-EthA-22 under air at a rate of 5 °C/min; **b)** Comparison with pure amine EthA-22, and definition of the weight ratios used in Equations E1 and E2: α , β , x and y , with $\beta = \beta_{EthA} + \beta_{SIT}$. By definition: $\frac{x}{y} = \frac{\alpha}{\beta_{EthA}}$ and $y = 1 - x$.

Around 130 °C, an 8.1% weight loss was attributed to water. Repetitions of the same measurement led to water contents varying between 0% and 10%, suggesting that the material is highly hygroscopic. A large fall in weight (60.5%) was observed at 325 °C, which was attributed to the deterioration of the canopy. This was slightly earlier than for the pristine amine EthA-22, whose main weight loss occurred at 360 °C, indicating that the presence of sHSPs lowers its thermal stability.¹⁰⁷ This observation differed from the study of Sheng *et al.* where the amine is covalently grafted to the surface of the core and its degradation occurred at higher temperatures than the pure amine.⁴⁶ Also, a small weight loss at 500 °C in the signal of the pure amine (11.7%) was attributed to a molecular weight dispersion of the commercial EthA, and it was visible in the decomposition of the PL as well. Unfortunately, it overlapped

with the deterioration of the SIT corona, and both contributions accounted for 19.8% of the total weight. To extract the SIT contribution only, a simple calculation was done, assuming that the ratio between the main loss (x) and the small loss (y) in the signal of the pure amine was kept the same in the signal of the PL (see Equations **E1** and **E2**, **Figure 31b** for notations). Hence, the SIT (carbon backbone and sulfonate head only) and the EthA-22 accounted for 11.2% and 69.1% of the weight respectively. The residual weight percentage finally gave the silica content of the PL (11.6% in this case). The organic:inorganic weight ratio was 6.9. **Table 6** gives the chemical composition of the PL before and after correction of water. The measurements were performed for all other PLs-sHSPs-EthAs (Chapter III, **Figure 59**) and the results will be discussed in Chapter III, Section 2.4.

$$\beta_{EthA} = \alpha \frac{1-x}{x} = \frac{\alpha}{x} - \alpha \quad (E1)$$

$$\beta_{SIT} = \beta - \beta_{EthA} \quad (E2)$$

Where α and β are the main and small weight losses observed in the TGA signal of the PL respectively, and β_{EthA} and β_{SIT} correspond to the contributions of the small weight loss attributed to the amine and SIT degradation respectively. x is the main weight loss in the signal of the pure amine EthA-22 (87.5%). By definition: $\frac{x}{y} = \frac{\alpha}{\beta_{EthA}}$ and $y = 1 - x$.

Table 6. Composition of PL-sHSPs-EthA-22 as determined by TGA (see **Figure 31**).

PL-sHSPs-EthA-22 (%)	Without correction from water	With correction from water
H ₂ O	8.1	x
SiO ₂	11.6	12.6
SIT	11.2	12.2
EthA-22	69.1	75.2
Orga:inorga		6.9

Note that in this reasoning, the condensation of free silanols forming siloxane is neglected. Indeed, solid NMR of silicon would have been very useful to know the structure of the silica network at each step of the PL synthesis, therefore allowing deducing the weight loss in TGA attributed to the siloxane formation. Nevertheless, TGA of sHSPs-1 after calcination (Appendix F, **Figure A10**) indicated that such a weight loss accounted for only 3.4% after correction from free water content.

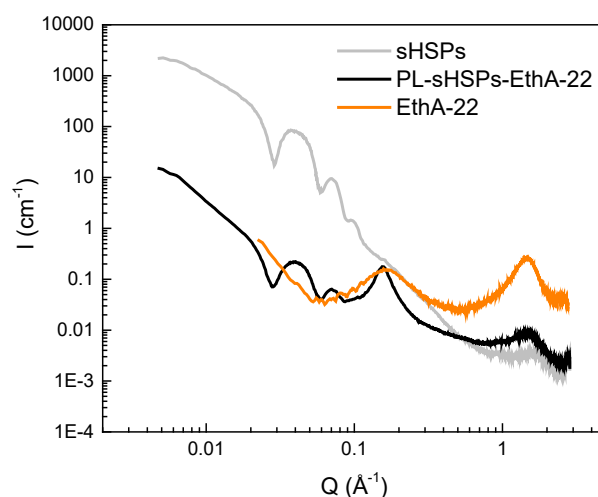


Figure 32. SAXS measurements of PL-sHSPs-EthA-22, EthA-22 and sHSPs.

In **Figure 32**, the SAXS analysis of PL-sHSPs-EthA-22 confirms the presence and the integrity of sHSPs, with the presence of the same oscillations than in the signal of sHSPs. The intensity was lowered due to the presence of the organic matrix around the sHSPs. The large band at wide angles (*c.a.* 1.5 \AA^{-1}) was consistent with the one characteristic of silica observed in the signal of sHSPs. The structural peak at 0.16 \AA^{-1} was also present in the signal of the pristine amine EthA-22 and it was attributed to a self-organization of the amine in nanodomains caused by the presence of water.⁵⁹

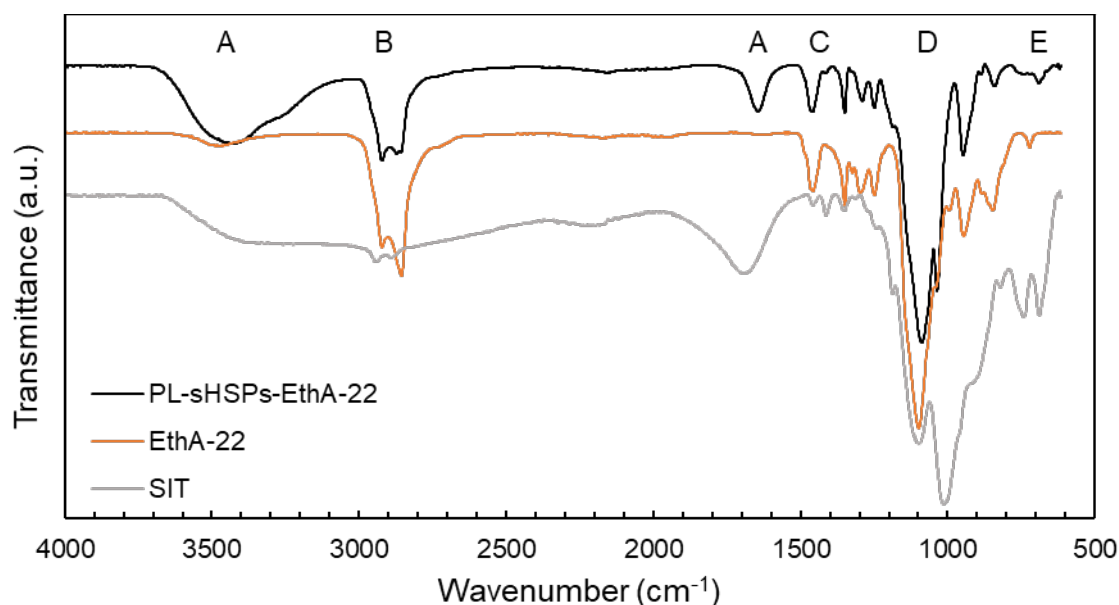


Figure 33. FTIR spectroscopy of PL-sHSPs-22, EthA-22 and SIT.

FTIR spectroscopy confirmed the efficient grafting of the organosilicon and of the polyethoxylated canopy (**Figure 33**). Two small absorption bands at 1413 cm^{-1} (C) and 687 cm^{-1} (E) appear after the

addition of the SIT onto the silica spheres, that are respectively assigned to the S=O stretching of the sulfonate and to the vibration of the CH₂ groups of the propyl chain. Two other peaks at 2918 cm⁻¹ and 2857 cm⁻¹ (B) correspond to the stretching of CH₂ groups and an increase in intensity of these peaks was observed after the addition of the amine due to its long alkyl chain. The very intense band at 1066 cm⁻¹ (D) includes both the Si-O-Si and the CH₂-CH₂-O stretching.^{54,108} The two broad bands at 3433 cm⁻¹ and 1645 cm⁻¹ (A) are reported to be characteristic of OH bonds in water molecules.^{54,109} In **Figure 34**, the FTIR signals of all the PL-sHSPs-EthAs normalized according to the peak (E) were consistent with an increase in the number of EG units when varying the amines from EthA-5 to EthA-50. The FTIR trace of PL-sHSPs-EthA-92 could not be normalized since the proportion of amine with respect to the organosilicon was too high to see a well-defined peak at 690 cm⁻¹.

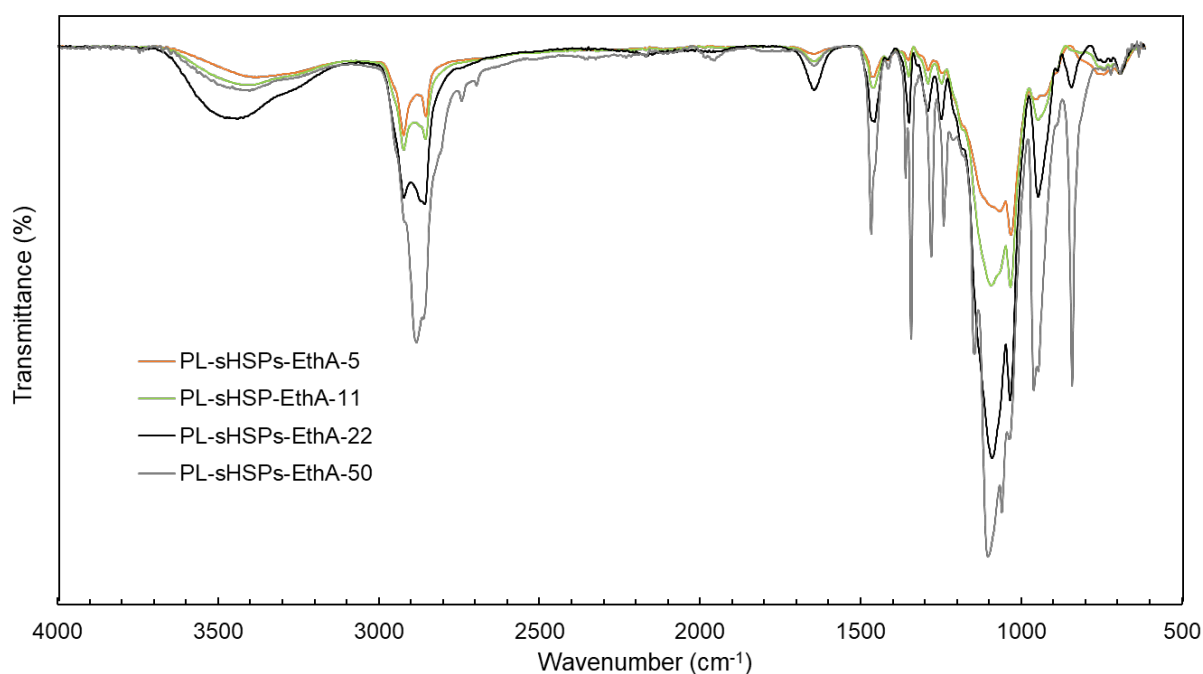


Figure 34. FTIR spectra of PL-sHSPs-EthAs (X from 5 to 50) in the range 615-4000 cm⁻¹, normalized on the peak at 690 cm⁻¹ specific of the organosilicon.

In conclusion, TEM, SAXS, TGA and FTIR data confirmed the successful grafting of SIT and EthAs onto the surface of sHSPs. TEM and SAXS also highlighted the conservation of the cavities and silica shells after grafting, with no trace of any damage.

3.1.2.2. PLs containing big hollow silica particles as hollow cores: PL-bHSPs-EthAs

A similar set of data was gathered for PL-bHSPs-EthAs to assess the success of the synthesis method applied on bHSPs. As an example, the characterization of PL-bHSPs-EthA-22 is presented in **Figure 35**.

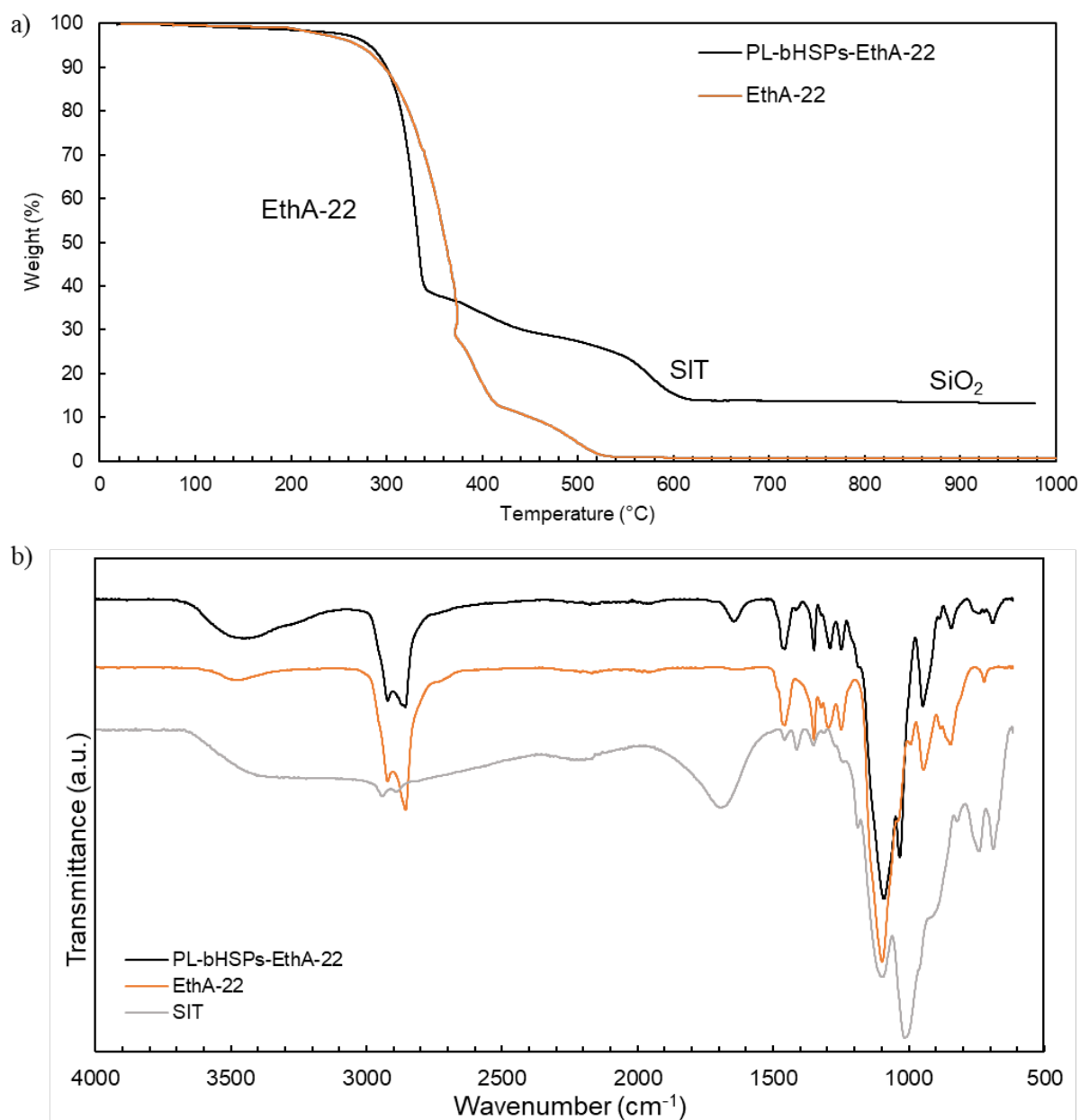


Figure 35. Grafting efficiency of bHSPs in PL-bHSPs-EthA-22 proved by **a)** thermal decomposition of PL-bHSPs-EthA-22 and EthA-22, **b)** FTIR spectroscopy of PL-bHSPs-EthA-22, EthA-22 and SIT.

The TGA (**Figure 35a**) allowed the deduction of the chemical composition, and no water was detected this time. The residual weight of inorganic SiO₂ was 13.3%, the organic part of the SIT molecule (carbon backbone and sulfonate head) accounted for 15.4%, and the canopy accounted for 71.3%, following the same calculation than described above. The organic:inorganic ratio was 6.5, that is very close to the one in PL-sHSPs-EthA-22 (6.9). The FTIR spectrum (**Figure 35b**) was very similar to the one of PL-sHSPs-EthA-22 in **Figure 33** with the same characteristic peaks confirming the efficient grafting of the corona and the canopy.

Again, the successful grafting of SIT and EthA at the surface of bHSPs was assessed thanks to these characterization.

3.1.2.3. Grafting yield and grafting density of sulfonated organosilicon (SIT)

During the synthesis of PL-EthAs, the surface modification of HSPs with the sulfonated organosilicon (SIT) is a key point of the synthesis. Indeed, this step implies the use of surface silanol groups for covalent binding and their quantification might be carried out by Fourier-transformed infrared (FTIR) spectroscopy, as found in literature. In particular, Gallas *et al.* identified a band around 4600 cm^{-1} they attributed to the $\nu + \delta$ vibration of the free Si-OH bonds.¹¹⁰ Yet, for an unknown reason, no such band could be observed in the signal of sHSPs-2 (Appendix F, **Figure A11**). The maximum density of silanol that is commonly admitted is around 5 SiOH/nm^2 , even though more recent studies reported it was underestimated, and would probably be around 8 SiOH/nm^2 .¹¹⁰ Therefore, the grafting density of SIT in sHSPs@SIT (intermediate to form any of the PL-EthAs) was expected to be in this order of magnitude.

Experimental determination of the grafting yield

Herein, different experimental analyses were conducted on a set of sHSPs grafted with SIT molecules (sHSPs-2@SIT), and they could lead to a determination of the amount of SIT in this intermediate (all the calculations are detailed in Appendix E).

First of all, TOC measurements of the dialysates from the washing process after grafting give the amount of ungrafted SIT that passes through the membrane: it was found that 16% of the SIT initially introduced was well grafted (it was 24% for sHSPs-1@SIT, as mentioned previously, but the difference is linked to reproducibility problems discussed in Section 2.4). However, not all the sHSPs-2 were grafted and about 90% of the initial weight of sHSPs was recovered. According to these data, a grafting yield of 41 mmol per gram of dry sHSPs-2 was calculated.

This result was not coherent with the pH monitoring of the addition of EthA-11 during the next step of the PL synthesis (Appendix F, **Figure A12**). When the neutralization occurred, it indicated a proton quantity of 3.3 ± 0.7 mmol per gram of dry sHSPs-2. This is 12 times less than the quantity deduced from TOC. An explanation could be that excess of SIT caused a polycondensation between the SIT molecules, thus forming large objects that could not pass the dialysis membrane. In this case, it seemed that such agglomerates were retained by the ion-exchange column, thus explaining the difference between the two values.

In order to validate the result of pH monitoring, TGA and elemental analysis of sHSPs-2@SIT were carried out. The TGA traces of sHSPs-2, sHSPs-2@SIT, and SIT are given in **Figure 36**. The intermediate sHSPs-2@SIT disclosed a clear weight loss of 25.5% at around $400\text{ }^\circ\text{C}$ attributed to the degradation of the organosilicon (**Figure 36**). According to the heat flow signal, the loss is exothermic. Moreover, SiO_2

content can be determined by the residual mass at 950 °C (64.4%). It is important to notice that for sHSPs-2@SIT, the powder was black at the end of the analysis. Therefore, not all the carbon was totally removed, so the silica content was probably overestimated, and the SIT content was underestimated. In this sample, the water content was 10.1% (weight loss below 200 °C) but it is worthy of note that all silica powders were hygroscopic so that this amount could vary between about 4 and 13% depending on the relative humidity of the day. Computation in Appendix E led to 3.6 mmol of SIT per gram of dry sHSPs-2, while elemental analysis gave 5 mmol of SIT per gram of dry sHSPs-2.

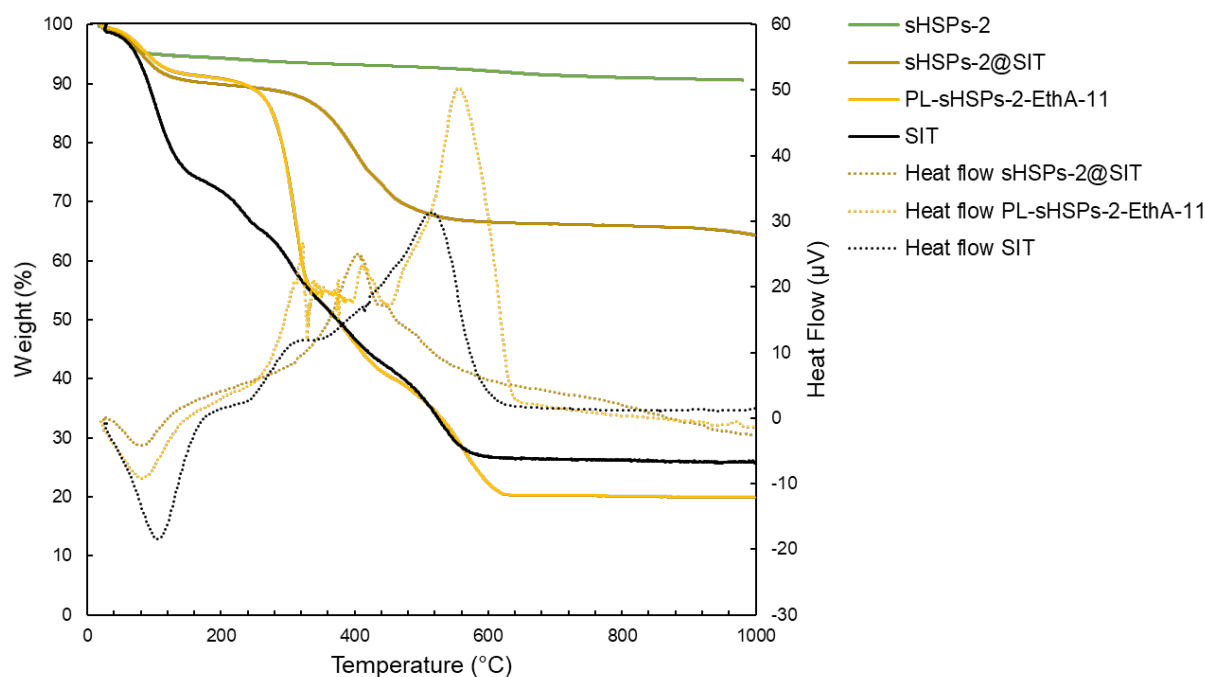


Figure 36. TGAs and TDAs of sHSPs-2, sHSPs-2@SIT, PL-sHSPs-2-EthA-11 and SIT under air at a heating rate of 5 °C/min. DTA of sHSPs does not appear for clarity.

To conclude, a mean grafting yield of 4 mmol of SIT per gram of dry sHSPs-2 can be reasonably adopted.

Estimation of the grafting density

The grafting density of SIT could be estimated by considering the mean particle size of sHSPs-2 given by the TEM imaging (see Section 2.4), eventually coupled to the results of the nitrogen sorption experiment (showed in Section 1.1.2. of Chapter III). For a spherical particle having a diameter of 37.3 nm, the external area is $4.4 \cdot 10^3 \text{ nm}^2$. According to a calculation based on sHSPs-2 density detailed in Appendix E (the density was obtained by weighing the powder packed in a graduated container), the total external area contained in 100 mg of dry sHSPs-2 is $2.1 \cdot 10^{19} \text{ nm}^2$. Then, a grafting density of SIT would be 9.6 grafts/ nm^2 , but this value is not coherent with a reasonable silanol coverage (see

above). On another hand, when including the surface of the micropores of the shell as deduced from nitrogen sorption experiments ($S_{\text{BET}} = 268 \text{ m}^2/\text{g}$), the grafting density drops to 4 grafts/nm², and this value is closer to the one given by Bourlinos *et al.* for NIMs.⁶⁵ It was assumed here that no SIT would be grafted on the internal surface of the cavity.

Therefore, these calculations show that penetration of SIT inside the pores was unfortunately occurring, for an excess of SIT introduced in the reaction medium. As a perspective, by decreasing the amount of SIT, and reducing the temperature to ambient, one could contemplate grafting the external surface of HSPs exclusively, then avoiding any pore blockage. Alternatively, grafting the SIT before removing the template by a soft washing could also be a way to favor superficial grafting.

3.1.2.4. Corona-canopy grafting ratio

After SIT grafting, the addition of the EthAs onto the sulfonated corona could be monitored through pH evolution, so the amine:SIT ratio could be accurately collected. Indeed, the grafting was stopped just after the equivalence, implying that the amine was in very little excess (around 1.2 equivalent). An overview of the molar ratios obtained for all the syntheses is provided in **Table 7**. For PL-sHSPs-EthA-92, it was not possible to determine the real equivalence, because the slope at inflexion point was very low. For PL-bHSPs-EthA-5, the equivalence was exceeded (2.3 equivalent) to see whether a liquid could be obtained by increasing the amine excess. However, it appeared to remain a solid.

Table 7. Amine:SIT molar ratios for all PL-EthAs.

Amine:SIT (mol)	5	11	22	50	92
PL-SiNPs		1.3	1.8		
PL-sHSPs	1.2	1.2	1.2	1.1	-
PL-bHSPs	(2.3)	1.3	1.5		

Surprisingly, these ratios consistently differed from the ones deduced from TGA traces. For instance, the TGA of PL-sHSPs-EthAs-22 presented in Section 3.1.2.1 (**Figure 31**) gave a EthA-22:SIT molar ratio of 0.64. It could be partially explained by a high uncertainty about the SIT content in TGA (estimated to 2-3% depending on spectrum interpretation), as well as a slow proton release from sulfonates inside the silica pores due to a confinement effect increasing their pKa.¹¹¹ This would lead to an apparent equivalence earlier than the real one when monitoring pH.

3.1.2.5. Stability and density of ionic PLs

Since PLs contain nanometric silica particles, and because they are destined to act as extracting organic phases in LLE processes, their stability overtime and their density must be known.

Positively, PL-sHSPs-EthAs were very stable overtime. As an example, PL-sHSPs-EthA-22 remained stable on shelf after two years, with no hint of any sedimentation (**Figure 37**).

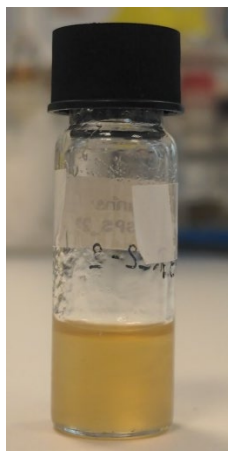


Figure 37. PL-sHSPs-EthA-22 two years after its synthesis.

In addition, the density of PL-sHSPs-EthA-22 has been accurately measured at different temperatures, with no previous outgassing (**Figure 38**). At 20 °C, the density was 1.16 g/cm³ and it linearly decreased to reach 1.11 g/cm³ at 80 °C.

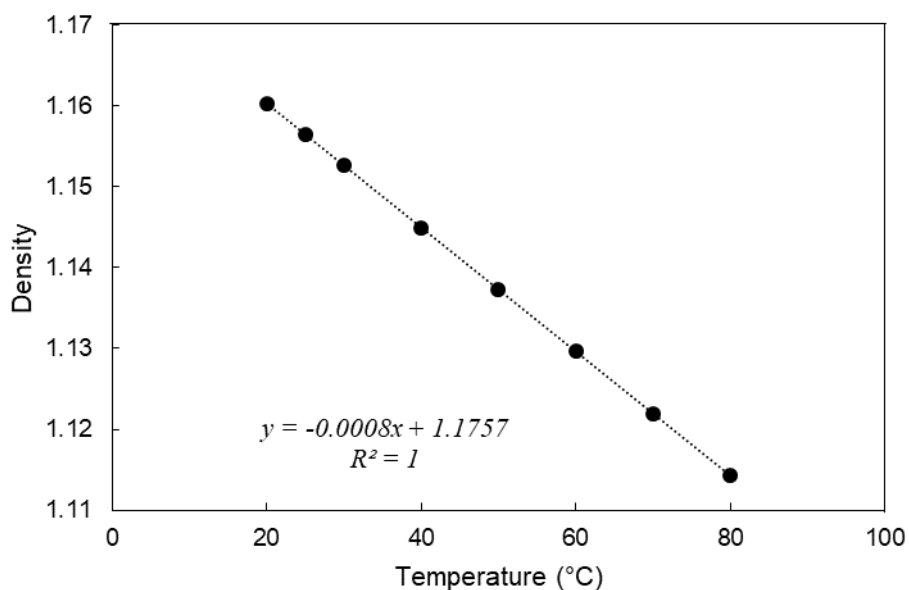


Figure 38. Density of PL-sHSPs-EthA-22 linearly decreasing with temperature.

3.2. Neutral porous liquid with hydrophobic canopy: PL-sHSPs-PPG

3.2.1. Synthesis development

As described in Section 1.3, PL-sHSPs-PPG (*cf.* bookmark No. 5) was synthesized by contacting a silanized PPG₂₀₀₀ with sHSPs under argon leading to a surface covalent grafting (**Figure 22** and **Figure 23**). A similar synthesis was also performed with PPG₇₂₅ to study the influence of the polymer length

(number of propylene glycol (PG) units) onto the physical state of the final porous material, and this part will be discussed in Chapter III, Section 2.4. The method is described in Appendix A, and the development of each step of the synthesis are detailed below.

3.2.1.1. Step 1: Silanization of PPG

The silanization of PPG was achieved in two steps. A PPG-allyl intermediate was first obtained by activating PPG with NaH before adding allyl bromide in dry tetrahydrofuran (THF). The $^1\text{H-NMR}$ analysis of the polymer after this allylation confirmed that the polymer was mostly mono-allyl functionalized (**Figure 39**). This was assigned to the presence of primary and secondary terminal hydroxyl groups in PPG, and stoichiometric conditions favored the reaction of primary ones.

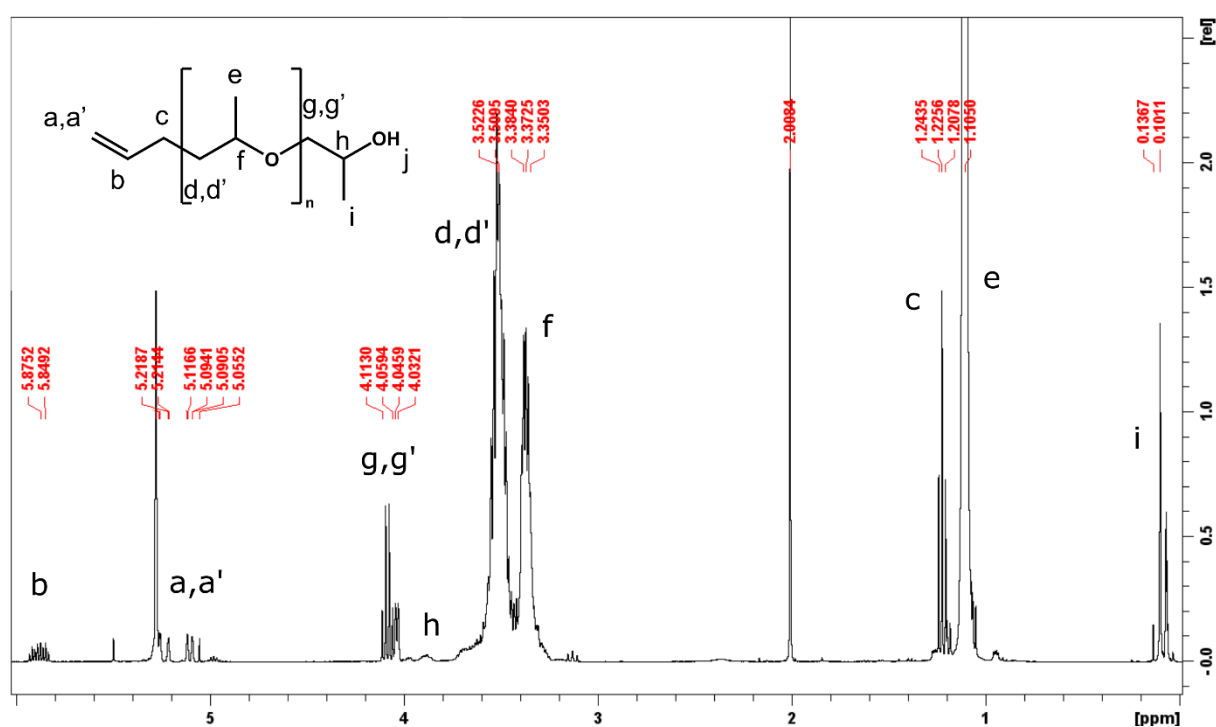


Figure 39. $^1\text{H-NMR}$ spectrum of PPG_{2000} -allyl in CDCl_3 in the range 7 – 0 ppm. Signals of grafted allyl groups are observable at 5.11 and 5.87 ppm (vinylic protons).

Then, silanization was carried out by reacting PPG-allyl with 1.2 equivalent of triethoxysilane in presence of a Karstedt catalyst¹⁰⁶ (3-3.5 mol%Pt vs vinyl-terminated polydimethylsiloxane) at 80 °C. After one night, the disappearance of the allyl group was controlled by $^1\text{H-NMR}$ (**Figure 40**). After catalyst and solvent removal, the dry silanized polymer (PPG-Si) was collected to be used at once, or stored under argon for up to six months.

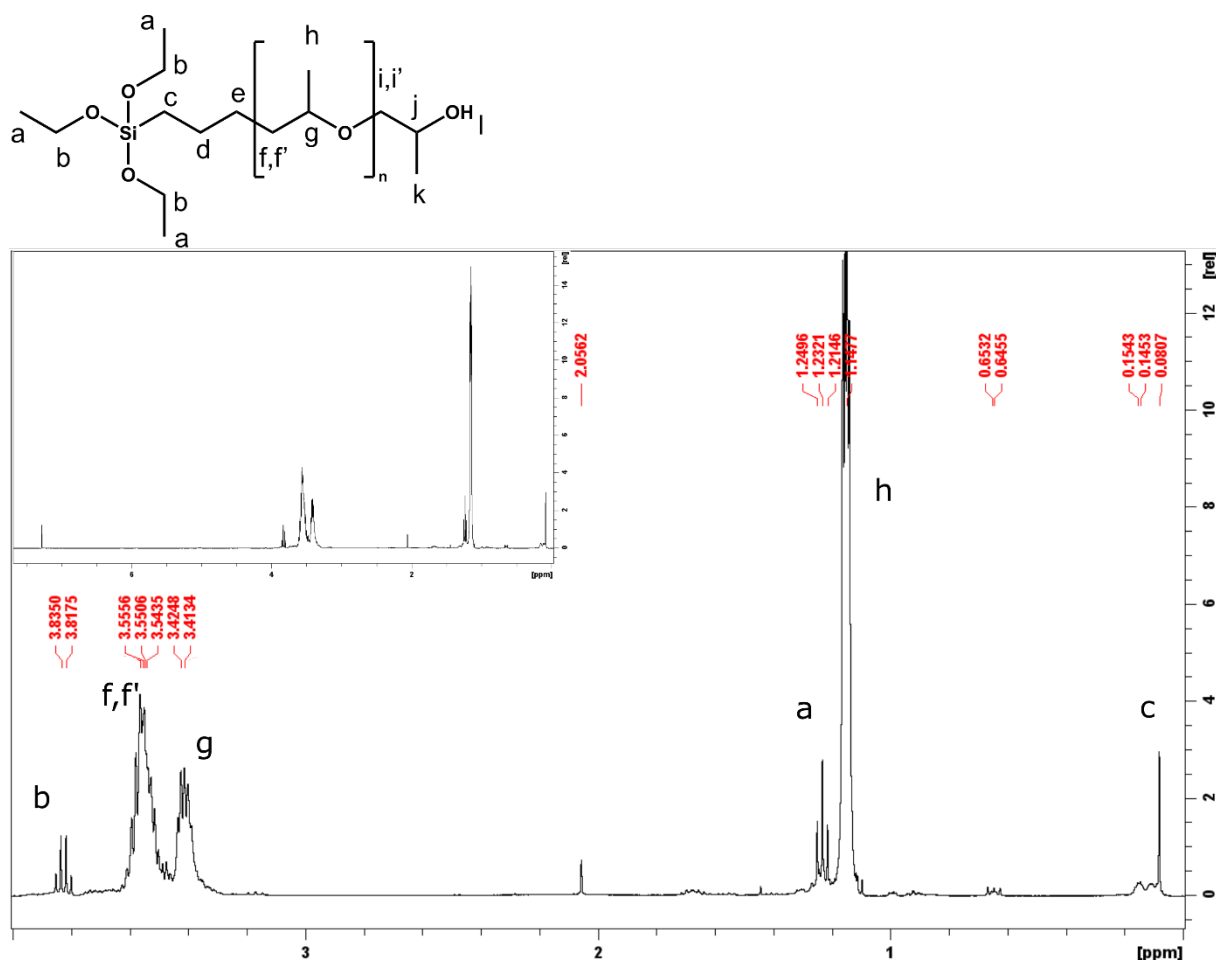


Figure 40. $^1\text{H-NMR}$ spectrum of $\text{PPG}_{2000}\text{-Si}$ in CDCl_3 . The inset shows the full range while the main frame shows a zoom in the range 5 – 0 ppm. Full disappearance of vinylic protons demonstrated the quantitative conversion of PPG-allyl into the expected silanized derivative.

3.2.1.2. Step 2: Covalent grafting

The covalent grafting of $\text{PPG}_{2000}\text{-Si}$ onto pre-activated sHSPs (a treatment with nitric acid followed by intensive drying was applied to activate the surface silanols) was performed in THF overnight at room temperature, under argon. After that, the stirring was stopped and the medium was left at rest for 15 min. As for sHSPs@SIT (*cf. supra*), a significant amount of powder felt down to the bottom of the flask (**Figure 41**). It could be separated from the bulk by sucking the supernatant with a pipette (no centrifugation was used to avoid any loss of PL, which was believed to stay in the bulk). Afterward, THF was evaporated from the bulk and an oil was obtained after further drying under high vacuum at 35 °C.

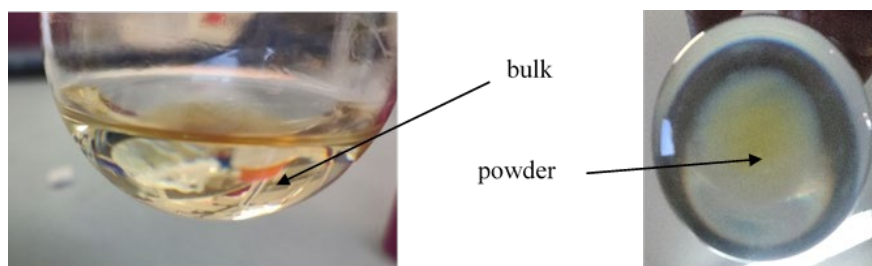


Figure 41. End of the reaction of PL-sHSPs-PPG: the round-bottom flask contains a sediment and a bulk.

In parallel, the precipitate was analyzed by TGA coupled with differential thermal analysis (DTA) giving the heat flow curve (**Figure 42**). It could be determined that this powder mainly contained poorly grafted sHSPs. Indeed, the washing step allowed removing most of the ungrafted PPG₂₀₀₀-Si (exothermic weight loss occurring at about 240 °C before washing and 215 °C after washing, as indicated by the heat flow signal), and less than 15% of condensed PPG₂₀₀₀ remained in the material.

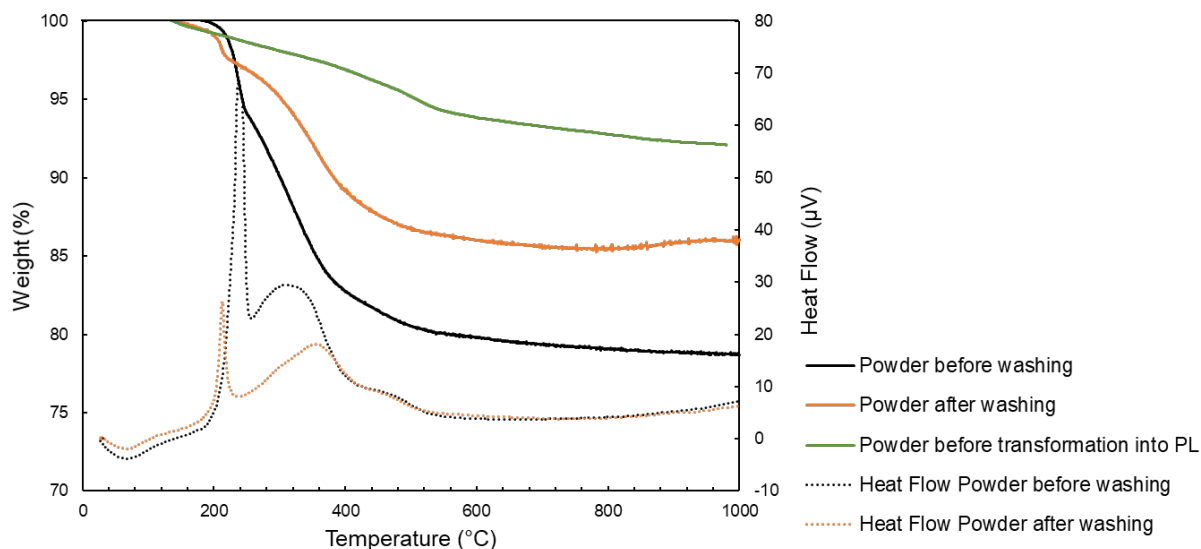


Figure 42. Organic content in the sediment before and after washing, analyzed by TGA and DTA. The TGA of sHSPs before synthesis is also shown for comparison. The weights were corrected from solvent loss (below 100 °C), see Appendix B.

The yield of sHSPs properly incorporated in the PL with this method was 43.4%: it was much higher than in the case of SIT grafting in water. Indeed, observations of the bulk appearance during the reaction suggested that THF (containing PPG) was a better dispersing medium for sHSPs than water (containing SIT), because the suspension was clearer; and this could partially explain the higher yield. Yet, perspectives should include synthesis optimization, such as a different route involving a bromopropyl-trimethoxysilane grafted onto the surface of sHSPs before a direct reaction with PPG₂₀₀₀.

3.2.1.3. Competitive reactions and synthesis conditions

This synthesis route was interesting because it did not introduce any functional groups inside the canopy. Therefore, in the context of LLE, it prevents any metal from being trapped inside the canopy instead of diffusing inside the HSPs.⁵⁷ However, a polycondensation side-reaction was expected, as described in **Figure 43**.

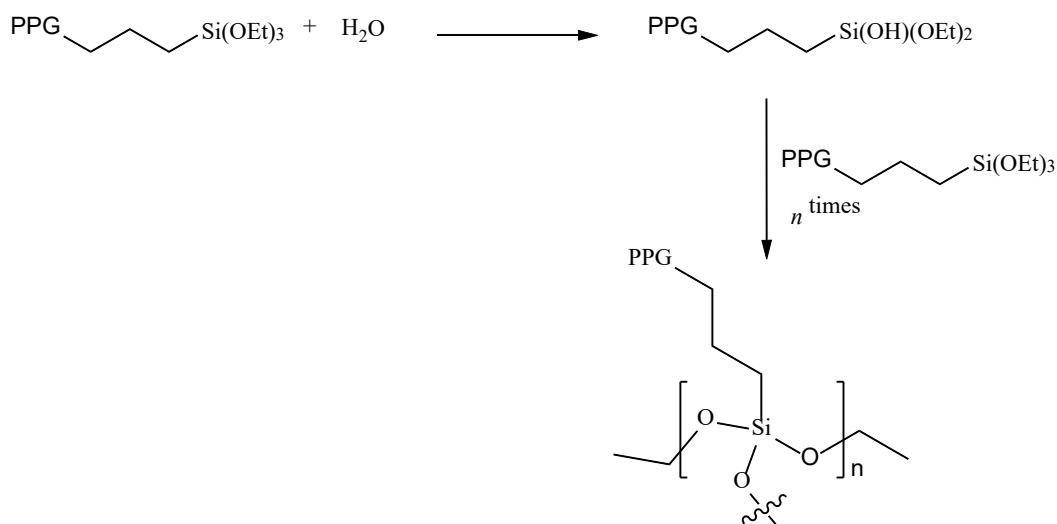


Figure 43. Polycondensation of PPG-Si might occur as a side-reaction.

For this reason, different synthesis conditions have been tested to select the best way promoting the grafting despite the high hindering of PPG₂₀₀₀ (**Table 8**): any condition that would speed up the hydrolysis process was expected to facilitate the polycondensation. Instead, a dry medium, a high dilution and room temperature could help the grafting occurring faster than polycondensation. Besides, the sHSPs were dried for 2 h at high temperature (100-120 °C) under vacuum. Nevertheless, it was assumed that because bound water would certainly remain in silica pores, the water molecules adsorbed close to the surface could act as a catalyst of the hydrolysis reaction.¹¹²

Table 8. Synthesis conditions tested to obtain PL-sHSPs-PPG. All the reactions were performed at room temperature. The last column mentions whether the sediment was separated from the bulk before solvent removal or not.

	$m_{\text{PPG-Si}}$	m_{sHSPs}	Dilution (PPG)	Solvent	Time (h)	Separation?
PL-a	908.6 mg	177.1 mg	40 mL + 3mL 21 g/L	Toluene:THF (13:1)	17.75	Yes
PL-b	1.0854 g	181.1 mg	18 g/L	THF	112.25	No
PL-c	304.6 mg	45.5 mg	10 g/L	THF	136.5	Yes
PL-d	2.25 g PPG-allyl	385 mg (before drying)	22 g/L	THF*	18	Yes

*THF was not perfectly dry.

At first, toluene was used as anhydrous solvent (PL-a), but the silanized polymer PPG-Si was not properly solubilized and few milliliters of THF should be added as a co-solvent. Therefore, dry THF was selected for the next syntheses (PL-b to PL-d) and a comparison of PL-a and PL-d done under the same conditions (except for the solvent) indicated that the change did not have significant impact on the nature of the resulting materials.

Two other variations were introduced: first, the reaction time was varied from one night to five days. Second, the separation of the sediment from the bulk at the end of reaction (before drying, **Figure 41**) was also suppressed (PL-b) to see its influence of the physicochemical properties of the final PL. It was immediately observed that no separation led to the formation of a gel sticking to the walls of the round-bottom flask (along with a residual oily phase at the very bottom) whereas drying the bulk alone led to a viscous liquid (PL-c).

The influence of the solvent and reaction time on the homogeneity and stability of the synthesized PLs are discussed in the next section.

3.2.2. Characterization

3.2.2.1. Homogeneity and stability of PL-sHSPs-PPG

A PL-sHSPs-PPG was synthesized by grafting a silanized PPG₂₀₀₀ at the surface of sHSPs-2 (*cf.* bookmark No.5). As described above, the bulk was separated from the sediment at the end of the reaction, so that most part of ungrafted sHSPs were removed at this step. After drying the bulk, an oil was obtained, and it was labeled PL-sHSPs-PPG. However, it appeared to be unstable overtime: depending on the synthesis conditions (see Section 3.2.1.3), it underwent a phase separation leading to three phases (like PL-a) or two phases (like PL-d). Investigation based on SAXS measurements were conducted to determine the origin and the stability of these different phases, and it is detailed in Appendix G.

In summary, it was shown that in all cases, the bottom phase contained a high amount of sHSPs, increasing its viscosity such that it was more gel-like, while the top phase was more fluid, with a lower sHSPs content. It underwent a slow sedimentation reaching a plateau after 20-30 days, suggesting that partially grafted sHSPs were in suspension in free molecules of PPG. Increasing the reaction time lead to a more stable (with one main phase) but also more viscous liquid. In the end, the conditions used to make PL-d (dry THF, 22 g/L of PPG₂₀₀₀, room temperature, overnight, see **Table 8**) were retained, and the two phases were separated after centrifugation, to give a fluid phase (named PL-sHSPs-PPG-fluid) and a gel phase (PL-sHSPs-PPG-gel) (**Figure 44**). In the following section, these two phases are characterized separately.

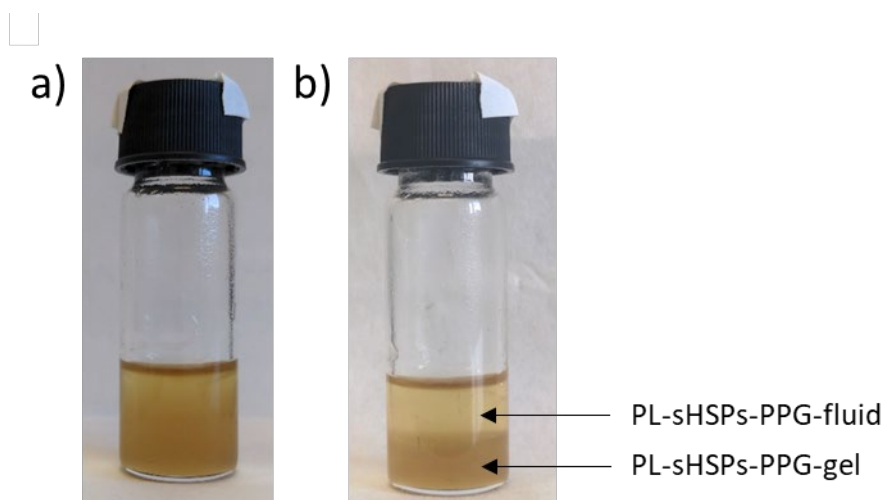


Figure 44. a) Fresh PL-d, b) Evolution after 13 days.

3.2.2.2. Characterization of the two liquid phases of PL-sHSPs-PPG

Since PL-d was obtained in greater quantities, and because the two phases deriving from its synthesis were stable overtime, it was chosen as a reference material to further investigate in what extent these phases could be suitable materials for LLE. Hence, the phases were separated after centrifugation, and individually characterized by TGA, SAXS, TEM and FTIR analyses. As described above, the bottom phase was gel-like so it was labeled “PL-sHSPs-PPG-gel” whereas the top phase was oil-like so it was labeled “PL-sHSPs-PPG-fluid”.

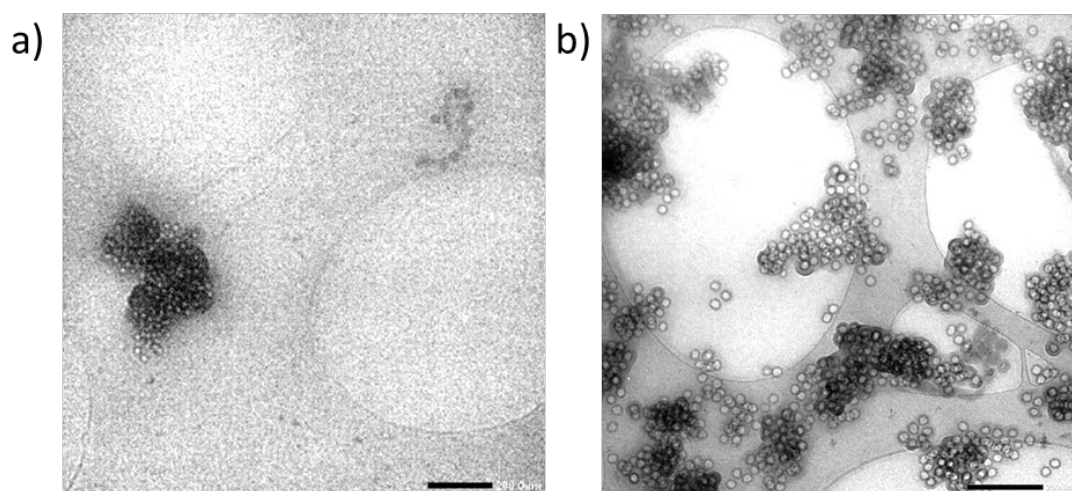


Figure 45. TEM images of a) PL-sHSPs-PPG-fluid (x25k), and b) PL-sHSPs-PPG-gel (x30k). Scale bars: 200 nm.

First of all, TEM images of the two phases gave insight into the dispersion of the nanoshells in the polymeric matrix (**Figure 45**). For this analysis, the samples were put directly on the TEM grids without dilution into a solvent. As expected, the gel phase (**Figure 45b**) contained a higher density of sHSPs

than the fluid phase (**Figure 45a**). However, in both cases, sHSPs were mostly found as aggregates, surrounding by organics, and this could explain the sedimentation observed above.

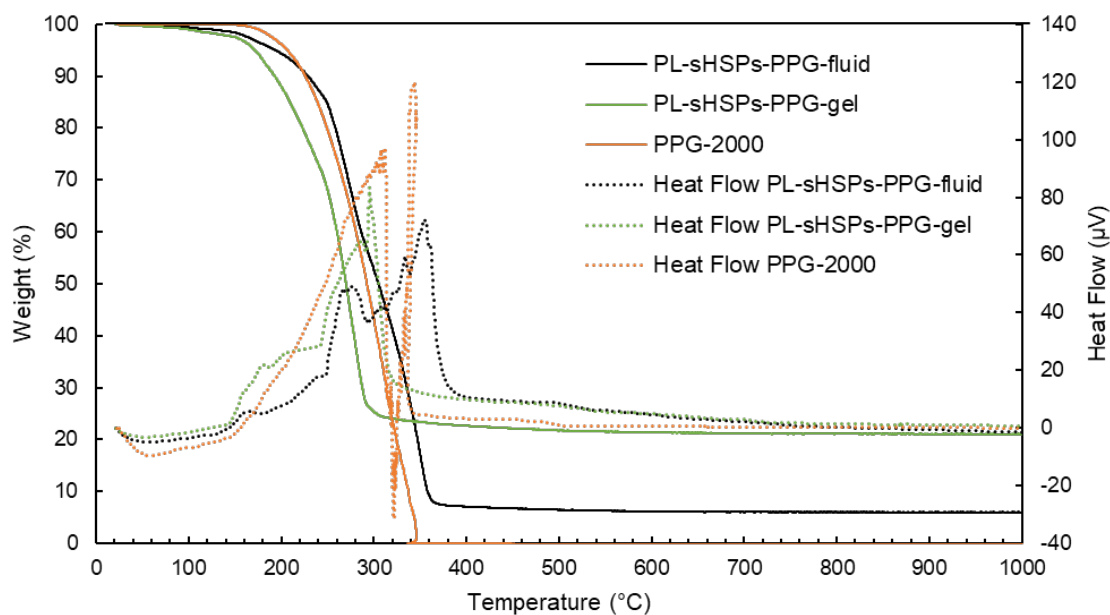


Figure 46. TGA and DTA of PPG₂₀₀₀, PL-sHSPs-PPG-gel, PL-sHSPs-PPG-fluid.

According to the TGA (**Figure 46**), no water was observed in any of the two phases. The residual weight at 950 °C corresponding to the silica content in the PL was 3.5 times higher in the gel phase (21%) than in the fluid phase (6%). The degradation of PPG₂₀₀₀ occurred in two steps, at lower temperatures (165-320 °C) for PL-sHSPs-PPG-gel than for PL-sHSPs-PPG-fluid (165-385 °C). This difference could mean that PPG in PL-sHSPs-PPG-gel is less grafted than PPG in PL-sHSPs-PPG-fluid. In other words, there are proportionally fewer sHSPs fully grafted in PL-sHSPs-PPG-gel than in PL-sHSPs-PPG-fluid. In all cases, the tendency of reducing the thermal stability of the pure organic moiety by the presence of a high amount of sHSPs that was observed previously with PL-EthAs (Section 3.1.2), is confirmed here with PL-sHSPs-PPG-gel.

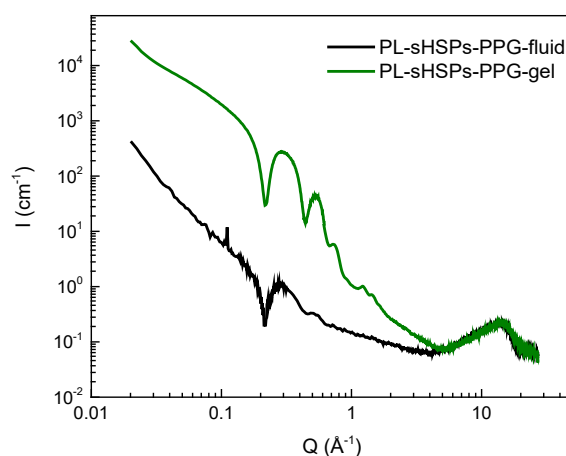


Figure 47. SAXS and USAXS signals of PL-sHSPs-PPG-gel and PL-sHSPs-PPG-fluid in the range 0.02 – 30 Å⁻¹.

The oscillations in the SAXS signal (**Figure 47**) validate the presence of the sHSPs, and the difference in intensity at low angles is coherent with the higher silica content of the gel phase. However, no change in the structure can be evidenced because no structural peak -apart from the ones due to PPG and silica- was visible in both cases.

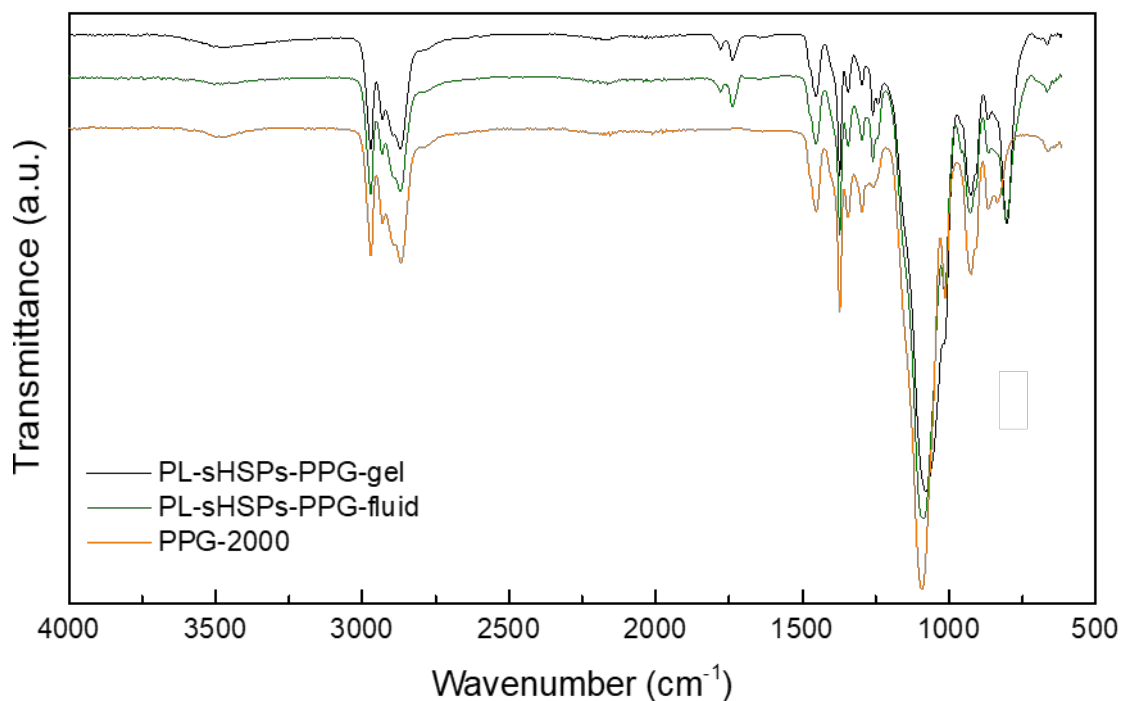


Figure 48. FTIR spectra of PPG₂₀₀₀, PL-sHSPs-PPG-gel and PL-sHSPs-PPG-fluid in the scanning range 4000 – 615 cm⁻¹.

FTIR spectroscopy (**Figure 48**) confirmed that the two phases contain the characteristic vibration bands of PPG and sHSPs. CH₂ symmetric stretching bands and shearing band were visible at 2973-2869 cm⁻¹ and 1457 cm⁻¹ respectively,¹¹³ along with alkyl CH₃ and CH deforming band at 1375 cm⁻¹ and 1342 cm⁻¹ respectively.¹¹⁴ The -C-C-O- group stretching is responsible for a characteristic band at 1296 cm⁻¹, and two harmonic bands at 929 cm⁻¹ and 907 cm⁻¹.¹⁰⁸ The -C-O-C- stretching features occurred at 1089 cm⁻¹, and the hydroxyl contribution was a large band at 3550-3400 cm⁻¹ in the spectrum of pure PPG and PL-sHSPs-PPG-gel. This band was less intense in the signal of PL-sHSPs-PPG-fluid, because there were less sHSPs than in PL-sHSPs-PPG-gel and there were less terminal hydroxyl groups than in pure PPG due to the mono-silanization. The broad band of -C-O-C- stretching overlaps with the asymmetric stretching vibrations of Si-O-Si (TO mode at 1154 cm⁻¹ and LO mode at 1089 cm⁻¹) only visible in the spectra of PL-sHSPs-PPG-gel and PL-sHSPs-PPG-fluid (in particular, a broadening of the band was clearly visible for PL-sHSPs-PPG-gel).⁵⁴ The symmetric vibrations give a strong band at 803 cm⁻¹ that is absent in the signal of the pure PPG.⁵⁴ The peak at 1260 cm⁻¹ was stronger in PL-sHSPs-PPG-gel and PL-sHSPs-PPG-fluid signals and it was attributed to Si-C stretching vibration,¹¹⁵ while the peak at 957 cm⁻¹ is characteristic of the Si(OEt) group,¹¹⁶ indicating that the PPG was not totally hydrolyzed, especially for PL-sHSPs-PPG-fluid. The two peaks at 1778 and 1735 cm⁻¹, as well as a third smaller one at 1235 cm⁻¹ occurring in the signals of the two phases, but not in the signal of pure PPG, are due to ethyl acetate used to redisperse the PL after the synthesis to facilitate their collection.

Finally, mass spectrometry (MS-ESI) of the two phases (after dilution and filtration) were carried out but it did not show any significant difference: in both phases, the major part of the m/z distribution was around 1900, with a small part of dimers around 4000, which was also visible in the raw polymer. This result suggests that free PPG molecules were present in both phases, with no polycondensation occurring for these molecules, supporting the hypothesis of suspensions where the content of sHSPs rules the viscosity (gel or liquid).

In conclusion, the two phases of PL-sHSPs-PPG (gel and liquid) disclose very similar chemical properties: they are likely two suspensions of sHSPs in PPG, with different silica contents impacting their viscosity and density: the gel phase contained more sHSPs and it was more dense than the fluid phase. However, after a slow sedimentation, the phases were stable overtime in terms of silica content. This is assigned to the successful grafting of dispersed sHSPs with silanized PPG. This hypothesis will be confirmed by other stability tests with the PL in contact with water (see Chapter IV, Section 5.2).

Conclusion

In the end, a range of silica-based PLs have been synthesized and deeply characterized. Two types of HSPs, with different sizes (25 nm for sHSPs and 236 nm for bHSPs) were successfully turned into liquid thanks to a dual corona-canopy ionic system. TEM, TGA, FTIR and SAXS analyses confirmed the success of the grafting which did not alter the silica core. The canopy was made of a tertiary amine containing one hydrophobic chain (C₁₆-C₁₈) and two PEG chains whose sizes could be varied, introducing another degree of tunability in the synthesis method that will be discussed in the following chapter. The overall yields of the syntheses was low (between 5 and 7% of initial HSPs remained in the final PLs) and further optimization would include a better dispersion of HSPs before SIT grafting (by changing the solvent, or by continuing investigations about an ultrasonic-assisted SIT grafting step). Furthermore, reproducibility of HSPs syntheses was not completely satisfying, because HSPs sizes and yields varied a lot from one batch to another. Perhaps a better control of temperature and precursors addition could help dealing with these issues. However, these variations did not prevent from pursuing investigations about PLs.

A neutral hydrophobic PL was also obtained thanks to the silanization of a PPG₂₀₀₀ before grafting it onto sHSPs. Under the conditions selected in this thesis, the PL-PPG underwent a spontaneous phase separation. The two phases were characterized independently: they showed different viscosities (a gel-like and a liquid-like), with two degrees of sHSPs volume fraction. The most fluid phase contained 6% of sHSPs and it was retained as the most suitable for LLE application.

As a perspective, a more efficient grafting of PPG could be obtained by firstly grafting a bromo-terminated organosilicon onto HSPs, before adding a PPG (but the activation of the latter could be tricky). Another route could also consist in the silanization of PPG by the mean of an isocyanate [3-(Triethoxysilyl)propyl isocyanate, ICPTES]. This route is widely applied to silanize PEG in quantitative yields; however, it would incorporate a chelating group in the organic part of the PL. This may impact the efficiency of the latter in LLE.

Moreover, grafting bHSPs with PPG might be easier because of the bigger size, preventing hindrance due to the big size of PPG. This could not be done in the course of this thesis because the synthesis route of bHSPs resulted in less material than for sHSPs.

At this point, it is still hard to determine which PL could be the best for REEs extraction. Indeed, factual information about intrinsic porosity of HSPs, PL's permeability to aqueous phases, their affinity toward water, and their viscosity, balanced with the silica content, still miss. In the following chapter, a confrontation of all these physicochemical properties for each PL type will be detailed.

Chapter III

Studying and tuning the physicochemical properties of porous liquids

PLs are very recent materials owning unusual combinations of physicochemical properties. Indeed, porosity is not a concept that generally applies to liquids, and the idea that it could exist in the liquid state still needs to be defended with strong proofs. More importantly, the state-of-the-art already showed the possibility of tuning this porosity by playing on the nature of the host, and the method to make it flowing (bulky solvents, covalent grafting, liquid polymers...). The first section of this chapter will focus on the characterization of porosity profiles of the silica hosts (sHSPs and bHSPs) employed in this thesis, as a prerequisite to showing whether the differences in their porous structure may alter both the porosity of the PL and its potential to be a good candidate for LLE of metals. Afterwards, a method to measure the permeability of PLs will be described and applied to an ionic silica-based PL.

Furthermore, the physical state (at room temperature), the viscosity and hydrophobicity of PLs can also be tuned by changing the nature of organic moieties and hosts. Herein, a range of organic moieties has been studied, to bring a better comprehension of their influence onto the physicochemical properties of PLs, and to identify key parameters to properly tune them. In particular, the presence or absence of ionic interactions, the role of temperature and particles size and density will be discussed in Section 2 of this chapter, along with the organic:inorganic ratio identified as a key parameter to tune PLs' physical state and viscosity. Finally, the influence of the organic moiety onto the hydrophobicity

of PLs (also having an impact onto the permeability of PLs depending on the solvent) will be evaluated apart in Section 3.

1. Studying porosity and permeability

For a certainty, the first properties of PLs interesting to tune are their porosity and permeability. However, measuring them in a PL is not straightforward, given that the methods developed for porous solids generally do not fit for PLs (see Chapter I, Section 2.2). Therefore, it is important to study the intrinsic porosity of the silica cores (herein, HSPs) in good details before any measurement concerning PLs. Indeed, it was demonstrated by TEM in the previous chapter that the cavities were maintained after surface modification of HSPs. In this section, nitrogen sorption will be firstly applied to SiNPs, sHSPs and bHSPs before surface modification. The differences in porous properties assigned to a lack of reproducibility in the synthesis method will also be underlined. Then, in the context of the targeted LLE application, a method for assessing the permeability of PLs to liquids will be introduced.

1.1. Porosity of hollow silica particles

1.1.1. Porosity characterization with N_2 sorption

Knowing the size of the hollow cavity and the shell thickness of HSPs (Chapter II, Section 2), nitrogen sorption experiments were carried out at 77 K to compare the parameters defining the porosity of the spheres: microporous and mesoporous volumes, pores sizes distributions and specific areas. **Figure 49** shows the isotherms and the pore size distributions while **Table 9** summarizes the key features of porosity profiles of SiNPs, sHSPs and bHSPs. Appendix D introduces the technical details about N_2 sorption measurements and models used in this thesis.

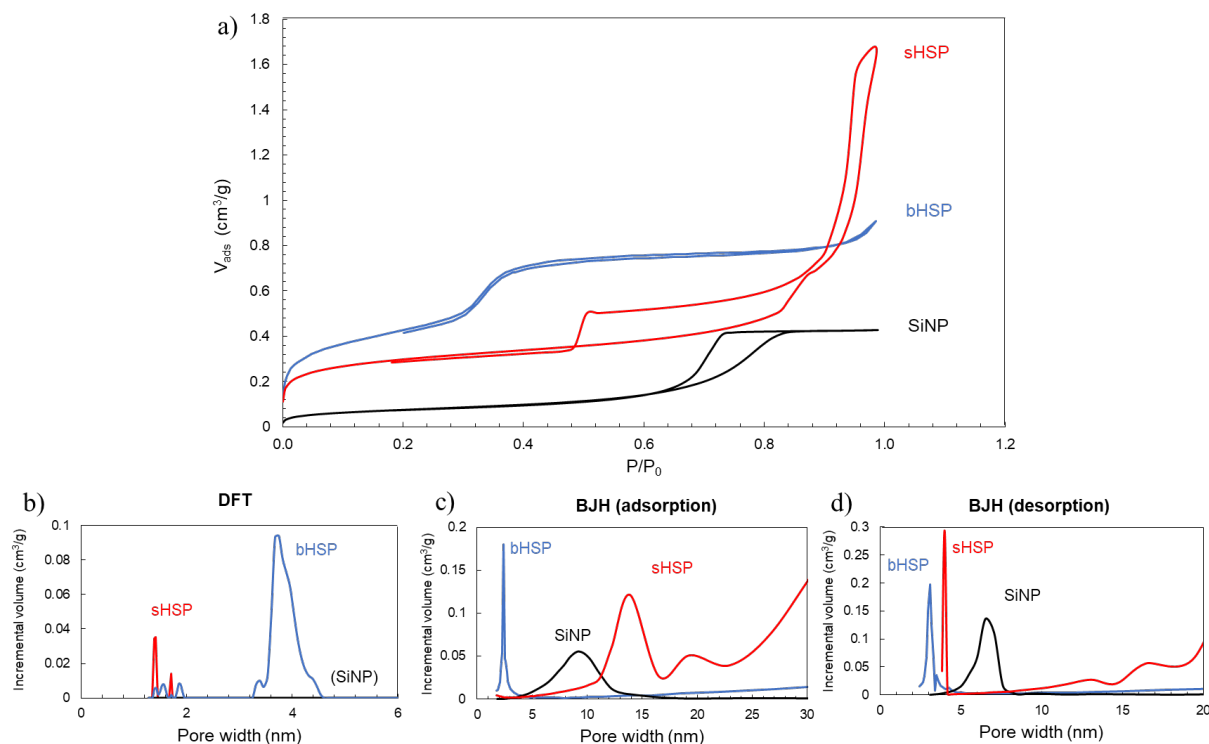


Figure 49. a) Nitrogen sorption isotherms of SiNPs, sHSPs and bHSPs. Pore sizes distributions obtained by **b)** DFT calculations, **c)** BJH model applied to the adsorption branch, **d)** BJH model applied to the desorption branch.

In **Figure 49a**, SiNPs displayed a Type IV isotherm according to the IUPAC classification, with a H2 hysteresis at relative pressures P/P_0 between 0.65 and 0.85 characteristic of the liquefaction of nitrogen in interconnected mesopores. These mesopores are created by the self-assembly of SiNPs during drying, forming a mesoporous silica¹¹⁷ (commercial SiNPs was supplied as a suspension in water). This resulted in a quite higher porous volume than expected (0.42 cm³/g), while the Brunauer-Emmett-Teller (BET) specific area was 175 m²/g.

sHSPs (sHSPs-1 set) displayed a Type IV isotherm, with a H1 hysteresis at relative pressures between 0.48 and 0.87 characteristic of the hollow mesoporous cavity. The presence of an additional microporosity (so that it was a Type I + Type IV hybrid isotherm actually) has been evidenced thanks to the analyses of low and middle pressure zones by the t method and the BET equation (0.2 - 0.7 and 0.004 - 0.13 P/P_0 , respectively): the difference between the BET specific surface (691 m²/g) and the surface obtained by linear extrapolation of the t-plot (271 m²/g) clearly proves the presence of micropores (see Appendix D). This isotherm was therefore similar to the ones that can be obtained with reference materials of SBA-15 type, that are micro- mesoporous silica nanoparticles made using Pluronic triblock copolymers as soft templates.¹¹⁸ The total adsorbed volume at $P/P_0 = 1$ was much higher than for SiNPs (1.67 cm³/g) but mainly due to the interparticle void (second hysteresis above

0.87 P/P_0). The total volume adsorbed at $P/P_0 = 0.87$ and probably corresponding to the uptake inside the particles was $0.66 \text{ cm}^3/\text{g}$ instead. The microporous volume (taken at $P/P_0 = 0.02$) was $0.21 \text{ cm}^3/\text{g}$, contributing to one third of the total pore volume.

The signal of **bHSPs** approached a hybrid Type II + Type IV curve typical of a macroporous solid containing micro- and mesopores. In this case, the cavity inside the particle is considered as a macropore because its diameter overcomes 50 nm. Moreover, the presence of two steps (for relative pressures around 0.005 and 0.3) instead of one indicates two different populations of micro- or mesopores in the shell. It is characteristic of MCM-41 materials (nanoparticles made using CTAB as a soft template in basic conditions).¹¹⁸ The adsorbed volume of gas at $P/P_0 = 0.87$ was $0.78 \text{ cm}^3/\text{g}$ in this case (it excludes the interparticle void even though it cannot be entirely uncorrelated from the large core of bHSPs) and the BET specific area and the surface computed from the t method were $1121 \text{ m}^2/\text{g}$ and $1210 \text{ m}^2/\text{g}$ respectively. Despite a less pronounced difference between these two areas than for sHSPs, the microporous volume is still higher ($0.27 \text{ cm}^3/\text{g}$) in agreement with the significantly higher specific surface area.

Table 9. Porosity parameters of SiNPs, sHSPs and bHSPs determined from N_2 sorption experiments. Underlined pore sizes correspond to the main proportion of pores.

	Total adsorbed volume (cm^3/g) ^a	Microporous volume (cm^3/g) ^b	Mesoporous volume (cm^3/g)	Pores sized (nm)
SiNPs	0.42*	0.04	0.38	(10)
sHSPs	0.66	0.21	0.45	<u>1.4/1.7</u>
bHSPs	0.78**	0.27	0.51	<u>1.5/3.7</u>

^a $P/P_0 = 0.87$; ^b $P/P_0 = 0.02$; *mainly due to interparticle void created when drying the aqueous dispersion; **this excludes the volume adsorbed by the macroporous core.

Besides, mesopores distribution has been deduced from a Barrett-Joyner-Halenda (BJH) model while density functional theory (DFT) calculations have been applied to determine the distribution of micropores and small mesopores (below 5 nm) and their contribution to the porous volume and the specific surface (Appendix D, **Figure 49b-d**). Generally, the capillary condensation occurring during the adsorption prevents from reaching a thermodynamic equilibration, such that the desorption branch is usually used for the BJH model. However, for signals showing a hysteresis due to pores with at least two characteristic sizes (for instance ink bottle-shaped pores), the desorption branch reports on nitrogen release from the narrowest part of the pore. In the case of sHSPs, the mesoporous internal core has openings connected to the silica shell, and one can presume that an analysis of the desorption branch only delivers the size of the openings (3.9 nm in this case, **Figure 49d**). To verify the size of the hollow core, the adsorption branch was considered instead (**Figure 49c**): a band around 14 nm

corresponded to the mean size of the hollow core, in good agreement with TEM and SAXS data (14.8 nm and 15.8 nm respectively).

The reader is referred to **Table 9** for a summary of the main pore sizes in silica shells. SiNPs showed interconnected mesopores due to particles self-assembly (the particles probably sintered during drying), with two characteristic sizes around 6 nm and 9 nm. They can explain the BET surface of 175 m²/g. Inside the shell of sHSPs, pores mainly have a size of 1.4 nm and a small portion have a diameter of 1.7 nm. Regarding bHSPs, two populations of pores sizes are visible: a small part have a diameter around 1.5 nm and the major part of pores have diameters around 3.7 nm. This last value is encouraging for application in LLE, because bigger complexes are more likely to diffuse inside the shell.

1.1.2. Effect of reproducibility problems on porosity

As presented in Chapter II, Section 2.4, the reproducibility of the synthesis of sHSPs was not satisfying, with a significant discrepancy in the size of the shell and the cavity from one set to another one. This difference can also be seen when characterizing porosity. In **Figure 50**, the N₂ sorption isotherm of sHSPs-2 (external diameter: 37.3 nm, internal diameter: 19.4 nm according to TEM) is compared to the one of sHSPs-1 presented in the previous paragraph (external diameter: 25.4 nm, internal diameter: 14.8 nm).

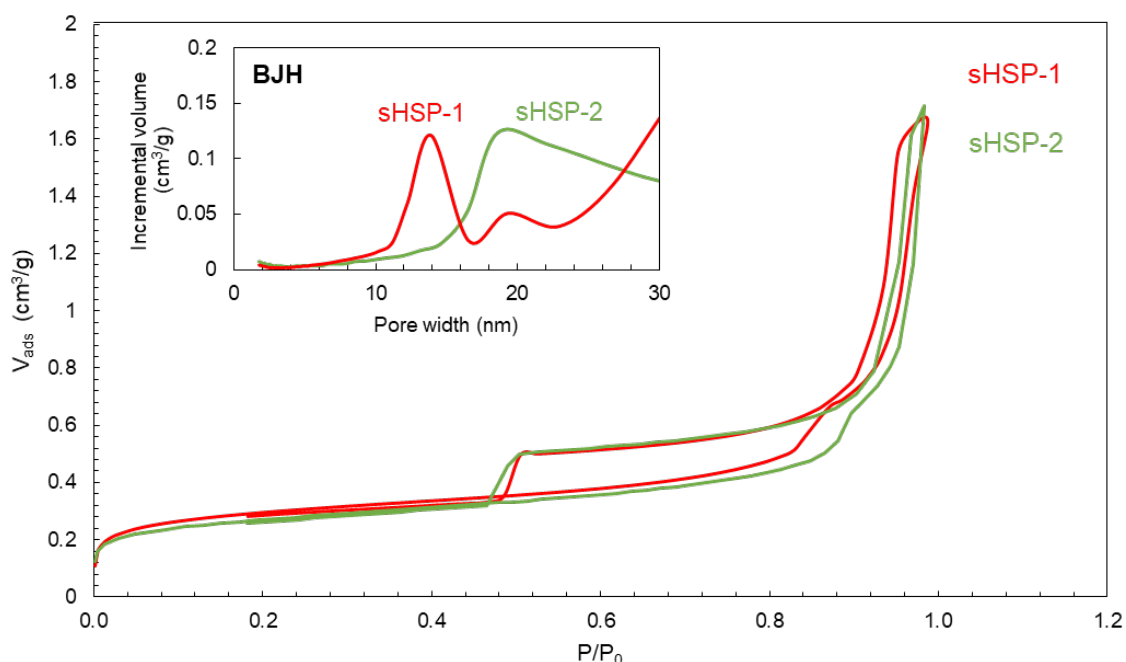


Figure 50. N₂ sorption isotherms of two sets of sHSPs. The inset shows the pore size distribution obtained from the BJH model applied to the adsorption branch.

If the microporous volumes and the BET specific surface areas are quite similar ($0.21 \text{ cm}^3/\text{g}$ and $691 \text{ m}^2/\text{g}$ for sHSPs-1; $0.19 \text{ cm}^3/\text{g}$ and $624 \text{ m}^2/\text{g}$ for sHSPs-2), the hysteresis at high relative pressures differs for sHSPs-2. The BJH model applied to the adsorption branch (**Figure 50**, inset) shows a mean cavity size of 18.6 nm for sHSPs-2 whereas it was 13.9 nm for sHSPs-1, in coherence with TEM imaging. The hysteresis was larger for sHSPs-2, suggesting that the pore openings were even smaller than for sHSPs-1.

For practical reasons, the following section concerning the impact of the template removal method on porosity (Section 1.1.3) will refer to sHSPs-2, that were also used to make PL-sHSPs-PPG. sHSPs-1 served to make PL-sHSPs-EthAs instead.

1.1.3. Impact of the template removal method on porosity

During the synthesis of sHSPs, the template was removed by calcination during 10 h at $450 \text{ }^\circ\text{C}$. This process might also induce a contraction of small pores, while strengthening the silica network.^{118,119} Furthermore, with the aim of functionalizing sHSPs for LLE (see Chapter IV), it was necessary to change calcination for a softer template removal. For these reasons, the effect of a soft acidic ethanol washing (pH 1, 24 h under reflux and vigorous stirring) on the porosity profile of sHSPs-2 was studied.

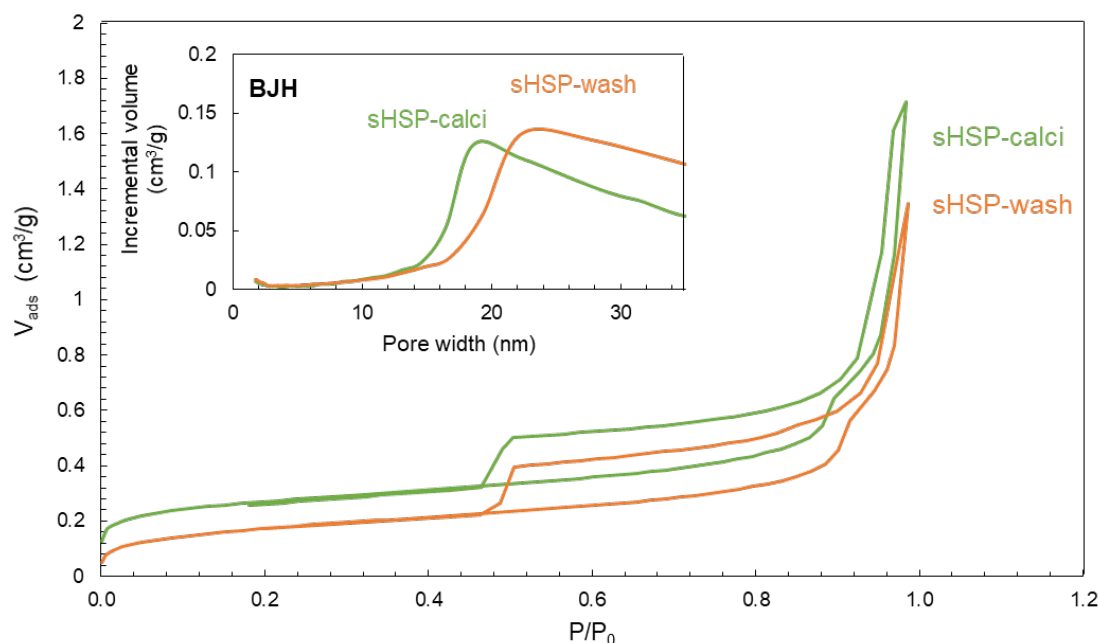


Figure 51. N_2 sorption isotherms of sHSPs-2 after calcination and after washing with hot acidic ethanol for 24 h. Inset: pore sizes distributions as deduced from BJH models applied to the adsorption branch.

Figure 51 reveals the N_2 sorption isotherm of sHSPs washed with ethanol, compared to the same set of sHSPs after calcination. The signals are very similar, and the hysteresis is still present in the sample

washed with ethanol, indicating that the hollow cavity is well accessible. However, it is slightly shifted toward higher pressures: in the pore sizes distribution obtained by applying the BJH model to the adsorption (**Figure 51**, inset), the size of the hollow core was bigger (22.3 nm after a soft washing instead of 18.6 nm after calcination). The BET specific area was 400 m²/g, which is lower than the reference (620 m²/g), and this could be explained by the loss of microporosity (the volume taken at $P/P_0 = 0.02$ was 0.11 cm³/g compared to 0.19 cm³/g for the reference): either the smallest micropores were still obstructed, or coalescence of micropores occurred. In any case, the presence of the hysteresis indicated that the the cavity was accessible to the gas, so the shell porosity was maintained with this soft template removal method.

Based on all these data, it was obvious that the two types of HSPs constituted good building blocks to make PLs with a high free volume. In the next section, measurement of porosity and permeability of such PLs are discussed.

1.2. Porosity and permeability of porous liquids

1.2.1. Failure of conventional measurement techniques

In literature, it has been previously reported that nitrogen sorption experiments did not allow measuring the porosity of silica-based PLs, under normal conditions of outgassing (48 h at 80 °C or 100 °C), despite the good porosity of the intermediate modified porous core in the case of corona-canopy dual systems.^{44,60} Only one study reported a possibility to get a measure after very long equilibration times.⁴²

Once more in this study, it has been shown that it was not possible to measure any porosity in PL-sHSPs by this mean (**Figure 52**). In the case of PL-sHSPs-EthAs, the porosity of the intermediate sHSPs@SIT was already obstructed because of the small size of SIT molecules: DFT calculations reported that the hollow core was still accessible, but the quantity of adsorbed gas was greatly reduced, suggesting that higher pressures would be necessary to fill the remaining porosity.

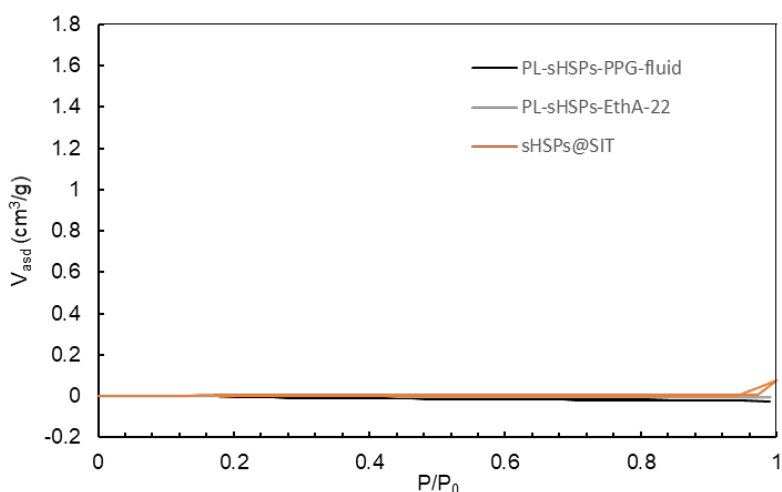


Figure 52. Nitrogen sorption experiment of sHSPs@SIT, PL-sHSPs-EthA-22 and PL-sHSPs-PPG giving few or no signal of porosity.

Concerning PL-sHSPs-PPG however, no such trouble arose since the polymer was far well hindered to penetrate the pores. This lack of signal was therefore attributed to the low temperature (77 K) preventing the mobility of organic chains, necessary for any species to diffuse through the organic canopy.⁴⁴

Facing this obstacle of porosity measurement, and in the aim of using them for LLE, another method has been developed to assess the permeability of PLs to liquids – that is their ability to be filled by liquids, with no additional pressure stress.

1.2.2. Permeability of a hydrophilic PL to polar liquids

For the first time, a direct demonstration of the permeability of a hydrophilic ionic PL-sHSP to polar liquids has been brought thanks to a Small-Angle Neutron Scattering (SANS) experiment performed in the course of the PhD thesis of Justine Ben Ghozi Bouvrande and published in the course of this thesis.^{60,119} This study was conducted onto the PL-sHSP firstly synthesized by Pr. Dai *et al.* with a cationic corona and a sulfonated PEG canopy. The only difference was its functionalization with thiols.¹⁷

Briefly, SANS experiments were performed by measuring a PL-sHSP sample after its immersion in solutions with various ratios of hydrogenated and deuterated compounds. A mixture of hydrogenated and deuterated ethanol (EtOH/EtOD) was used as a solvent, and the x_{EtOD} ratio was tuned until reaching a minimum of signal contrast. The scattering length density (sd) of the mixture at this minimum matches the sd of the PL, relating to its density. The contribution of an incoherent signal (due to hydrogens) could be subtracted afterward. A total matching indicates a full permeability of the PL to the solvent. The presence of a residual signal at the minimum of signal contrast can be either due to

unfilled pores, or to unmatching parts of the hybrid material. Fitting this residual signal would help to conclude. Details are provided in Appendixes C and G. Results obtained with the investigated PL are presented in **Figure 53**.

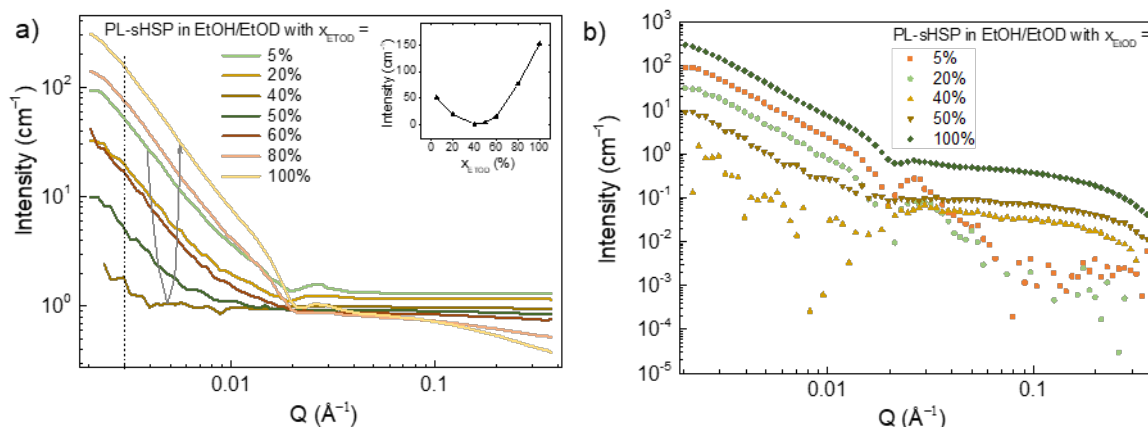


Figure 53. SANS spectra of a thiol-functionalized hydrophilic PL-sHSP immersed in EtOH/EtOD mixtures with various x_{EtOD} ratios **a)** before and **b)** after incoherent signal subtraction. The rotating arrow indicates the trend of evolution in intensity at 0.003 \AA^{-1} from $x_{EtOD} = 5\%$ to $x_{EtOD} = 100\%$. Top inset of Figure 53a displays the variation of intensity at 0.003 \AA^{-1} . For sake of clarity, some ratios were not plotted in Figure 53b. Reproduced from Reference ⁶⁰.

As plotted in the top inset of **Figure 53a**, the scattering intensity at small angles (arbitrarily measured at 0.003 \AA^{-1}) shows a strong variation with the x_{EtOD} ratio. The maximum contrast matching (*i.e.*, the signal with the minimum intensity) occurs for $x_{EtOD} = 43\%$, corresponding to a *sld* of the EtOH/EtOD mixture of $2.42 \cdot 10^{-6} \text{ \AA}^{-2}$. This value is consistent with a matching of the PL made up of silica and organics.

To verify if the PL is fully permeable to ethanol, the residual scattering signal after incoherent subtraction (noisy signal “ $x_{EtOD} = 40\%$ ” in **Figure 53b**) was analyzed at this ratio of maximum contrast matching. The residual signal that can be assigned to inhomogeneity of the PL between organic and inorganic moieties was compared to calculated curves corresponding to three scenarios (**Figure 54**):

- i) the solvent penetrates only the organic part of the PL,
- ii) the solvent also penetrates the silica shell but not the internal cavity,
- iii) the solvent penetrates the totality of the PL.

Calculated data were obtained by considering a spherical core-shell form factor and a sticky hard sphere structure factor. At higher angles, a residual signal of the organic chains in ethanol was

calculated thanks to an Ornstein Zernike model. The parameters used for calculation are listed in Appendix C.

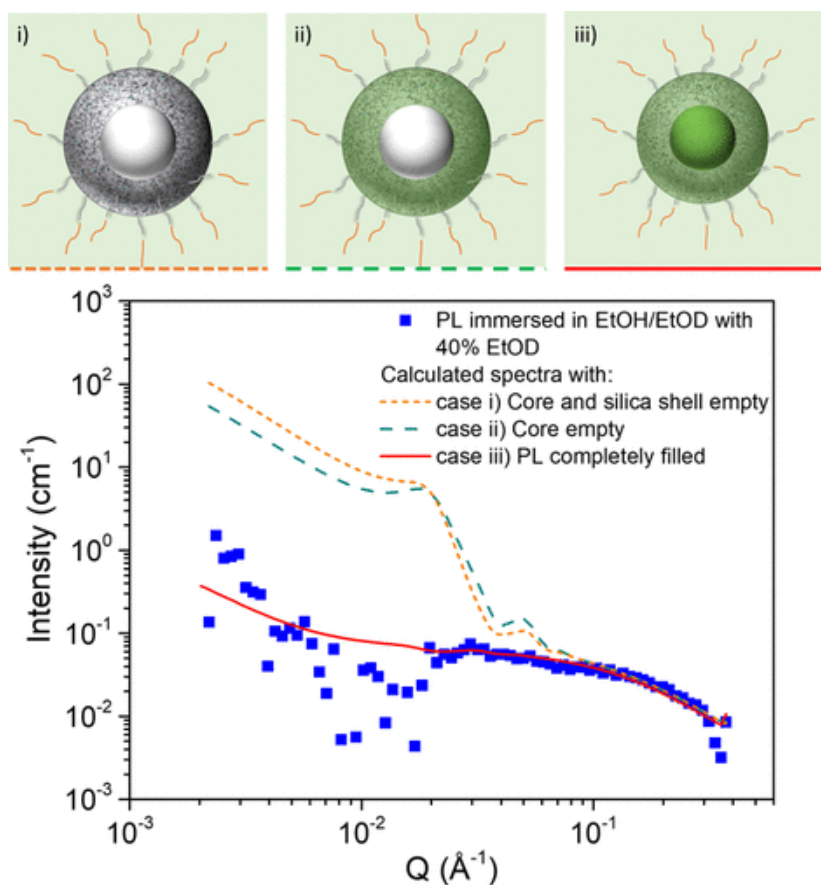


Figure 54. Small-Angle Neutron Scattering (SANS) measurement of PL permeability and calculated curves according to three scenarios: i) the solvent penetrates the organic moieties only, ii) the solvent also penetrates the silica shell, iii) the solvent penetrates the totality of the PL. Reproduced from Reference ⁶⁰.

Figure 54 clearly shows that scenario iii) was the only one capable of explaining the observed residual signal, showing that both micropores and internal cavities contained in the PL are fully accessible to ethanol.

It was not possible to apply the same approach to prove the permeability to water, because an additional peak in the signal due to a structural organization of the canopy around water domains prevented a complete fit of the residual data (See **Figure 55** and analysis details in Appendix G or in ref ⁶⁰). However, as shown in **Figure 55**, the variation contrast experiment performed with H₂O/D₂O mixtures reveals a consequent decrease of scattering intensity at $x_{D_2O}=50\%$, which strongly suggests that PLs are also permeable to aqueous solutions.

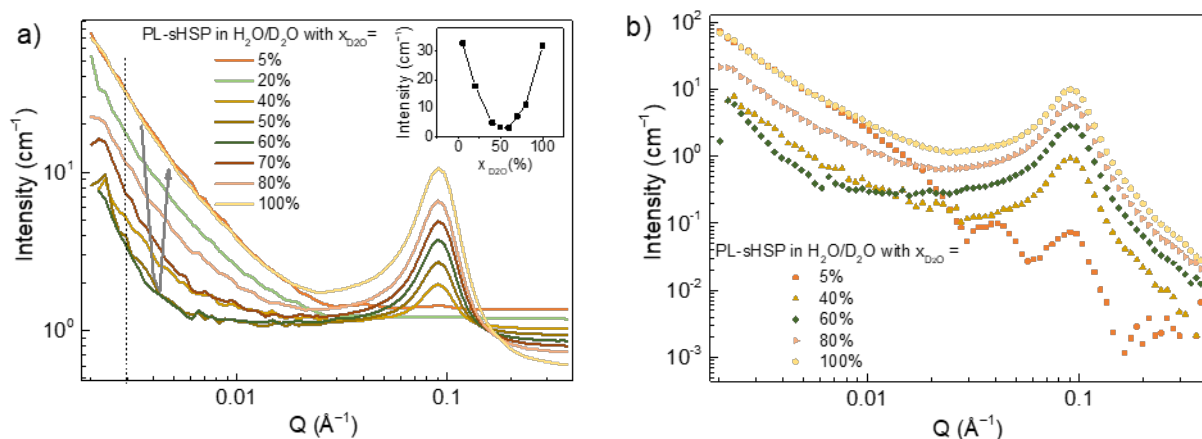


Figure 55. SANS spectra of PL-sHSP immersed in $\text{H}_2\text{O}/\text{D}_2\text{O}$ mixtures with various ratios $x_{\text{D}_2\text{O}}$ **a)** before and **b)** after incoherent signal subtraction. The rotating arrow indicates the trend of evolution in intensity at 0.003 \AA^{-1} from $x_{\text{D}_2\text{O}} = 5\%$ to $x_{\text{D}_2\text{O}} = 100\%$. Top inset of Figure 55a displays the variation of intensity at 0.003 \AA^{-1} . For sake of clarity, some ratios were not plotted in Figure 55b. Reproduced from Reference ⁶⁰.

This experiment allowed therefore showing that both micropores and internal cavities contained in the PL are fully accessible to polar liquids, which confirms that this material can be considered as a candidate for metal extraction by LLE.

A drawback of this method lays in the need of accessing a neutron source, thus restricting the possibilities of experimenting. Therefore, another method to probe PLs' porosity is under development, based on the gas sorption at high pressure and room temperature, followed by gravimetry. Among other advantages, this method could help the comparison with other types of MOFs-based PLs, and the impact of the core change (sHSPs vs bHSPs for example) on the PL porosity could be easily assessed.

2. Tuning solid-to-liquid physical state and viscosity

One of the aims of this thesis is to open discussion about the origin of the fluid behavior of PLs, in order to increase the knowledge about their physicochemical properties before harnessing their high tunability. In particular, "designing" the liquid state – instead of the solid state – seemed to rely on some parameters that had to be better defined. For this reason, two families of PLs have been investigated and compared in terms of physical state and viscosity. The first group (PL-EthAs) contained a dual SIT corona - EthA canopy system⁹⁹ grafted on SiNPs, sHSPs or bHSPs. The second group (PL-PPGs) consisted of a neutral hydrophobic PPG grafted on sHSPs (*cf.* Appendix A, Bookmark).

Table 10 gathers melting temperatures, physical states at room temperature and viscosities at 50 °C and 10 s⁻¹ of PLs-EthAs and PL-PPGs synthesized with various number of EG units in EthA (from 5 to 92) and two different PPGs (PPG₇₂₅ and PPG₂₀₀₀), onto three types of silica spheres: SiNPs, sHSPs and bHSPs. Viscosities are taken at 50 °C so as to be able to make comparison between materials which are solid at room temperature. **Figure 56a** shows pictures of PL-sHSPs-EthAs at room temperature and **Figure 56b** shows the two PL-sHSPs-PPGs.

Table 10. Physicochemical properties of PL-EthAs and PL-PPGs depending on the nature of the silica particles (SiNPs, sHSPs, bHSPs) and the length of the organic moiety (X being either the number of EG units in EthAs or the number of PG units in PPGs). Viscosities are measured at 50 °C and 10 s⁻¹. PL-sHSPs-PPG-2000 refers to the fluid phase presented at the end of Chapter II.

PL-EthA-X						PL-sHSPs-PPG-X	
X =	5	11	22	50	92	725	2,000
PL-SiNPs		liquid	liquid 14.2°C 10.8 ± 0.5 Pa.s*		solid 54.8°C		
PL-sHSPs	solid no melting	liquid 10°C 28.6 ± 2.0 Pa.s*	liquid 2.8°C 3.1 ± 0.5 Pa.s*	solid 40.6°C 17.9 ± 6.0 Pa.s*	solid 54.8°C	solid no melting	liquid 0.14 ± 0.05 Pa.s
PL-bHSPs	solid 50.5°C	liquid	liquid 15.3°C 36.1 ± 0.5 Pa.s*				

*viscosities are given at 50 °C and 10 s⁻¹

a) PL-sHSPs-EthAs-X



X = 5 11 22 50 92

b) PL-sHSPs-PPGs-X



725 2000

Figure 56. Pictures of **a)** PL-sHSPs-EthAs with various EthAs (in ascending order of EG chain length), and **b)** PL-sHSPs-PPG-725 and PL-sHSPs-PPG-2000.

By studying **Table 10**, it is obvious that melting temperatures of solids and viscosity of liquids depend on the length of the oligomeric or polymeric chains as well as the silica core nature.⁵⁹ Alternatively, ionic interactions and hydrogen bonding may play an important role in the fluidity of the PL. Thus, the comparison of PL-sHSPs-EthAs and PL-sHSPs-PPGs will help clarifying this point too.

Based on these results, the following sections will discuss the influence of four key parameters on the physical state and viscosity of the PLs:

- The influence of the ionic interaction is treated in Section 2.1,
- The influence of temperature is presented in Section 2.2,
- The nature of the silica particles, their size and density, are studied in Section 2.3,
- The influence of the organic:inorganic ratio is considered in Section 2.4.

Note that PL-sHSPs-EthAs were made with sHSPs-1 while PL-sHSPs-PPGs were made with sHSPs-2, for technical reasons.

2.1. Influence of ionic interactions on the liquid behavior

As heritage from the fields of nanoscale ionic materials (NIMs) and ILs, weak interactions like ionic and hydrogen bonding are often supposed to generate local and global mobility into complex systems.⁶⁵ Yet, different PLs with good fluidity were synthesized through covalent binding of neutral molecules or in suspension with neutral bulky solvents.^{42,53} These PLs were all containing small molecular cages as hosts.

To verify whether a liquid based on silica nanoshells could be obtained without ionic interactions, a neutral chemical modification has been tested at the surface of sHSPs: two PPG of two molecular weights (725 and 2,000 g/mol, labeled PPG₇₂₅ and PPG₂₀₀₀) have been silanized and grafted onto the surface of sHSPs under the same conditions (Appendix A, *cf.* bookmark No.5). After the post-treatments detailed in the previous chapter (separation between PL and unreacted powder), the two materials were yielded: PL-sHSPs-PPG-725 was a sticky solid that did not melt whereas PL-sHSPs-PPG-2000 was liquid at room temperature (**Figure 56b**), after its separation from the gel phase described in Chapter II (Section 3.2). The later was one to two orders of magnitude less viscous than PL-sHSPs-EthAs (0.14 Pa.s at 50 °C, **Table 10**).

According to the literature, PLs have already been synthesized by grafting 2 nm-large nanocages with PPG of various sizes.⁴² The conclusion was similar: liquids were obtained with 25 and 40 propylene glycol (PG) units; corresponding to molecular weights of 1,450 and 2,320 g/mol. Shorter or longer oligomers led to solids (glassy or powders). Of course, the size and density of the nanocages and the grafting density of PPG were not comparable, but it appeared that the polymer length window for

obtaining a liquid with their system was very similar as this observed in the present study. This point will be further discussed from the point of view of the organic:inorganic ratio (Section 2.4).

In conclusion, the presence of ionic interactions in a PL is likely to increase the viscosity, as observed for ILs when compared to deep eutectic solvents. Going one step further, it seems that stronger ionic interactions (in a certain point of view, approaching the covalent link) would induce a decrease in viscosity. According to a study of Bourlinos *et al.* conducted on NIMs,⁶⁵ a too weak interaction like the one between a quaternary amine and an isostearate failed providing fluidity to SiNPs. Other molecular dynamics simulations of ionic silica-based PLs showed that strong ionic interactions increased chains mobility compared to weaker ionic bonding.⁴⁹

2.2. Influence of temperature on physical state and viscosity

The PL-sHSPs-EthAs were synthesized by grafting all the available EthAs-X onto sHSPs-1@SIT. The picture in **Figure 56a** reveals their physical state: not all the materials are liquid at room temperature and this can be linked to the nature of the silica core (see Section 2.3) and to the organic:inorganic ratio (see Section 2.4). From **Table 10**, it can also be observed that some solids have a low melting point (like PL-sHSPs-EthA-50 at 40.6 °C) while others do not melt at all (like PL-sHSPs-EthA-5).

In order to understand the influence of temperature onto the physical behavior of a PL, differential scanning calorimetry (DSC) of all PL-sHSPs-EthAs were performed at a rate of 4 °C/min (**Figure 57**).

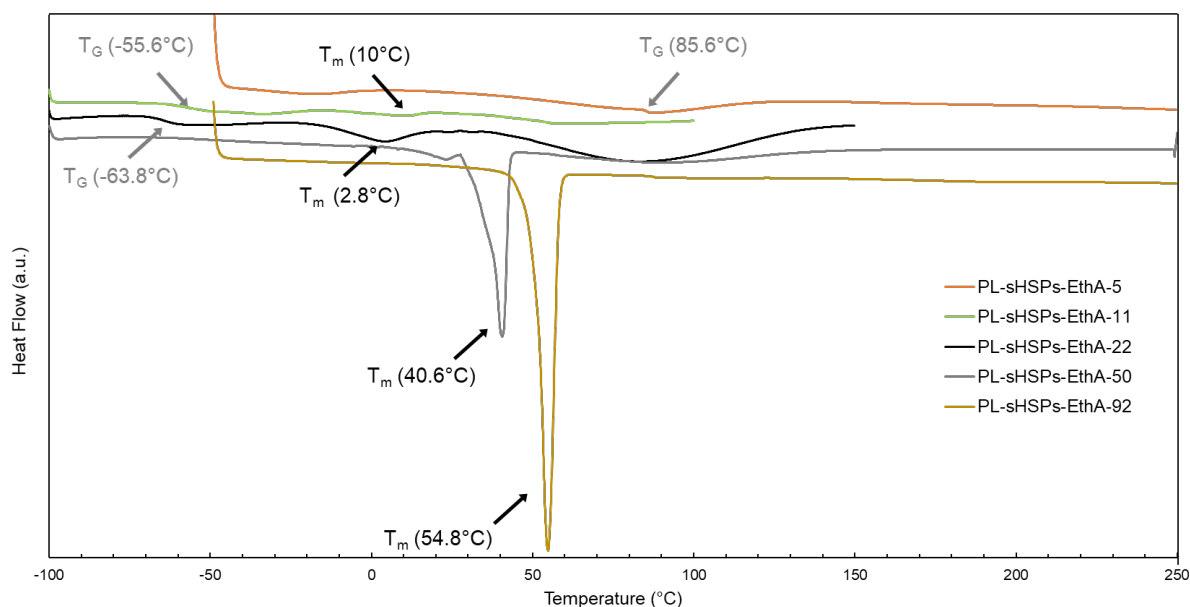


Figure 57. DSC profiles of PL-sHSPs-EthAs with tagged melting temperatures. No melting was observed for PL-sHSPs-5 but it underwent a glass transition at 85.6 °C. At the opposite, no glass transition was observed for PL-sHSPs-EthA-50.

A clear melting peak was observed for PL-sHSPs-EthA-50 and PL-sHSPs-EthA-92, at temperatures close to the melting temperatures of the corresponding pure amines EthA-50 and EthA-92. In the case of PL-sHSPs-EthA-11 and PL-sHSPs-EthA-22, only weak peaks were visible making interpretation difficult. No fusion was observed for PL-sHSPs-EthA-5 but a glass transition at a temperature T_G of 85.6 °C. Furthermore, for the two liquids PL-sHSPs-EthA-11 and PL-sHSPs-EthA-22, a slight variation in the signal could also be interpreted as a glass transition (at -55.6 °C for PL-sHSPs-EthA-11 and -63.8 °C for PL-sHSPs-EthA-22). This would be in agreement with the data reported by Zhang *et al.* and Kumar *et al.* for PL-sHSPs with hydrophilic ionic grafting: in both works, T_G of PLs were around -55 °C.^{17,44} In contrast, Sheng *et al.* reported T_G in the range [0°C; 35°C] when simulate the thermal behavior of silica-based PLs with four different amines as canopies.⁴⁹

Unfortunately, no analyses could be conducted on PL-sHSPs-PPG during this project, but Lai *et al.* published glass transitions of the liquids (made of nanocages and PPGs of different lengths) occurring between -40 °C and -70 °C (Figure S4 in the Supporting Information of the publication).⁴²

In addition to being a good indicator for a better comprehension of the fluidity of PLs, the viscosity is an important parameter for industrial applications: in LLE, a viscosity under 2 mPa.s is required to separate the phase without centrifugation (by natural decantation).¹²⁰ Therefore, the viscosities of liquid PL-EthAs were measured on a rheometer at different temperatures. **Figure 58a** and **Figure 58b** the results for PL-sHSPs-EthA-22.

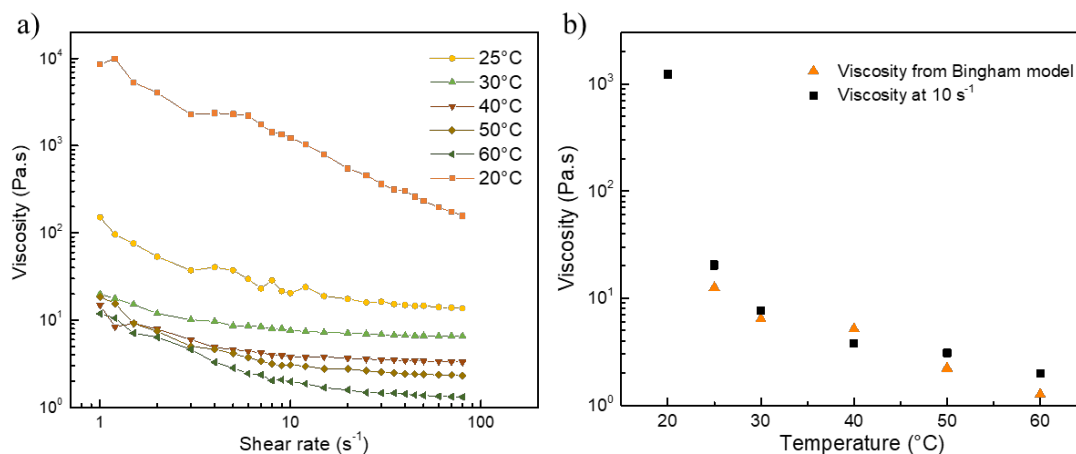


Figure 58. **a)** Viscosity of PL-sHSPs-EthA-22 plotted at different temperatures versus the shear rate (log-log scale); **b)** Viscosity of PL-sHSPs-EthA-22 at different temperatures (log-log scale), recorded at 10 s⁻¹ (black squares) or extracted from a Bingham fitting of the measurements (blue triangles). Error bars are added, but there are too small to be visible in the logarithm scale.

Note that condensation occurred at 15 °C, leading to a significant decrease in viscosity, therefore the corresponding value has not been reported on the figures. At 20 °C, the viscosity of PL-sHSPs-EthA-22 is very high (10^4 Pa.s), but it exponentially decreases when increasing the temperature: at 50 °C, the viscosity is around 3 Pa.s. This trend is consistent with the results obtained by Lin *et al.* for SiNPs-based NIMs (SIT corona and linear diblock amine canopy),¹²¹ and it is consistent with the behavior of many liquids (among which hydrocarbons) ruled by an empirical equation introduced by Whalter in 1928 and credited to Le Chatelier.¹²²

As expected, a non-Newtonian behavior was observed for the liquids (**Figure 58a**), and the curves could be modelled by a Bingham fitting (with an exception for the viscosity at 20 °C that did not follow the same behavior). This means that a threshold value exists between a zone of non-Newtonian behavior (at low shear rates) and a zone of Newtonian behavior (at higher shear rates). The values of viscosities obtained with this model (**Figure 58b**) were close to the one obtained at 10 s^{-1} for each PL (corresponding to a shear rate at the beginning of the zone of Newtonian behavior).

Even though viscosities are strongly decreasing when the temperature increases, they are still three or four orders of magnitude higher than viscosities of conventional solvents used for LLE processes. The phase separation step would then require relying on centrifugation instead of natural decantation. Counterintuitively, it has been shown in literature that the use of branched molecules (in the present case, tertiary amines) are not the best option to decrease the viscosity of PLs.^{16,49} Hence, the use of a linear amphiphilic or hydrophobic amine could lead to less viscous PLs.

The viscosity of PL-sHSPs-PPG-2000-fluid was measured at 25 °C and 50 °C on a microviscosimeter. It decreased from 0.41 Pa.s at 25 °C to 0.14 Pa.s at 50 °C.

As expected, higher temperatures significantly decrease the viscosity of PLs, which is very promising for LLE processes. Furthermore, the ability of the PL to be filled by water should drastically increase its density during the contact, thus facilitating the decantation process.¹²⁰

In the following sections, the viscosity will be used as an indicator to highlight the role of the silica particles and the organic:inorganic ratio on the physical properties of PLs. In order to compare with PLs that were solid at room temperature, viscosities at 50 °C will be retained. They are the ones indicated in **Table 10**.

2.3. Influence of size and density of silica particles on physical state and viscosity

In Section 1.1.1, porosity profiles of three types of silica particles (SiNPs, sHSPs, bHSPs) have been presented. **Table 11** shows how this porosity could be strictly related to the particles density. Indeed, SiNPs were the densest particles ($1 \pm 0.06\text{ g/cm}^3$) because they were non-porous. The gap with the

density of pure silica (2.2 g/cm^3) is due to interparticle free volume. sHSPs were half less dense ($0.5 \pm 0.1 \text{ g/cm}^3$) because of the presence of the hollow cavity and the micropores inside the silica shell, implying less matter in the same volume. Finally, bHSPs were even less dense ($0.1 \pm 0.06 \text{ g/cm}^3$) because of their larger cavity, and a great proportion of larger pores (3.7 nm) inside the shell. The latter were also strongly porous.

Table 11. Main characteristics of SiNPs, sHSPs and bHSPs: internal and external diameters are statistically deduced from TEM images, the packing density was measured by weighing a powder in a graduated container, and information on porosity were taken from nitrogen sorption experiments presented in Section 1.1.1.

	External diameter (TEM) [nm]	Internal diameter (TEM) [nm]	Packing density [g/cm^3]	S_{BET} [m^2/g]	Porous volume ^b [cm^3/g]	Pores size ^c [nm]
SiNPs	17.4 ± 2.8	-	1.02 ± 0.06	175	0.42	-
sHSPs-1	25.4 ± 1.4	14.8 ± 1.3	0.56 ± 0.1	691 ^a	0.66	1.4/1.7/3.9
bHSPs	236.0 ± 64.4	203.6 ± 58.8	0.12 ± 0.06	1121	0.78	1.5/ <u>3.7</u>

^a The presence of micropores overestimates the specific surface; ^b $P/P_0 = 0.87$; ^c Size of pores in silica shell; Underlined pores sizes correspond to the main proportion of pores.

According to **Table 10**, PL-SiNPs-EthA-22 was more viscous ($10.8 \pm 0.5 \text{ Pa.s}$) than PL-sHSPs-EthA-22 at $50 \text{ }^\circ\text{C}$ ($3.1 \pm 0.5 \text{ Pa.s}$). Given that SiNPs and sHSPs are in the same size range (17 and 25 nm, respectively), the difference can be essentially attributed to the spheres density. Yet the density was not the only cause for a high viscosity: PL-bHSPs-EthA-22 was the most viscous PL ($36.1 \pm 0.5 \text{ Pa.s}$), although bHSPs were the lightest spheres. Given that the silica content was similar in both cases (this point will be developed in the following section 2.4), their larger size (one order of magnitude higher) therefore contributes to decreasing the molecular mobility. Lin *et al.* reported no influence of the silica core on viscosity.¹²¹ However, the size variation of SiNPs they studied ranged between 7 nm and 22 nm, so it cannot be compared with the size variation considered herein. *Idem* in another study considering different sizes of HSPs:⁴⁵ a slight shift in viscosity was observed at $25 \text{ }^\circ\text{C}$ (0.66 Pa.s for the smallest cores (9 nm) and 0.25 Pa.s for the biggest cores (32 nm)), but viscosities at $50 \text{ }^\circ\text{C}$ were all equal.

As a conclusion, the obtained results illustrate a balance between particles sizes and densities in the contribution to the physical state and viscosity (when liquid) of the final material. While varying the density (with the same organic canopy) comes down to varying the organic:inorganic weight ratio (see the following section 2.4), the particles size acts separately. For designing a convenient PL in terms of viscosity and physical state, it will be necessary to take into account both parameters.

2.4. Influence of organic:inorganic ratio on viscosity

The impact of the organic:inorganic ratio on the physicochemical properties of PLs was evidenced by the comparison of different PL-sHSPs-EthAs: among the five materials synthesized, not all of them were liquid at room temperature (**Table 10, Figure 56a**). In the case of PL-sHSPs-EthA-5, the organic:inorganic ratio was not sufficient to liquefy the HSPs and the formed solid did not even melt (it underwent degradation before melting). EthA-11 and EthA-22 led to liquids at room temperature, with lower melting temperature and viscosity for PLs containing EthA-22 (which is again counterintuitive because EthA-22 is more viscous than EthA-11 when taken alone). Finally, two solids melting at low temperature (40.6 °C and 54.8 °C) were obtained with EthA-50 and EthA-92. These temperatures were close to the melting temperatures of corresponding pure amines, suggesting that at higher organic:inorganic ratio, the PL behaves more like the pure amine. This was not observed in the simulations of Sheng *et al.* from which they conclude that longer canopies contribute to PL mobility (provided a sufficient grafting yield).⁴⁹

As expected, the viscosity at 50 °C followed the same tendency as the melting temperature (**Table 10**). A minimum of viscosity was found for PL-sHSPs-EthA-22 (3.1 ± 0.5 Pa.s at 50 °C), whereas PL-sHSPs-EthA-11 was more viscous (28.6 ± 2 Pa.s) than PL-sHSPs-EthA-50 (17.9 ± 6 Pa.s). However, the viscosity of PL-sHSPs-EthA-92 was measured at 57 °C, just above its melting point (55 °C), and it happened to be lower than other PLs, with a value of 2.0 ± 0.5 Pa.s. This result suggests that at high molecular weights, PEGylated amines are playing a role of plasticizer and decrease the viscosity, even if the melting point remains relatively high.

All these results can be translated in terms of organic:inorganic weight ratio (φ), by looking at the chemical composition of PLs given by TGA (**Figure 59, Table 12**). Indeed, this number depends on four key parameters all impacting the physical state and viscosity of the materials: the core size, the core density, the grafting length, and the grafting density (depending itself on the core surface and the grafting size).

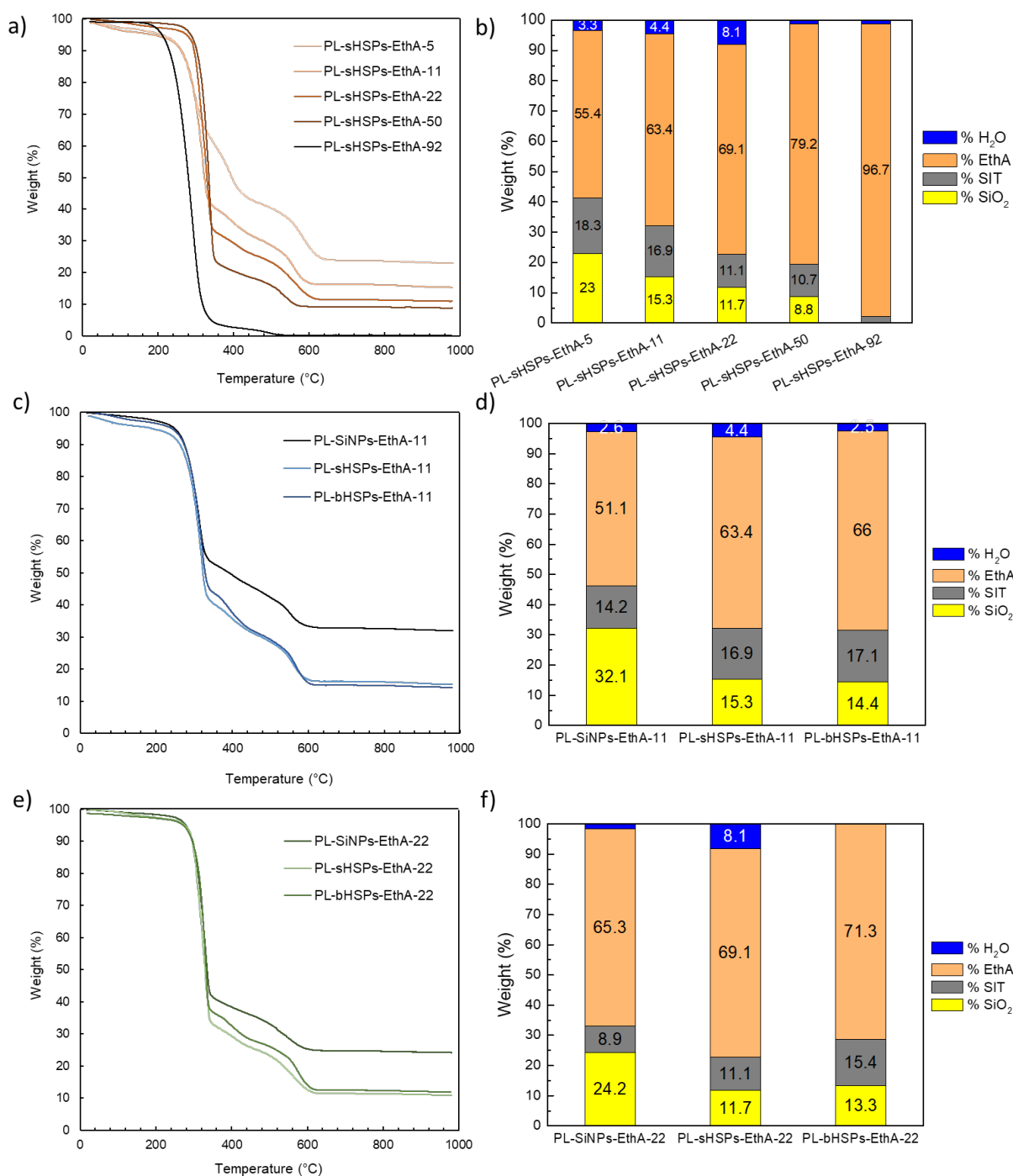


Figure 59. a) TGA of PL-sHSPs-EthAs, b) Chemical compositions of PL-sHSPs-EthAs given by TGA, c) TGA of PL-EthAs-11, d) Chemical compositions of PL-EthAs-11, e) TGA of PL-EthAs-22, f) Chemical compositions of PL-EthAs-22. PLs are made with sHSPs-1 set. Adapted from Reference ⁵⁹.

Reasonably, the silica content logically decreases with the increase in the EthA size. Thus, liquids at room temperature were obtained for (EthA+SiT):SiO₂ weight ratios φ of 5.2 (PL-sHSPs-EthA-11) and 6.9 (PL-sHSPs-EthA-22). These results are in line with the work of Lin *et al.* about NIMs, where it has

been shown that the viscosity increased linearly with the silica core fraction (increasing of 20% when the silica content increased from 15% to 30%).¹²¹

Table 12. Organic:inorganic weight ratios φ of PLs deduced from TGA. Note that PL-bHSPs-EthA-5 was made with 2.3 eq. of EthA-5 (see Chapter II), and the number indicated for PL-sHSPs-PPG-2000 corresponds to the fluid phase. The gel phase has a weight ratio of 3.8 instead.

Organic:inorganic (w/w) ratio φ		PL-EthA-X				PL-PPG-X	
X =	5 solid	11 liquid	22 liquid	50 solid	92 solid	725 solid	2,000 liquid
PL-SiNPs		2.0	3.1				
PL-sHSPs	3.2	5.2	6.9	10.2	>400	2.1	15.7
PL-bHSPs	(5.6)	5.8	6.5				

For a given length of EthA (for instance EthA-11 or EthA-22, **Figure 59c-f**), it is interesting to note that the organic:inorganic ratio was always lower (~2.5 times) for PL-SiNPs than PL-sHSPs or PL-bHSPs (**Table 12**). This can be correlated to *i*) the calculations of SIT grafting density at the surface of sHSPs detailed in Chapter II, Section 3.1.2.3: the SIT molecule was not only grafted on the external surface of HSPs, but it also diffused inside the shell before grafting at the surface of micro- or mesopores, thus increasing the SIT content; *ii*) the higher density of SiNPs inducing more inorganic weight for the same area of grafted particles. By this way, the proportion of organics in PLs was greatly increased with respect to non-porous references, explaining the higher viscosities recorded with PL-SiNPs (**Table 10**).

As described above, PL-sHSPs-PPG-725 was a solid at any temperature (below its degradation). From TGA, it can be deduced that its organic:inorganic weight ratio was 2.1 (32.6% of SiO₂, **Figure 60**), so the observation is in good coherence with what found for PL-sHSPs-EthAs.

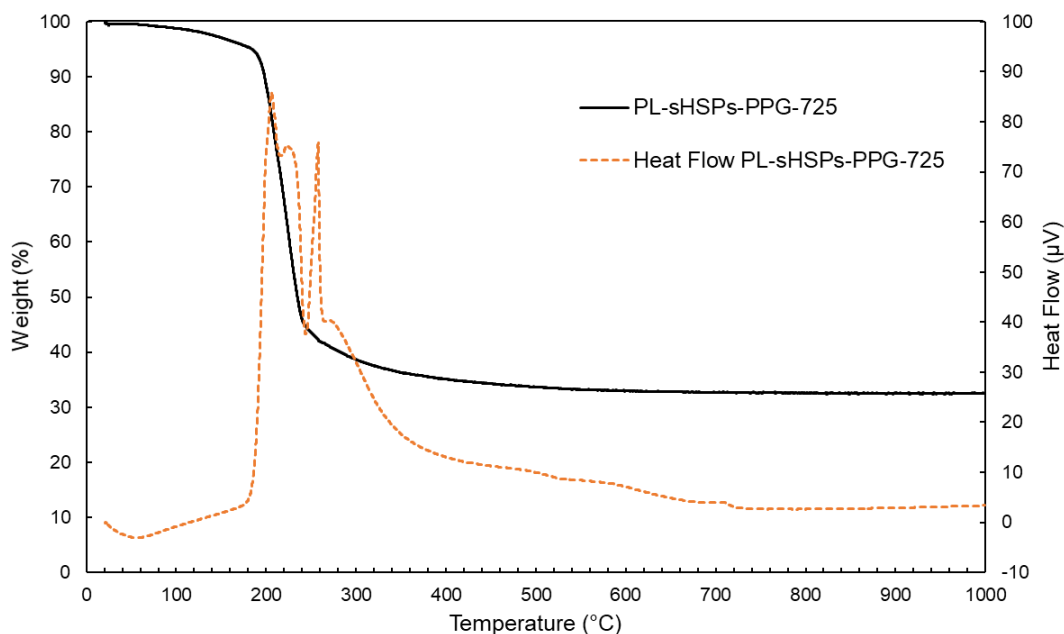


Figure 60. TGA and DTA of PL-sHSPs-PPG-725 under air at 5 °C/min.

From TGA spectra of fluid and gel phases of PL-sHSPs-PPG-2000 presented in Chapter II, Section 3.2.2.2, the organic:inorganic weight ratios were 15.7 and 3.8 respectively. Interestingly, these ratios are out of the scale obtained for PL-sHSPs-EthAs: PL-sHSPs-PPG-2000-fluid shows a higher organic:inorganic ratio than PL-sHSPs-EthA-50 (15.7 vs 10.2) when the latter was a powder at room temperature (melting at 41 °C), and the former was very fluid (0.14 Pa.s at 50 °C). In addition, PL-sHSPs-PPG-2000-gel displayed a slightly higher organic:inorganic ratio than PL-sHSPs-EthA-5 which was solid (3.8 vs 3.2), but this one was almost liquid. The fact that not all PPG molecules are covalently grafted probably contributes to a better fluidity of both phases. Furthermore, the absence of ionic interactions and the use of a linear polymer instead of a tertiary amine may have a great impact on the window of organic:inorganic ratios leading to liquids.

Figure 61 shows the viscosities of PLs at 50 °C plotted over their organic:inorganic weight ratio φ . However, no general trend could be deduced from this graphics, because the two grafting types are not comparable, as underlined above. In the literature concerning liquid composites (inorganic particles acting as “fillers” in a liquid polymeric matrix), the mathematical models used to predict the viscosity of a composite all rely on the volume fraction of particles.¹⁵⁶

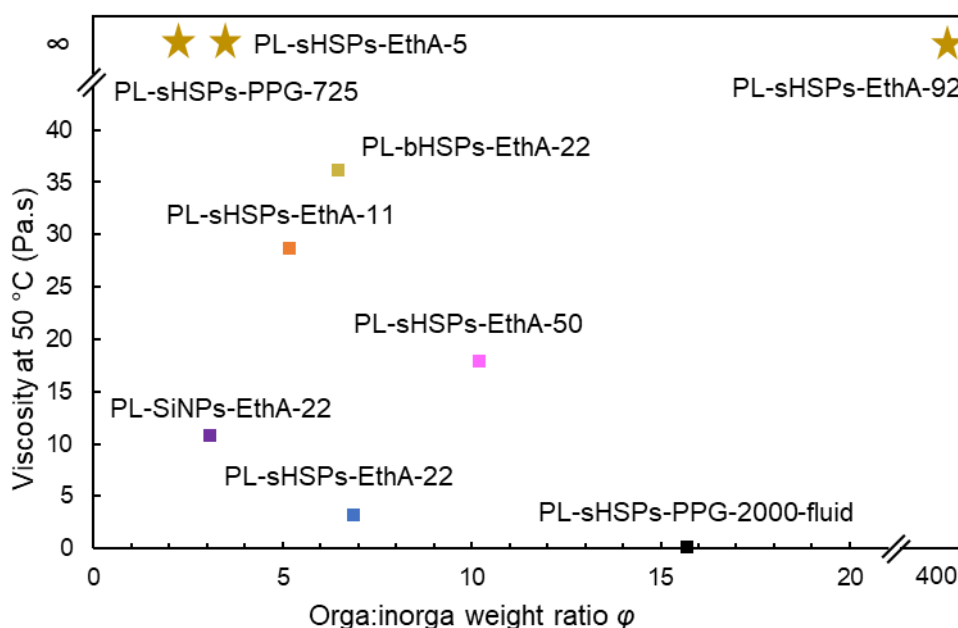


Figure 61. Viscosity of PLs at 50 °C and 10 s^{-1} over their organic:inorganic weight ratio ϕ as deduced from TGA.

In the present case, by a simple line of reasoning, the volume of canopy (roughly linked to the number of atoms) useful to get a liquid was reckoned: a SIT molecule contains 5 atoms on the main chain (3 C, 1 S, 1 O). EthAs contain 17-19 atoms on the hydrophobic chain (16-18 C + 1 N). Apart from EthA-5, the lateral chains are longer than the carbon chain: 20 atoms for EthA-11, 36.5 for EthA-22, and 78.5 for EthA-50 but they are likely to fold. Therefore, the organic moiety of the PL needs to have a volume roughly ranging from 25 to 45 atoms in order to provide the liquid behavior (by adding the SIT contribution). Regarding PL-sHSPs-PPGs, a chain of PPG₇₂₅ contains 42 atoms in average (excluding the branched methyl), and this was too short to get a liquid after grafting on sHSPs. PPG₂₀₀₀ contains 108 atoms in average but its folding is expected to be important, reducing the length by almost two. However, the volume ratio window for getting a liquid was not the same than for the ionic PLs.

As a result, an organic:inorganic volume ratio could be estimated based on the length and width of the organic chains described above along with the size of the particle as deduced by TEM. The values are gathered in **Table 13**. It is worthy of note that more precise volumes of canopies may be deduced from simulations of the molecular organization around the particle, or by other average methods like SAXS.

Table 13. Organic:inorganic volume ratios (ψ) of PLs.

Organic:inorganic (v/v) ratio ψ	PL-EthA-X					PL-PPG-X	
	X = 5 solid	11 liquid	22 liquid	50 solid	92 solid	725 solid	2,000 liquid
PL-SiNPs			2.22				
PL-sHSPs	0.65	0.71	1.34	3.55	8.99	0.84	1.39
PL-bHSPs			0.11				

In **Figure 62** are plotted the viscosities of PLs at 50 °C depending on the organic:inorganic volume ratio ψ . In this plot, a minimum of viscosity is obtain for volume ratios about 1.2. However this graphics cannot explain why solids (PL-sHSPs-EthA-5 and PL-sHSPs-PPG-725) are obtained at the same volume ratio as a liquid (PL-sHSPs-EthA-11). This is because the volume fraction only depends on the core size and the grafting length, but not on the core density nor the grafting density.

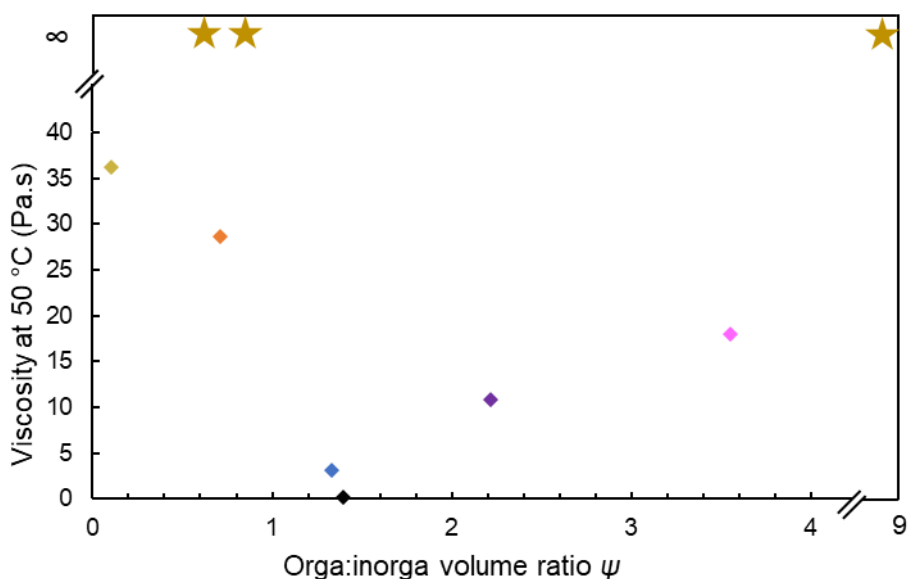


Figure 62. Viscosity of PLs at 50 °C and 10 s^{-1} over their organic:inorganic volume ratio ψ as deduced from TEM (core size) and estimation of the canopy volume by considering molecular folding of long chains. Refer to **Figure 61** for labels of each point (with corresponding colors).

Therefore, it has been empirically tested to plot the viscosity over the product ξ of the organic:inorganic weight and volume ratios ($\xi = \varphi \times \psi$, **Figure 63**). In this case, PLs with acceptable viscosity are found in a middle zone ($\xi \in [9 - 30]$), while solids are obtained for very low and very high numbers. However, one has to remember that PL-sHSPs-EthA-92 was a fluid liquid after its melting point (55 °C). Therefore, this empirical law may find limitations for very far ξ numbers.

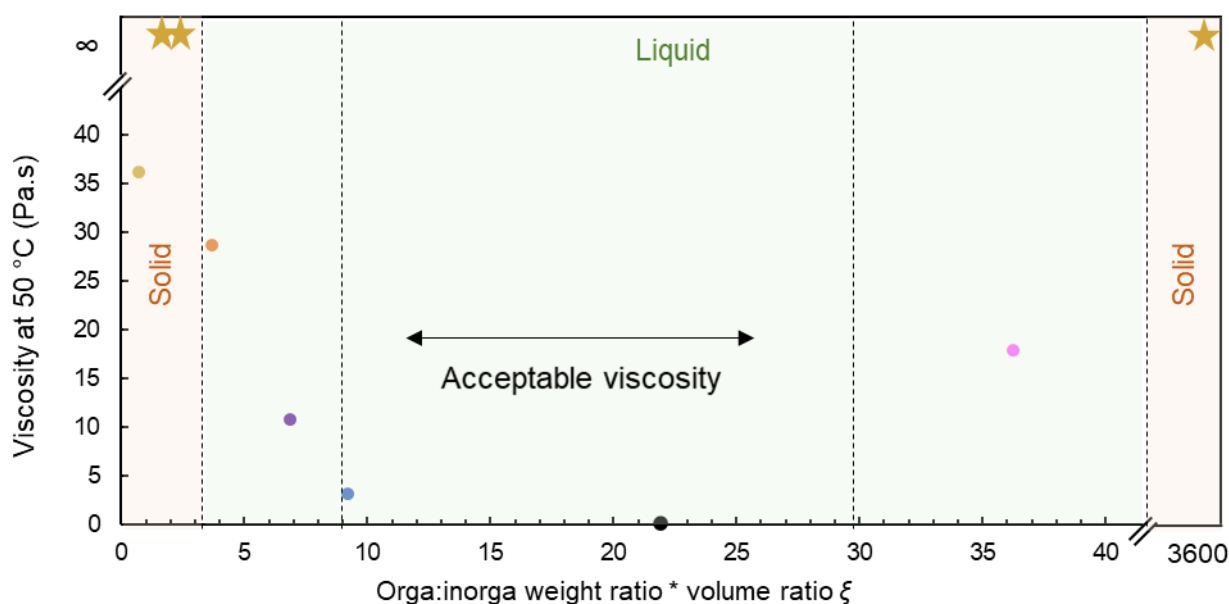


Figure 63. Viscosity of PLs at 50 °C and 10 s⁻¹ over the product of organic:inorganic weight and volume ratios $\xi = \varphi \times \psi$. Refer to **Figure 61** for labels of each point (with corresponding colors).

All these studies indicated that the physical state of a hybrid porous material could be predicted by considering:

- The size and density of the inorganic cores (a larger size induced less mobility),
- The inorganic:organic ratio (with a suitable window related to the fluidity of the pure molecule serving as a canopy, as well as to the size and density of the cores). It can be highlighted that a ξ number between 9 and 30 seems to be a general rule to design a fluid PL,
- The temperature, which drastically decreases the viscosity of liquids.

Moreover, it was obvious that the presence of ionic interactions and the use of branched amines increased the viscosity and reduced the window of organic:inorganic weight ratios suitable to obtain liquids. However, all these parameters – and especially the nature of the canopy – also had an effect on the affinity of the PL toward water.

3. Tuning hydrophobicity

The aim of this work consisted in developing hydrophobic PLs to use them as single extracting agent in LLE of metals. Nevertheless, the PL chosen as extractant should not be completely immiscible to water, so the metal diffusion can take place. Unfortunately, hydrophobicity was not easy to assess by quantitative methods. Indeed, the logP method consisting in calculating the theoretical sharing coefficient of water between the PL and octanol, was not relevant in the case of such complex materials. Furthermore, the PLs were often too viscous to form microdrops in a water bulk that could

have given quantitative information about their surface tension. For these reasons, only a qualitative assessment has been conducted.

Considering the amphiphilicity of EthAs, hydrophobicity of the corresponding ionic PLs was expected to be tuned by varying the length of the two PEG arms (*cf.* bookmark No.4), and observations about this evolution will be reported in the first section. Then, the results will be used to compare with the affinity of the PL made of PPG₂₀₀₀ and sHSPs toward water (*cf.* bookmark No.5). A peculiar attention will be paid to the effect of ionic interactions.

3.1. Amphiphilic canopy-based ionic porous liquids: PL-EthAs

Because EthAs are amphiphilic, it was expected that some of the PL-EthAs would be hydrophobic whereas others would be hydrophilic, depending on the length of the two EG arms.

The two PL-sHSPs-EthAs that are liquid at room temperature – PL-sHSPs-EthA-11 and PL-sHSPs-EthA-22 – have been contacted with water. The behavior of the two phases after contact are presented in **Figure 64**.

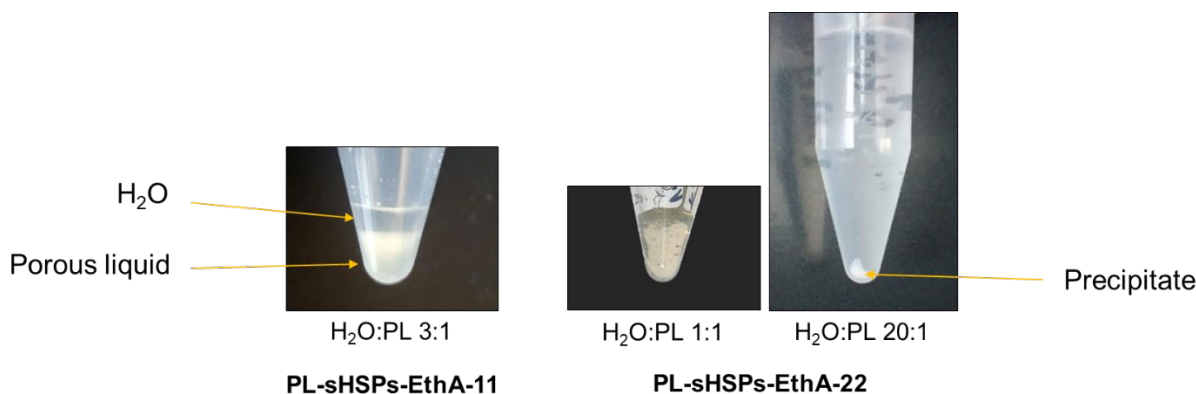


Figure 64. PL-sHSPs-EthA-11 and PL-sHSPs-EthA-22 in contact with water.

In the case of PL-sHSPs-EthA-11, a phase separation was observed, while with PL-sHSPs-EthA-22, the PL was soluble. After adding more water and centrifuging, this hydrophilic PL-sHSPs-EthA-22 was even destabilized: the amine was solubilized into water, while the sulfonated silica precipitated. These observations were supported by TOC analyses of the water phase: around 10% of EthA-11 was solubilized in water, and 100% of EthA-22 (see calculation in Appendix B). This suggests the presence of an EG arm-length threshold for the amine to provide sufficiently hydrophobic behavior to the PL.

The stability of PL-sHSPs-EthA-11 in contact with water was also confirmed by TGA and SAXS data (**Figure 65**).

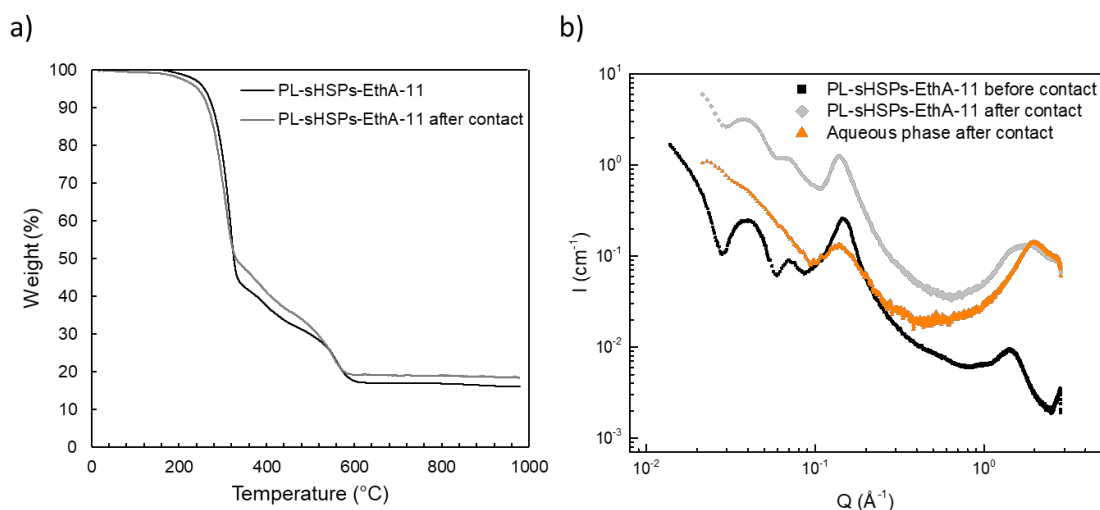


Figure 65. a) TGA of PL-sHSPs-EthA-11 before (black) and after (grey) contact with water. The signal before contact was corrected from water loss; **b)** SAXS of PL-sHSPs-EthA-11 before and after contact with water, along with the aqueous phase after contact.

In **Figure 65a**, a slightly higher silica content in the PL after contact (18.4% instead of 16.1% after applying a correction from water loss) corroborates the slight loss of amine solubilized in water. The weight losses of EthA and SIT were at the same temperatures, indicating no structural change caused by the contact of water. In **Figure 65b**, the SAXS signature of sHSPs was the same before and after contact, with similar slope and oscillations. The apparition of a characteristic peak at 1.5 \AA^{-1} in the signal of PL after contact reflected the presence of some water into the organic phase. However, a quantification of this water by Karl-Fisher titration was not possible owing to the high viscosity of PL-sHSPs-EthA-11 making it impossible to correctly charge into the device. In the signal of TGA, no weight loss linked to free water occurred before 200 °C. However, it was noticed that 51% of the initial weight poured inside the crucible disappeared before the analysis started (few hours passed between the crucible preparation and the analysis). This was probably due to spontaneous water drying. On the other hand, the aqueous phase after contact showed no oscillations in SAXS (**Figure 65b**), but only a structural peak at *c.a.* 0.2 \AA^{-1} attributed to the residual amine in a diluted phase.

As a result, the hydrophobicity of PL-EthAs could be adjusted by simply changing the length of PEG arms of commercially available EthAs (basically found in cosmetics industry). In this study, the PL-sHSPs-EthA-11 allowed a spontaneous separation from the water, so it can be considered for the LLE application.

3.2. A neutral single-component canopy-based porous liquid: PL-sHSPs-PPG-2000

Grafting PPG polymer onto the surface of sHSPs (*cf.* bookmark No.5) was also achieved with the aim of increasing the hydrophobicity of the PL. In this regard, the stability of the fluid phase of PL-sHSPs-

PPG-2000 against water was investigated in the same way as for PL-EthAs. Results are presented in **Figure 66**.

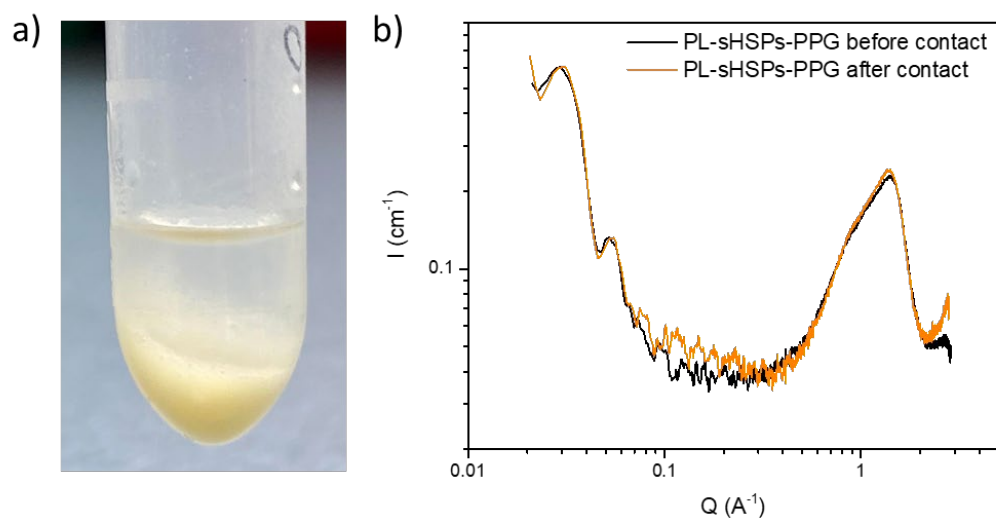


Figure 66. a) Phase separation of PL-sHSPs-PPG-2000-fluid and water (PL: H₂O 1:5 w/w), b) SAXS of PL-sHSPs-PPG-2000-fluid before and after contact.

In **Figure 66a**, the phase separation was clearly visible, confirming that the polymer conferred a high hydrophobicity to the PL. The meniscus was not perfectly horizontal because the PL also stuck to the plastic walls of the tube. The opacity of the PL could suggest the presence of microdrops of water inside the PL. Unfortunately, Karl Fisher titration of water could not be carried out because of the high viscosity of the PL preventing its proper loading into the device. However, in **Figure 66b**, the SAXS signal before and after contact revealed that there was no structural difference in the sample before and after contact (in the size scale 1-100 nm). In particular, no water characteristic peak was visible at wide angles (expected at 2 \AA^{-1}), and this could be due to spontaneous drying after phase separation and capillary preparation. Besides, the TOC analysis of the aqueous phase indicated that 6% of the PL had been dissolved: this is twice less than PL-sHSPs-EthA-11.

In order to verify whether the silanization and grafting was necessary for making a stable PL, a control made of a simple suspension of sHSPs-2 in PPG₂₀₀₀ (labeled mPPG-sHSPs) was also put in contact with water (**Figure 67**).

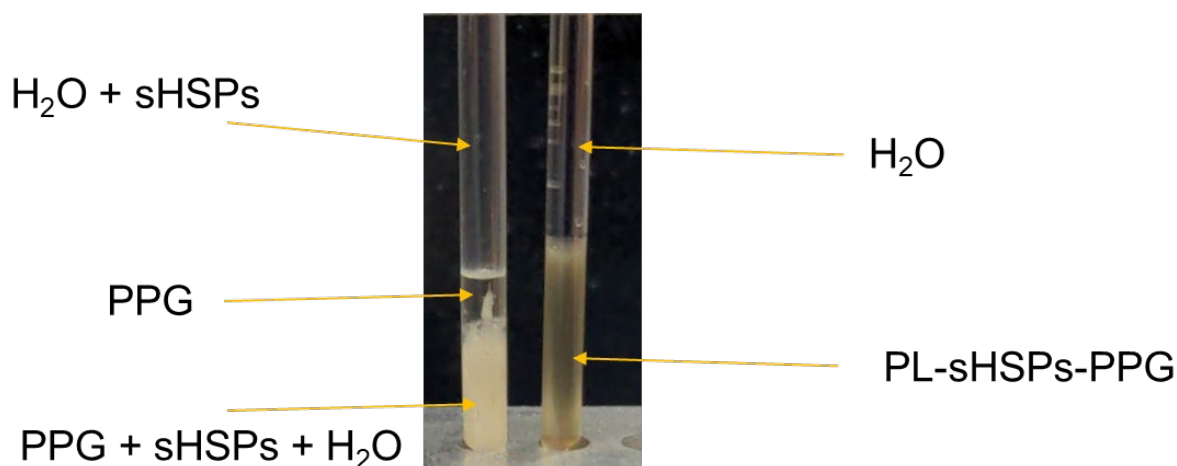


Figure 67. mPPG-sHSPs (left) and PL-sHSPs-PPG-2000-fluid (right) in contact with water. The phase separation was spontaneous in both cases.

A simple observation of the two capillaries (control and PL) in **Figure 67** revealed that three distinct phases were formed during the contact of the control (mPPG-sHSPs) with water, while only two were visible when the PL was contacted with water. As for the PL, the control underwent a clear phase separation with water. Yet, a second phase separation probably due to instability of the suspension also occurred.

The five phases were analyzed through SAXS measurements for accurate interpretation (**Figure 68**).

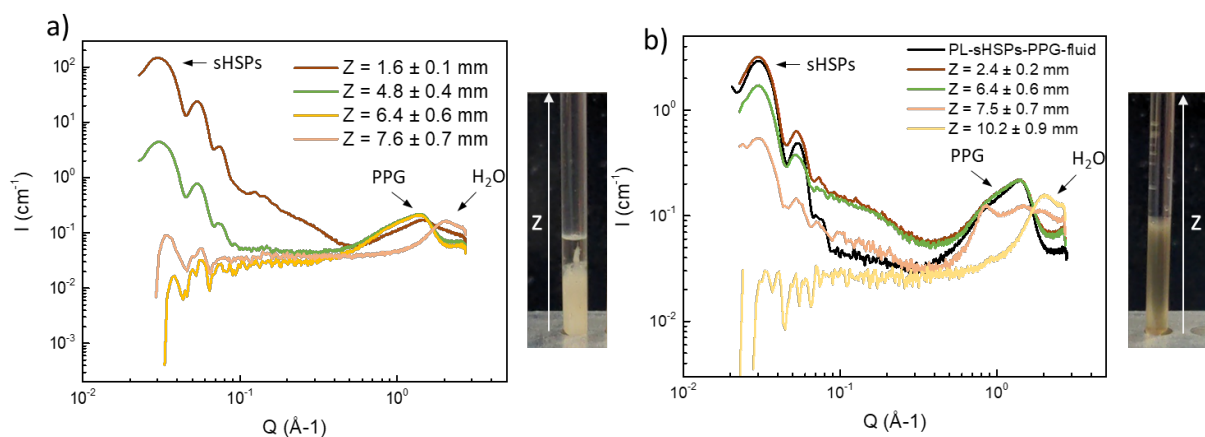


Figure 68. Phase separation of **a)** mPPG-sHSPs after contact with water, **b)** PL-sHSPs-PPG after contact with water, studied by SAXS at various altitudes Z of the capillary.

On the one hand, SAXS spectra of the mPPG-sHSPs control (**Figure 68a**) showed that most sHSPs precipitated while a little part were dissolved in water. The precipitate also contained PPG and water, as shown by the analysis of the wide angles zone (above 0.5 \AA^{-1}) in the signal at low Z altitude ($1.6 \pm 0.1 \text{ mm}$). When going up along the capillary, water disappeared from the signal, and the quantity of

sHSPs was reduced (less intensity in the oscillations part) while the presence of PPG was more pronounced. Then, a phase with PPG alone was clearly visible at $Z = 6.4 \pm 0.6$ mm. Finally, the water phase ($Z = 7.6 \pm 0.7$ mm) also contained few sHSPs as suggested by the very weak oscillations at small angles, but no PPG (only the water peak was visible at 1.1 \AA^{-1}).

On the other hand, PL-sHSPs-PPG-2000-fluid was far more stable, because only two phases formed in contact with water (**Figure 68b**): the bottom phase mainly contained PL-sHSPs-PPG-2000-fluid, with a slight decrease in silica content when approaching the interface. The interface ($Z = 7.5 \pm 0.7$ mm) contained a mixture of PL and water. Finally, the water phase displayed a signal with no trace of oscillations (no sHSPs were dispersed in water). This result proves that sHSPs were stable in the PL phase.

As a conclusion, even though quantitative assessment of PLs hydrophobicity was not possible, simple contact experiments with water allowed demonstrating the correct phase separation between hydrophobic PLs and water, that is desirable for LLE. In the case of ionic PL-EthAs, too long PEG arms in the amine induce a too high affinity with water, thus deconstructing the PL. In this particular case where amphiphilicity is present, a balance between hydrophobicity and PL fluidity (a too short amine led to a solid) must be considered. In addition, it was found that PL-PPGs were more stable when in contact with water (modest losses in the water phase), assigned to the neutrality and the higher hydrophobicity of the polymer.

Conclusion

In this chapter, the tunability of silica-based Class A PLs was highlighted. On the first place, the nature of their porosity could be varied thanks to the use of two different types of hollow silica particles: sHSPs were relatively small (around 25 nm in diameter) and their shells contained micropores (1.4 nm in average). bHSPs were larger (around 240 nm in diameter) and they contained mesopores (3.7 nm in average) as well as micropores in their shells. If the small size of sHSPs led to less viscous PLs, the small pores could be a disadvantage for metallic complexes diffusion in LLE.

Unfortunately, the techniques used to assess porosity of solids can hardly be transferred to PLs. Indeed, the low temperature at which nitrogen sorption adsorption is generally performed induce a liquid-to-glass transition in the PL, thus blocking the access to the porosity of the inorganic pore. In the context of an application in LLE, the permeability toward liquids was an important feature to assess. Therefore, an original SANS experiment has been developed and allowed to show that a hydrophilic ionic silica-based PL was fully permeable to polar liquids. It would be very interesting to perform the same measurement on the new hydrophobic PLs presented in this thesis. However, given that SANS are not easily accessible, another method to assess the permeability of PLs to gas could be considered:

it consists in loading the PL in a micro-balance, placed in a chamber able to hold high gas pressures. In consequence, the measurement could be performed at room temperature and the high pressure could allow overcome the problem of slow gas diffusion in the organic matrix. This technique has already been applied in other types of PLs made of a mixture of MOFs and ILs.

Furthermore, it was found in this study that the physical state and viscosity of PLs strongly depend on the organic:inorganic weight ratio, as well as the size and density of the inorganic core. This result is consistent with the literature. Temperature could also have a great impact in decreasing the viscosity of PLs that were liquid at room temperature, and this is very promising for any application in LLE. However, the presence of ionic interactions was not necessary to liquefy HSPs, because it was possible to obtain liquids by grafting a neutral polymer, and the viscosity was even lower. This polymer also conferred a stronger hydrophobicity to the PL as compared to the amphiphilic tertiary amines employed to make the canopies of the first range of ionic PLs (PL-EthAs). It is expected that this hydrophobic character would affect the permeability of the PL to water. Thinking about hydrometallurgical applications, it would also be interesting to study the miscibility of these PLs in other solvents (polar, protic, aprotic, non polar, ILs...).

In the following chapter, the two kinds of hydrophobic PLs (ionic and neutral) will be evaluated as candidates for LLE. The work focused on the extraction of three rare earth elements widely spread in modern technologies and classified as critical metals: neodymium, praseodymium and dysprosium. The functionalization of PLs will be introduced before presenting preliminary extraction tests

Chapter IV

Porous liquids for liquid-liquid extraction of rare earth elements

After all the efforts deployed to synthesize, characterize, and explore the tunability of the new silica-based PLs, the research can be orientated toward the targeted application of metal extraction. This chapter is focused on the extraction of rare earth elements (REEs) which are of particular interest in the current geopolitical context, as it is described in the first section. The general methods to obtain functional PLs are further developed in the second section, before presenting the synthesis of the first functional PL. In the third section, preliminary tests of extraction are reported. Next, some optimizations of the extraction performances of simple systems are detailed in section 4. Finally, the assessment of PLs' stability completed the evaluation of these new candidates for LLE in section 5.

1. Context

1.1. Rare Earth Elements (REEs) in Europe

This thesis aims to demonstrate the potentiality of PLs to be applied in LLE of metals, and particularly “critical metals” such as REEs. REEs are a family of metals containing the 15 lanthanides plus yttrium and scandium. They share the electronic f-orbitals conferring them unique properties such as high conductivity, interesting luminescence, exceptional thermal stability etc. They are found in many fields, like micro-electronics, photochemistry, energy as well as in defense and medical solutions.^{96,123,124}

Most times, they are used as residual ingredients of a metallic “cocktail”, designed for associating specific properties of each metal to be performant in the target application.

Despite that they are often used in low quantities, REEs have been classified as “critical metals” by the European Union, because they have become necessary to achieve the numerical transition as well as to develop technologies for harnessing renewable energies.¹ Even though their abundance is relatively high in the Earth’s crust, it exists few places where they are found in high yields, sufficient for industrial exploitation.¹²³ Therefore, there are almost no mines on the European territory and only three countries – China (40%), Malaysia (31%) and Russia (25%) – owned the quasi-monopole of their exportation in 2022 (**Figure 69**).

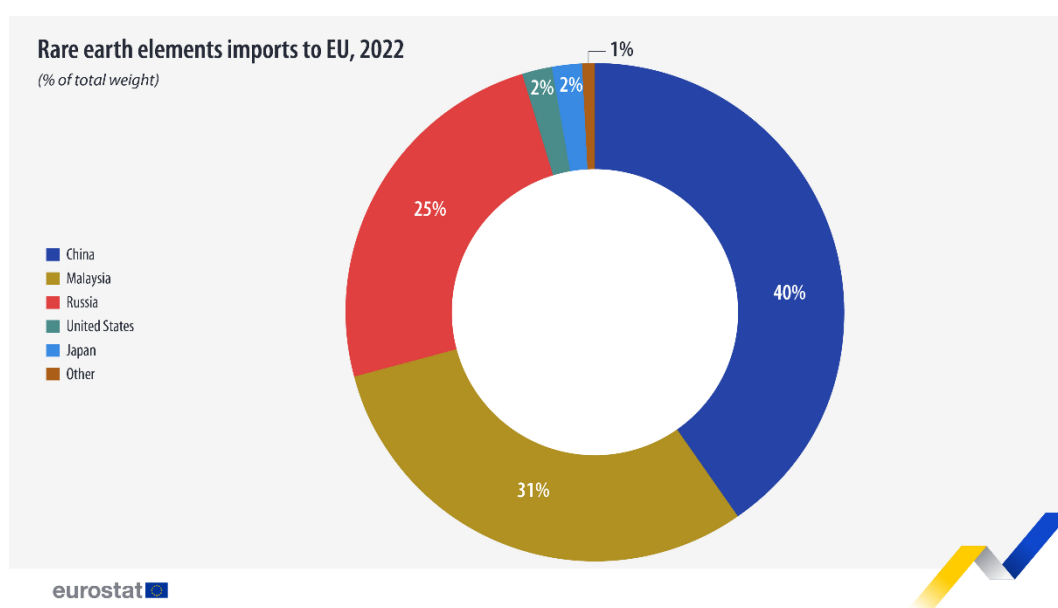


Figure 69. Share of REEs imports countries in European Union in 2022. Source: Eurostat.

REEs share very similar chemical properties. Very often, they are split into two categories: light REEs refer to the lightest lanthanides: lanthanum to gadolinium, while heavy REEs include the rest (terbium to lutetium, plus yttrium). Scandium is an exception because it possesses a much smaller ionic radius, and it does not belong to any of the two groups (**Figure 70**).¹²³

¹ For more information about predictions of metals consumption for new technologies by 2050, the reader is referred to the work of Olivier Vidal.^{125,126}

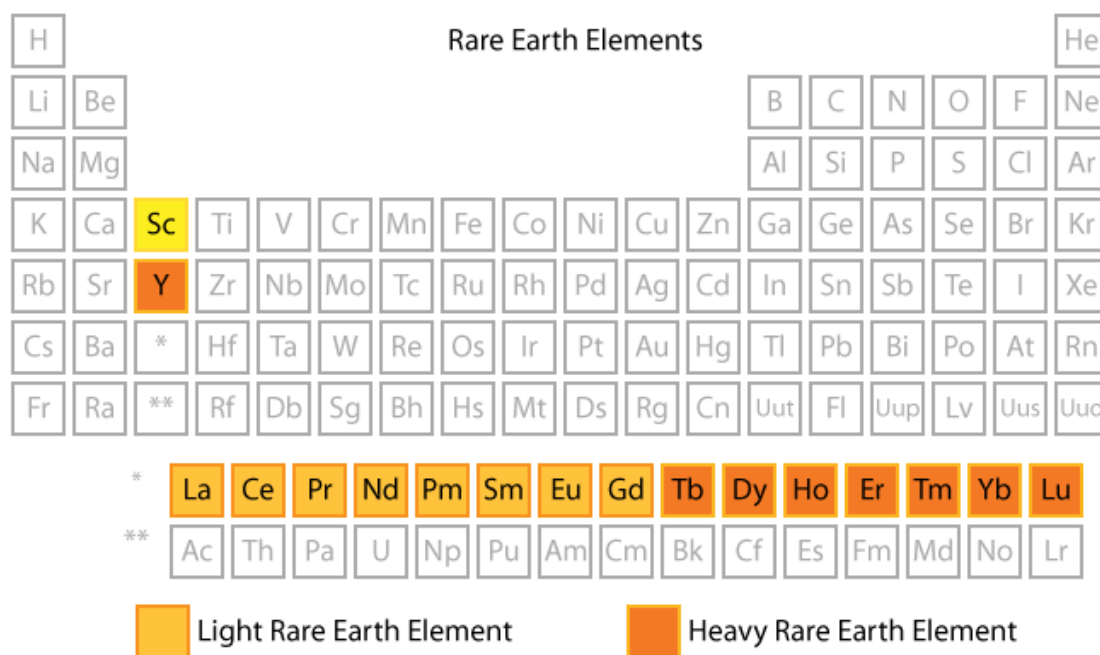


Figure 70. Periodic table of elements defining light REEs and heavy REEs. Source: Science Notes.

Recycling REEs from electric and electronic devices already present in Europe has raised as the best solution to decrease the geopolitical dependence to these countries, by ensuring an alternative supply. For instance, permanent magnets used in hard disk drives, electric vehicles and off-shore wind turbines consist in an important urban mine of neodymium (Nd), praseodymium (Pr) and dysprosium (Dy), together with iron (Fe) and boron (B).

1.2. Conventional techniques of REEs extraction

In 2012, the United States Environmental Protection Agency identified four steps in REEs processing from secondary sources: collection, dismantling, separation, and processing.¹²³ The dismantling step consists in removing the host matrix without changing the chemical composition of the ore. Extraction techniques are involved in the separation process to obtain concentrates in REE oxides. Processing these concentrates allows producing them under interesting chemical forms with high purity grade.

In industry, REEs extraction is commonly achieved by the combination of pyro- and hydrometallurgical operations. The latter generally include a leaching of metallic species in acidic or alkaline medium, which can be selective or not, followed by a separation by selective precipitation, solid-liquid extraction (SLE), LLE or ion-exchange processes.

1.2.1. Selective precipitation

Crystallization and selective precipitation were the first methods to be applied to REEs separation, even before ion-exchange columns.¹²⁴ Although they allowed the isolation of all REEs in the early 1900s, they could not reach high selectivity between the different elements, and a high number of

successive steps was necessary, leading to poor yields. Selective precipitation can be driven by affinity differences toward a ligand, or by redox switches.

1.2.2. Solid-liquid extraction of REEs

SLE is a very efficient method for metal extraction, because it uses small volumes of sorbents for the extraction process, with generally correct regeneration abilities thanks to good chemical stability.⁶ As a result, SLE processes often generate few wastes. In addition, the use of resins or membranes facilitate continuous processes implementation.

In some cases, the immobilization of good extractants onto porous supports like silica or polymeric resins through covalent bonding allows high efficiency along with improved selectivity.¹²⁷ Very often, the extractants used in SLE are the same than the ones used in LLE (*cf.* following section). Regarding REEs extraction, the family of diglycolamides (DGA) has been identified as particularly good chelating agents, showing interesting selectivity when they are immobilized on a support.^{127–129} For instance, **Figure 71** represents an example with three different DGA [diglycol-2,4-diamido-propyltriethoxysilane (DGA-N), 3,6-dioxaoctanediamido-propyltriethoxysilane (DOODA-N), and furan-2,4-diamido-propyltriethoxysilane (FDGA-N)] grafted inside the pores of a KIT-6 mesoporous silica (cubic pores of about 10 nm). Depending on the chelating angles, affinity toward specific REEs could be observed.¹²⁷

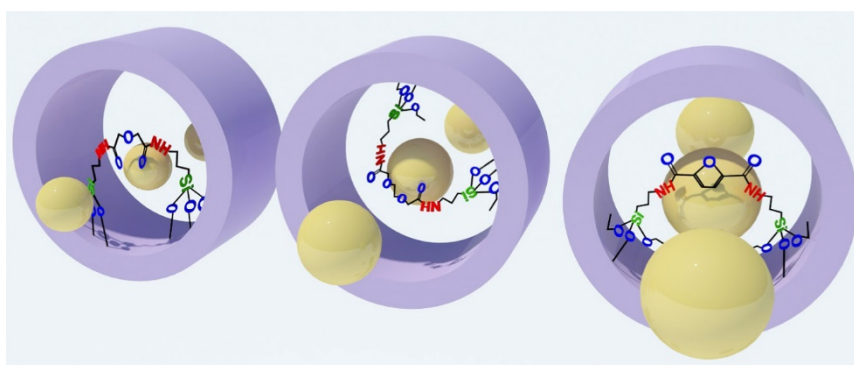


Figure 71. Scheme of three DGA [diglycol-2,4-diamido-propyltriethoxysilane (DGA-N), 3,6-dioxaoctanediamido-propyltriethoxysilane (DOODA-N), and furan-2,4-diamido-propyltriethoxysilane (FDGA-N)] fixed inside silica pores with different chelating angles. Balls represent REEs. Reproduced from Reference ¹²⁷.

However, in most cases, the selectivity of SLE processes is low, and extraction capacities are moderate. In consequence, they are favored where few competitive metals are present in the leachate.

1.2.3. Liquid-liquid extraction of REEs

As presented in Chapter I, Section 5.1.1, LLE (or solvent extraction) consists in contacting an organic phase containing selective extracting agents with an aqueous phase containing the targeted species and impurities. The choice of the good extracting agent allows dealing with large volumes of very complex mixtures of metals,⁹⁶ with substantially higher selectivity and efficiency than in SLE.

Typically, three types of extracting agents are commonly employed in industrial LLE of REEs: cationic (di-(2-ethyl-hexyl) phosphoric acid (D2EHPA, Cyanex 272), solvating (tributyl phosphate (TBP)), and anionic (Aliquat 336, Versatic 10) solvents (**Table 14**).^{96,123,130} In particular, they are chosen depending on the nature of the aqueous phase deriving from the leaching (pH, counterion like chloride, nitrate, sulfate...). Other ligands acting by solvation, such as diglycolamides, are also deeply investigated, because they can easily be synthesized and show lower affinity toward transition metals and actinides than toward trivalent lanthanides.^{127,131,132}

In terms of extraction performances, some extracting agents are reported to be more selective of light REEs while others would preferentially extract heavy REEs. Especially for solvation extractants,⁹⁶ it is usual that extraction efficiency increases with the atomic number across the lanthanides series. However, Aliquat 336 (anionic exchanger) shows better affinity toward light REEs in nitrate medium,¹²³ while DGAs with short alkyl chains display better extraction capacity for Ln(III) and An(III).¹³² In addition, europium and cerium can be extracted separately more easily because they are not trivalent like other lanthanides.

Despite the good efficiency and selectivity that can be reached with these LLE systems, they often consume much material. It is admitted that one ton of solvent are generally required to produce one tone of REE oxide.¹²⁴ LLE also encounters several other problems, such as third phase formation leading to process complications, low contact area, and large amounts of waste.⁶

Table 14. Conventional industrial extractants for REEs in LLE. Adapted from Reference ¹²³.

Extractants	Chemical Name	Structure
Cyanex 272	Di-2,4,4-trimethylpentyl phosphinic acid	
D2EHPA	Di-2-ethylhexyl phosphoric acid	
PC 88A	2-Ethylhexyl phosphonic acid mono 2-ethylhexyl ester	
TBP	Tri-n-butyl phosphate	
Kelex 100	7-(4-Ethyl-1-methyloctyl)-8-hydroxyquinoline	
LIX 84	2-Hydroxy-5-nonylaceto phenoneoxime	
Versatic 10	Alkyl monocarboxylic acids	
Aliquat 336	Tri-octyl methylammonium chloride	

1.2.4. Ion-exchange processes for high-grade REEs

In the 1950s, ion-exchange was the only method available to separate REEs industrially. Nowadays, it is still employed to treat small quantities of REEs up to high-grade purity.^{96,133} Very often, REEs complexes are in the cation form, so cationic exchanges are mostly implemented. In particular, ethylenediaminetriacetic acid (EDTA) and N-hydroxyethylethylenediaminetriacetic acid (HEDTA) have been identified as good eluants to strip the trapped REEs from ion-exchange columns.^{124,134} The two

molecules are represented in **Figure 72**. With these systems, the stability constants of the complexes are usually higher for heavy REEs, such that REEs are eluted in decreasing order of atomic number.¹³³

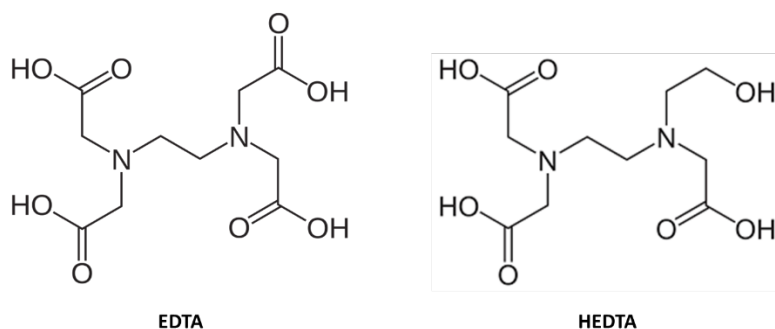


Figure 72. Ethylenediaminetriacetic acid (EDTA) and N-hydroxyethylethylenediaminetriacetic acid (HEDTA) used in ion-exchange REEs extraction.

1.3. Innovation for REEs extraction

To reduce the toxicity and energy requirements of conventional processes, the scientific literature has given rise to a number of alternatives, from synergistic systems to ion foam flotation, passing by the substitution of volatile solvents in LLE by ILs or deep eutectic solvents (DES). In this regard, PLs could also constitute an innovative solvent extracting phase in LLE.

1.3.1. Synergistic liquid-liquid extraction or solid-liquid extraction

Recently, synergistic LLE or SLE have emerged as interesting processes for metal extraction.^{6,95} They consist in the association of two extractants, whose one plays a synergistic role: the combination of their extracting properties generally enhances the selectivity toward a metal, thus boosting the extraction performances of the system, and reducing the volumes of organics required to treat the same amount of leachate. In LLE, synergy can also be harnessed to prevent the third phase formation.

For instance, D2EHPA (phosphoric acid) and Cyanex 272 (phosphinic acid) were successfully used together to extract dysprosium and separate it from europium,¹³⁵ while a mixture of N,N,N',N'-tetra(n-octyl)diglycolamide (TODGA) and tri(n-butyl)phosphate (TBP) in an IL gave access to very high intra-lanthanides selectivity.¹³⁶

1.3.2. Ionic liquids and deep eutectic solvents

Since conventional LLE means high volumes of solvents, often accompanied by aqueous ammonia used for the saponification of acidic extractants, ILs are seen as a greener alternative. Indeed, they have lower toxicity than organic solvents due to their zero vapor pressure, and they can show a very good extraction efficiency.^{137,138} They also show the advantage of suppressing the third phase manifestation. However, their high viscosity is an obstacle for scaling up ILs-based processes. Therefore, supercritical

CO₂ can be used as a low viscous diluent to enhance mass transfer. Interestingly, functional groups can be introduced in the design of the IL, bore by either one of the two ions, or both.^{137,139} The main extraction mechanism encountered for REEs in ILs is a cationic exchange, but it is unfortunately suppressed by the presence of long alkyl chains on the cation. Thus, the IL hydrophobicity – mandatory for LLE – must be obtained through a hydrophobization of the anion instead.

Being ILs' cousins, DES have recently emerged as a new class of non-volatile solvents with lower viscosity and simpler synthesis.¹⁴⁰ Even more recently, the first hydrophobic DES have been reported, and few studies investigated their ability for LLE.^{36,141–143} Concerning lanthanides extraction with hydrophobic DES, it has been observed that a compromise had to be found between loading and selectivity.¹⁴⁴

1.3.3. Ion foam flotation

Ion foam flotation has been studied for 65 years,¹⁴⁵ and it presents the advantages of releasing few wastes, with a good and cost-effective regeneration of the extracting material. It was shown to work well with ultra-trace levels of metal concentration, so it can be suitable for effluents decontamination.¹⁴⁶ A scheme of the process is presented in **Figure 73**. Ion concentration is achieved by complexation with a specific surfactant of opposite charge, able to form a foam under gas sparging. Forming the foam allows increasing the interface between effluent and surfactant. After the foam collapses, it leads to a liquid retentate, highly concentrated in metal.

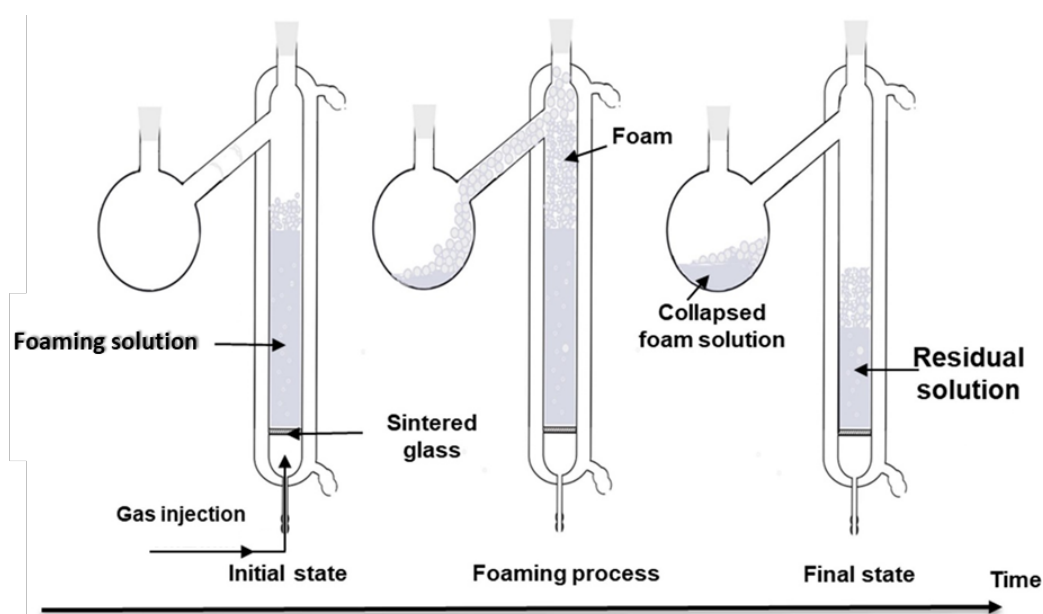


Figure 73. Principle of ion foam flotation. 1: rotameter, 2: sample syringe and port, 3: gas cylinder, 4: flotation column, 5: gas dispersion frit, 6: foamate reservoir. Adapted from Reference ¹⁴⁷.

1.3.4. Porous liquids

Because they permit the cohabitation of a high porosity with the liquid state, silica-based PLs could combine the high efficiency and selectivity of LLE with the material regeneration ability found in SLE. It would also suppress the emission of volatile organic compounds, and it could prevent the formation of a third phase. As reported in Chapter I, two studies already have shown the possible extraction of lead in PLs.^{57,60} However, no work has been published in the field of REEs extraction yet.

Therefore, this thesis was inspired from investigation as much in LLE as in SLE: good stability, hydrophobicity and low viscosity were imposed by the LLE process, while good selectivity and efficiency were foreseen with the functionalization of the silica hosts following methods applied in SLE. Indeed, it has already been observed that the functionalization of a PL with thiols was necessary to extract lead.¹¹⁹ Therefore, it is likely that no REEs extraction will be observed without functionalization with a specific ligand.

A slight difference with SLE processes relied in the relatively small size of pores (1.4 – 3.7 nm) in PLs, because HSPs must not be too large to maintain the liquid state (Chapter III, Section 2.3), unlike conventional SLE sorbents usually owning large pores (*e.g.* KIT-6 mesoporous silica have a 10 nm pore width).¹²⁷ Finally, the regeneration of the PL would be a great advantage over conventional LLE processes.

2. Functionalization of a porous liquid

As mentioned above, the functionalization of the PL is presumed to be necessary for the success of REEs extraction. To do so, the presence of silica nanoparticles has to be harnessed: it is believed that not only can they introduce porosity into the liquid but serve also as functional hosts for metals. With the aim of enhancing efficiency and selectivity toward REEs, functional moieties are anchored in the silica pores. The methods to perform functionalization of silica are described hereafter. Then, the choice of the functional group and the synthesis of a functional PL for REEs extraction are described.

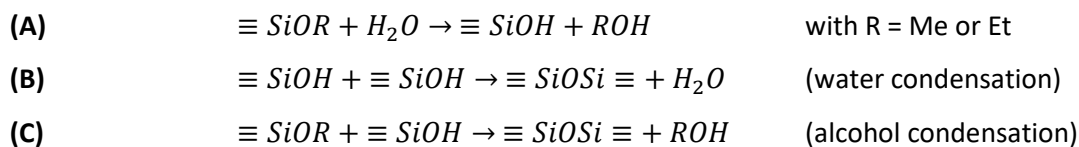
2.1. Methods for particles functionalization: state-of-the-art

In general, two methods are employed to functionalize silica: post-grafting and co-condensation. Post-grafting consists in grafting a functional group onto the silica surface by the mean of surface silanols. Co-condensation is the incorporation of the functional group inside the silica network during its formation. Both methods start from an organosilicon, bearing the functional moiety.

2.1.1. Post-grafting

Post-grafting reaction can be decomposed into two steps: the first step is the hydrolysis of terminal ethoxy or methoxy groups to form Si-OH bonds at the end of the functional organosilicon (Chemical

equation **A**). The second step is a condensation of either two silanols (Chemical equation **B**) or a silanol and an alkoxide (Chemical equation **C**) to form a siloxane bond (Si-O-Si), and releasing water or alcohol respectively.¹⁴⁸



Adding water in the medium would promote hydrolysis against condensation. On the reverse, the presence of ethanol (or methanol for methoxy groups) would slow down hydrolysis and promote water condensation. Furthermore, hydrolysis can be favored by an acidic medium (silanols in the protonated form) with an excess of water, while condensation can be catalyzed in a basic medium (silanols in the deprotonated form). Playing on this balance is significant when taking into account the competitive reaction of condensation between two organosilicon molecules.

2.1.2. Co-condensation

Functionalizing silica materials by co-condensation consists in introducing the functional group directly when forming the silica network during the sol-gel process (**Figure 74**). In this method, the functional organosilicon is introduced as a silica co-precursor along with tetraethyl orthosilicate (TEOS) or tetramethyl orthosilicate (TMOS), the most common silica precursors. In general, small organosilicons like aminopropyl triethoxysilane (APTS) and vinyl triethoxysilane (VTS) are used to avoid any structure alteration of the silica network.^{149,150}

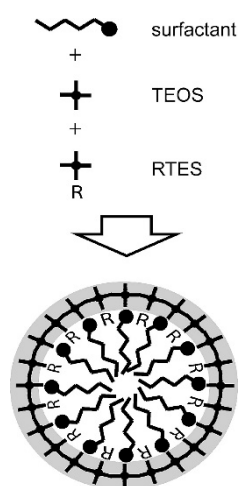


Figure 74. Co-condensation reaction between TEOS and a functional alkoxy silane (RTES stands for “R-triethoxysilane”) with a micelle-forming surfactant. Reproduced from reference ¹⁴⁹.

This method can disperse the functional groups more homogeneously in the silica material than the post-grafting, but the latter can be less accessible for complexation.

2.2. A functional porous liquid for REEs extraction

2.2.1. Choice of the functional group

EDTA (**Figure 72**) was selected because it is generally reported as a good extractant for REEs¹³⁴ and it was commercially available in the organosilicon form. However, it was also reported in literature that it displayed a poor *intra*-REEs selectivity (the complexation free enthalpy between two adjacent REEs being about 6.5 KJ/mol, this is not sufficient to reach a correct *intra*-REE selectivity¹²⁴). It was presumed that whatever the strategy adopted for functionalization, it should be transferable to diglycolamides, that are similar in size, and show better selectivity.^{127,128} Nevertheless, it should be noticed that EDTA acts as an cation-exchanger extractant, while DGAs are solvating extracting agents instead. Therefore, the optimization of conditions for extraction (especially the pH) may differ.

2.2.2. From functional silica particles to the first functional porous liquid

Regarding silica-based PLs as hybrid organic-inorganic materials, this work focused on functionalizing only the inorganic part for REEs extraction. No additional task-specific groups to capture REEs were added in the organic moieties. Therefore, the same synthesis routes as described in Chapter II for non-functional PLs were applied starting from EDTA-functionalized hollow silica particles (HSPs-EDTA).

In particular, the first extraction tests were carried out using a hydrophobic ionic PL based on sHSPs functionalized with EDTA by co-condensation (denoted PL-sHSPs-EDTA-c-EthA-11). Note that the presence of organic EDTA in the silica network implied to use a soft template removal technique instead of calcination. To avoid the penetration of SIT inside the pores (an issue that has been discussed in Chapter II, Section 3.1.2.3 and Chapter III, Section 1.2.1), this template removal was performed after tethering SIT molecules at the surface of sHSPs-EDTA. The complete synthesis pathway is described in **Figure 75**.

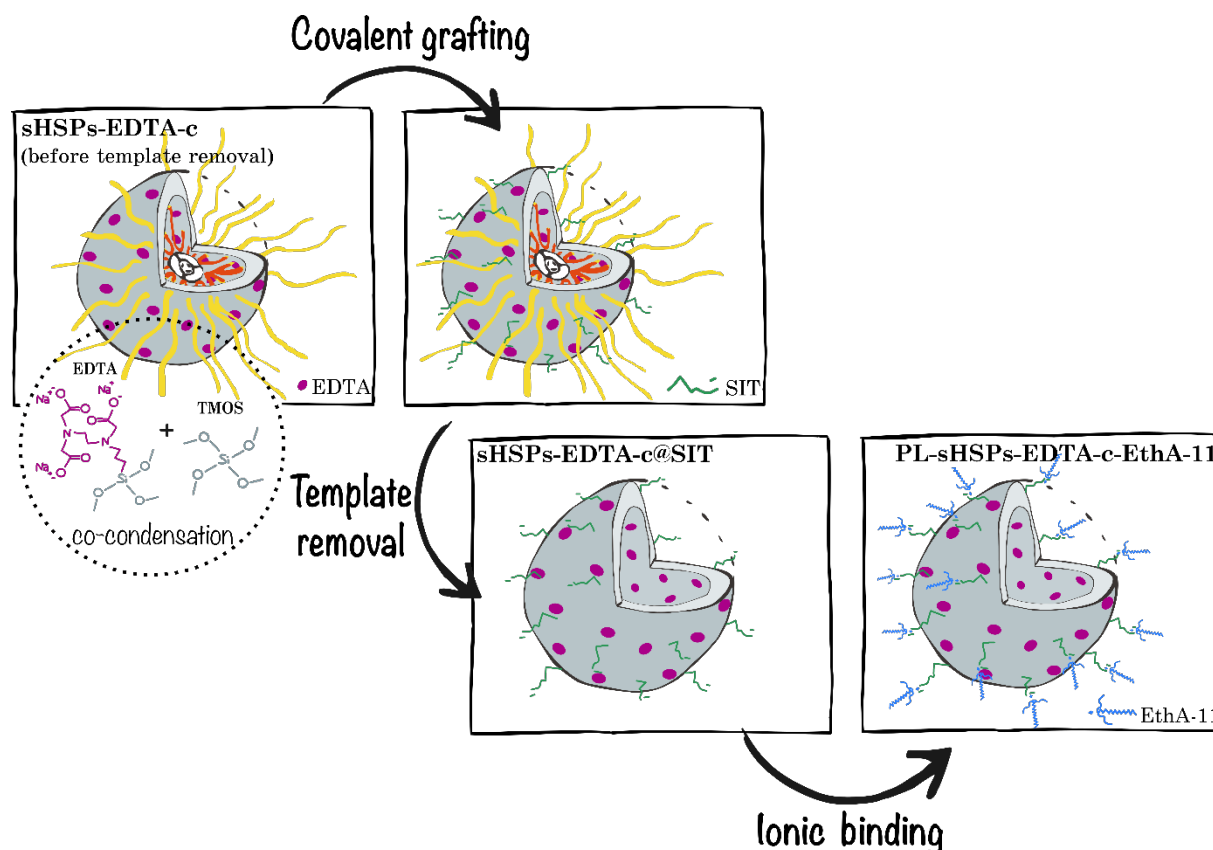


Figure 75. Method for the synthesis of a functional ionic PL (PL-sHSPs-EDTA-c-EthA-11) by sHSPs functionalization with EDTA using co-condensation.

2.2.2.1. Functional hollow silica particles

Co-condensation was chosen in the first place to functionalize HSPs. Indeed, it was probable that post-grafting would induce pore-blockage, as well as creating a barrier for the SIT when fabricating the PL's organic corona-canopy. Nevertheless, the fact that EDTA was a large molecule compared to more spread APTS or VTS exposed to the risks of size exclusion during the sol-gel process, and silica shell weakening.

The detailed method is given in Appendix A. Briefly, a micelle was formed exactly as for the synthesis of non-functional sHSPs described in Chapter II. Around this soft template, co-condensation of TMOS and silanized EDTA (SiEDTA) led to the formation of a core-shell particle denoted sHSPs-EDTA-c ("c" standing for "co-condensation") (Figure 75).

2.2.2.2. Functional porous liquid based on an ionic amphiphilic canopy

After the functionalization of sHSPs, the sulfonate SIT was grafted at the surface of the particles following the same method as previously. In order to remove the template without damaging EDTA and SIT groups, a soft acidic ethanol washing was further adopted, as the one already presented in the

previous chapter, Section 1.1.3. This sHSPs-EDTA-c@SIT intermediate was then used to make a functional ionic PL with EthA-11 canopy (PL-sHSPs-EDTA-c-EthA-11) as before (**Figure 75**).

2.2.2.3. Characterization

sHSPs-EDTA-c (*cf.* bookmark No.6) have been imaged by TEM before SIT grafting and template removal (**Figure 76a**). The micrograph confirms the good formation of hollow silica spheres, with rougher surface compared to sHSPs (see Chapter II). A small proportion of the spheres were also partially broken. The statistical analysis of their sizes (**Figure 76c-d**) indicated a mean external diameter of 36.3 ± 3.7 nm and a mean internal diameter of 23.8 ± 3.4 nm. If their size is similar to the calcined reference sHSPs-2 (37.3 nm), their cavity is larger (it was 19.4 nm for sHSPs-2). Indeed, the presence of hindered molecules during the sol-gel process may have contributed to the size reduction of the shell thickness.

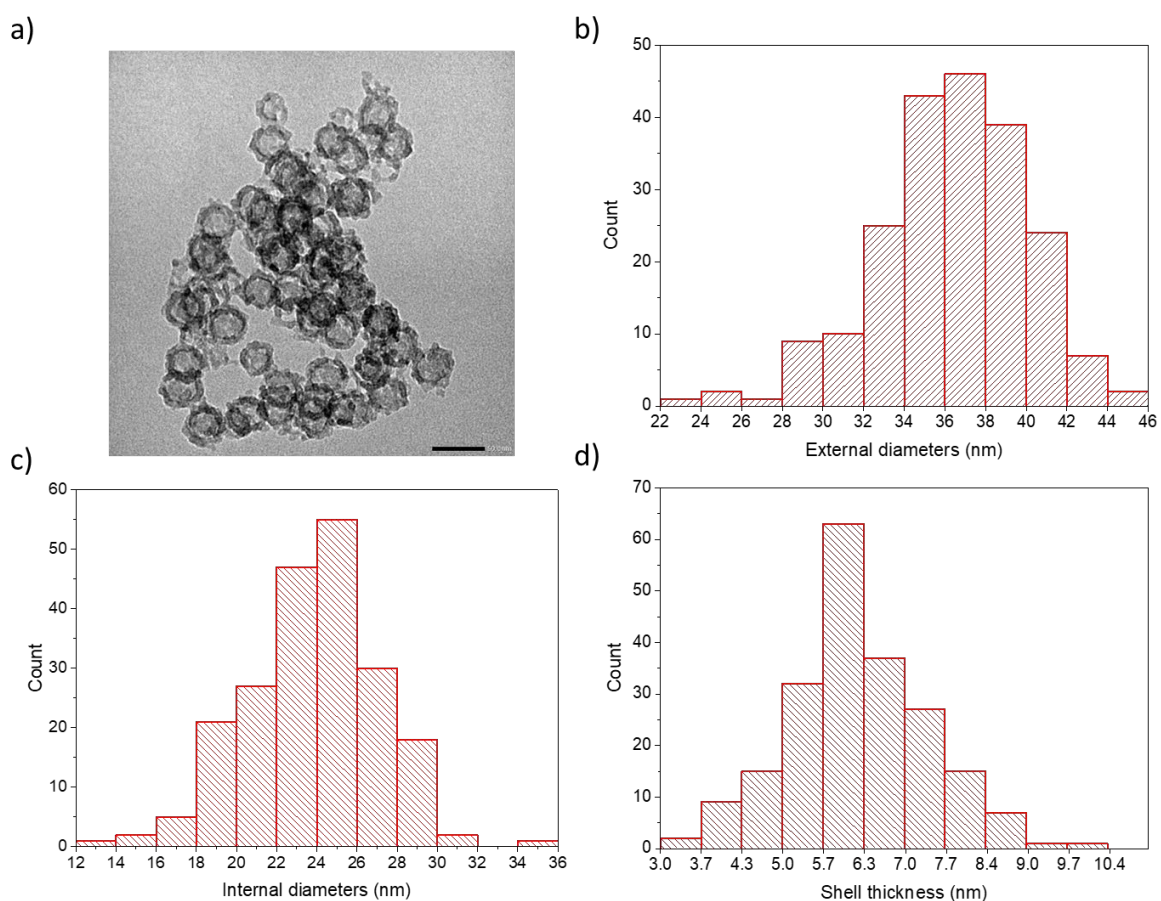


Figure 76. a) TEM image of sHSPs-EDTA-c before SIT grafting and template removal. Scale bar: 50 nm; Statistical sizes distributions ($\# = 210$): **b)** external diameter, **c)** internal diameter, and **d)** shell thickness.

The presence of EDTA could hardly be monitored by FTIR (FTIR spectrum presented in **Figure 77**): the signal of sHSPs-EDTA-c (before SIT grafting and template removal) was compared to a non-functional reference also containing the template (named sHSPs-3 hereafter). A strong carbonyl peak

was expected in the 1600-1700 cm^{-1} region accounting for the presence of EDTA. In fact, two peaks were visible at 1634 and 1602 cm^{-1} , in both signals. They were enhanced for the sHSPs-EDTA-c. However, it was not clear to what extent this increase in intensity could be attributed to the carbonyl groups. Indeed, the quantity of EDTA groups in the silica network was weak (SiEDTA:TMOS molar ratio was 1:16 when initiating the sol-gel process), and the presence of OH groups (that were more numerous in the functionalized powder of EDTA) could hid the signal of the carbonyl. In addition, the wide -OH band at 3500-3200 cm^{-1} was also stronger for sHSPs-EDTA-c than for sHSPs-3, even after extensive drying. It could be assumed that the presence of EDTA groups induces more water molecules bound to the surface, or more silanols groups due to a less condensed silica network, along with the three hydroxyl groups of the carboxylates in EDTA.

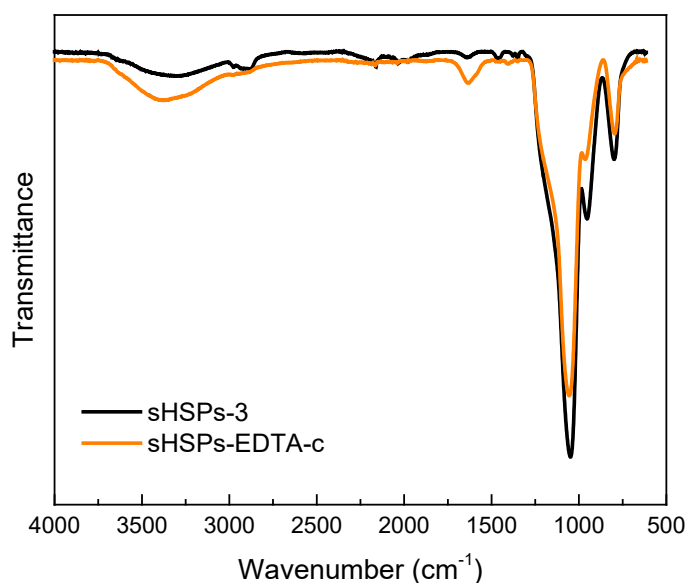


Figure 77. FTIR spectra of sHSPs-EDTA-c before SIT grafting and template extraction compared with sHSPs-3 before calcination (a non-functional reference containing the template).

Besides, high resolution TEM (HRTEM) coupled with energy-dispersive X-Ray (EDX) spectroscopy has been tested onto sHSPs-EDTA-c to probe the presence of nitrogen from EDTA molecules in the silica network. Unfortunately, the presence of organics prevented from obtaining a resolution high enough to draw any conclusion.

Finally, elemental analysis of sHSPs-EDTA-c before SIT grafting and template removal was performed, and 42.1 mmol of nitrogen were found in 100 mg of powder. This would mean a concentration of 210 mmol/g of EDTA groups in the powder. In the TGA of the same sample (see Appendix F, **Figure A13**), the contribution of the organic content to the weight loss was 11.3%.

Combining both techniques, it could be deduced that the contribution of EDTA groups to this amount was 5.8% (see also the calculation in Appendix F). It would mean a SiEDTA:TMOS molar ratio of 0.0149 instead of the expected 0.0625 (1:16), being 4 times less than the amount of SiEDTA initially introduced. This could be due to an exclusion of SiEDTA during the co-condensation process. Note that in this reasoning, the contribution of siloxane bonds formation due to the presence of free silanols at the surface is not taken into account. Solid NMR of silicon and nitrogen would have been helpful to determine precisely the number of EDTA groups in the sample, and the silanols content likely to form siloxane bonds during the TGA. This content is probably higher than for non-functionalized sHSPs after calcination because SiEDTA are not necessarily linked by the three ends of Si(OEt)₃ groups.

Further information about chemical composition of the functional PL (PL-sHSPs-EDTA-c-EthA-11) could be deduced from TGA presented in **Figure 78**. Below 200 °C, a 9.3% weight loss corresponded to free water molecules, and this content was similar to the one in the non-functional reference PL-sHSPs-2-EthA-11. Then, three successive weight losses (75.5%) that can hardly be uncorrelated were attributed to the degradation of the amine EthA-11, EDTA groups and SIT groups. Finally, the SiO₂ inorganic content at 950 °C was 15.2% (16.8% after correction from the water content). The difference with the inorganic content of the non-functional reference (19.9%, or 21.9% after water correction) can be attributed to the presence of EDTA as well as a slightly different amine content. This would mean that the EDTA content is below 5%. A calculation to estimate the real content of EDTA groups in the PL was performed based on TGA and elemental analysis (see above), and it is described in Appendix F. It resulted that about 1% of organic EDTA were present in the PL (being $36.3 \cdot 10^{-2}$ mmol/g).

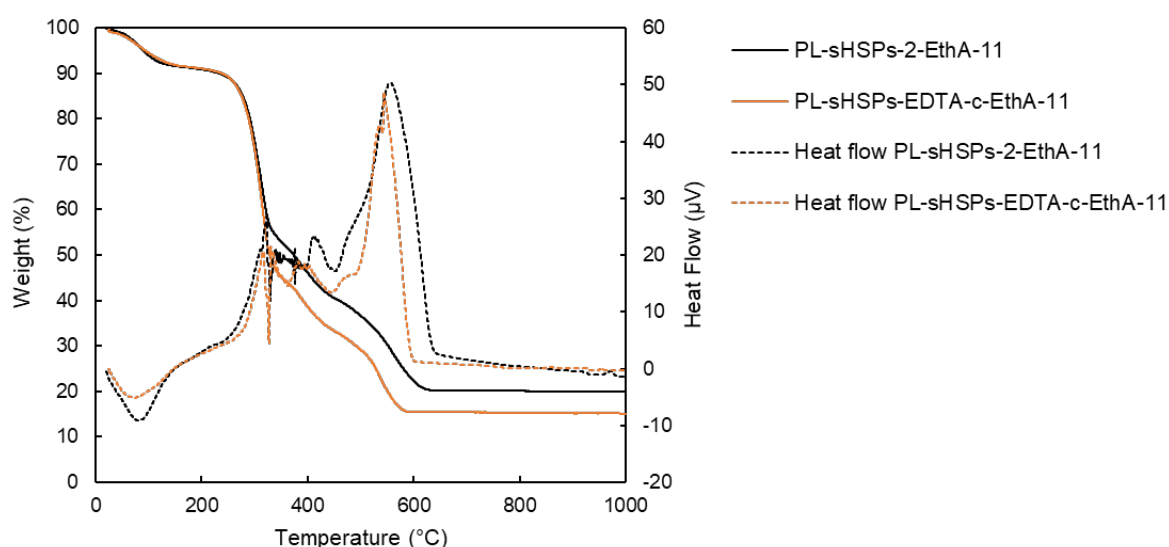


Figure 78. TGA and DTA of PL-sHSPs-EDTA-EthA-11 (orange) and a non-functional reference (PL-sHSPs-2-EthA-11; black), under air at a rate of 5 °C/min.

In the following sections, extraction tests were performed on functional and non-functional materials to verify whether extraction was observed with both types or only with the functional materials.

3. Extraction of REEs from permanent magnets with a functional porous liquid

3.1. Case study of permanent magnets

Permanent magnets are present in many technological objects, such as hard drive disks, batteries, wind turbines etc. It exists different types of permanent magnets, but the most commonly used in high quantities are the so-called Nd-Fe-B magnets. Such magnets contain significant amounts of Nd, Pr and Dy, along with iron and bore.

Precisely, the extraction of these three REEs is targeted in this thesis, and the presence of iron as a competitive cation is also considered.

Concerning extraction of Nd and Dy through conventional LLE processes, phosphorous-based extractants such as TBP or D2EHPA show good efficiency when the metals are in a nitric medium. The quaternary amine Aliquat 336 also achieve good selectivity.⁹⁵ Most processes involving Nd and Dy primarily extract both REEs simultaneously, before separating them by chelating the dysprosium (heavy REEs generally have better affinity to chelatants).

In the present case, EDTA does not allow good intra-REEs selectivity (Section 2.2.1), so a co-extraction of the three REEs was expected.

3.2. Extraction method

Preliminary extractions tests were carried out by following a general method: 25 mg of materials (HSPs or PLs) were contacted with 5 mL of a solution **S1** containing metals (Fe 1600 ppm, Nd 500 ppm, Pr 68 ppm, Dy 50 ppm) in nitric acid at pH 2, to imitate a leachate from hard drive disks recovery.¹³¹ For the functional PL PL-sHSPs-EDTA-c-EthA-11, only 5 mg were introduced because of the lack of material. The contact was performed under vertical agitation at 40 rpm during 24 h. The phase separation was performed after centrifugation at 4500 rpm for 10 min. The aqueous phase was then analyzed by TOC and ICP to determine the quantity of carbon and metals and to compare with the mother solution before contact.

Inspired from the SLE field, the extraction capacity Q_M ($\text{mmol}_M/\text{g}_{\text{mat}}$) of a material for a specific metal M was defined as:

$$Q_M = \left[\frac{c_i^m \times V}{MW_M} - \frac{c_f^m \times V}{MW_M} \right] \times \frac{1}{m_{mat}} \quad (1)$$

Where c_i^m and c_f^m are the initial and final mass concentrations of metal respectively (mg/L), V the volume of solution **S1** in contact with the material (L), MW_M the molecular weight of the metal (g/mol), and m_{mat} the mass of material used for the extraction test (g).

3.3. Preliminary results

3.3.1. Hollow silica particles

Extraction tests were firstly performed with sHSPs-EDTA-c@SIT intermediate because the spheres were emptied (from the template) after SIT tethering. The calcined reference sHSPs-1 was also used for comparison, but no extraction was recorded for any metal. Extraction capacities for each metal are gathered in **Table 15**.

Table 15. Extraction capacities of sHSPs-EDTA-c@SIT for each metal contained in **S1**.

	Extraction capacity Q_M (mmol/g _{sHSP})	Extraction capacity Q_M (mmol/g _{SiO₂})
Fe	1.006	1.137
Nd	0.144	0.163
Pr	0.018	0.020
Dy	0.006	0.007

Surprisingly, iron was extracted more preferentially than REEs, when EDTA is known to be more selective toward REEs than toward iron. However, its presence potentially catalyzed the precipitation of iron with the silica powder at this pH. Indeed, HRTEM and EDX analyses performed after contact showed the presence of iron aggregates around the sHSPs (**Figure 79**); but it is possible that these aggregates just formed during drying on the grid. In any case, the prevalence of iron in the mother solution would have saturated chelating sites if its extraction had involved a chemical process. Instead, extraction of neodymium, praseodymium and dysprosium implied that EDTA groups were present and accessible to the REEs.

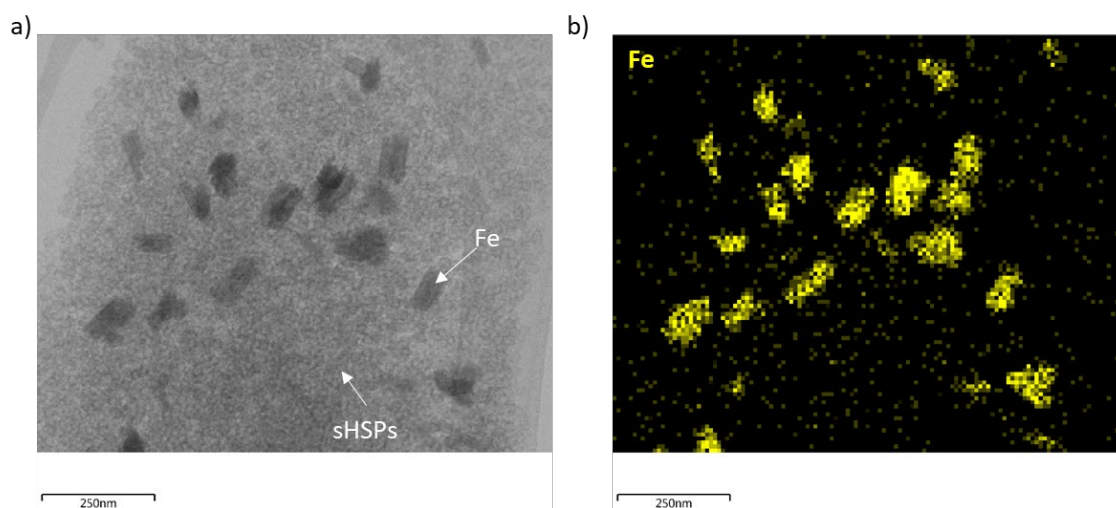


Figure 79. HRTEM of sHSPs after contact with S1: **a)** electronic image; **b)** EDX cartography showing the presence of aggregates of iron.

3.3.2. Ionic porous liquids

Functional PL-sHSPs-EDTA-c-EthA-11 and non-functional PL-sHSPs-EthA-11 were tested in the same extraction conditions. Again, no extraction was observed for the non-functional PL, except for the precipitation of iron. This indicates that no contribution of the corona-canopy system in the extraction of REEs was to be expected. **Table 16** shows the extraction capacities for each metal obtained for the functional PL.

Table 16. Extraction capacities of PL-sHSPs-EDTA-c-EthA-11 for each metal.

	Extraction capacity Q_M (mmol/g _{PL})	Extraction capacity Q_M (mmol/g _{SiO₂})
Fe	4.172	27.4
Nd	0.072	0.47
Pr	0.027	0.18
Dy	0.012	0.079

At first sight, extraction of Nd (0.072 mmol/g_{PL}) seems to be reduced by two when compared to the spheres alone. Nevertheless, it has to be considered that only 15.2% of silica was present in the PL, according to TGA (**Figure 78**). In consequence, the extraction capacity of Nd is even exalted in the PL (0.47 mmol/g_{SiO₂} is thrice more than 0.163 mmol/g_{SiO₂} found for sHSPs-EDTA-c@SIT). Concerning the minor elements Pr and Dy, the capacity of PL was higher than the one of the spheres alone (and even higher when considering only 15.2% of silica in the PL: 0.18 mmol_{Pr}/g_{SiO₂}, and 0.079 mmol_{Dy}/g_{SiO₂}). This may be explained by a slower diffusion of metals inside the PL than inside the sHSPs,⁵⁷ thus allowing Pr and Dy to occupy sites before their saturation with Nd.

By comparison, it was shown that a similar but hydrophilic ionic PL functionalized with thiols and tested for lead extraction had a capacity of 0.058 mmol/g_{PL}, that was again higher than the capacity of the spheres alone, when normalized by the quantity of silica in the material.⁶⁰ Other solid sorbents used for REEs extraction showed similar capacities: a mesoporous silica functionalized with DGAs had a capacity for the lutetium of 0.069 mmol_{Lu}/g_{powder}.¹²⁸ However, SiNPs (139 m²/g) decorated with EDTA groups (13.1 μmol_{EDTA}/m², implying a multilayer formation) showed higher extraction efficiency for Nd and other REEs (2.5 mmol_{Nd}/g_{powder}, at pH 6).¹⁵¹ This could be due to the better availability of EDTA grafted on the external surface of SiNPs, along with the higher pH. In addition, a recent study of LLE of Nd, Pr, and Dy has been conducted with lipophilic derivatives of EDTA.¹⁵² It is reported that a loading capacity of 1.2 · 10⁻² mol_{Nd}/L for Nd in nitrate medium could be achieved with a concentration of extractant of 1.5 · 10⁻² mol/L. This would represent a capacity of 0.94 mmol_{Nd}/g_{EDTA_{lip}}. Considering an approximate EDTA content of 1% in the PL (see Section 2.2.2.3 and Appendix F), the loading capacity found for Nd in **Table 16** would be 7.2 mmol_{Nd}/g_{EDTA}, being almost 10 times more than the uptake found in LLE using free lipophilic derivatives of EDTA.

In conclusion, it was shown that extraction of REEs was possible with a hydrophobic PL, implying that EDTA groups were present and accessible to the cations. The performances can still be optimized, by playing on the pH and the amount of accessible EDTA groups. Moreover, the lack of selectivity between REEs is not surprising, because EDTA was not the most selective agent for this application. In the next section, a study for optimizing extraction capacities is performed on a simple system based on one single element (Nd).

4. Optimization of extraction performances

For sake of simplicity, the optimization of extraction was carried out with HSPs alone, with the aim of transferring the results to the PL afterward. First of all, EDTA is sensitive to pH and this part will be discussed in Section 4.1. Furthermore, a question raised about how increasing the EDTA:SiO₂ ratio inside the particle. For this, two other parameters will be investigated: the grafting method (co-condensation, as above, or post-grafting) (Section 4.2), and the size of the spheres (*i.e.*, sHSPs or bHSPs) (Section 4.3). Because selectivity was not regarded in the first place, all of these three studies have been conducted using single-metal solutions of neodymium in nitric acid.

4.1. Influence of pH on the extraction of neodymium

As most cations exchangers, EDTA is not efficient at very low pH.^{151,153} Indeed, its pK_a values (free form) are 2, 2.7, 6.2 and 10.3 but these values may differ for the silanized form of the molecule (only three carboxylic groups). To understand to what extent pH can impact extraction efficiency, six solutions of Nd (500 ppm) and HNO₃ (10⁻³ M) at pH 3, 3.5, 3.9, 4.5, 4.9 and 6, were prepared by adjusting pH with

NaOH. Extraction was performed with a new set of functional sHSPs (sHSPs-EDTA-c-2) that were emptied by soft template washing (in hot ethanol), so that no SIT molecules were present in this case. Characterization of this set of sHSPs-EDTA-c-2 is provided in Appendix F. Extraction tests were carried out using 15 mg of powder and 3 mL of solution, let in contact at room temperature during 24 h under stirring. After phase separation by centrifugation, the aqueous phase was analyzed by ICP as previously.

Figure 80 shows the extraction capacities of sHSPs-EDTA-c-2 for Nd as a function of pH. As expected, the extraction capacity of the functional spheres increased when increasing the pH (+ 68% between pH 3 and 6), with a less pronounced increase after pH 4.5. In comparison with the extraction capacity of sHSPs-EDTA-c@SIT in contact with **S1** (0.144 mmol_{Nd}/g), provided in the previous section (**Table 15**), the capacities are greatly enhanced here. Therefore, a good pH zone for the extraction would lie between pH 4.5 and pH 6.

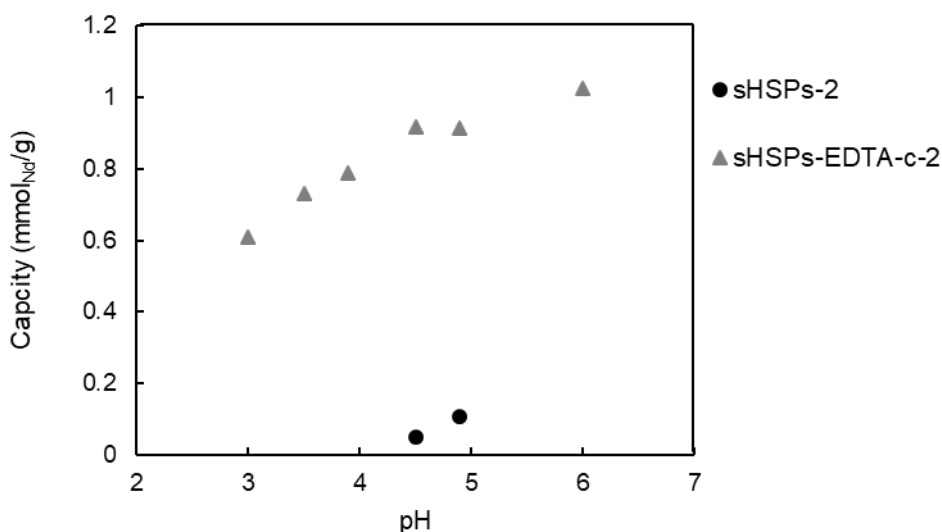


Figure 80. Extraction capacity of sHSPs-EDTA-c-2 for Nd in nitric acid as a function of pH, and comparison with a non-functional reference (sHSPs-2).

4.2. Effect of the grafting method on the extraction of neodymium

To avoid degradation of sHSPs during their formation, co-condensation was performed with only few amounts of EDTA groups (1:16 molar ratio SiEDTA:TMOS). In order to increase extraction performances of functional sHSPs, adding more functional groups would be desirable. Hence, the post-grafting functionalization of EDTA onto the surface of calcined sHSPs-1 has also been tested to compare extraction capacities (see section 2.1.1). It was performed in water at pH 5-6 as for SIT grafting (see Appendix A). The material was labeled sHSPs-SiEDTA-p (“p” standing for “post-grafting”, cf. bookmark No. 7), and characteristic information about this sample are supplied in Appendix F.

sHSPs-EDTA-p was tested in similar conditions as sHSPs-EDTA-c-2 in the previous section, with Nd solutions in nitric acid at pH 3, 3.5, 4, 4.9 and 6. Results are plotted in **Figure 81**, where the capacities of sHSPs-EDTA-c-2 and sHSPs-2 have been reported for comparison. From this graph, one can conclude that this new sample reaches very close extraction capacities to the ones obtained for sHSPs-EDTA-c-2. Here, a plateau was clearly reached after pH 4, so the pH zone suitable for a correct extraction lies between pH 4 and pH 5. Note that few repetitions of the experiment should have been done, but it has not been possible by lack of time.

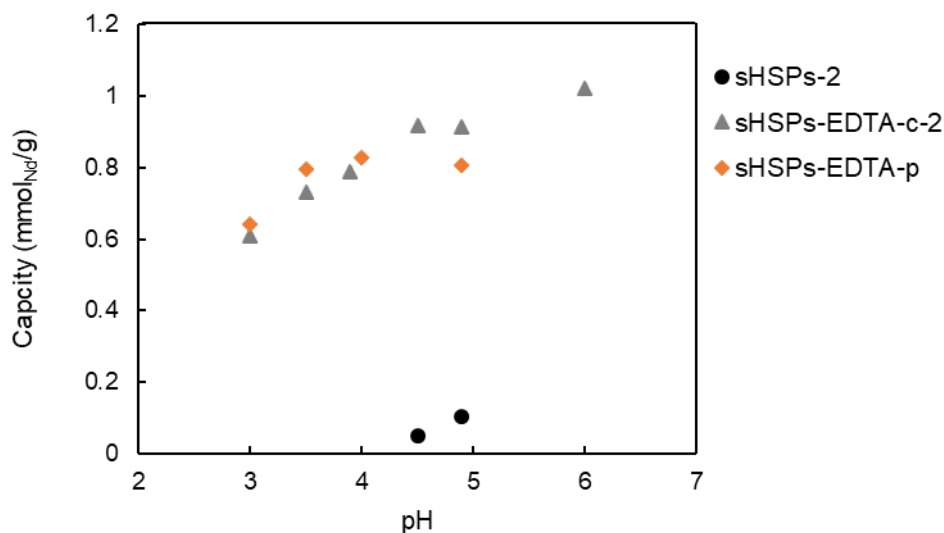


Figure 81. Extraction capacity of sHSPs-EDTA-p (post-grafting) for Nd in nitric acid as a function of pH, compared to sHSPs-EDTA-c-2 (co-condensation) and the non-functional reference sHSPs-2.

Yet, post-grafting and co-condensation do not substantially change the number of EDTA groups by gram of material that are accessible for extraction. According to the TGA of the two samples (after water correction), sHSPs-EDTA-c-2 contained 13.4% while sHSPs-EDTA-p contained 12.9% of organic EDTA (**Figure 82**). This result suggests a good diffusion of EDTA groups in the pores for both methods, allowing their grafting even deep inside the shell. In addition, the degradation of EDTA in sHSPs-EDTA-p occurred slower (between 250 and 600 °C) than in sHSPs-EDTA-c-2 (between 250 and 450 °C); and this may imply oligomerization processes at the surface of sHSPs-EDTA-p, conducting to a multilayer formation.

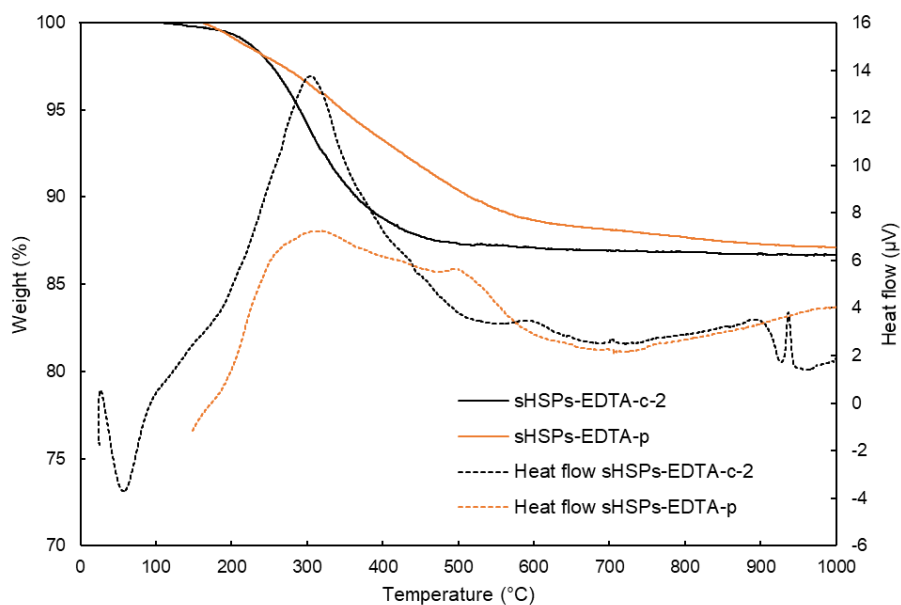


Figure 82. TGA and DTA of sHSPs-EDTA-c-2 and sHSPs-EDTA-p after water correction.

Besides, it was found that doing two successive EDTA post-grafting onto the same sample was not efficient in increasing extraction capacities. This can be explained by the absence of diffusion of SiEDTA molecules inside the pores of sHSPs because of their small size. Indeed, the nitrogen sorption isotherms of the powder before and after EDTA grafting are shown in **Figure 83**. Isotherms show the presence of hysteresis loops even after grafting, suggesting that the hollow cavity is still accessible to the gas. The BET specific area decreased by 15.6% after the first grafting step. After the second grafting step, no further significant decrease (< 6%) in the specific area was observed. The fact that only partial pore blockage occurred, with moderate loss of the specific surface area, confirms that SiEDTA molecules could not deeply diffuse inside the silica shell. TGA also corroborates these results, because the weight loss corresponding to organic EDTA was similar (14.9%).

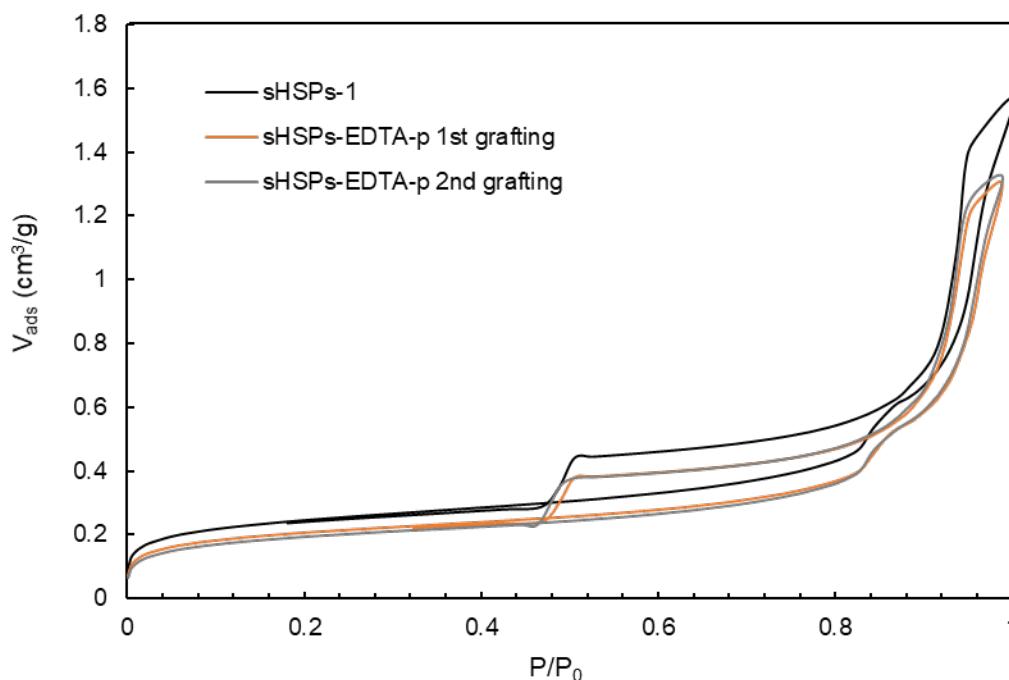


Figure 83. Nitrogen sorption isotherms of sHSPs-1 and sHSPs-EDTA-p after one single grafting, and two successive grafting of EDTA groups.

In conclusion, it seems that physical limitations prevent from increasing the capacities by simply increasing the number of EDTA groups. Alternatively, changing the particle nature (from sHSPs to bHSPs) was likely to have more impact because of the change in the specific surface area.

4.3. Effect of the size of hollow silica particles on the extraction of neodymium

For the third study concerning optimization of extraction performances, bHSPs were used as another support for EDTA post-grafting, and the method was identical to the one described above (Sections 2.1.1 and 4.2, Appendix A). This sample was named bHSPs-EDTA-p (*cf.* bookmark No. 7) and its characterization is detailed in Appendix F. It was tested with solutions of Nd in nitric acid at pH 3.5 and 4.9, and the extraction capacities were as high as **1.252** and **1.484 mmol/g of bHSPs**, respectively (**Figure 84**). This is 58% and 84% more than the capacities of sHSPs-EDTA-p at the same pH (0.794 and 0.808 mmol/g of sHSPs).

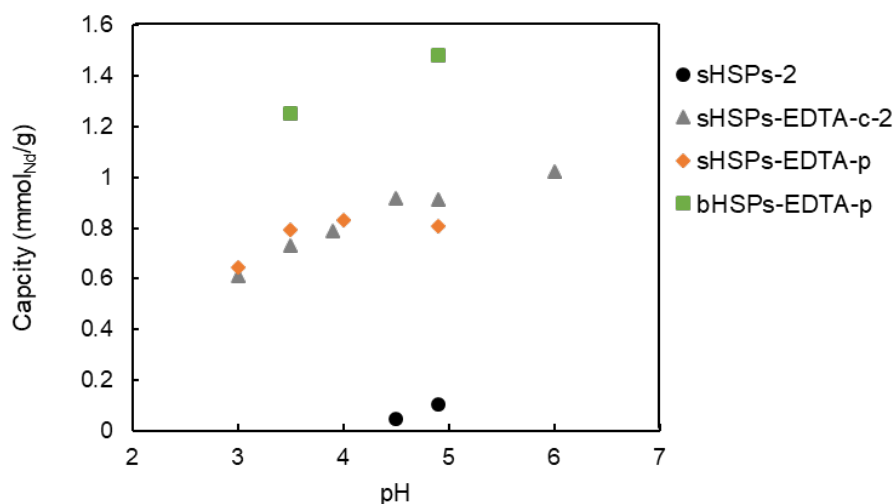


Figure 84. Extraction capacities of bHSPs-EDTA-p (post-grafting), compared to sHSPs-EDTA-c-2 (co-condensation), sHSPs-EDTA-p (post-grafting), and sHSPs-2 (non functional), as a function of pH.

To explain the result, the TGA of bHSPs-EDTA-p was compared to the TGA of sHSPs-EDTA-p (**Figure 85**). After applying a correction from the water content, bHSPs-EDTA-p contained 21.1% of organic EDTA (compared to 12.9% for sHSPs-EDTA-p). This result can be easily linked to the higher specific surface area of bHSPs along with their larger pores probably allowing more diffusion of SiEDTA molecules. Therefore, the higher EDTA content in bHSPs allows increasing the extraction capacities for a same powder mass.

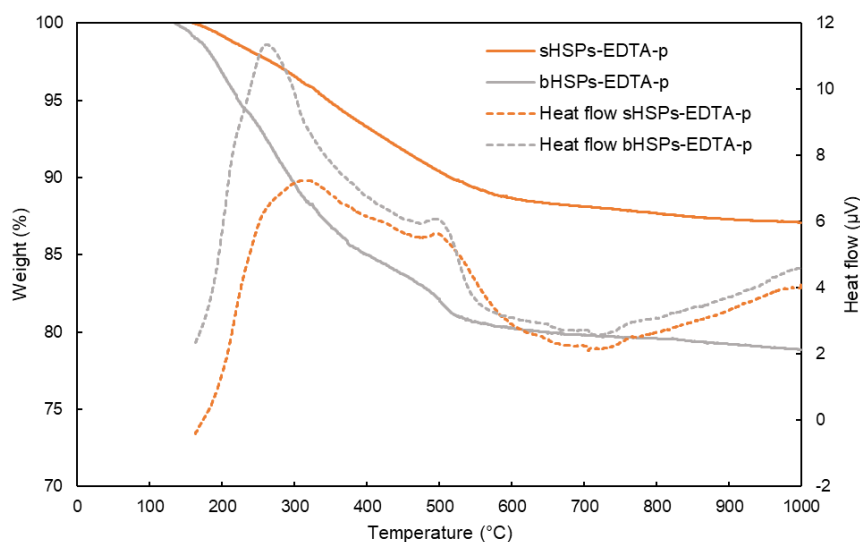


Figure 85. TGA and DTA of bHSPs-EDTA-p and sHSPs-EDTA-p.

All in all, these optimization tests allowed to fix that the better working condition would be at a pH between 4.5 and 5. It was found that post-grafting of sHSPs with EDTA groups did not allow to increase the amount of functional groups when compared to the functional sample synthesized by co-

condensation. However, the use of bHSPs as a support did increase the number of EDTA per gram of materials, because of the higher specific surface area of the big spheres, along with the larger pores facilitating the diffusion of the organosilicon during the grafting.

Interestingly, this method did not block the porosity of bHSPs (and sHSPs) as expected, and a perspective would be to turn these functional spheres into a PL before performing new extraction tests. However, the fact that EDTA groups are grafted onto the surface silanols would probably decrease the ability of bHSPs (or sHSPs) to be liquefied through covalent grafting. Another perspective would therefore consist in synthesizing bHSPs-EDTA by co-condensation. This could not have been done, because bHSPs are made with TEOS and not TMOS, while SiEDTA contained methoxy-terminated silane groups. Hence, an adjustment of the synthesis method to find the good conditions for a correct EDTA incorporation is required.

5. Stability of porous liquids toward acid and metals

Before considering a functional PL for any LLE process, assessing their stability in contact with an aqueous medium was of utmost importance. In this regard, simple contact tests of non-functional hydrophobic PL-sHSPs-EthA-11 and PL-sHSPs-PPG-2000-fluid were carried out with water, nitric and acetic acid solutions, and metals-containing aqueous solutions.

5.1. Hydrophobic ionic porous liquid: PL-sHSPs-EthA-11

The first hydrophobic PL to be synthesized and characterized was PL-sHSPs-EthA-11, and it contained an ionic bonding between corona and canopy, as depicted in the bookmark No. 4.

For contact tests, 25 mg of PL were contacted with 5 mL of water or aqueous solutions (**S1** to **S5**, **Table 17**). Nitric acid was tested in the first place for this stability study, because it is a very common leaching medium for REEs.¹²³ The pH was low (pH 2) because it corresponds to the conditions of the preliminary extraction tests presented in Section 3. Acetic acid was also tested for comparison, since it could be considered as an alternative leaching medium in the view of a less impacting hydrometallurgy.¹³¹

Table 17. Solutions used for contact tests.

	Acid	Metals
S1	Nitric acid 10 ⁻² M	-
S2	Acetic acid 0.5 M	-
S3	-	Fe (1260 ppm), Nd (500 ppm), Pr (68 ppm), Dy (50 ppm)
S4	Nitric acid 10 ⁻² M	Fe (1260 ppm), Nd (500 ppm), Pr (68 ppm), Dy (50 ppm)
S5	Acetic acid 0.5 M	Fe (1260 ppm), Nd (500 ppm), Pr (68 ppm), Dy (50 ppm)

After 24 h, the phases were separated and TOC present in the aqueous phase was analyzed to determine the amount of amine EthA-11 solubilized (implying a PL instability). In the cases of water and nitric acid, the ratio of amine solubilized in the aqueous phase was calculated from the concentration of carbon according to Equation (1):

$$\frac{(m_{EthA})_{aq}^f}{(m_{EthA})_{PL}^i} = \frac{\left[\frac{m_C^f}{MW_C} \times \frac{MW_{EthA}}{N_C^{EthA}} \right]}{(m_{EthA})_{PL}^i} \quad (2)$$

Where $(m_{EthA})_{aq}^f$ and $(m_{EthA})_{PL}^i$ are the masses of EthA-11 in the aqueous phase after contact, and in the PL before contact (from TGA), respectively; m_C^f is the mass of carbon in the aqueous phase after contact, as deduced from TOC, MW_C and MW_{EthA} are the molecular weights of carbon and EthA-11 (12.02 g/mol and 725 g/mol, respectively), and N_C^{EthA} is the number of carbon in EthA-11 (38, considering a mean aliphatic chain of 16 carbons).

In the case of acetic acid, the carbon weight in the aqueous phase m_C^f was corrected from acetic acid contribution, deduced from the initial concentration (0.5 M). The results are gathered in **Table 18**.

Table 18. Amount of amine EthA-11 solubilized in the aqueous phase, after contacting PL-sHSPs-EthA-11 for 24 h, as determined by TOC analysis. Uncertainties for acetic acid are coming from the exclusion of the calculated contribution of acetic acid.

	Amine EthA-11 loss (%)
Water	~10%
S1 (nitric acid)	18%*
S2 (acetic acid)	22 ± 2%
S3 (water + REEs)	66%
S4 (nitric acid + REEs)	all
S5 (acetic acid + REEs)	38 ± 2%

*slightly underestimated due to a manipulation error.

Visually, the phase separation between PL-sHSPs-EthA-11 and water was well defined, as discussed in Chapter III, Section 3.1. Despite this observation, TOC analysis allowed to determine that about 10% of the amine was already solubilized in water. Furthermore, the same experiment conducted in nitric acid (10^{-2} M, solution **S1**) almost doubled this instability, with *c.a.* 18% of EthA-11 present in aqueous solution. Finally, adding a mixture of REEs (solution **S4**) led to a total dissolution of the amine in the aqueous phase. Tests with acetic acid (0.5 M, solution **S2**) destabilized the PL in the same way, with about 22% loss of EthA-11. However, adding the metals in this medium (solution **S5**) only solubilized 38% of the amine, that is curiously even less than with the mixture of REEs in pure water (66%, solution **S3**).

In the end, even though the PL stability does not affect its potential for extraction, it appeared obvious that an ionic system was not the best system for an application in LLE, because it would induce difficulties for recycling the PL. Other stability tests were therefore conducted with PL-sHSPs-PPG-2000-fluid, containing a neutral hydrophobic polymer, the polypropylene glycol.

5.2. Hydrophobic neutral porous liquid: PL-sHSPs-PPG-2000-fluid

A scheme showing the chemical nature of PL-sHSPs-PPG-2000-fluid is presented in the bookmark No.5. In the absence of ionic interactions and with no amphiphilic behavior of the organic part, it was expected that the stability toward acid and metals would be improved with respect to PL-sHSPs-EthA-11. For the contact tests, 40 mg of the sample PL-a-fluid (see Chapter II) was contacted with either 1 mL of water, or solutions **S1**, or **S4** (see **Table 17**). The aqueous phases were analyzed by TOC, and the dissolution of PPG in the aqueous phase determined using Equation (1) (replacing EthA by PPG).

Table 19. Amount of PPG lost in the aqueous phase, after contacting PL-sHSP-PPG-2000-fluid for 24 h with different solutions, as determined by TOC analysis.

	% of PPG in the aqueous phase
Water	6%
S1 (nitric acid)	25%
S4 (nitric acid + REEs)	19%

From the results in **Table 19**, one can conclude that this PL was more stable in water than PL-sHSPs-EthA-11, with hardly 6% of PPG₂₀₀₀ transferring to the aqueous phase. Surprisingly, nitric acid had a strong destabilizing effect, because 25% of PPG₂₀₀₀ was dissolved in the acidic solution. This could be explained by the high amount of ungrafted polymer in PL-sHSPs-PPG-2000-fluid, as presented in Chapter II, Section 3.2.2. In this case, the PL should be more stable after the first contact, losing less material. Further, the addition of metals had little impact on the PL stability, and they even contribute

to stabilize them. The metals may prevent from the formation of solvation shells surrounding free PPG molecules.

To complete the investigation, the organic phases were analyzed by SAXS after contact and phase separation (**Figure 86**).

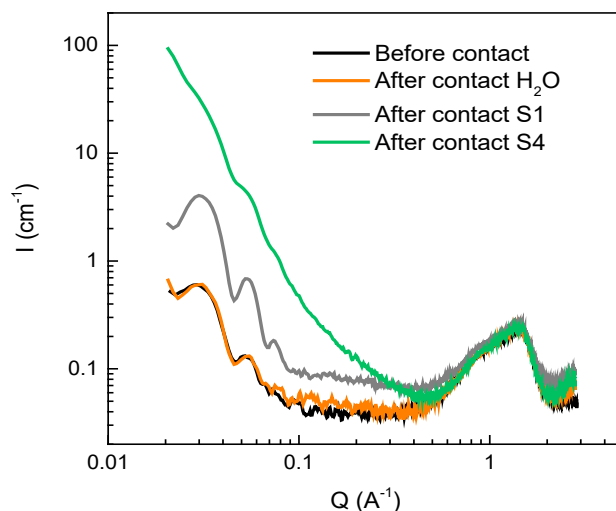


Figure 86. SAXS analyzes of PL-sHSPs-PPG-2000-fluid before and after contact with aqueous solutions and further phase separation (water, nitric acid **S1**, nitric acid + metals **S4**).

The contact with water did not alter the structural organization of the PL, as demonstrated by the perfect superposition of the signals. Even the peak of water (expected at 2\AA^{-1}) was not visible in this case, suggesting a poor water uptake. After contact with nitric acid, the intensity of oscillations increased. This may be caused by the concentration of sHSPs in the PL, due to the partial dissolution of ungrafted PPG in the aqueous phase during contact, as discussed above. Finally, after contact with metals in nitric acid, the signal is even more intense at small angles (below 0.5\AA^{-1}), and oscillations are almost invisible. This suggests a higher contrast between silica and the surroundings. For instance, the presence of iron aggregates in the PL could increase the scattering intensity and change the contrast. Indeed, such aggregates were observed when imaging sHSPs alone, after extraction (see Section 3.3.1). Iron could also be present inside the nanometric cavities: as a perspective, a fit would be necessary to confirm this hypothesis. Aggregation of iron could moreover modify the shape of sHSPs, thus leading to less defined oscillations.

These results are encouraging because they show a good structure conservation for the PL. However, they also illustrate the difficulty to deal with suspensions instead of covalent binding for hydrometallurgical applications. As a perspective, they should be completed by an investigation on the effect of successive contacts on this stability.

6. Opening: extraction of a neutral hydrophobic and functional porous liquid

Despite time was running out to perform deeper investigation with neutral PPG-based PLs, preliminary tests were carried out with the single-element optimized system (Nd in HNO₃ at pH 4.5). The three sets of functional HSPs: sHSPs-EDTA-c-2, sHSPs-EDTA-p, and bHSPs-EDTA-p, were grafted by silanized PPG₂₀₀₀ to form PLs. For each of them, the fluid phase was separated from the gel phase. Both phases were contacted with the metallic aqueous solution for 24 h at room temperature. Then, the separation was performed by centrifugation and the aqueous phase was analyzed by ICP. However, no extraction could be observed from any of the three PLs, even for the gel phases containing a high amount of HSPs (~20%).

From the result of the stability study in the previous section, it was assumed that contact with nitric acid could allow washing the PL from non-grafted PPG molecules that may hinder the chelating sites. Therefore, the functional PL based on sHSPs-EDTA-c-2 was washed four times with 1.0 mL of HNO₃ 10⁻² M. The aqueous phases were analyzed by TOC to determine the amount of PPG removed at each cleaning step (**Table 20**). Even at the fourth washing (lasting one night), carbon was still found in the aqueous phase. A small precipitate was also visible at the bottom, suggesting a destabilization of the PL: SAXS of the PL (the remaining fluid phase) after the washing also showed a significant decrease in the intensity of the oscillations, implying that some sHSPs were washed out as well.

Table 20. Amount of PPG washed out at each step of PL washing with nitric acid, as determined from TOC analysis.

	PPG ₂₀₀₀ washed out (%)
Washing #1 (1.25 h)	5.8
Washing #2 (2 h)	2.7
Washing #3 (1.2 h)	1.6
Washing #4 (17.7 h)	9.9
Total	20

Nevertheless, the PL after washing was put into contact with the Nd-containing solution at pH 4.5, and a small extraction of 3% was observed (**0.049 mmol_{Nd}/g_{PL}** corresponding to about **2.5 mmol_{Nd}/g_{SiO₂}**). Therefore, the free PPG molecules could effectively be the cause of the loss of extraction. This could be remediated by optimizing the grafting. In addition, warming the tube during the extraction test could help chain mobility and free the chelating sites from hydrogen presence (hydrogen bonding due to PPO patterns, and terminal hydroxyl groups of PPG).

Conclusion

This chapter broaches the subject of PL potentiality for LLE from the perspective of REEs recovery. Regarding silica-based PLs as hybrid organic-inorganic materials, this work focused on functionalizing only the inorganic part for REEs extraction. EDTA was selected as a functional group because it is generally reported as a good extractant for REEs and it was commercially available in the organosilicon form. In a first approach, EDTA was introduced inside the silica shells by co-condensation during the sol-gel synthesis, and TEM confirmed the right formation of hollow spheres. Then, a functional hydrophobic ionic PL was obtained based on these functional spheres and a corona-canopy system with the amine EthA-11. Extraction of neodymium, praseodymium and dysprosium was possible, implying that EDTA groups were present and accessible to the REEs. Extraction capacities of the PL were even exacerbated when compared to the functional spheres alone. However, EDTA displayed only poor selectivity between the different REEs.

To optimize extraction performances, regardless of the selectivity, further studies were conducted with single-metal solutions containing Nd and functional HSPs. In coherence with the fact that EDTA is a pH-sensitive molecule, it was found that pH had a great influence on extraction capacities, with an increase by + 68% between pH 3 and 6. If changing the functionalization method for post-grafting had no impact on extraction capacities, switching from sHSPs to bHSPs (functionalized by post-grafting) allowed increasing by up to 84% the Nd loading in the powder.

To promise PLs as relevant candidates for LLE, it was also necessary to assess their integrity after contact with the aqueous phases. Concerning the ionic PL, it was unfortunately not stable in a mixture of REEs in nitric acid, and the amine was totally solubilized in the aqueous phase. Even though the PL stability does not affect its potential for extraction, it appeared obvious that an ionic system was not the most suitable system for a virtuous application in LLE, because of a poor ability to recycling. On the other hand, the neutral PL based on PPG₂₀₀₀ was twice more stable in water than the ionic one, and only 19% was lost in the REEs solution. If these results are encouraging because they show a good structure conservation for the PL, it was also believed that losses could be reduced by optimizing the grafting yield of PPG at the surface of HSPs (instead of having partially grafted HSPs@PPG in suspension in non-grafted PPG). In fact, these experiments illustrate the difficulty to deal with suspensions instead of covalent binding for hydrometallurgical applications, and they should be completed by an investigation on the effect of successive contacts on this stability, as well as on its extraction performances and recyclability. Furthermore, this property of the acidic solution could be harnessed to wash out free PPG molecules from a functional neutral PL. This washing step was necessary to further observe neodymium extraction with this PL. Indeed, it seemed that the presence of an excess of PPG prevented the chelation of the metal to EDTA groups.

As further perspectives, it would be also interesting to study the mechanisms of extraction in a PL. Since PLs can combine adsorption and solvation (or ionic exchange) processes that are usually completely distinct, it would be worthy to conduct a deep study: would the extraction mechanisms be closer to the ones in LLE or in SLE? Would they be more complex? In addition, the substitution of EDTA by diglycolamides would probably open routes to more selective and efficient extractions, as it is already the case in the SLE field.

Moreover, it would be interesting to suppress the internal cavity by producing very porous particles with large pores to increase the surface contact. A high metal uptake could then increase the particles density, thus inducing a fast sedimentation of the loaded PL, facilitating the separation process despite the quite high viscosity of PLs. Furthermore, varying the pore sizes in the silica particles could also allow favoring the selectivity toward a specific lanthanide or another.

General conclusion and outlook

The work presented in this report aimed to evaluate the potential of silica-based porous liquids (PLs) for liquid-liquid extraction (LLE) of metals. In particular, it focused on the synthesis of new hydrophobic and functional PLs, able to extract rare earth elements such as neodymium, praseodymium and dysprosium. To reach this goal, the tunability of these hybrid materials was harnessed for controlling their porosity, their affinity toward water, and their viscosity.

This PhD work has been compiled in the manuscript, which was divided into four chapters. **In the first chapter**, PLs and their applications were introduced with the support of state-of-the-art literature. **In the second chapter**, the synthesis and characterization of a new range of PLs were developed. **The third chapter** dealt with porosity and permeability assessment of PLs, along with their tunability, so as to design the best material for LLE. An effort to increase fundamental knowledge about them, and in particular the origin of fluidity was also part of this chapter. **In the final chapter**, functionalization of PLs and an application in rare earth elements extraction was addressed.

The recent concept of PLs (born in 2007) implies that porosity can exist in the liquid state. The first publication described three types of PLs: Type I consists of liquid materials composed of discrete, molecular porous hosts whose melting point has been lowered by chemical modification. Type II involves dissolving molecular hosts in a bulky solvent that is unable to penetrate the pores. Finally, Type III PLs are a stable suspension of porous frameworks in a bulky solvent that does not penetrate the pores. In 2021, a fourth type was added, designating porous networks whose melting temperature has been lowered to make them liquid at low temperatures.

While this classification has allowed the diversification of studies, giving researchers free rein to play with the nature of the porous hosts and the way in which they are given a liquid behavior, a new classification is proposed in **Chapter I**, intended to be more faithful to the interactions at play conferring the liquid state, and making it possible to extend the concept to as yet unsynthesized materials. Thus, Class A PLs refer to porous hosts (molecular, supramolecular, or solid particles) whose melting point is lowered by chemical modification. Class B contains dispersions or suspensions of porous hosts in a solvent that does not penetrate the pores. Class C consists of composite materials, where the porous solids are trapped in a weakly cross-linked, fluid matrix. In Class D, the porous hosts themselves are connected to form a porous network that is sufficiently disorganised to exist in a liquid state.

The definition of a PL is open to discussion, especially considering what a “pore” can be in the liquid state. In fact, the presence of porosity should not be restrained to open pores existing in the free-guest state, because pores are just holes (absence of matter) in a solid structure (molecular, supramolecular, or particles), and the pores filling with a continuous fluid phase (gas or liquid) do not suppress this intrinsic porosity. In the case of solvent (or grafted organic moieties) penetration, porosity should be considered only if it is still possible to replace them by other fluid guests.

Among the different types of PLs, the ones based on hollow silica nanoparticles (HSPs) were synthesized for the first time in 2015 by Prof. Sheng Dai and his team. Belonging to Class A, they are obtained by grafting an organic corona-canopy system around each shell, inducing steric hindrance preventing flocculation of particles. With the advantage of being solvent-free, these PLs have nanometric cavities, accessible via a network of micropores within the silica shell surrounding the cavity. Silica is also easy to functionalize, so it was decided to produce new silica-based PLs suitable for extracting metals. Their synthesis and characterization appear in **Chapter II**, while **Chapter III** states the tunability of their physico-chemical properties, as solid-to-liquid transition, viscosity, and hydrophobicity.

Hence, two types of hollow silica particles (HSPs) were firstly synthesized: small hollow silica particles (sHSPs) were spherical and 25 nm-large, with a hollow cavity of 15 nm and micropores of 1.4 nm inside the silica shell. Big hollow silica particles (bHSPs) were more heterogeneous in size and shape, with a mean diameter of 240 nm, a cavity of 200 nm and pores of 3.7 nm inside the silica shell. Then, two synthesis routes were applied to obtain PLs with these HSPs: a method based on an ionic corona-canopy system, where the corona was a sulfonate covalently linked to the surface of HSPs, and the canopy was a tertiary amine with long chains, bonded by ionic interactions to the sulfonate; and another method using a neutral hydrophobic polymer, the polypropylene glycol (PPG) that was silanized prior to be grafted onto HSPs.

In the first method, amines were made of an aliphatic chain (16-18 carbon atoms) and two PEG chains with a various number of ethylene glycol units. The shorter these chains, the more hydrophobic the PL. However, the balance between hydrophobicity and fluidity was important, because a too short amine did not bring fluidity to HSPs, and the material was solid. Hence the organic:inorganic weight ratio appeared as the most significant parameter to monitor the physical state and viscosity (when liquid) of the hybrid porous materials. This result was corroborated by the second method, because a too short PPG (725 g/mol) led to a solid, whereas a longer PPG (2,000 g/mol) allowed obtaining a PL at room temperature. Although the viscosity of PLs remained high (10^4 Pa.s for ionic PLs, 0.41 Pa.s for the neutral PL based on PPG₂₀₀₀), it was found that increasing the temperature up to only 50 °C reduced it

drastically (10^0 - 10^1 Pa.s depending on the ionic PL, 0.14 Pa.s for the neutral PL). In addition, the size and density of HSPs also played a role on PL's viscosity, because of the combination of two mechanisms: for a same organic:inorganic ratio, the lower density of bHSPs would decrease the viscosity, but their big size reduced chains mobility so that the PL's viscosity was finally higher. All these studies indicated that the physical state of a hybrid porous material could be predicted by considering:

- The size and density of the inorganic cores (a larger size induced less mobility),
- The organic:inorganic ratio (with a suitable window related to the fluidity of the pure molecule serving as a canopy, as well as to the size and density of the cores). It can be highlighted that organic:inorganic weight ratios superior to 5 seem to be a general rule to design a fluid PL,
- The temperature, which drastically decreases the viscosity of liquids.

In the second method, a 2,000 g/mol PPG could be grafted onto sHSPs, but the steric hindrance of the polymer, along with the relatively poor dispersion of sHSPs in the solvent, did not allow to incorporate all the sHSPs, while free PPG molecules remained. This led to an inhomogeneous material, displaying two or three phases (depending on the synthesis conditions) with different viscosities and densities. After small angle X-ray scattering analysis of the phases, it appeared that the densest phase contained more silica spheres, while the lightest phase underwent very slow sedimentation. If the synthesis remains to be optimized, the lightest phase was considered as sufficiently stable to select it as a candidate for LLE. Also, its high fluidity when compared to ionic systems is a real advantage for the extraction process.

Chapter III also focused on PLs' porosity and permeability assessment. While the porosity of HSPs can be easily determined by standard methods applied to porous solids, such as nitrogen sorption measurement performed at 77 K, it is harder to transfer them to the assessment of PL's porosity. On one side, measurements performed at low temperature induce a transition of organic moieties from liquid to glass, thus blocking the access to the porosity of inorganic cores. On the other side, switching from N₂ to CO₂ (or other gas) to perform the measurement at higher temperatures rises other issues owing to the interaction of CO₂ with most compounds. An alternative could be to use an intelligent gravimeter placed in a chamber able to hold high gas pressures (10-20 bar) to force the diffusion barrier. Considering an application in LLE, the permeability of PLs toward liquids (and especially aqueous phases) was more interesting to assess. In this regard, a method has been developed by using small-angle neutron scattering technique: the contrast between the PL and the polar phase reached a minimum close to zero, suggesting the total filling of the PL.

Moreover, the incorporation of ethylene diamine triacetic acid (EDTA) functional groups in the HSPs was performed via co-condensation and post-grafting (**Chapter IV**). It led to solid porous hosts able to

extract three rare earth elements: Nd (major), Pr, and Dy (minors). These functional spheres were also turned into a PL, and the extraction capacity of the latter was increased by 3 times for Nd and 10 times for Pr and Dy, with respect to the spheres alone, when considering the low silica content in the PL (15%). Iron was also introduced as a competitive metal: its aggregation and precipitation were observed, but it did not block the chelating sites, which remained free for REE extraction.

Finally, the stability of two hydrophobic PLs toward acidic solutions containing metals was studied. It appeared that ionic PLs based on corona-canopy systems were not stable in presence of nitric acid and metals, because of the amphiphilicity of the canopy: the amine was totally solubilized in the aqueous phase while the sulfonated HSPs precipitated with the extracted metals. In contrast, the neutral PL made of sHSPs and PPG was much stable, with 19% of polymer loss in the metals-containing aqueous phase.

As first perspectives, further development would be required to improve the syntheses yields. A number of ideas have already been identified. In particular, preventing the HSPs aggregation by maintaining them wet at any step of the PL's synthesis could help addressing the poor dispersion of HSPs, which was observed in every media and was pointed out as very limiting. Achievement of ultrasonic-assisted reactions according to appropriate methods would likely represent a promising strategy pathway. Lastly, performing repetitive grafting steps onto the same set of HSPs could be indeed a less elegant but certainly an efficient procedure.

For sure, other hydrophobic PLs could also be interesting for LLE. For instance, other porous materials than silica could be used (like carbon), and different organic grafting could also be considered. A straightforward alternative to the syntheses presented in this thesis could consist in making another ionic PL with enhanced hydrophobicity, thanks to a canopy made of a tertiary amine carrying one aliphatic chain and two PPG chains (called "PrA" for propoxylated amine, **Figure C1**). Indeed, the synthesis route employed herein to make PL-EthAs should be easy to adapt for such amines. A first attempt has been carried out, by grafting two PPG₇₂₅ arms onto an octadecylamin, but the corresponding PL turned out to be a solid at room temperature, which started to melt only around 70 °C. However, it was assumed that longer PPG chains should allow obtaining a liquid. Thus, even though the amine separates from the HSPs during contact with metallic solutions, the fact that it is hydrophobic should make it easier to collect after contact, thanks to its hydrophobicity, so as to make a new PL after metal stripping from precipitated HSPs.

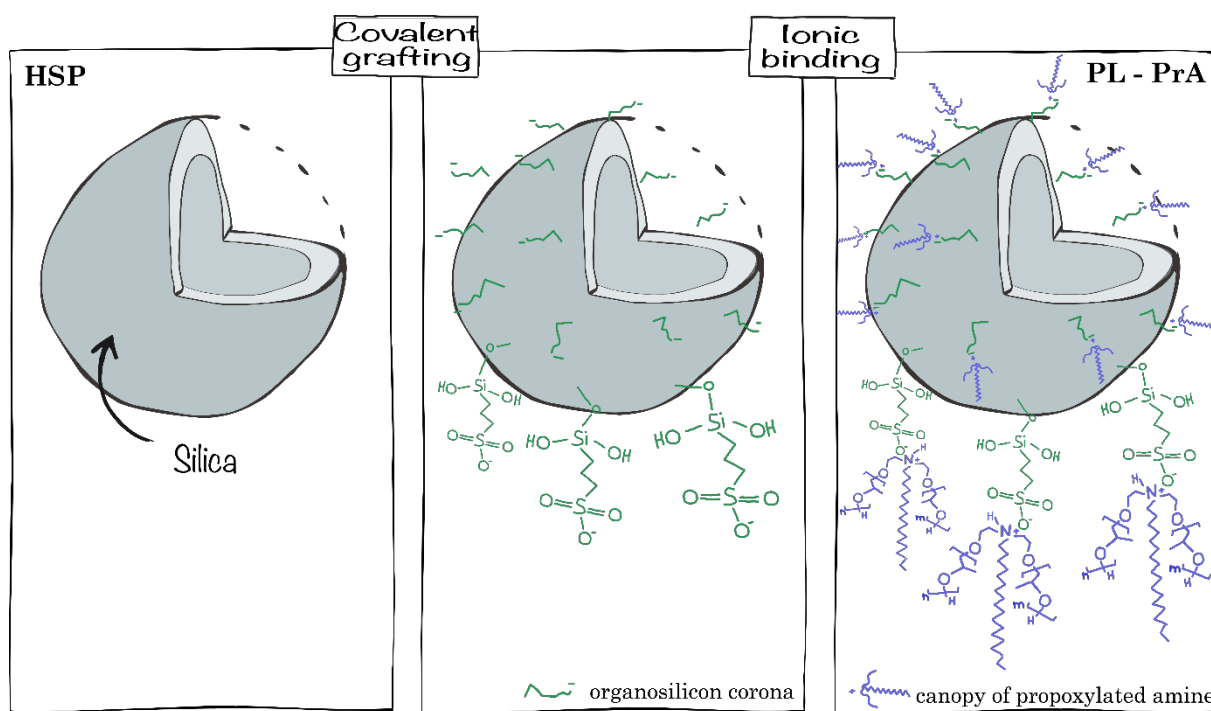


Figure C1. Synthesis of an ionic PL based on a hydrophobic canopy (PrA standing for propoxylated amine).

Nevertheless, it was presumed that a neutral PPG canopy-based PL would make a more suitable extracting phase for LLE processes. Based on considerations about the organic:inorganic ratio, grafting PPG₂₀₀₀ onto the surface of bHSPs should turn the latter into a liquid, even if the big size of bHSPs may require a longer PPG (like a 4,000 g/mol PPG) to decrease viscosity. Given that bHSPs showed superior porosity than sHSPs, with a thicker shell and larger pores, they can be functionalized with a higher amount of functional groups. Therefore, they probably make the best hosts for metals. Alternatively, silica particles of same size and pore distribution but with no internal cavity would permit an even higher specific surface. In all cases, a determination of the critical size of pore channels for metal diffusion would be useful to balance the high specific area and a good diffusion of cations. Finally, the grafting of PPG onto the surface of HSPs should be further optimized, to obtain stable and homogeneous materials, with no phase separation. To this end, another route can be considered, involving the covalent grafting of bromopropyl trimethoxysilane onto HSPs, before making them react with (previously activated) PPG. Assuming that a too strong hydrophobicity may impact the extraction process negatively, a diblock linear copolymer with a hydrophilic head (silanized) and a hydrophobic tail could be designed and synthesized, with a good organic:inorganic ratio. Such an oligomer could be directly grafted onto a porous silica particle to obtain a hydrophobic PL separating with water, while maintaining a good diffusion of metal ions along the polymeric brushes.

Because they may combine solvation and ion-exchange, PLs could show very interesting global mechanisms of extraction. Indeed, the ligands being anchored onto a solid support, it is probable that the mechanism of extraction would be – at least locally – similar to that observed in solid-liquid extraction. Besides, the substitution of SiEDTA with silanized diglycolamides (DGAs) would be interesting to enhance selectivity between different REEs: because of the solid substrate, the selectivity would be dependent on the chelating angle of the DGA molecule and the grafting density, as already reported in literature. Moreover, a very efficient extraction might involve a high increase in the density of silica particles (especially if they have no internal cavities), and this could help the phase separation during LLE process in spite of the relatively high viscosity of the PL phase.

Another possibility to avoid silica functionalization would consist in pre-impregnating a powder of particles containing very large pores in a solution of nanoparticles of the targeted metal, to create nucleus inside the cavities of particles. Turning such particles into liquid could form a very efficient PL for the extraction of the specific metal, benefitting from the presence of the internal cavity.

In this regard, the stability of PL after successive contact with water should be investigated, and its regeneration ability should also be deeply studied. Metal stripping could be performed by lowering the pH to destabilize the complexes. In addition, a comparative life cycle assessment of a PL proposed as an extracting phase in LLE would be useful to quantify the impact of such a process on environment, compared to processes already implemented.

Finally, PLs could also be used in other hydrometallurgical processes than LLE. For instance, a hydrophilic PL could be used as a selective and recyclable medium for metal leaching. Regarding metal extraction, binary aqueous systems containing an aqueous leachate and a miscible PL could undergo phase separation by addition of salts. All these prospects are promising for the future of PLs in hydrometallurgy.

Appendix A

Methods for the syntheses of hollow silica particles and porous liquids

Materials

Ludox HS40, tetramethyl orthosilicate (TMOS), (3-mercaptopropyl)trimethoxysilane (MPTMS), potassium sulfate (K_2SO_4), tetraethyl orthosilicate (TEOS), cetyltrimethylammonium bromide (CTAB), Pluronic F127, 1,3,5-trimethylbenzene (TMB), poly(propylene) glycol [PPG-725, PPG-2000 ($M_n \sim 725$ and $2,000$ g/mol respectively)], sodium hydride (NaH, 60% in mineral oil), acetone, and celite were purchased from Sigma-Aldrich. Allyl bromide (99%), aqueous ammonia (NH_4OH , 25%), dry tetrahydrofuran (THF), and activated charcoal were purchased from Fisher. Ethanol (EtOH, 96%), pure toluene, nitric acid (HNO_3 , 69.5%), and sodium hydroxide (NaOH) were purchased from Carlo Erba (Fisher). 3-(trihydroxysilyl)-1-propane sulfonic acid (SIT, 30-35%) was purchased from Gelest. Triethoxysilane (TES, 97%), silanized ethylenediaminetetraacetic acid (SiEDTA, 45%), and platinum-divinyltetramethyldisiloxane complex in vinyl terminated poly(dimethylsiloxane) (3-3.5% Pt) (Karstedt catalyst) were purchased from ABCR-Roth Sochiel, France. Ethoxylated amines (EthAs) came from three different sources: Rokamin SR5 (EthA-5), Rokamin SR11 (EthA-11), and Rokamin SR22 (EthA-22) were supplied by PCC Group, Ethox SAM50 (EthA-50) was supplied by Ethox Chemicals, and EthA-92 was synthesized according to the method reported by Atta *et al.*¹⁵⁴ The detailed procedure as well as NMR spectra of EthA-22, EthA-50 and EthA-92 are included at the end of this Appendix. Deionized water with a resistivity of 18.2 M Ω .cm and a TOC value below 5 ppb was provided by a Milli-Q direct 8 water purifier device (Merck, France).

For metals solutions: neodymium (Nd) (III) nitrate hexahydrate (99.9%) and praseodymium (Pr) (III) nitrate hexahydrate (99.9%) were purchased from Sigma-Aldrich. Dysprosium (Dy) (III) nitrate pentahydrate (99.9%) was purchased from Alfa-Aesar. Iron (Fe) (III) nitrate nonahydrate (99+%) was purchased from Acr o s Organics (Fisher).

Synthesis of sHSPs

8.33 g (0.66 mmol) of F127, 8.33 g (69.3 mmol) of TMB, and 7.25 g (41.6 mmol) of K_2SO_4 were mixed together with 500 mL of water in a 1L-round bottom flask maintained at 13.5 °C, and stirred during 4 h. Then, 20.25 g (133.0 mmol) of TMOS and 6.5 g (33.1 mmol) of MPTMS were added and the mixture was let at 13.5 °C during 24 h then aged at 100 °C under stirring during 24 h. The product was then filtered on a 5-13 μ m paper and washed three times with water. It was then calcined during 10 h at 450 °C and the solid (*c.a.* 10 g) was grinded before being used.

Synthesis of sHSPs-wash

To investigate the influence of the template removal method on the porosity, another set of sHSPs, named sHSPs-wash, was synthesized exactly as sHSPs, until the washing and filtration step. However, the template removal was performed through a soft ethanol washing (200 mL containing HCl 10^{-1} N) at reflux overnight.

Synthesis of sHSPs-EDTA-c-2

sHSPs-EDTA-c-2 was a sample corresponding to sHSPs functionalized with EDTA groups by co-condensation. The low molar ratio 1:16 of SiEDTA:TMOS silica precursors was chosen to preserve the shell integrity. Apart this modification, the synthesis was identical to sHSPs-wash.

Synthesis of sHSPs-EDTA-p

1.17 mL (0.9 mmol) of SiEDTA (45% in water) was solubilized in 20 mL of water, while 500 mg of sHSPs was dispersed in 30 mL of water and mixed at 15,000 rpm with an Ultra-turrax rotor during 5'. After one minute of sonication (30 W), the silica suspension was added dropwise to the SiEDTA solution under vigorous stirring. The pH was adjusted at pH 5-6 with HCl 1 M, then the solution was heated at 70 °C to start the hydrolysis and it was left at 70 °C during 19 h. It was then filtered on polyvinylidene difluoride (PVDF) 0.45 µm membrane filters to remove the excess of HCl and unreacted SiEDTA.

Synthesis of bHSPs

0.450 g (1.23 mmol) of CTAB were dissolved in a solution containing 52.5 mL of EtOH, 150 mL of deionized H₂O, and 3 mL (40.2 mmol) of a 25% aqueous NH₃ solution. 3 mL (13.4 mmol) of TEOS was added quickly and the suspension was let under stirring during 24 h at room temperature to make the condensation of TEOS. The product was washed three times with EtOH by centrifugation, before being incubated in 1.2 L of water and heated at 70 °C during 20 h to dissolve less-condensed silica in the particles' core. The bHSPs were washed again three times with EtOH. To remove the CTAB template, 360 mL of an EtOH solution containing HCl (10⁻³ N) was heated at 60 °C, and the spheres were suspended overnight in this medium. The spheres were recovered after centrifugation and they were then washed three times in EtOH prior to a further extraction performed in acidic (HCl 10⁻² N) aqueous EtOH heated at 60 °C during 3 h. The final product (*c.a.* 400 mg) was obtained after washing three times in EtOH and drying under vacuum.

Synthesis of bHSPs-EDTA-p

bHSPs-EDTA-p were functional bHSPs obtained by post-grafting of the previous sample (100 mg of powder were dispersed in 30 mL of water), using SiEDTA [500 µL (0.4 mmol) in 20 mL of water] as described for sHSPs-EDTA-p above.

Synthesis of PL-SiNPs-EthAs

2.860 g (19.0 mmol) of Ludox HS40 solution were diluted in 25 mL of deionized water (from Milli-Q). 6.4 g (10.1 mmol) of SIT solution were diluted in 25 mL of deionized water, in a 100 mL-round bottom flask. The silica suspension was added dropwise to the SIT solution under vigorous stirring. The pH was adjusted at pH 5-6 with NaOH 1 M, then the solution was heated at 70 °C to start the hydrolysis and it was left at 70 °C during 24 h. It was then dialyzed with a 6000-8000 kDa membrane to remove the excess of NaOH and unreacted SIT prior to elution through an ion-exchange column (Dowex 50W-X8) to protonate the sulfonate salts. The Total Organic Carbon (TOC) analysis of the dialysis external water baths allowed determining the amount of unreacted SIT (\approx 76%). Hence, 2.4 mmol of SIT were grafted upon 1.14 g (19.0 mmol) of silica spheres. Finally, a v:v 100 times diluted aqueous solution of EthA was prepared (the dilution was only ten times for EthA-92) and added dropwise to the solution of grafted nanospheres. The addition, which was followed by pH measurement, could be stopped just after the equivalence point. The product was dried under vacuum at 35 °C before yielding the expected material,

namely PL-SiNPs-EthA-X, where X is the global number of the ethylene oxide units in the EthA (*e.g.* PL-SiNPs-EthA-22 when using EthA-22). As an example, the overall yield of PL-SiNPs-EthA-11 was 2%, mainly due to a poor dispersion of the silica spheres in water.

Synthesis of PL-sHSPs-EthAs

2 g of sHSPs were dispersed in 325 mL of deionized water and mixed at 15,000 rpm with an Ultra-turrax rotor during 5'. After 1 min of sonication (30 W), the dispersion was added dropwise to a solution containing 14.3 g (22.6 mmol) of SIT solution and 325 mL of deionized water under vigorous stirring. The following steps (pH adjustment, dialysis, protonation of tethered sulfonate groups, and subsequent neutralization by the EthA) were performed according to similar procedures to those described for PL-SiNPs-EthAs but with two slight adaptations. First, the solution recovered after the reaction with the SIT was concentrated by evaporation under reduced pressure to 100 mL before pouring it into dialysis tubes. Second, the solution recovered after the dialysis was centrifuged at 4000 g for 10' in order to eliminate some precipitated aggregates. PL-sHSPs-EthA-11 was obtained with an overall yield of 6%.

Synthesis of PL-bHSPs-EthAs

PL-bHSPs-EthAs synthesis was achieved following a similar procedure to that described above. 300 mg of bHSPs were dispersed in 50 mL of deionized water and the resulting solution was then added dropwise to a solution containing 3 g (4.75 mmol) of SIT solution and 50 mL of deionized water under vigorous stirring. Subsequent treatments and procedures were applied using the same method as described for PL-sHSPs-EthAs. PL-bHSPs-EthA-11 was obtained in 7% overall yield.

Synthesis of PL-sHSPs-SiEDTA-EthA-11

The synthesis of PL-sHSPs-EthA-11 was modified to introduce functional groups inside the shell of sHSPs, and create PL-sHSPs-SiEDTA-EthA-11. F127 (1 g), K₂SO₄ (0.72 g), TMB (1.2 mL) were dissolved in 60 mL of deionized water and left for 4 h at 13.5 °C under stirring. Then, 2.48 g (16.0 mmol) of TMOS and 0.87 g (1.0 mmol) of SiEDTA were added to the solution. After 24 h, the temperature was set to 100 °C for another 24 h. Afterward, the mixture was filtered on 5-13 µm paper and washed three times with water to obtain a wet white gel. The material was dissolved in 50 mL of deionized water and dispersed with an Ultra-turrax rotor (5') then sonicated for 1'. A solution of SIT (3.58 g) in 50 mL of deionized water was prepared, and the suspension of silica spheres was added dropwise under vigorous stirring. The pH was adjusted to 5-6 with NaOH 1 M and the mixture was heated for 24 h at 70 °C. After 5 days of dialysis with deionized water (8 batches), the suspension was centrifuged to eliminate non-grafted spheres. The supernatant was dried and dispersed again in an EtOH/aqueous HCl mixture (pH 1). The dispersion was heated to reflux under stirring for 24 h to extract the template. After a filtration and three washing with ethanol, the solid was dried and dispersed again in water, before elution through an ion-exchange column to protonate the sulfonate salts and obtain sHSPs-EDTA@SIT. Finally, it was grafted with EthA-11 by following the previous procedure and the functionalized PL (PL-sHSPs-EDTA-EthA-11) was collected after drying under vacuum.

Synthesis of PL-sHSPs-PPG-2000

5 g of NaH (60% stabilized in mineral oil) was washed three times with pentane under argon and dissolved in 50 mL of dry THF. 10 g of dry PPG₂₀₀₀ previously dissolved in 90 mL of THF was then added

to the reactive solution under argon. The mixture was stirred overnight at room temperature to activate the polymer, then 1 mL of an allyl bromide solution (5 mmol, dilution factor 2.33) was added. After 48 h at 80 °C, the excess of NaH was quenched with 7 mL of EtOH (96%) and the salts were filtered and washed with THF. The filtrate was evaporated and the yielded polymer was dissolved again in 120 mL of ethyl acetate. The organic phase was washed with 70 mL of deionized water. After decantation (20 min), the organic phase was washed again with NaCl saturated water (70 mL) and the decantation process lasted one night. Then the organic phase was dried with sodium sulfate, dispersed again three times with dichloromethane, and the solvent was removed to obtain the dry mono-allyl functionalized PPG (PPG-allyl) in a 90% yield.

2.25 g (1.0 mmol) of PPG-allyl was diluted in 50 mL of dry THF under argon. A solution made of 230 μ L of triethoxysilane (1.2 mmol) and 50 mL of dry THF was prepared under argon, and added to the PPG-allyl solution under vigorous stirring. 34 μ L of a Karstedt catalyst (3-3.5%Pt in vinyl-terminated polydimethylsiloxane) was then injected with a syringe to start the reaction. The reaction medium was heated at 80 °C during one night, and the disappearing of the allyl group was controlled by $^1\text{H-NMR}$. After that, it was filtered onto celite and activated charcoal to remove the catalyst. Then, the solvent was removed and the dry silanized polymer (PPG-Si) was used at once, or stored under argon for few days. The yield was 88%.

Meanwhile, 510 mg of sHSPs were activated for 2 h in 200 mL of 10% nitric acid solution at 100 °C. They were then washed three times with ultra-pure water and strongly dried (80 °C during one night and under high vacuum at 130 °C for 4 h). After drying, the weight of the powder was 385 mg.

The last step consisted in grafting the silanized PPG onto sHSPs. The PPG-Si was dissolved in 100 mL of dry THF and the activated sHSPs were poured inside the flask. They were left reacting overnight at room temperature under argon. After that, the stirring was stopped and the medium was left at rest for 15 min, so that the unreacted powder could be separated from the bulk by pipetting the bulk (no centrifugation was used to avoid any loss of PL). THF was evaporated from the bulk and the PL was obtained after further drying under high vacuum at 35 °C. About 43% of the initial amount of sHSPs were present inside the final PL. Usually, two phases were obtained and they were separated after centrifugation before distinct characterization. To facilitate the collection of the PL from the round-bottom flask and transferring it into the centrifuge tube, it was dispersed in ethyl acetate and the solvent was allowed to evaporate slowly at room temperature.

Synthesis of PL-sHSPs-PPG-725

The same synthesis route was applied to obtain PL-sHSPs-PPG-725 from sHSPs and PPG₇₂₅. 4 g of PPG₇₂₅ were activated in 50 mL of dry THF with 5 g of NaH (60% in mineral oil) previously washed three times with pentane. After one night, 1.1 mL of the allyl bromide solution was added (see above) and the flask was heated at 80 °C for 24 h under argon. NaH was then quenched with 7 mL of EtOH (96%) and the solution was filtered and washed with THF before removing the solvent with a rotavapor. The polymer was dispersed again in 60 mL of ethyl acetate. The organic phase was washed with 50 mL of deionized water. After decantation (20 min), the phases were separated and the organic phase was washed again with 50 mL of NaCl saturated water. Then, the organic phase was dried with sodium sulfate (10 min stirring) before being filtrated. The solvent was removed under reduced pressure (rotavapor), and the intermediate PPG-allyl was collected.

0.544 g (0.705 mmol) of this product was dispersed again in 25 mL of dry THF under stirring. 130 μL of triethoxysilane was dissolved in 25 mL of dry THF and this solution was added dropwise to the polymer solution. After that, 17 μL of the Karstedt catalyst (3%) were added quickly. The reaction lasted 4 h at 80 $^{\circ}\text{C}$ under argon. Finally, the PPG-Si was filtered through activated charcoal to remove the catalyst before immediate use.

sHSPs were activated in nitric acid as described above. 0.293 g of dry activated sHSPs were dispersed in 50 mL of solution of PPG-Si-725 in THF. The reaction lasted overnight at room temperature and the bulk was then separated from the unreacted powder with a pipette. The bulk was dried to yield the PL-sHSPs-PPG-725 (0.49 g).

Synthesis of mPPG-sHSPs

A mixture of sHSPs and PPG₂₀₀₀ in dry THF was performed in the same proportions than for PL-sHSPs-PPG. The mixture was let under argon overnight at room temperature. There was no sediment after 15 min of rest, so the whole mixture was dried under vacuum.

Synthesis of EthA-92

The procedure was reported in ref ¹⁵⁴. A mixture of 13.5 g (50.1 mmol) of octadecylamine (ODA), 200 g (97.6 mmol) of poly(ethylene glycol) (Mn \sim 2050 g/mol, Sigma-Aldrich) (PEG-2050), 14.2 g (99.3 mmol) of 2,2-dichlorodiethyl ether (DDE), and 7.9 g (197.5 mmol) of NaOH in 270 mL of xylene was refluxed under N₂ atmosphere for 5h. After cooling to room temperature, the solvent was filtered under suction in order to remove the precipitated salt (NaCl) and the filtrate was evaporated under reduced pressure. The residual powder was washed with diethylether (to remove unreacted amine and low molecular weight by-products) and then recrystallized in ethylacetate. Crystals were collected after filtration under suction and subsequent washing with cold ethylacetate and pentane. The product was dried under vacuum for 4h to yield 165g (75%) of the expected compound as a white powder, and it was characterized by NMR and compared to commercial EthAs (**Figure A1**).

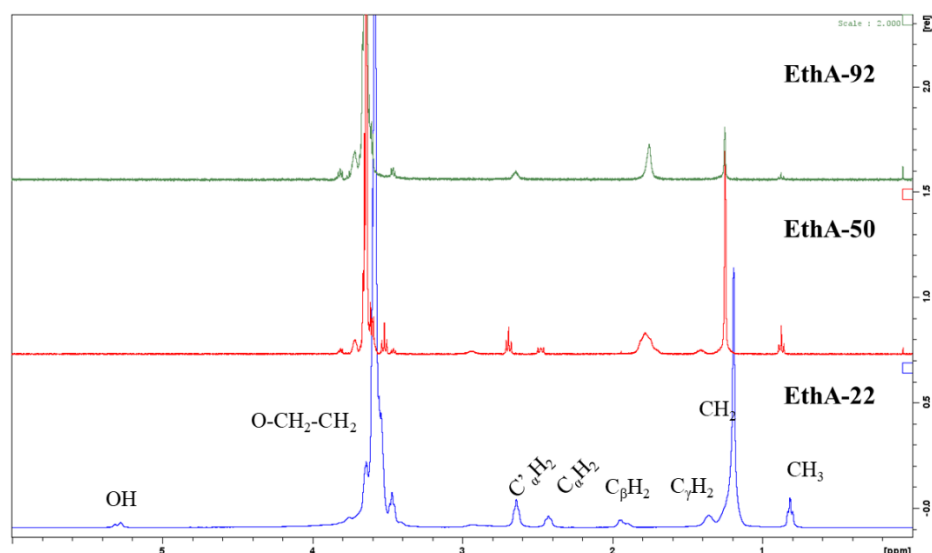


Figure A1. Stacking of the ¹H NMR spectra of EthA-22 (blue), EthA-50 (red) and EthA-92 (green). Similar spectra can be observed, be it for commercial or synthesized amines. Reproduced from ref ⁵⁹.

Appendix B
Techniques for Characterization of Materials

Appendix B

Techniques for Characterization of Materials

	Full name / device location	Device	Device calibration	Sample preparation	Measurement method	Software & data treatment
¹H-NMR	Nuclear magnetic resonance / ICSM, Marcoule, France	Brüker Advance 400 MHz		Dissolution in CDCl ₃	8 scans, d1 30 s	TopSpin
Densimeter	ENS de Lyon, France	Anton Paar DSA 5000	Air, water at 25 °C	2 mL syringe with no bubbles	20-80 °C	
DSC	Differential scanning calorimetry / ICGM, Montpellier, France	Mettler Toledo DSC1	Empty pan	~10-20 mg in capped 40 µL aluminum crucibles	N ₂ , cooling -100 °C at 5 °C/min, isotherm 5 min, heating to 150 °C at 4 °C/min	Melting temperature taken at the melting peak maximum
Elemental analysis	ICGM, Montpellier, France	varioMICRO CHNS V4.0.2, Elementar Analysensysteme GmbH		2 mg		
FTIR	Fourier-Transformed Infrared / ICSM, Marcoule, France	PerkinElmer Spectrum 100		Solid or liquid, homogeneously dispersed on the beam path	ATR mode; 615-4,000 cm ⁻¹ ; resolution 4 cm ⁻¹ ; 4 scans.	PerkinElmer Spectrum V 10.4.3
MS	Mass spectrometry / PAC Chimie Balard, Montpellier, France	Synapt G2-S (Waters)		Dilution in dichloromethane, filtration PTFE 0.2 µm	ESI mode; 0 – 8,000 m/z	
N₂ sorption	ICSM, Marcoule, France	Micromeritics TriStar II 3020, outgassing: Micromeritics VacProp 061		Outgassing 80 °C, 48 h minimum	77 K, P/P ₀ 0.001 – 0.99	BET/t-method/BJH/NLDFT
pH-meter	ICSM, Marcoule, France	781 pH/Ion Meter Metrohm	Standards at pH 4.01, 7.00, 10.00		Equilibration under stirring	
Rheology	ICSM, Marcoule, France	RM200 CP-4000 cone-plate rheometer (Lamy Rheology),	Gap 50 µm, temperature	>5 min equilibration after loading the sample	1-10 s ⁻¹ up and down twice then 5-50 s ⁻¹ by	Bingham fitting, Rheomatic-P V2.1.0.4

Appendix B
Techniques for Characterization of Materials

		MK-CP2020 cone (angle 2°, diameter 20 mm), Peltier plate (15-60 °C)	equilibration 20-30 min		increment, T°: 15, 20, 25, 30 40, 50, 57 °C	
SANS	Small-angle neutron Scattering / Institut Laue-Langevin (ILL) Grenoble, D11 beamline	Monochromatic beam (relative FWHM 10%), 3He detectors. Configurations: wavelength of 4.6 Å and sample-to-detector distance of 1.7 and 16.5 m (Q-range 0.002-0.4 Å ⁻¹)	1 mm H ₂ O	Quartz cuvettes type 120-QS of 1 mm pathway (Hellma, Müllheim, Germany)	10 min-4 h depending on the Q range and on the sample	Grasp 9.25b for data reduction* SasView 5.0.4 for modeling
SAXS	Small-angle X-Ray Scattering / ICSM, Marcoule, France	Home-made, bench by Xenocs, X-Ray source: molybdenum anode (0.71 Å), MAR Research 345 detector (770 mm from the sample)	Polyethylene standard	2mm-thick capillaries (Kapton adhesive tape for PL-bHSPs-11 that was too viscous)	1800 s (600 s for sHSPs)	PySAXS 3.26 for data treatment (by Olivier Taché, CEA Paris-Saclay), SasView 5.0.4 for modeling
USAXS	Ultra-small angle X-Ray Scattering / SWACS-Lab Platform (CEA, Saclay, France)	Home-made, X-ray source: 8 keV, beam of 0.8x0.8 mm and flux of 108 photons.s ⁻¹ , detector: Dectri Pilatus 200K (114 cm from the sample)	tetradecanol	Capillaries and tape, depending on the samples	3-6 h depending on the sample	PySAXS 3.26 for data treatment, SasView 5.0.4 for modeling
TEM	Transmission Electron Microscopy / Microscopy Platform, Montpellier, France	JEOL 1400+ 100 kV, sCMOS JEOL Matataki Flash camera, LaB6 filament		Solid were dispersed in EtOH and deposited on a carbon-coated grid (Holey type), liquids were directly deposited		ImageJ for statistical size distribution (>200 spheres, except for sHSPs-2: 103)
TGA	Thermogravimetric analysis / ICSM, Marcoule, France	Mettler Toledo	Empty pan	~10-20 mg in 70 µL alumina's crucibles	Air, 5 °C/min, 25-1000 °C	STARe Software V13.00
TGA/DTA	Thermogravimetric analysis/Differential thermal analysis / ICSM, Marcoule, France	Setaram	Empty pan	~10-20 mg in 100 µL alumina's crucibles	Air, 5 °C/min, 25-1000 °C	Calisso
TOC	Total Organic Carbon / ICSM, Marcoule, France	Shimadzu TOC-VCSH	Potassium phthalate standard	Dilution d10	Total organic carbon	

* Dewhurst, C. D. Graphical Reduction and Analysis Small-Angle Neutron Scattering Program: GRASP. *J. Appl. Crystallogr.* **2023**, *56* (5), 1595–1609. <https://doi.org/10.1107/S1600576723007379>.

Correction from water (or solvent) content in TGA

From a given TGA curve, with a H₂O (or solvent) content of α_{H_2O} , the corrected silica content $\alpha_{SiO_2}^{corr}$ in the corresponding material can be deduced from the equation (1):

$$\alpha_{SiO_2}^{corr} = \frac{\alpha_{SiO_2}^{uncorr}}{1 - \alpha_{H_2O}} \quad (1)$$

Then, for each temperature, the new weight ratio y^{corr} can be deduced from the uncorrected y^{uncorr} one thanks to equation (2):

$$y^{corr} = \left[1 - (1 - y^{uncorr} - \alpha_{H_2O}) \times \frac{\alpha_{SiO_2}^{corr}}{\alpha_{SiO_2}^{uncorr}} \right] \quad (2)$$

Where y^{uncorr} and y^{corr} are the weight ratios of the initial curve and the corrected curve at any temperature, respectively. α_{H_2O} is the water content, $\alpha_{SiO_2}^{uncorr}$ and $\alpha_{SiO_2}^{corr}$ are the silica weight ratios of the initial curve and the corrected curve, respectively.

To obtain the corrected TGA curve, y^{corr} is calculated at each temperature, and multiplied by 100.

Concentration of amine in water from TOC

The ratio of amine solubilized in the aqueous phase was calculated from the concentration of carbon according to Equation (3):

$$\frac{(m_{EthA})_{aq}^f}{(m_{EthA})_{PL}^i} = \left[\frac{m_C^f}{MW_C} \times \frac{MW_{EthA}}{N_C^{EthA}} \right] \quad (3)$$

Where $(m_{EthA})_{aq}^f$ and $(m_{EthA})_{PL}^i$ are the masses of EthA-11 in the aqueous phase after contact, and in the PL before contact (from TGA), respectively; m_C^f is the mass of carbon in the aqueous phase after contact, as deduced from TOC, MW_C and MW_{EthA} are the molecular weights of carbon and EthA-11 (12.02 g/mol and 725 g/mol, respectively), and N_C^{EthA} is the number of carbon in EthA-11 (38, considering a mean aliphatic chain of 16 carbons).

Appendix C

Small Angle X-Ray Scattering (SAXS) and Small Angle Neutrons Scattering (SANS)

Small Angle X-Ray Scattering

Principle

SAXS is a technique used to obtain structural information about nano-objects between 1 and 100 nm. It is based on matter-light interaction: the X-ray emission wavelengths lie in the range 10^{-8} - 10^{-12} m so the photons directly interact with electron clouds of atoms.

For laboratory apparatus, a monochromatic X-ray source (generally copper or molybdenum) generates a beam (wave vector \vec{k}_0) that crosses the sample (**Figure A2**). The intensity is collected by a detector as a function of the scattering angle 2θ . This angle depends on the electronic density of the atoms in the sample.

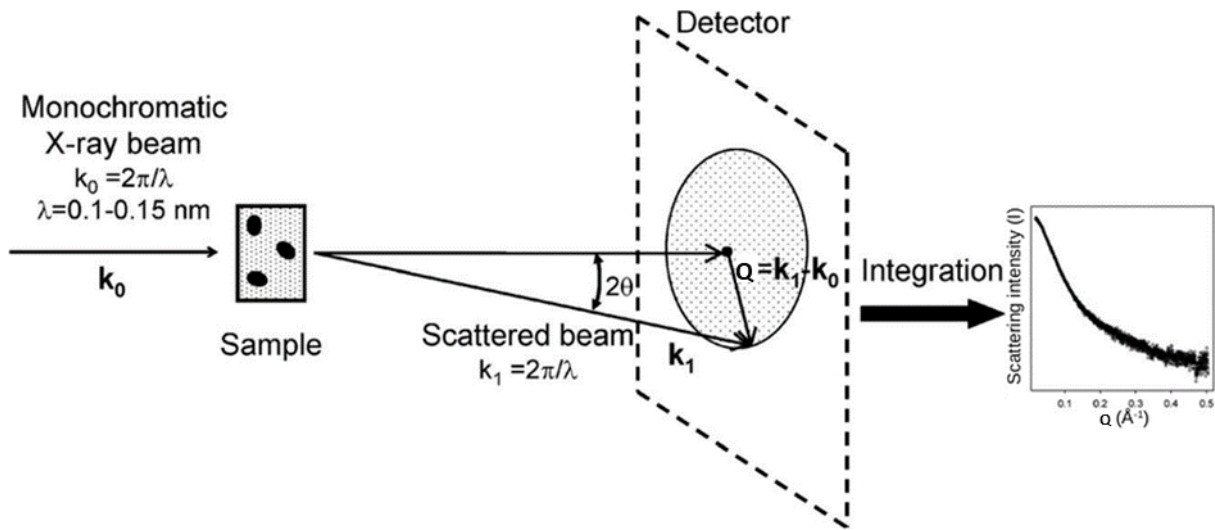


Figure A2. Principle of SAXS measurements. Adapted from Reference ¹⁵⁵.

Interactions between photons and electrons are elastic, so the scattered wave vector \vec{k}_1 has the same modulus as the incident wave vector:

$$|\vec{k}_0| = |\vec{k}_1| = \frac{2\pi}{\lambda} \quad (1)$$

Where λ is the incident wavelength. The scattering vector Q is defined as:

$$Q = |\vec{k}_i - \vec{k}_f| = \frac{4\pi}{\lambda} \sin(\theta) \quad (2)$$

In the simple case of monodisperse particles, the scattered intensity can be expressed as a function of the scattering vector by:

$$I(Q) = n_p P(Q) S(Q) \quad (3)$$

With $n_p = \frac{\phi_p}{V_p}$ the number of scattering particles per volume unit, ϕ_p is the volume fraction of particles, V_p is the particle volume. $P(Q)$ is the form factor, it only depends on the particle size and shape. $S(Q)$ is the structure factor, it reflects correlations between particles, like specific organization and interactions.

For monodisperse spheres, the form factor $P(Q)$ can be computed according to:

$$P(Q) = (V_p \cdot \Delta\rho \cdot 3 \frac{\sin(Qr_p) - Qr_p \cdot \cos(Qr_p)}{(Qr_p)^3})^2 \quad (4)$$

Where $\Delta\rho$ is the scattering length density contrast between a particle and its environment, and r_p is the particle radius. Note that $\lim_{Q \rightarrow 0} P(Q) = (V_p \cdot \Delta\rho)^2$.

For core-shell spheres, the form factor is the linear combination of the form factors of empty cores and solid (full) particles.

$$P(Q) = (F(Q)_{core} + F(Q)_{Full\ particle})^2 \quad (5)$$

With

$$F(Q)_{core} = V_{core} \cdot (\rho_{core} - \rho_{shell}) \cdot 3 \frac{\sin(Qr_{core}) - Qr_{core} \cdot \cos(Qr_{core})}{(Qr_{core})^3} \quad (6)$$

$$F(Q)_{Full\ particle} = V_{Full\ particle} \cdot (\rho_{shell} - \rho_{env.}) \cdot 3 \frac{\sin(Qr_{Full\ particle}) - Qr_{Full\ particle} \cdot \cos(Qr_{Full\ particle})}{(Qr_{Full\ particle})^3} \quad (7)$$

Where radii $r_{Full\ particle}$ and r_{core} , and scattering length densities ρ_{core} , ρ_{shell} , and $\rho_{env.}$ are defined in **Figure A3**:

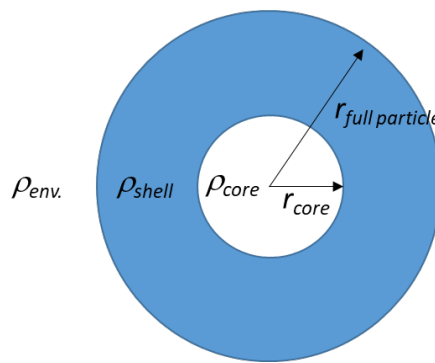


Figure A3. Parameters definition describing a hollow silica particles: radii r and scattering length densities ρ .

Analytical equations of various form and structure factors are available in literature. For a pair of monodisperse spheres, the structure factor $S(Q)$ has the expression:

$$S(Q) = 1 + \frac{\sin(2Qr_p)}{2Qr_p} \quad (8)$$

The most typical structure factor in case of solution of particles is the hard sphere structure factor. It considers that each particle cannot occupy the volume of another sphere (also named excluded volume structure factor). A sticky hard sphere structure factor is also often used to account for particles that attractively interact at short distances.

For a copper source, the wavelength λ is 1.54 Å; for a molybdenum source, the wavelength λ is 0.71 Å.

Ultra small angle X-ray scattering (USAXS) relies on the same principle but, thanks to either a longer sample-to-detector distance, or a smaller beamsize and beamstop, or to a higher wavelength, it is able to detect scattered intensity at lower angles, allowing the characterization of bigger objects like large particles or aggregates of particles.

In practice, the sample-to-detector distance was calibrated for each run by using silver behenate as a reference. All samples were loaded into 2 mm quartz capillaries.

Data treatment

Data treatment was performed using PySAXS software, developed by Olivier Taché (CEA Paris-Saclay, LIONS lab). First of all, a mask was applied to hide the direct beam and focus only on the scattering signal. After isotropic integration of the 2D signal, the absolute intensity I_{obs} is calculated from the measured intensity I_{mes} thanks to the following expression:

$$I_{mes} = \Phi_{eff} \cdot \Delta\Omega \cdot \delta \cdot T \cdot t \cdot I_{abs} \quad (9)$$

Where Φ_{eff} is the effective detector diameter, $\Delta\Omega$ is the solid angle, δ the sample thickness (cm), T the sample transmission (ratio between incident intensity and transmitted intensity), and t the time of measurement (s). The instrument factor ($\Phi_{eff} \cdot \Delta\Omega$) was corrected thanks to the lupolene standard. In practice, the correction factor $K = \Phi_{eff} \cdot \Delta\Omega$ is obtained by measuring a calibrated standard, here a polyethylene for which $I_{abs} = 6.13 \text{ cm}^{-1}$ at $Q = 3.7 \text{ \AA}^{-1}$.

The signal of an empty capillary (EC) obtained in the same conditions as the sample is also subtracted to exclude the walls contribution, according to the expression:

$$I_{abs}^{sample} = \frac{1}{\Phi_{eff} \cdot \Delta\Omega} \cdot \frac{1}{\delta} \left[\frac{I_{mes}}{T \cdot t} - \frac{I_{mes}^{EC}}{T^{EC} \cdot t^{EC}} \right] \quad (10)$$

Data analysis

The fit of signals was achieved with Sasview software (V 5.0.4) below 1 \AA^{-1} . In Equation 3, two factors contribute to the signal: the form factor $P(Q)$ and the structure factor $S(Q)$.

Form factor

When fitting sHSPs and PLs signals, the form factor of core-shell particles was the most suitable. The core-shell form factor $P(Q)$ of a hollow particle with an external diameter of 37.3 nm and an internal diameter of 19.4 nm is represented in **Figure A4**. For this figure, the scattering length density of porous silica was set to $8 \cdot 10^{-6} / \text{\AA}^2$.

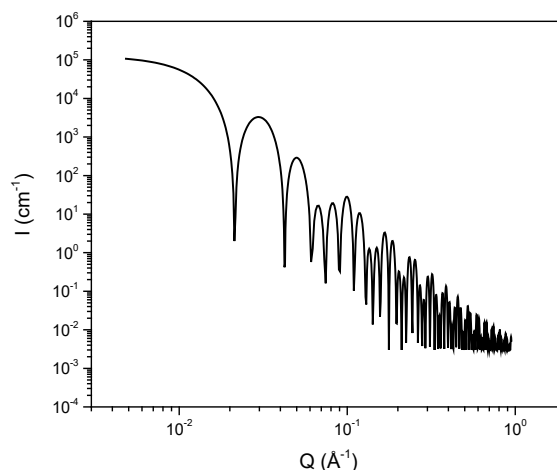


Figure A4. Form factor $P(Q)$ of a hollow silica particle contributing to the total SAXS signal.

Structure factor

Regarding the structure factor $S(Q)$, it depends on the presence of the aggregation of particles and on the structural organization of the sample. A structure peak visible at a specific Q angle reveals a correlation distance of $\frac{2\pi}{Q}$, caused by a repetitive pattern. For instance in **Figure A5** presenting the SAXS signal of an ionic porous liquid, a structure peak at 0.16 \AA^{-1} is visible. Note that in diluted medium, structure peaks can be quenched to see only the form factor contribution.

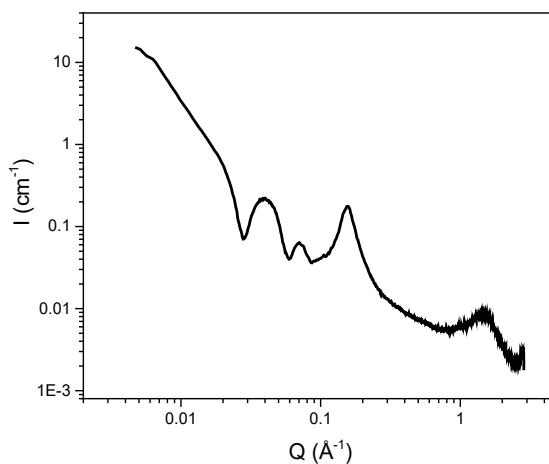


Figure A5. SAXS of PL-sHSPs-EthA-22 (see Chapter II) containing a structure peak at 0.16 \AA^{-1} .

Aggregates or stickiness may induce a characteristic slope at low angles instead of a plateau.

Peaks in the wide angle region (over 0.5 \AA^{-1}) are characteristic of the crystallinity of the different compounds. In the case of amorphous silica particles (alike sHSPs-2 presented in Chapter II), a broad peak is present at 1.64 \AA^{-1} (**Figure A6**).

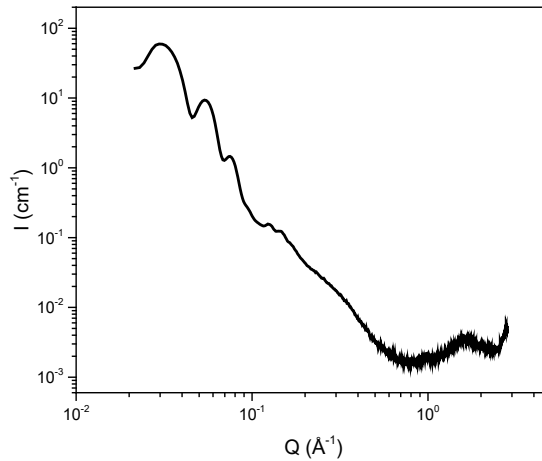


Figure A6. SAXS of sHSPs-2 (see Chapter II).

Contrast

As explained above, the scattering depends on the contrast of density between scattering objects and the continuous phase. It is expressed as the difference between scattering length densities (ρ) of two media (in cm^{-2}). For X-rays, it writes:

$$\rho = \frac{\sum_{i=1}^N Z_i \cdot r_0}{V_m} \quad (11)$$

Where V_m is the molecular volume of the medium, $(Z_i \cdot r_0)$ is the coherent scattering length of each scattering atom, with Z_i their atomic number and r_0 the Thompson scattering length ($2.82 \cdot 10^{-5} \text{ \AA}$).

The scattering length density of dense silica is typically $1.8 \cdot 10^{-5} \text{ \AA}^2$. For porous silica shells, the fit allows to deduce their real scattering length density, that is included between 0 and $1.8 \cdot 10^{-5} \text{ \AA}^2$. Hence, their volume pore content can be assessed quantitatively by this method.

Volume fraction of objects

When $Q \rightarrow 0$, $P(Q)$ and $S(Q) \rightarrow$ constants (Equations 4 and 8), so that the absolute intensity of the plateau at very small angles is proportional to the $(\Delta\rho^2 \phi_v V_P)$ factor value. Knowing the volume of objects and the contrast of density, the intensity of SAXS signal at low angles q is therefore proportional to the volume fraction of scattering objects ϕ_v . In the case of PL-sHSPs-PPG-2000 showing different phases (Chapter II), this volume fraction corresponds to sHSPs density in the polymeric matrix. Given that sHSPs are big (compared to X-ray characteristic wavelengths), the plateau was not reached at $Q = 0.02 \text{ \AA}^{-1}$. However, the evolution of the maximum intensity of the first oscillation was assumed to be representative of sHSPs density evolution (**Figure A7**).

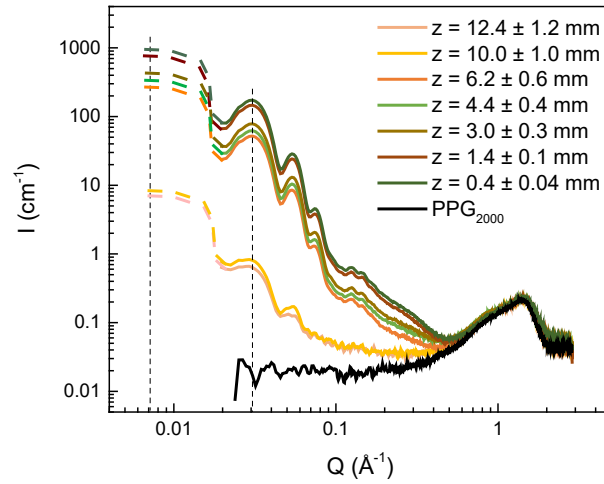


Figure A7. SAXS of PL-sHSPs-PPG-2000 at various altitudes Z along the capillary. $\Delta\rho$ is deduced from the difference of maximum intensities of the first oscillation because it is assumed to represent the difference of absolute intensities of the plateau (see dash bars).

Small Angle Neutrons Scattering

Principle

The principle of small-angle neutrons scattering (SANS) is the same, with the differences being that:

- measurements are performed on nuclear reactors,
- neutrons do not interact with electrons but with protons in the material,
- the signal scattered by the material is not governed by the same contrast.

For neutrons, the scattering length density depends on the coherent scattering length b_{cor} of the scattering atoms:

$$\rho(\text{neutrons}) = \frac{\sum_{i=1}^N b_{cor} i}{V_m} \quad (12)$$

Unlike X-rays, the coherent scattering length of neutrons is not linear with the atomic number of the elements and can vary significantly between closely related elements. The large difference in b_{cor} between hydrogen and deuterium ($b_{cor}(\text{H}) = 3.74 \cdot 10^{-15} \text{ m}$ and $b_{cor}(\text{D}) = 6.67 \cdot 10^{-15} \text{ m}$) is often exploited to vary the contrast of a solution.

The SANS data presented in this thesis were measured on the D11 beamline at the Institut Laue-Langevin (ILL) in Grenoble in collaboration with Sylvain Prévost. The D11 beamline allows access to wave vectors Q ranging from 0.003 to 1 \AA^{-1} . To access a wide range of angles, measurements are taken at several sample-to-detector distances. Samples were measured in 2 mm quartz cells.

Assessing the permeability of porous liquids to liquids

Principle of contrast variation analysis

The objective of this work was to use the cavities of the porous liquid (PL) to extract metals in solution. Therefore, it was necessary to assess whether aqueous solutions carrying metal cations can diffuse into the silica shells and their internal cavities. To this end, the study presented in Chapter III, Section 1.2.2 consisted in measuring the SANS signal of a PL in the presence of partially hydrogenated and deuterated solutions. By varying the contrast $\Delta\rho$ of these solutions, this method allows the evaluation of the material's permeability to the tested solution by collapsing the SANS signal when the hydrogen/deuterium solution has a scattering length density equal to that of the material. For this purpose, H₂O/D₂O mixtures with different ratios were prepared.

The scattering length density (SLD) of silica for neutrons is $\rho_{\text{SiO}_2} = 3.68 \times 10^{10} \text{ cm}^{-2}$. Given that the SLD of hydrogenated water is $\rho_{\text{H}_2\text{O}} = -0.56 \times 10^{10} \text{ cm}^{-2}$ and that of deuterated water is $\rho_{\text{D}_2\text{O}} = 6.39 \times 10^{10} \text{ cm}^{-2}$, an estimation of the proportions of the H₂O/D₂O mixture needed to extinguish the signal from the silica can be obtained using the following equation:

$$x \cdot \rho_{\text{H}_2\text{O}} + y \cdot \rho_{\text{D}_2\text{O}} = \rho_{\text{SiO}_2} \quad (13)$$

With x and y being the proportions of each component. For dense silica with a mass density of 2.33 g/cm³, the values expected to extinguish the signal are therefore:

$$x = 0.39 \text{ et } y = 0.61$$

In order to observe the extinction of the SANS signal as a function of the H₂O/D₂O ratio, several ratios were selected around this value as well as at the extremes of each component. The samples were prepared in 2 mm thick quartz cells, in which between 150 and 300 μL of H₂O/D₂O solution were mixed with 50 to 150 mg of material.

It is important to note that neutrons are also sensitive to the incoherent scattering length b_{inc} of each element. This produces a constant signal that contains no structural information and it adds to the coherent scattering signal, thus contributing to the overall signal as background noise.

The value of the incoherent scattering length of hydrogen is very high compared to that of deuterium ($b_{\text{inc}}(\text{H}) = 25.3 \times 10^{-15} \text{ m}$ and $b_{\text{inc}}(\text{D}) = 4.00 \times 10^{-15} \text{ m}$), so neutron measurements are commonly performed by replacing hydrogenated solvents with deuterated solvents. In the present case, where the contrast between materials and the solution was varied by changing the hydrogenated/deuterated ratio, it was necessary to subtract the incoherent signal from the data containing hydrogenated water.

SANS experiment for PL permeability demonstration

To verify if the PL is permeable to liquids, SANS experiments were performed by measuring a PL sample immersed in solutions prepared with various ratios of hydrogenated and deuterated compounds. In such experiment, the filling of the porous cavities of the PL is expected to match the scattering contrast when the scattering length density of the solution equals to the one of the material. This experiment is described in part 1.2.4 of Chapter III. The residual signal was compared to calculated curves corresponding to three scenarios (**Figure A8**):

- i) the solvent penetrates only the organic part of the PL,
- ii) the solvent also penetrates the silica shell but not the internal cavity,

iii) the solvent penetrates the totality of the PL.

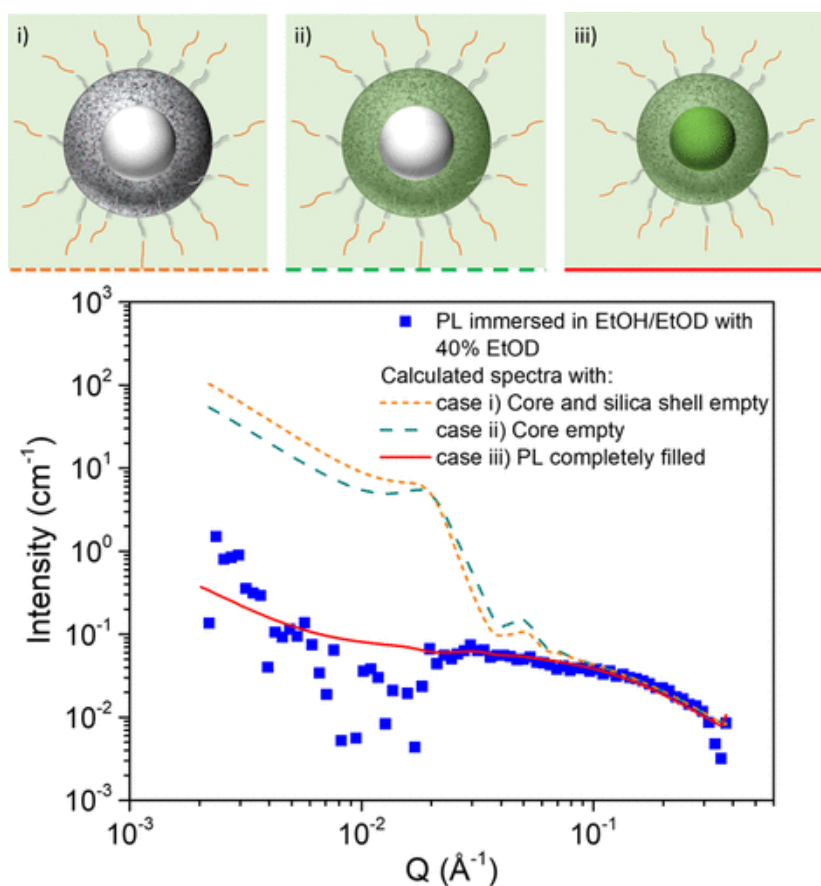


Figure A8. SANS measurement of PL permeability and calculated curves according to three scenarios: i) the solvent penetrates the organic moieties only, ii) the solvent also penetrates the silica shell, iii) the solvent penetrates the totality of the PL. Reproduced from Reference ⁶⁰.

The parameters used for this calculation of each scenario are listed in **Table A1**. A spherical core-shell form factor and a sticky hard sphere structure factor were used to model the SANS data. At higher angles, a residual signal of the organic chains in ethanol was calculated thanks to an Ornstein Zernike model.

Appendix C
Small Angle X-Ray Scattering (SAXS) and Small Angle Neutrons Scattering (SANS)

Table A1. Parameters used to calculate SANS signal of a silica-based PL (containing thiols) in presence of EtOH/EtOD solution with $x_{\text{EtOD}} = 40\%$ according to case i) the solution enters the organic shell but not the micropores of the silica spheres ii) the solution fills most of the micropores of the silica sphere but the internal cavity is not accessible iii) the PL is fully penetrated by the solution.

Sample PL with $x_{\text{EtOD}} = 40\%$	Shape Factor "Core-multishell Sphere"				
	Background (cm^{-1})	Scale 1	Core radius (\AA)	Silica Shell Thickness (\AA)	Organic Shell Thickness (\AA)
Case i), ii), iii)	0.001	0.3	115	68	40

Sample PL with $x_{\text{EtOD}} = 40\%$	Shape Factor "Core-multishell Sphere"			
	<i>sld</i> core ($10^{-6}/\text{\AA}^2$)	<i>sld</i> silica shell ($10^{-6}/\text{\AA}^2$)	<i>sld</i> organic shell ($10^{-6}/\text{\AA}^2$)	<i>sld</i> solvent ($10^{-6}/\text{\AA}^2$)
Case i)	0.1	2.06	2.17	2.23
Case ii)	0.1	2.33	2.17	2.23
Case iii)	2.23	2.33	2.17	2.23

Sample PL with $x_{\text{EtOD}} = 40\%$	Ornstein Zernike		
	Scale 2	I_0 (cm^{-1})	ξ (\AA)
Case i), ii), iii)	0.7	0.085	7

Sample PL with $x_{\text{EtOD}} = 40\%$	Polydispersity		Structure Factor « Sticky hard sphere »		
	Radius PD (\AA)	Shell PD (\AA)	Volume Fraction	Perturbation	Stickiness
Case i), ii), iii)	0.12	0.12	0.1	0	0.097

The scaling factors were fixed to the volume fraction of PL and of ethanol solution. They were estimated by considering the mass of PL of 106.3 mg immersed in 0.2mL of the ethanol solution (the

density of PL being equal to $1.05 \text{ g}\cdot\text{cm}^{-3}$). A core multi-shell form factor was considered as a contrast is expected between the organic shell and the ethanol. For $x_{\text{EtOD}} = 40\%$, it gives:

$$\begin{aligned}\rho_{\text{solv}} &= 0.4 \times \rho_{\text{EtOD}} + 0.6 \times \rho_{\text{EtOH}} = 0.4 \times 6.095 \cdot 10^{-6} + 0.6 \times (-0.344 \cdot 10^{-6}) \\ \rho_{\text{solv}} &= 2.23 \cdot 10^{-6} / \text{\AA}^2\end{aligned}\quad (14)$$

In all cases i), ii) and iii), the organic shell was considered to be filled with the ethanol solution. Its thickness was approximated to 30 \AA , leading to a $\rho_{\text{organic shell}}$ of $2.17 \cdot 10^{-6} / \text{\AA}^2$, which is consistent with 3% of organic PEG and OS and 97% of ethanol solution.

In cases ii) and iii), the shell was considered to be filled with 12% of EtOH/EtOD mixture (40%) with:

$$\rho_{\text{silica shell}} = 0.12 \times \rho_{\text{solv}} + 0.88 \times \rho_{\text{SiO}_2\text{-SH}} = 2.33 \cdot 10^{-6} \text{ \AA}^{-2}$$

In case iii) the core was considered to be filled with the ethanol solution at $x_{\text{EtOD}} = 40\%$, corresponding to a SLD of $2.23 \cdot 10^{-6} \text{ \AA}^{-2}$.

To fit the data at higher angles, an Ornstein Zernike (OZ) correlation length model was considered to simulate the density fluctuation between the ethanol solution and the organic chains of OS and PEG. The following equation was taken:

$$I_{\text{OZ}}(Q) = \frac{I_0}{1 + (Q\xi)^2}\quad (15)$$

Where I_0 and ξ are the intensity at small Q (cm^{-1}) and the correlation length (\AA).

Appendix D

Nitrogen sorption experiments

Principle

Measurement

In general, porosity of microporous or mesoporous solids (pore width < 50 nm) is quantified by the mean of nitrogen sorption isotherms at 77 K. Samples are primarily dried under high vacuum (10^{-2} mbar) and heating (about 100°C) for one or more days. Adsorption and desorption of gas are recorded at relative pressures between 0 and 1. The general shape of isotherms allows identifying porous structures of materials.

Description of isotherms

Isotherms are classified into six categories presented in **Figure A9a**, according to the International Union of Pure and Applied Chemistry (IUPAC). Some of them present hysteresis loops which can give additional information about pores distribution profiles.

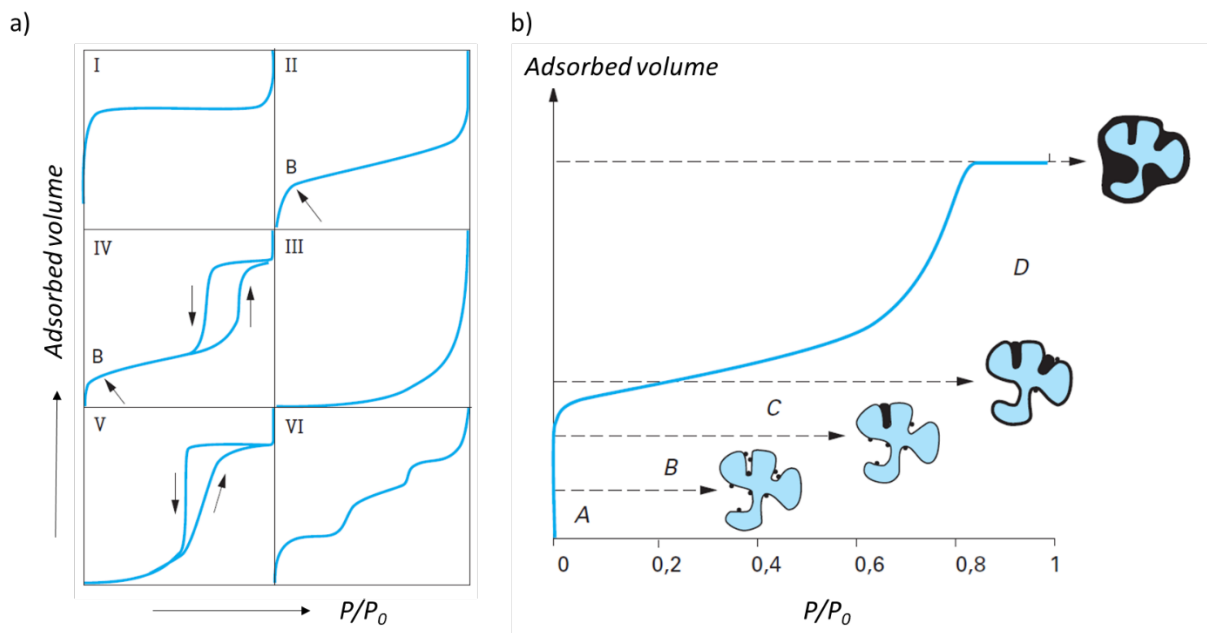


Figure A9. a) IUPAC Classification of nitrogen adsorption-desorption isotherms at 77K; **b)** Description of the adsorption branch of an isotherm (hybrid I + IV).

Most current isotherms are Type I, Type II and Type IV isotherms: Type I are characteristic of microporous materials: pores fill at low pressures (the narrower the pores, the lower the pressure) and after their saturation, a horizontal line is obtained. Type II discloses multimolecular adsorption at the surface of non-porous or macroporous objects: the layer of adsorbed gas progressively thickens.

Finally, a Type IV isotherm is obtained in the case of mesoporous materials: capillary condensation occurs, and desorption is no more reversible, so that a hysteresis loop is observed.

In most cases, complex adsorbants are associated to hybrid isotherms. For instance, a material containing both micro- and mesopores would probably show a hybrid I+IV isotherm.

In **Figure A9b**, interpretation of the adsorption branch of a hybrid I+IV isotherm is schemed: at very low pressures (point A), micropores start to fill up with gas molecules, and the volume of adsorbed gas strongly increases. At the inflexion point B, the smallest pores saturate and the microporous volume can be read directly on the isotherm. In the next domain C, monomolecular adsorption occurs: when it ends, all the solid surface is statistically covered by one layer of gas molecules. Finally, multimolecular adsorption occurs at the surface of biggest pores (point D), with a layer-by-layer filling. In this domain, above a specific pressure, the volume of adsorbed gas increases more quickly, due to the capillary condensation in mesopores. When the pressure is equal to the vapor pressure, liquefaction of gas implies the divergence of adsorbed gas quantity.

Data analysis

To obtain quantitative information about porosity of materials, different mathematical models can be applied to the isotherms. Among them, t-plot and Brunauer-Emmett-Teller (BET) theory are used to obtain values of specific pore areas. They are based on the hypothesis of layer-by-layer adsorption of gas at the surface of pores. The Barrett-Joyner-Halenda (BJH) model can also be applied to determine the distribution of mesopores inside a material. Finally, Density Functional Theory (DFT) calculations can complete the analysis with providing information about the distribution of micropores.

BET

BET theory relies on many hypotheses. The most important ones are a multilayer filling, and the adsorption energy being worth the liquefaction enthalpy from the second layer. In addition, the Langmuir hypothesis is also applied, assuming that there is only one type of independent site, with no interaction between adsorbed gas molecules. Therefore, a BET specific area can be deduced from Equation (1), at relative pressures below 0.35.

$$\frac{\frac{P}{P_0}}{n^a \left(1 - \frac{P}{P_0}\right)} = \frac{1}{n_m^a C} + \left[\frac{C-1}{n_m^a C}\right] \cdot \frac{P}{P_0} \quad (1)$$

With n^a the quantity of adsorbed gas (mol/g), $\frac{P}{P_0}$ the equilibration relative pressure, n_m^a the quantity of adsorbed gas that is necessary to cover all the surface with a monomolecular layer (mol/g), and C a constant linked to the adsorption molar energy. n_m^a and C are defined as:

$$C = \frac{a}{b} \quad \text{and} \quad n_m^a = \frac{1}{bC} \quad (2)$$

With a the slope and b the intercept of the line obtained from Equation (1).

The quantity of adsorbed gas that is necessary to cover all the surface with a monomolecular layer is linked to the surface itself by the equation:

$$A_{BET} = n_m^a \cdot \sigma_m \cdot N_A \quad (3)$$

With σ_m the area occupied by a molecule of gas (0.16257 nm² for nitrogen), and N_A the Avogadro number (6.022 · 10²³ mol⁻¹).

t-method

The t-method was proposed by de Boer to determine the surface of pores large enough to welcome a multimolecular adsorption layer (“external surface”). This area is equal to the BET specific area in the case of non-porous, mesoporous or macroporous materials. However, when micropores are present, the BET specific area is only “apparent”, because hypotheses mentioned above are no more verified.

Therefore, a significant difference between the t-area and the BET area is necessarily due to the presence of micropores.

In this method, the thickness t of a multimolecular layer is linked to number of adsorbed layers N and the thickness of a monomolecular layer e (0.354 nm for nitrogen):

$$t = Ne \quad (4)$$

For a non-porous solid taken as a reference, N can be calculated with the expression:

$$N = \frac{n^a}{n_m^a} \quad (5)$$

Where n^a is measured at each relative pressure and n_m^a is deduced from the BET equation. Hence, for nitrogen at 77K and t expressed in nm, we have:

$$t = 0.354 \frac{n^a}{n_m^a} \quad (6)$$

And the external surface $a(t)$ can be computed, by taking into account the volume of adsorbed molecules, as:

$$a(t) = 0.0346 \cdot s(t) \quad (7)$$

Where $s(t)$ is the slope of the line obtained with Equation (6).

This principle can be applied for porous materials, by plotting t as a function of n^a/n_m^a , and looking at the linear region corresponding to multimolecular adsorption.

To avoid depending on the BET equation, other analytical expressions of the thickness t as a function of P/P_0 were proposed, like the Harkins and Jura equation:

$$t = \left(\frac{0.1399}{0.034 - \log\left(\frac{P}{P_0}\right)} \right)^{0.5} \quad (8)$$

This equation allows to fit to the linear plot $n^a = f(t)$ for $P/P_0 < 0.8$. It is the one that has been employed in this work.

Interestingly, this method has not been applicable on all sets of bHSPs because the linear plot led to non-physical values. It could be due to their high heterogeneity and their complex pore architecture challenging the basic hypotheses of the method. However, data from the sets presented in this thesis could be analyzed by the t-method.

BJH

To characterize the distribution of mesopores, the BJH model taking advantage of capillary condensation inside mesopores was applied. It assumes that mesopores are all independent with a well-defined geometry, the adsorption at the surface of mesopores is similar to an adsorption onto a plane surface, and the Kelvin law giving the relationship between gas condensation pressure and curvature radius r_K of the meniscus is applicable. For nitrogen, the Kelvin law can be written:

$$r_K = -\frac{0.415}{\log\left(\frac{P}{P_0}\right)} \quad (9)$$

It is commonly admitted that the surface of the material already covered by nitrogen is perfectly wetting, so that the contact angle is null. For cylindrical pores, the pore radius r_P is linked to the Kelvin radius r_K by:

$$r_P = r_K + t \quad (10)$$

The thickness t was determined by the Harkins and Jura equation (8).

Usually, the desorption branch is more representative of interactions because the equilibrium is not completely reached during adsorption process. For most materials, it can be used for calculations. However, in the present case, the presence of internal mesoporous cavities inside sHSPs induces a very large hysteresis loop in the isotherm, completely changing the characteristic sizes determined from the BJH model. It was assumed that the adsorption branch was more representative of the internal cavity, while the desorption branch revealed the size of smaller mesopores inside the shell, connected to the cavity.

In both cases, the pore volume at the n^{th} step of adsorption or desorption can be related to the thickness of the multimolecular layer at this step (Equation 11):

$$V_{p,n} = \left(\frac{\overline{r_{p,n}}}{\overline{r_{p,n}} - t_n}\right)^2 \left[V_n^l - t_n \sum_{i=1}^{n-1} A_{p,i} \left(1 - \frac{t_n}{\overline{r_{p,i}}}\right) \right] \quad (11)$$

With $V_{p,n}$ the pore volume at the n^{th} step, $\overline{r_{p,n}}$ the mean radius of pores at the n^{th} step, t_n the thickness of the multimolecular layer at the n^{th} step, V_n^l the volume of liquid evaporated (desorption) or added (adsorption), and $A_{p,i}$ the area of pores at the i^{th} step.

DFT

Unfortunately, the distribution of micropores could not be directly measured experimentally with the device available in the laboratory. Therefore, density functional theory calculations were performed. The model used was the one generally introduced for oxide surfaces and cylindrical pores, and it was implemented directly in the software. Note that the fit was not completely satisfying because of the lack of points recorded at very low pressures, but it was sufficient to provide consistent estimations of the pore sizes.

Appendix E

Grafting Yield and Grafting Density of SIT

Grafting yield

The grafting yield of the sulfonated organosilicon SIT could be estimated from different analyses. TGA, Elemental Analysis, TOC analysis of the dialysate, and pH-metry during EthA grafting are all methods that could lead to a quantification of the SIT grafted on the sHSPs.

A comparison of these methods was performed on one single set of calcinated sHSPs.

TOC of the dialysate

First of all, the TOC amount measured in the dialysate just after the grafting indicated that 84% of the SIT introduced initially was washed during the dialysis (when counting 6 carbon in one molecule, then assuming no polycondensation at all). Hence 16% of the SIT introduced initially was successfully grafted onto the spheres. Moreover, a precipitate mass of sHSPs poorly grafted by SIT (as verified by TGA afterward) was separated from the bulk. The weight of this precipitate was about 970 ± 20 mg (the initial weight of sHSPs was 1.0008 g, including ~9% of water), but contained 84% of silica according to TGA (the rest being SIT (4%) and water (12%)). All in all, the weight of sHSPs that were well grafted ($m_{sHSPs}^{grafted}$) could be estimated to $96 \text{ mg} \pm 20 \text{ mg}$ out of the gram of sHSPs initially introduced (931 mg of dry sHSPs) (Equation 1) ; and the amount of SIT well grafted on these spheres was estimated to 3.9 mmol (Equation 2), being 4.1 mmol per 100 mg of dry sHSPs.

$$m_{sHSPs}^{grafted} = \alpha m_{sHSPs}^{ini,dry} - \beta m_{res} = 0.91 \times 1.0008 - 0.84 \times 0.97 = 0.096 \text{ g} \quad (1)$$

With m_{sHSPs}^{ini} (g) is the weight of sHSPs initially introduced for the grafting of SIT, m_{res} (g) is the weight of powder recovered after the dialysis (unwell grafted sHSPs), α and β are the proportion of dry sHSPs in these two powders according to TGA (excluding water, SIT and residual carbon).

$$n_{SIT}^{grafted} = n_{SIT}^{ini} - n_{SIT}^{res} = \gamma \times \frac{m_{SIT}^{ini}}{MW_{SIT}} - \delta \times \frac{m_{res}}{MW_{SIT}^{grafted}} \quad (2)$$

$$n_{SIT}^{grafted} = 0.16 \times \frac{5.250}{202.6} - 0.04 \times \frac{0.97}{122} = 0.0042 - 0.0003 = 0.0039 \text{ mol}$$

With n_{SIT}^{ini} (mol) and m_{SIT}^{ini} (g) the molar quantity and the weight of SIT initially introduced for the grafting, respectively, n_{SIT}^{res} (mol) the molar quantity of SIT found in the precipitate of unwell grafted sHSPs, γ the proportion of SIT grafted according to TOC analysis (0.16), δ the proportion of SIT contained in the precipitate after dialysis, MW_{SIT} (g/mol) the molecular weight of ungrafted SIT and $MW_{SIT}^{grafted}$ (g/mol) the molecular weight of the organic part of the SIT as considered by TGA (excluding the three condensed O-Si).

pH monitoring of PL-EthA-11

The pH monitoring of the addition of EthA-11 to a solution of sHSPs@SIT lead to 0.31 mmol of SIT for about 96 mg \pm 20 mg of sHSPs (estimated), being 0.33 \pm 0.07 mmol of SIT/100 mg of sHSPs. This is 12 times less than the quantity deduced from TOC.

An explanation could be that excess of SIT caused a polycondensation between the SIT molecules, thus forming large objects that could not easily pass the dialysis membrane. However, these agglomerates were retained by the ion-exchange column because of their charge.

TGA of sHSPs@SIT

TGA of sHSPs@SIT gave the mass composition of this material: 10.1% of H₂O, 25.5% of SIT and 64.4% of SiO₂. Considering that the SIT is linked by three arms to the silica network, this can be converted into 0.21 mol of SIT for 90 g of dry material (so 61 g of sHSPs) (Equations 3 and 4). Therefore, TGA gave a total grafting yield of 0.36 mmol per 100 mg of sHSPs, in good agreement with pH monitoring.

$$n_{SIT}^{grafted} = \frac{m_{SIT}^{grafted}}{MW_{SIT}^{grafted}} = \frac{25.5}{122} = 0.21 \text{ mol} \quad (3)$$

$$m_{sHSPs}^{grafted} = m_{SiO_2} - m_{SiO_2}^{SIT} = m_{SiO_2} - n_{SIT}^{grafted} \times MW_{Si} = 64.4 - 0.21 \times 28 = 60.6 \text{ g} \quad (4)$$

With $m_{SIT}^{grafted}$ (g) and m_{SiO_2} (g) the weight of SIT and inorganic SiO₂ determined by TGA for 100 g of material, respectively, and the molecular weight MW_{Si} (g/mol) of silicon.

Elemental analysis of sHSPs@SIT

Elemental analysis of sHSPs@SIT indicated a quantity of SIT of 0.31 mol per 100 g of material. Using the TGA composition above, this meant 0.31 mol of SIT for 61 g of sHSPs, *i.e.* 0.5 mmol of SIT per 100 mg of sHSPs.

As a result, a mean grafting yield is 0.4 mmol of SIT ($2.4 \cdot 10^{20}$ molecules) per 100 mg of dry sHSPs.

Grafting density

For a diameter of particle of 37.3 nm (sHSPs-2) at room temperature and humidity, the external surface S_{part} and the volume V_{part} of the sphere are $4.4 \cdot 10^3 \text{ nm}^2$ and $2.7 \cdot 10^4 \text{ nm}^3$ respectively. The density of the powder of sHSPs d_{sHSPs} (at room humidity and temperature) is about $0.5 \pm 0.06 \cdot 10^{-21} \text{ g/nm}^3$. The particle packing factor P of an unpacked powder is generally admitted to be about 0.6. Therefore, the total external area A contained in 100 mg of dry sHSPs (130 mg of sHSPs at room humidity) is about $2.1 \cdot 10^{19} \text{ nm}^2$ (Equation 5). Therefore, the grafting density would be 9.6 molecules/nm² (Equation 6).

$$A = N_{part} \times S_{part} = \frac{P \times V_{tot}}{V_{part}} \times S_{part} = \frac{P \times m_{sHSPs}}{V_{part} \times d_{sHSPs}} \times S_{part} \quad (5)$$

$$A = \frac{0.6 \times 130 \cdot 10^{-3}}{2.7 \cdot 10^4 \times 0.5 \cdot 10^{-21}} \times 4.4 \cdot 10^3 = 2.5 \cdot 10^{19} \text{ nm}^2 / 100 \text{ mg of dry powder}$$

$$\text{Grafting density} = \frac{\text{Grafting yield} \times N_A}{A} = \frac{0.4 \cdot 10^{-3} \times 6.02 \cdot 10^{23}}{2.5 \cdot 10^{19}} = 9.6 \text{ molecules/nm}^2 \quad (6)$$

Where N_{part} is the number of sHSPs contained in 100 mg of dry powder and m_{sHSPs} (g) is the mass of the powder at room humidity and temperature.

However, the maximum silanol coverage of a silica surface is admitted to be 5 per nm², even though recent studies show a maximum of 8 silanol per nm².¹¹⁰ The hypothesis of the organosilicon partially penetrating the pores is then highly probable. Another possibility would be that an excess of SIT caused a polymerization of the latter around the silica particle, thus forming a corona with much more SIT than expected. In all cases, the porosity was lost when measuring isotherms of nitrogen sorption of sHSPs@SIT.

Considering that the BET specific area of sHSPs (624 m²/g) corresponds to the surface of the micropores of the shell (necessarily overestimated because of the condensation of the gas in micropores), and that the specific area deduced from the t method (268 m²/g) includes the internal and the external surface of the sphere, one can compute the grafting density of SIT in the case that all the micropores and the external surface are grafted (but not the internal surface) (Equations 7 to 9). Calculations are made considering an external diameter of 37.3 nm and an internal diameter of 19.4 nm.

$$S_{tmethod}^{sorption} = S_{int}^{sorption} + S_{ext}^{sorption} = 268 \text{ m}^2/\text{g} \quad (7)$$

We define:

$$y = \frac{S_{int}^{sorption}}{S_{ext}^{sorption}} = \frac{S_{int}^{TEM}}{S_{ext}^{TEM}} \quad (8)$$

$$S_{int}^{TEM} = 4\pi r_{int}^2 = 4 \times 3.14 \times (19.4/2 \cdot 10^{-9})^2 = 1.18 \cdot 10^{-15} \text{ m}^2$$

$$S_{ext}^{TEM} = 4\pi r_{ext}^2 = 4 \times 3.14 \times (37.3/2 \cdot 10^{-9})^2 = 4.37 \cdot 10^{-15} \text{ m}^2$$

$$y = \frac{1.12}{4.37} = 0.27$$

So that:

$$S_{ext}^{sorption} = \frac{S_{tmethod}^{sorption}}{(1 + y)} = 211 \text{ m}^2/\text{g}$$

And:

$$S_{int}^{sorption} = S_{tmethod}^{sorption} - S_{ext}^{sorption} = 57 \text{ m}^2/\text{g}$$

Hence,

$$A_2 = S_{BET} - S_{int}^{sorption} = 624 - 57 = 567 \text{ m}^2/\text{g} = 6.24 \cdot 10^{19} \text{ nm}^2/100 \text{ mg of dry powder}$$

Finally, we have:

$$\text{Grafting density} = \frac{\text{Grafting yield} \times N_A}{A_2} = \frac{0.4 \cdot 10^{-3} \times 6.02 \cdot 10^{23}}{6.24 \cdot 10^{19}} = 3.9 \text{ molecules/nm}^2 \quad (9)$$

Appendix F

Supplementary material

TGA of sHSPs-1

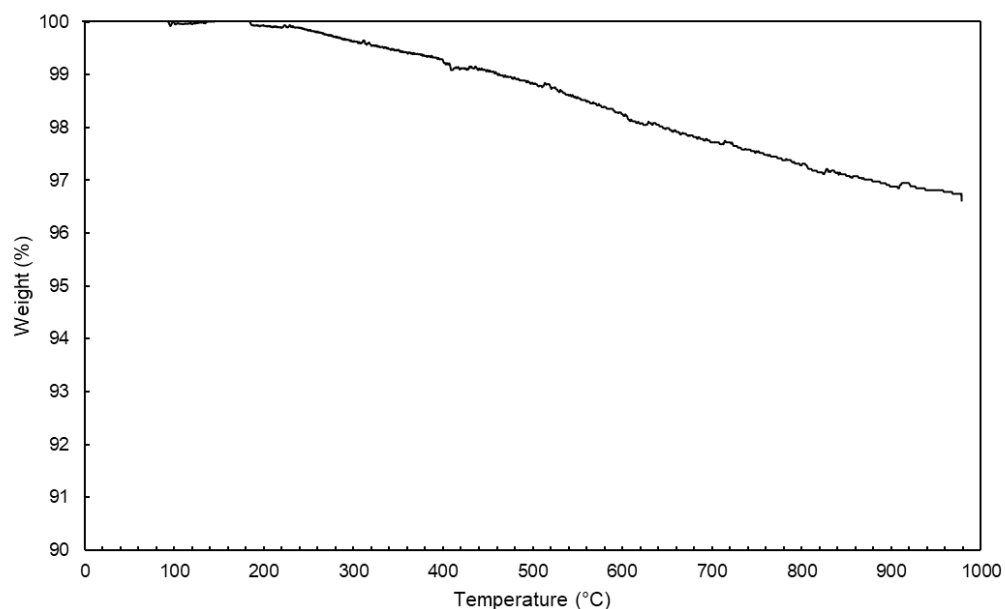


Figure A10. TGA of sHSPs-1 under air at 5 °C/min after correction from free water content. The siloxane formation (release of H₂O molecules) accounts for 3.4 % of the weight loss after water correction.

FTIR of sHSPs-2

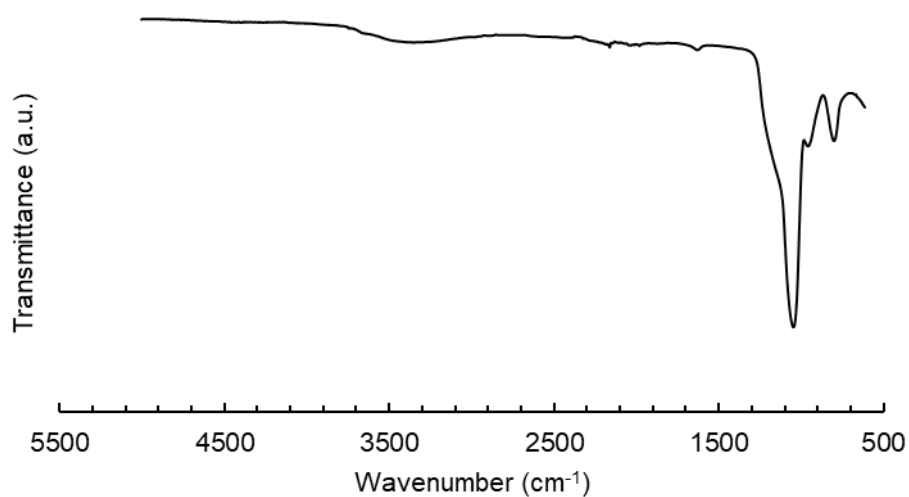


Figure A11. FTIR spectrum of sHSPs-2 in the range 5000-615 cm⁻¹. No vibration band of $\nu + \delta$ vibration of the free Si-OH bonds was seen at 4600 cm⁻¹.

Titration curve of the addition of EthA-11 to form PL-sHSPs-2-EthA-11

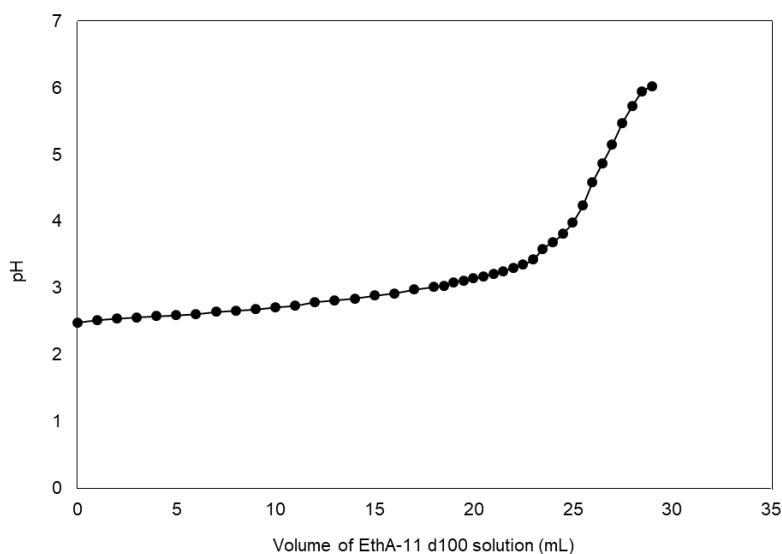


Figure A12. Titration curve of PL-sHSPs-2-EthA-11

EDTA content in sHSPs-EDTA-c and PL-sHSPs-EDTA-c-EthA-11

Based on TGA and elemental analysis, it was possible to estimate the amount of EDTA groups (weight ratio) which were present in the functional PL.

Elemental analysis of sHSPs-EDTA-c before template removal led to 210 mmol/g of EDTA in the powder stored at ambient humidity. Considering a molecular weight of 275.2 g/mol (corresponding to the organic part of SiEDTA : $C_{11}N_2O_6H_{19}$), the weight ratio of EDTA in sHSPs $\%EDTA^{sHSPs}$ is:

$$\%EDTA^{sHSPs} = n_{EDTA}^{sHSPs} \times \frac{MW_{EDTA_{org}}}{m_{sHSPs}} \times 100 = 5.8\% \quad (1)$$

Where n_{EDTA}^{sHSPs} , $MW_{EDTA_{org}}$, and m_{sHSPs} are the molar quantity of EDTA groups in sHSPs before template removal (mol), the molecular weight of the organic part of SiEDTA (275.2 g/mol), and the mass of powder (sHSPs-EDTA-c before template removal) at room humidity (g), respectively.

TGA of the same sample (**Figure A13**) indicated that 11.3% of organics were present in the powder at room humidity. From the calculation above, it can be decorelated between EDTA groups (5.8%) and template (5.5%). The inorganic content $\%SiO_2^{sHSP}$ was 84.8% and the water content was 3.9%. Here, the contribution of silanols condensation to the weight loss could not be quantified, so it was neglected.

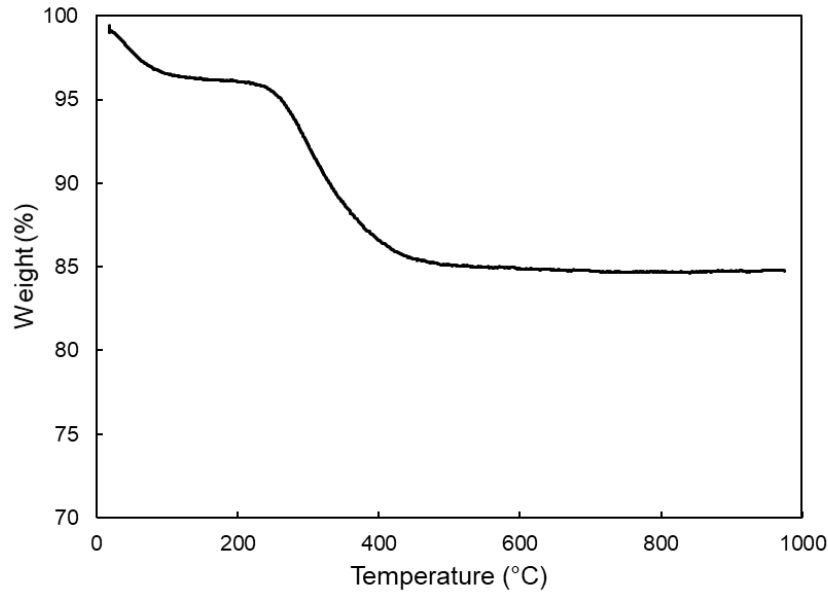


Figure A13. TGA of sHSPs-EDTA-c before SIT grafting and template removal (air, 5 °C/min).

Hence, in a powder sHSPs-EDTA-c after template removal, the amount of EDTA groups would account for:

$$[EDTA]^{sHSPs} = \frac{\%EDTA^{sHSPs}}{\%SiO_2^{sHSP} + \%EDTA^{sHSPs}} \times \frac{1}{MW_{EDTA_{org}}} = 23.3 \cdot 10^{-2} \frac{mmol}{g} \quad (2)$$

While the amount of TMOS would be:

$$[TMOS]^{sHSPs} = \% \frac{SiO_2^{sHSPs}}{\%SiO_2^{sHSP} + \%EDTA^{sHSPs}} \times \frac{1}{MW_{SiO_2}} - [EDTA]^{sHSPs} = 1.54 \cdot 10^{-2} \frac{mol}{g} \quad (3)$$

Therefore, the EDTA:TMOS ratio in the powder is:

$$\frac{[EDTA]^{sHSPs}}{[TMOS]^{sHSPs}} = \frac{0.0233}{1.54} = 0.0151$$

Initially, the molar ratio 1:16 (0.0625) was introduced for the co-condensation process, being 4 times more than what found experimentally.

After correction from water content, TGA (**Figure A13**) gives an organic content of 11.8% in the dry powder of sHSPs: by proportionality, this would mean a content of 6.1% of EDTA groups in the dry powder.

According to the TGA of PL-sHSPs-EDTA-c-EthA-11 (**Figure 78**), there is 15.2% of silica inside. By neglecting the contribution of SIT molecules to this inorganic content (because it is impossible to evaluate in this case), the weight ratio of EDTA groups in the PL $\%EDTA^{PL}$ is *in fine*:

$$\%EDTA^{PL} = \%EDTA^{dry\ sHSPs} \times \frac{\%SiO_2^{PL}}{\%SiO_2^{dry\ sHSPs}} = 1.0\% \quad (4)$$

Where $\%EDTA^{dry\ sHSPs}$, $\%SiO_2^{PL}$, and $\%SiO_2^{dry\ sHSPs}$ are the weight contents of EDTA in the dry powder of sHSPs-EDTA-c before template removal, the inorganic content in the PL, and the inorganic content in the dry powder, respectively.

This weight ratio of 1% corresponds to a concentration in EDTA groups of $36.3 \cdot 10^{-2}$ mmol/g of PL.

sHSPs-EDTA-c-2

sHSPs-EDTA-c-2 have been analysed by TEM and SAXS after template removal, before SIT grafting (**Figure A14**). The micrograph in **Figure A14a** confirms the good formation of HSPs, with rougher surface compared to nonfunctional sHSPs. A small proportion of the spheres were also partially broken. The statistical analysis of their sizes indicated a mean external diameter of 37.8 nm and a mean internal diameter of 24.2 nm. If their size is similar to sHSPs-2 (37.3 nm), their cavity seems to be larger (it was 19.4 nm for sHSPs-2). Oscillations in the SAXS spectrum (**Figure A14b**) originate from the good monodispersity of sHSPs-EDTA-c. The noise in $0.3\text{-}1\ \text{\AA}^{-1}$ is due to a problem in the calibration, but this does not affect the curve at smaller angles (much higher intensities).

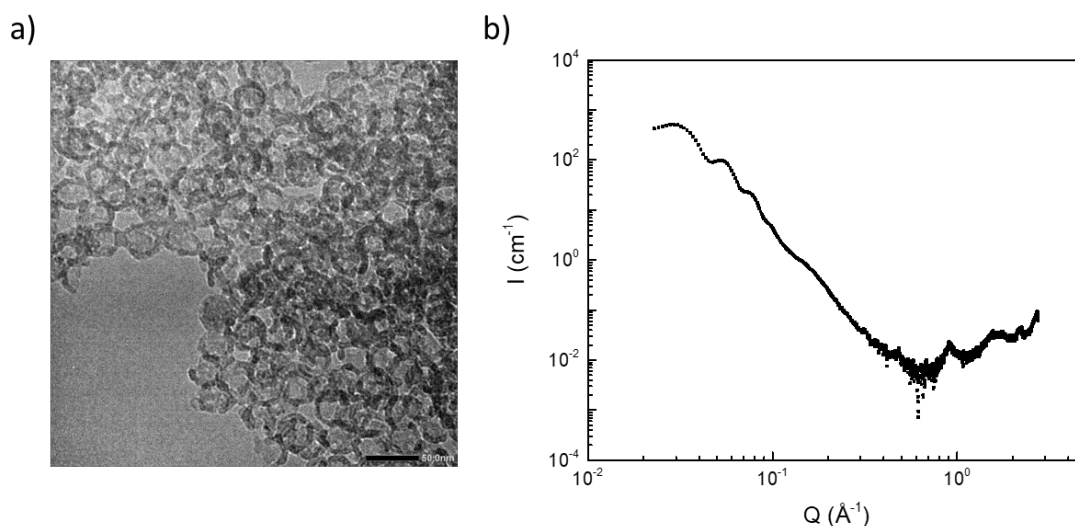


Figure A14. **a)** TEM image of sHSPs-EDTA-c-2, Scale bar: 50 nm; **b)** SAXS spectrum of sHSPs-EDTA-c-2.

Furthermore, nitrogen sorption measurements of sHSPs-EDTA-c-2 compared to the sHSPs-wash reference (see Chapter III, Section 1.1.3) washed with ethanol are shown in **Figure A15**. Interestingly, the hysteresis disappeared for the functionalized sample, which could mean two things: either the cavity was still filled with the template, because the presence of EDTA groups in the pores prevented an efficient removal, or the cavity was empty, but the access to it was blocked by EDTA groups. Given that the specific surface area was not negligible ($189\ \text{m}^2/\text{g}$), it was hard to believe that the template was still present (otherwise it would have blocked all the porosity). Plus, a finer analysis of the $0.8\text{-}0.9\ P/P_0$ zone suggested the presence of a first hysteresis before the one due to interparticles void.

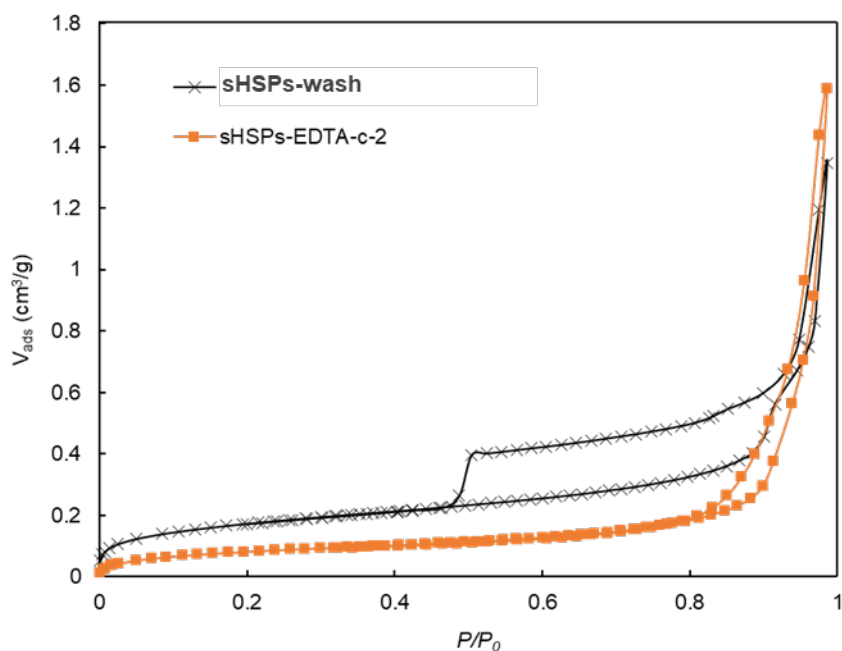


Figure A15. Nitrogen sorption isotherms of sHSPs-EDTA-c-2 and sHSPs-wash at 77K.

Therefore, the TGA of sHSPs-EDTA-c-2 before and after template removal helped confirming that the template was well removed (**Figure A16**). Indeed, after correction from water, the content in inorganic silica was 80.6% and 86.6% before and after the template removal, respectively. The earlier weight loss at 270 °C visible in the trace before template washing (with a corresponding peak in the heat flow measurement on the DTA curve) disappeared in the trace after template washing. After washing, the remaining weight loss (13.4%) was likely due to EDTA groups exclusively.

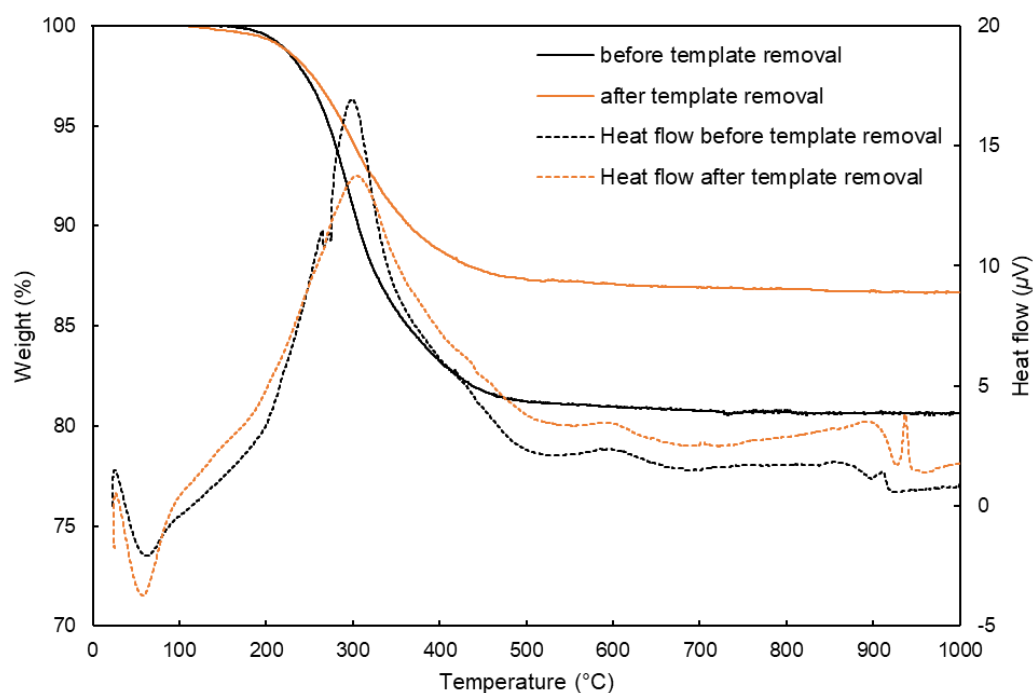


Figure A16. TGA and DTA traces of sHSPs-EDTA-c-2 before and after template removal by soft washing (under air, 5 °C/min).

Also, in the FTIR spectra, a clear diminution of the bands at 2882 and 2970 cm^{-1} accounting for CH_2/CH_3 stretching were assigned to the disappearing of the template. As explained in Chapter IV, the carbonyl group from EDTA groups did not give a strong peak in the 1700 - 1600 cm^{-1} region, because of the too strong signal of the silica network.

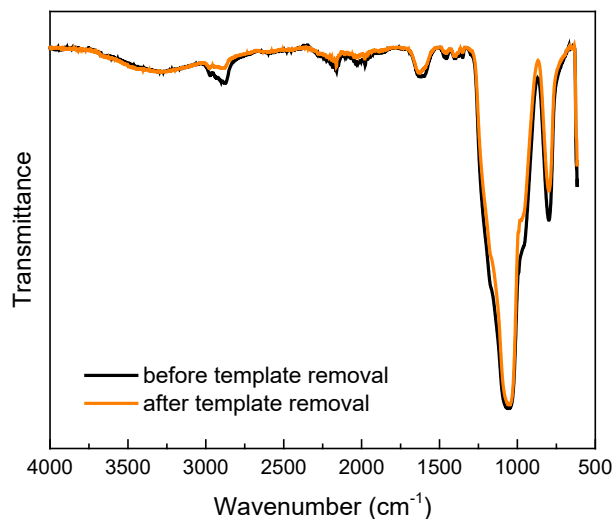


Figure A17. FTIR spectra of sHSPs-EDTA-c-2 before and after template removal.

sHSPs-EDTA-p

Silanized EDTA (SiEDTA) has also been tethered onto the surface of sHSPs-1, and the resulting powder was labelled sHSPs-SiEDTA-p. Characterization was performed using TEM, SAXS and nitrogen sorption isotherms. In **Figure A18**, the TEM images show smooth particles, as well formed as sHSPs-1. In some images as the one presented in **Figure A18b**, very small dark nanoparticles were also visible and they were attributed to excess of polycondensated EDTA forming aggregates that did not pass the filter during washing. The reason for this interpretation is that when achieving a second post-grafting onto the first one (in an attempt to increase the grafting yield), the amount of these dark nanoparticles increased (**Figure A18c**).

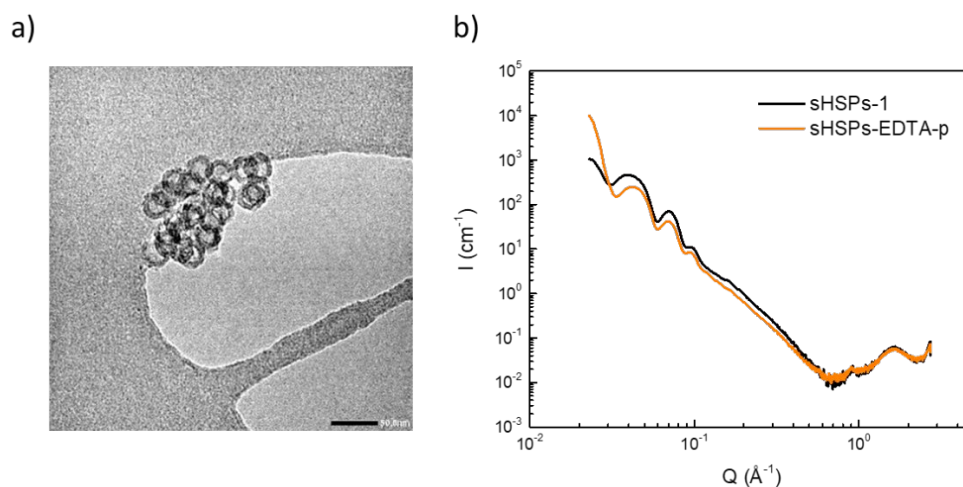


Figure A18. a) TEM image of sHSPs-EDTA-p. Scale bars 50 nm, b) SAXS of sHSPs-EDTA-p before (sHSPs-1) and after (sHSPs-EDTA-p) SiEDTA post-grafting.

From SAXS analysis in **Figure A18b** (before and after grafting), it can be deduced that the presence of EDTA did not affect the structure of the spheres (oscillations are at the same Q).

Finally, FTIR spectroscopy was carried out to check the presence of the chelatant, and in particular the carboxyl groups of EDTA (**Figure A19**). Surprisingly, the peak at 1722 cm^{-1} attributed to the C=O bond vibration was not strong as expected. As before, this might be explained by the strong signal of silica (Si-O-Si and Si-O bonds) shadowing the other vibrations, along with the overlapping with the –OH vibration.

Therefore, the TGA alone was used to confirm the good functionalization (note that elemental analysis could be interesting to do as well, but it has not been performed on this sample because of the lack of time).

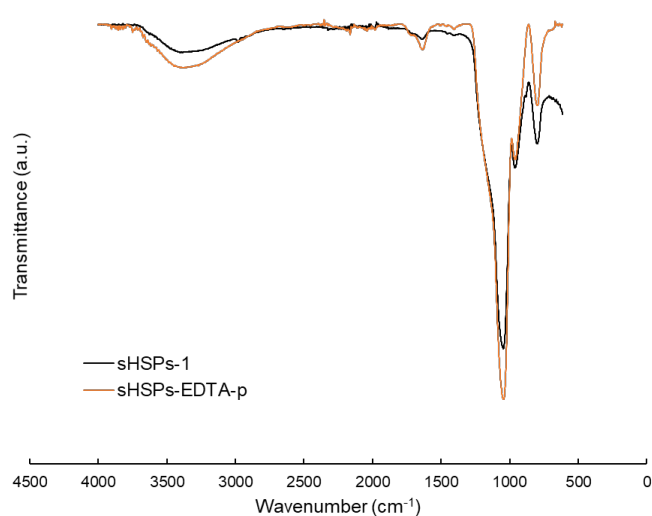


Figure A19. FTIR spectra of sHSPs-1 (before SiEDTA post-grafting) and sHSPs-SiEDTA-p (after grafting).

bHSPs-EDTA-p

TEM images of bHSPs-EDTA-p were identical to the ones of bHSPs (**Figure A20**), and the sizes were statistically distributed as before the grafting.

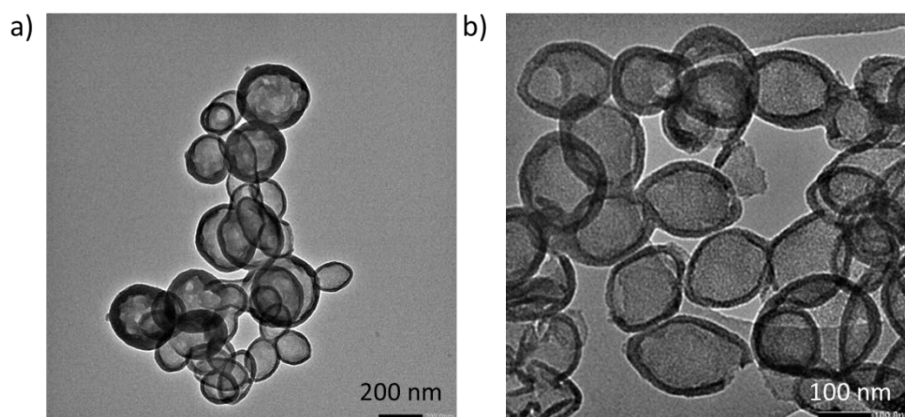


Figure A20. TEM images of **a)** bHSPs (before SiEDTA post-grafting) and **b)** bHSPs-EDTA-p (after grafting)

Similarly, the nitrogen sorption experiment in **Figure A21** led to the same type of isotherm as before the grafting, with BET specific surface area lower (749 m²/g). This was due to the diffusion of EDTA groups inside the larger pores (3.7 nm), as also demonstrated by TGA in Chapter IV (more EDTA groups were grafted by gram of materials than for sHSPs-EDTA-p). The size of the pores was reduced to 3 nm according to DFT calculations.

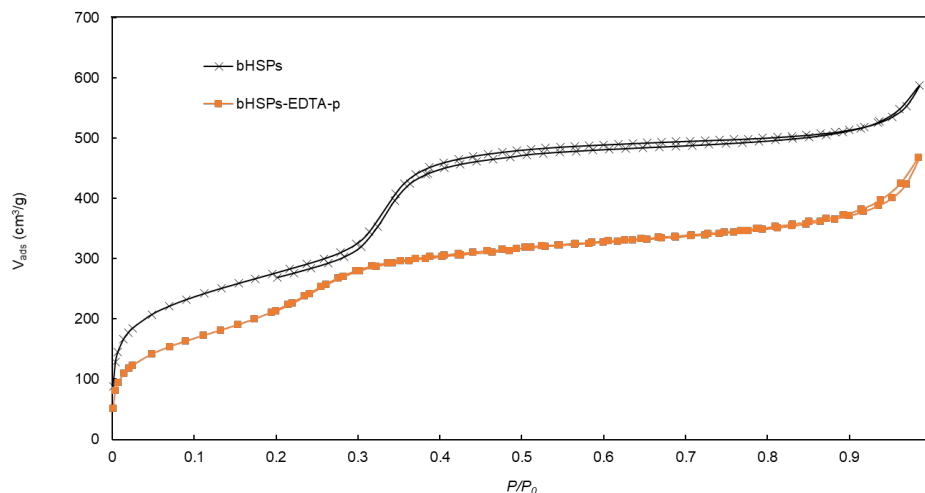


Figure A21. Nitrogen sorption isotherms of bHSPs-EDTA-p before (bHSPs) and after (bHSPs-EDTA-p) EDTA grafting.

Alike sHSPs-EDTA-p, the FTIR spectra before and after EDTA grafting (**Figure A22**) did not allow to clearly identify specific bands for the carbonyl groups, even though the band at 1630 cm⁻¹ was significantly more intense (the –OH band was also stronger, so it could be assigned to water molecules bounding to EDTA). In this particular sample, a band at 1400 cm⁻¹, that could be assigned to N-C elongation, was also visible. However, this band was already visible in all non functional HSPs samples (in a lesser extent), so the contribution of EDTA was not easy to accurately determine.

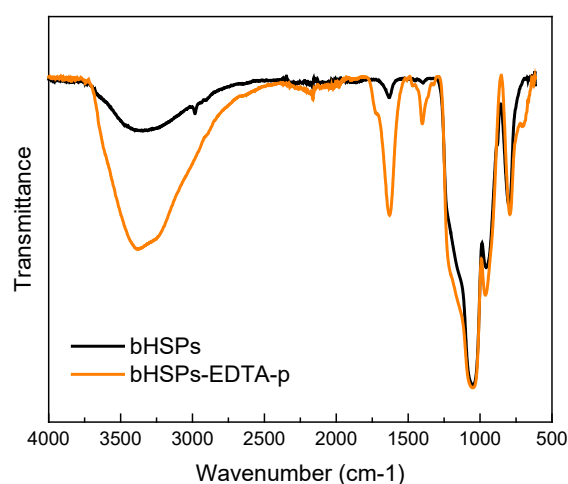


Figure A22. FTIR spectra of bHSPs-EDTA-p before (bHSP) and after (bHSPs-EDTA-p) EDTA grafting.

Appendix G

Stability and homogeneity study of PPG-based porous liquids (PL-sHSPs-PPG)

A neutral PL based on PPG was synthesized by grafting a silanized PPG₂₀₀₀ at the surface of sHSPs-2 (*cf.* bookmark No.5). As described in Chapter II, Section 3.2.1, there was a sediment of sHSPs-2 grafted with a very little amount of PPG at the end of the reaction. It was separated from the bulk, so that most part of ungrafted sHSPs was removed at this step. After drying the bulk, an oil was obtained, and it was labeled PL-sHSPs-PPG.

However, this PL appeared to be unstable overtime: depending on the synthesis conditions (see **Table A2**), it underwent a phase separation leading to three phases (like PL-a) or two phases (like PL-d). Investigation based on SAXS measurements were conducted to determine the origin and the stability of these different phases.

Table A2. Synthesis conditions tested to obtain PL-sHSPs-PPG. All the reactions were performed at room temperature. The last column mentions whether the sediment was separated from the bulk before solvent removal or not.

	$m_{\text{PPG-Si}}$	m_{sHSPs}	Dilution (PPG)	Solvent	Time (h)	Separation?
PL-a	908.6 mg	177.1 mg	40 mL + 3mL 21 g/L	Toluene:THF (13:1)	17.75	Yes
PL-b	1.0854 g	181.1 mg	18 g/L	THF	112.25	No
PL-c	304.6 mg	45.5 mg	10 g/L	THF	136.5	Yes
PL-d	2.25 g PPG-allyl	385 mg (before drying)	22 g/L	THF*	18	Yes

*THF was not perfectly dry.

The example of PL-a is given in **Figure A23**: a SAXS capillary was prepared on the day of the PL synthesis, and surprisingly after 2 days, three distinct phases were clearly visible (**Figure A23a**). The upper phase was limpid while the other two lower phases contained bubbles, as revealed by optical microscopy (**Figure A23b**). The first assumption consisted in a slow sedimentation of sHSPs inside the PL. However, the fact that the phases were distinct was not clear with this hypothesis. A first study was conducted overtime with SAXS measurements performed at different heights in the capillary when the three phases were in equilibrium, and after their separation. Then, the influence of the synthesis conditions (solvent and reaction time) on the phase separation was also studied. Finally, the stability of a control made of PPG and sHSPs (without grafting) served as a reference point.

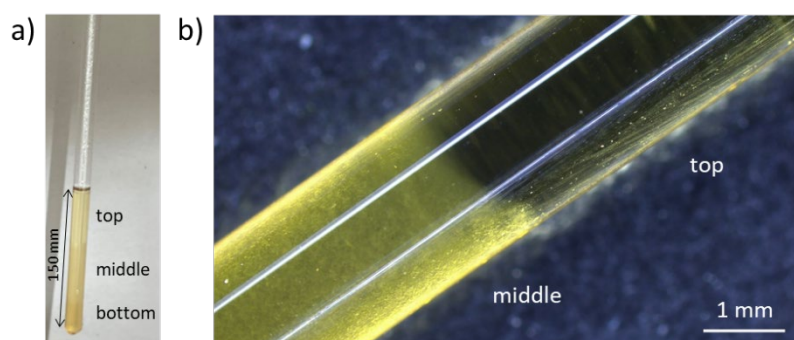


Figure A23. a) A SAXS capillary containing PL-a after three days of aging. Three phases were clearly visible. b) Interface of the two upper phases as seen with an optical microscope.

Comprehension of the natural phase separation

The **Figure A24** shows SAXS curves of the capillary containing PL-a, measured at various Z positions. As depicted in **Figure A24a**, SAXS performed on the three phases resulted in different SAXS intensities. As precisely demonstrated in Appendix C, the evolution of intensity at low angles Q along the capillary is proportional to the evolution of the volume fraction of silica nanoparticles. In the present case, the maximum intensity of the first oscillation has been plotted over the height Z in **Figure A25**: the intensity evolution with Z revealed three distinct phases. The bottom phase contained the highest amount of sHSPs, while this amount gradually decreased in the middle phase to finally reach a minimum in the top phase.

This evolution was consistent with a slight shift of the structure peak at 1.4 \AA^{-1} toward higher angles when increasing the silica content (see zoom in **Figure A24b**). Moreover, a weak increase in the intensity of the second structure peak at 0.9 \AA^{-1} in the middle phase was observed, suggesting a slight change in the organization of the polymer, but it could not be further understood with the available data.

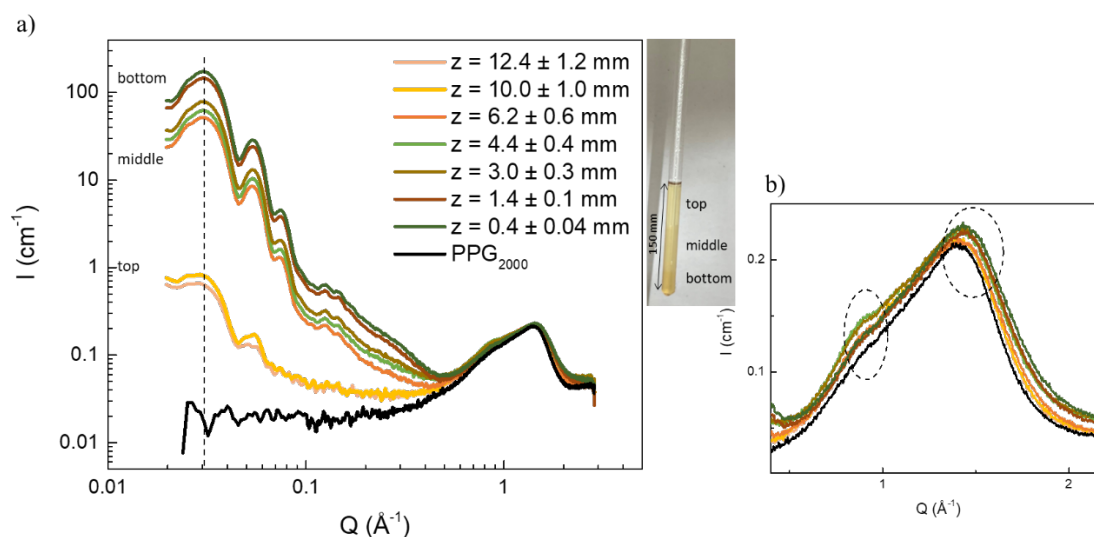


Figure A24. a) SAXS signals of PL-a after natural phase separation (measurement occurred 92 days after the capillary preparation). The maximal intensity at the first visible oscillation are representative of the sHSPs content at each altitude Z (dash line at 0.03 \AA^{-1}); b) Zoom on the structure peaks between 0.4 and 2.2 \AA^{-1} in a linear scale.

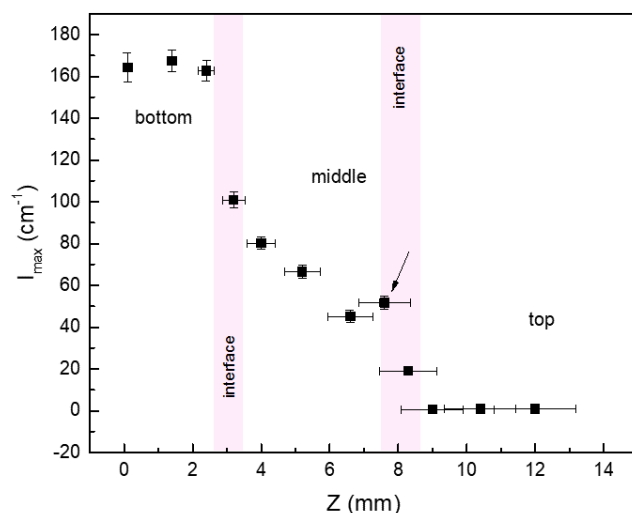


Figure A25. Maximum intensity (first oscillation at 0.03 \AA^{-1}) of the SAXS signal plotted as a function of the height Z in the capillary. The arrow highlights an unexpected increase in intensity just beneath the second interface.

The co-existence of these three phases remains unexplained, but it was also interesting to notice that a higher silica content was observed just beneath the second interface (indicated by the arrow in **Figure A25**). It can be assumed that these phases are due to a different level of surface grafting for sHSPs, as well as a different level of polycondensation between the polymeric chains, leading to immiscible materials with distinct densities.

Before using such a heterogeneous PL for LLE, it was important to assess the stability of these phases in equilibrium overtime: in 270 days, their height did not evolve. SAXS intensities at small angles were measured overtime for each phase. In **Figure A26**, the maximal intensities of the first visible oscillation at various altitudes Z were plotted over time in a linear scale. The first conclusion was to that the bottom and middle phase seemed stable overtime (**Figure A26a-b**), while the top phase underwent a significant decrease in silica content (72%) before reaching a plateau after about 25 days (**Figure A26c**). No sediment with very high silica content was visible in the bottom phase, but a thin deposit (less than 0.5 mm) would not have been measurable by SAXS. However, the phenomenon was emphasized when monitoring each phase separately after centrifugation. The top phase was very fluid whereas the bottom phase was gel-like, so after their separation, the “top” phase was labeled “PL-a-fluid” phase while the “bottom” phase was labeled “PL-a-gel” phase.

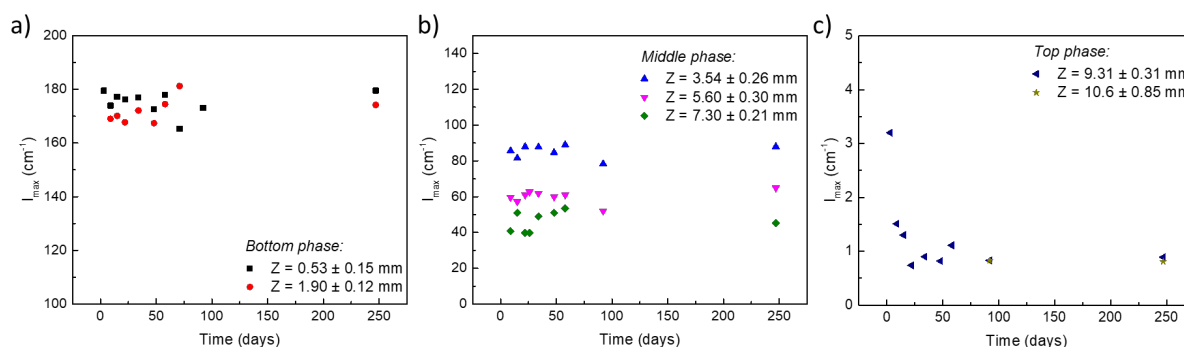


Figure A26. Stability of PL-a overtime followed by SAXS. Measurements at different altitudes Z along **a)** the bottom phase, **b)** the middle phase, **c)** the top phase.

Overtime, the fluid phase underwent a slow sedimentation (during about 30 days), with a decrease in silica content at every heights in the capillary. The sediment formation was tightly linked to the disappearing of the bubbles initially (**Figure A27a-b**) present, and it was visible to the naked eye after 10 days (**Figure A27c**).

However, the silica content seemed to be stable in the fluid phase after 30 days, even though the heterogeneity in altitude was still present (with a difference between the top and the bottom – just above the sediment – of about 66% with respect to the bottom silica content). It could be attributed to an equilibrium of sHSPs in suspension with sHSPs in the deposit.

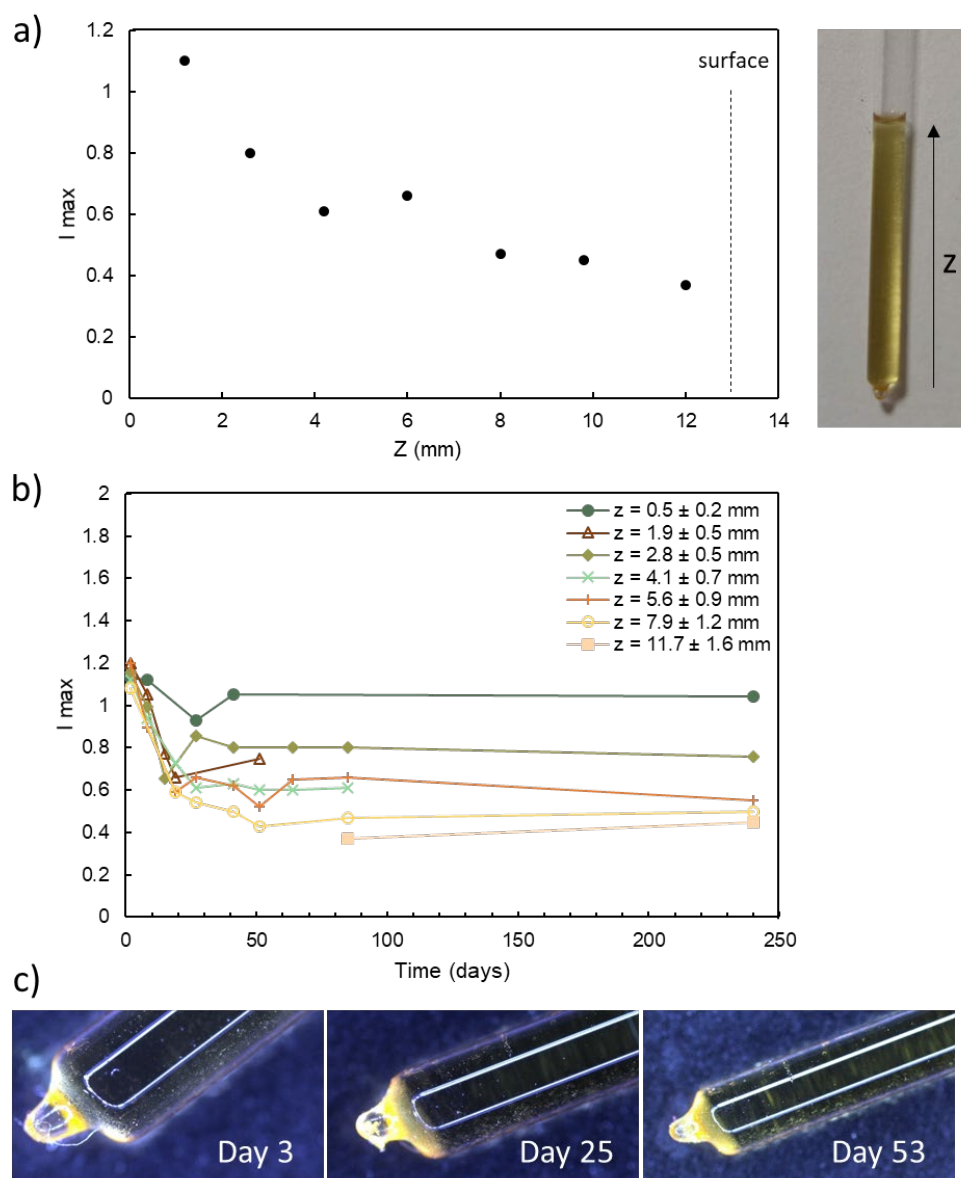


Figure A27. **a)** Evolution of the silica content along the capillary containing PL-a-fluid deduced from SAXS intensities variation; **b)** Evolution of the silica content overtime at different altitudes Z ; **c)** Formation of the sediment followed by microscopy: 3 days, 25 days, 53 days.

Unfortunately, the gel phase was not obtained in sufficiently high quantities to perform reliable measurements of stability. However, it is expected that a higher viscosity would lead to an even slower sedimentation if occurring. All in all, the separation of phases by centrifugation cannot prevent the

sedimentation from occurring in the fluid phase, but it is still slow (30 days) so the suspension can be seen as metastable.

For an application in LLE, the fluid phase seems more convenient, because of its lower viscosity, even if the gel phase seemed more stable in terms of sedimentation. To optimize this synthesis, a deeper investigation was required to provide lights onto the stability troubles, and to understand how improving it. As a result, different hypotheses were tested, such as the influence of solvent, reaction time, and post-treatment methods. They will be discussed in the next sections.

Influence of the solvent

The impact of the solvent used for the synthesis (from toluene: THF mixtures to THF alone) had little impact on the stability of the PL. This was deduced from the observation of a phase separation occurring with PL-d after few days (the picture was taken after 13 days in **Figure A28b**). However, only two distinct phases were visible in this case, and they were separated after centrifugation to give a fluid phase and a gel phase again. Initially, the same trend of very slow sedimentation was visible for the fluid phase, with a plateau at a low silica content after a long time (6%, according to TGA).

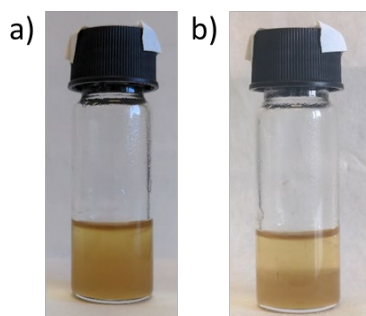


Figure A28. a) Fresh PL-d, b) Evolution after 13 days.

These two phases were further characterized (see Chapter II, Section 3.2.2.2), because they were synthesized in higher quantities than PL-a.

Influence of the reaction time

Obviously, only few sHSPs were successfully grafted by this method. Increasing the reaction time from one night to five days lead to a more stable but more viscous PL (PL-c, **Figure A30**).

The initial silica content was equivalent to the middle phase in PL-a, and it stayed homogeneous, with no significant loss after 183 days. A little sedimentation could be observed and confirmed by SAXS. However, after centrifugation of a larger amount of PL-c, a more significant upper phase could be observed (**Figure A29**).

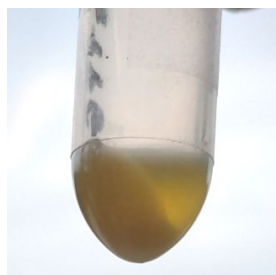


Figure A29. PL-c after centrifugation.

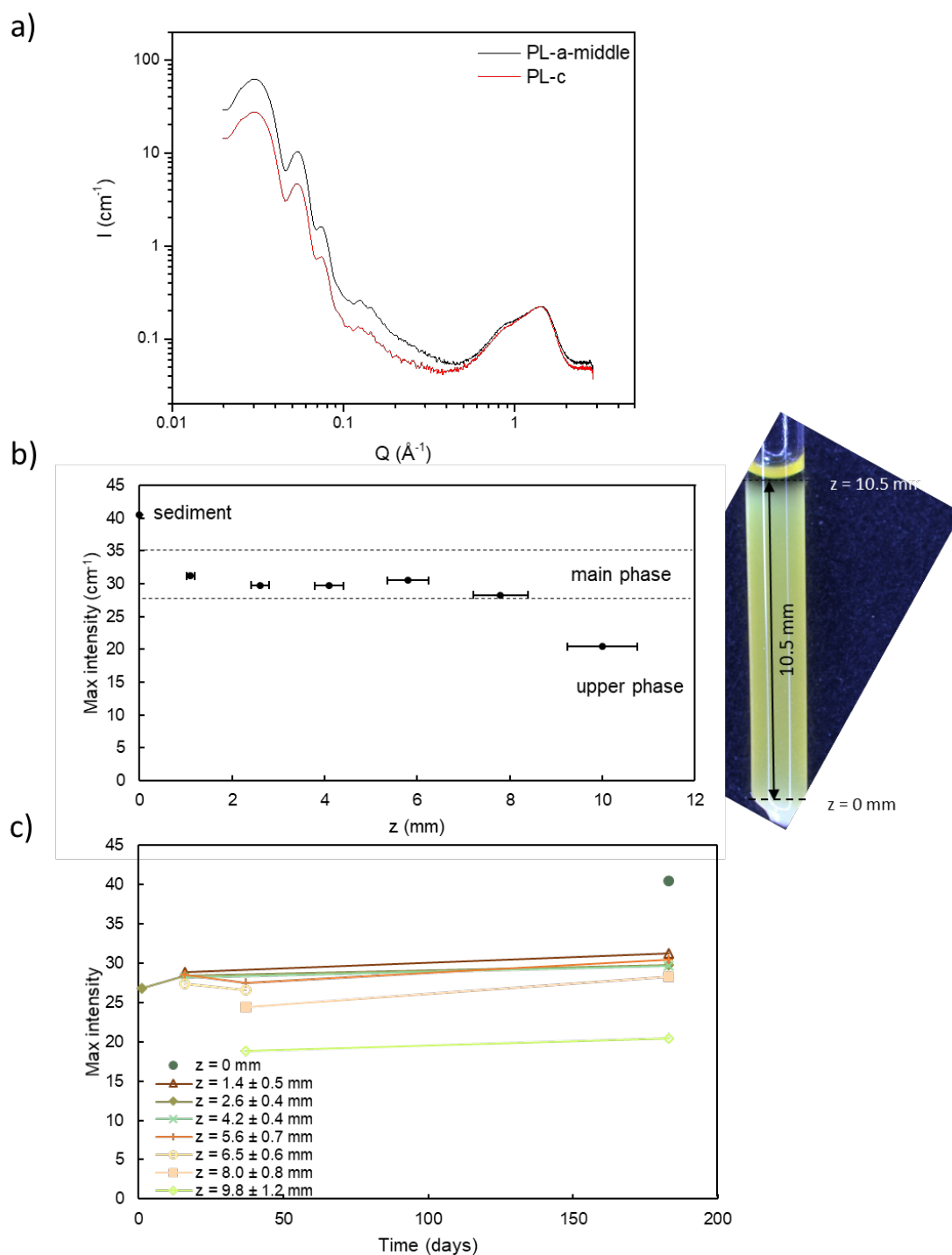


Figure A30. Stability and homogeneity of PL-c overtime, studied by SAXS. **a)** Comparison of PL-c structure with PL-a-middle by SAXS. Maximal intensities of the first visible oscillation are represented as a function of **b)** altitude Z at a given time (day 183), **c)** time for each altitude Z . The picture of the capillary was taken on Day 197.

This experiment confirmed that a longer reaction time could lead to a more cohesive material, thus increasing its stability but also its viscosity. For application in LLE however, a low viscosity is essential to ensure efficient phase separation for industrial processes. Therefore, the synthesis conditions leading to PL-d were selected and the fluid phase was systematically separated from the gel phase and stirred again before any manipulation.

Appendix H

Publications during the PhD

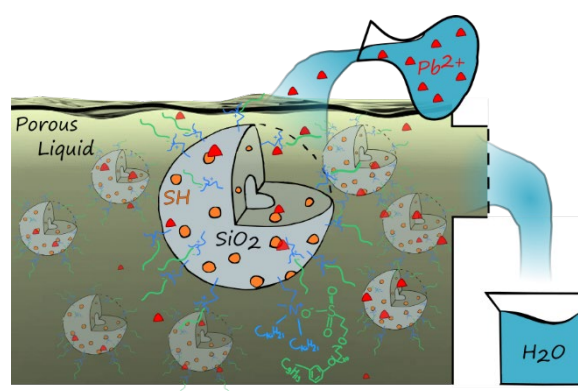
Lead Extraction in a Functionalized and Permeable Silica-Based Porous Liquid

Lorianne Ginot^a, Justine Ben Ghazi-Bouvrande^a, Sylvain Prévost^b, Stéphane Pellet-Rostaing^a, Sandrine Dourdain^{*a}

^aICSM, Univ Montpellier, CEA, CNRS, ENSCM, 30207 Marcoule, France

^bEuropean Neutron Source Institut Laue-Langevin, 38000 Grenoble, France

Email: sandrine.dourdain@cea.fr



To cite this: Lorianne Ginot, Justine Ben Ghazi-Bouvrande, Sylvain Prévost, Stéphane Pellet-Rostaing, and Sandrine Dourdain, *The Journal of Physical Chemistry B* **2024** 128 (10), 2550-2558, DOI: 10.1021/acs.jpcc.3c08295

Abstract

Silica based porous liquids (PLs) are innovative and versatile liquid materials with a high potential, although their application is often restricted to gas sorption. In this work, we propose to evaluate their potential to extract metals. For this goal, we have adapted their synthesis to provide PLs functionalized with thiols that are expected to chelate metallic contaminants, such as lead. As the accessibility of liquids and metals to the PL's porous network is one of the key points for their application, we developed an original small-angle neutron scattering experiment to verify that the PL is permeable to polar liquids. Then, preliminary extraction tests have successfully been carried out, with an extraction of lead cations by complexation on one-third of accessible thiol groups. This work demonstrates that the extraction of metal species by a PL is possible and opens many perspectives for optimization.

Keywords

porous liquids, nanomaterials, silica nanoshells, lead extraction, SANS.

Introduction

Porous liquids (PLs) are a novel kind of materials combining the properties of porous solids with fluid behavior. Their concept was first introduced by O'Reilly *et al.* in 2007:¹ they describe these materials as homogeneous liquids generally made of host particles or host molecules with a permanent porosity that are either dispersed in a sterically hindered solvent or chemically modified or physically treated to ensure a fluid behavior at room temperature. Among the different classes of PLs, those based on porous nanoitems are of great interest for metal extraction because of the possibility to have hollow cores of nanometric size. They were successfully synthesized by Zhang *et al.*² in 2015, who based their synthesis on the surface modification of silica nanoshells by two layers of organic molecules. Since then, an increased interest in these materials has risen.³⁻⁷

Despite their high potential, applications of PLs are nearly always restricted to gas sorption and gas separation, even when the host particles are large.^{2,8,9} While metal extraction using solid porous silica or other similar materials is well developed,^{10,11} it is surprising that very little research has been conducted to date with PLs.¹² PLs were recently considered for metal adsorption. Hemming *et al.* have shown the possibility of encapsulating nanoparticles of gold, platinum, and palladium during the synthesis of a functionalized silica-based PL with the aim of developing a liquid support for heterogeneous catalysis.¹³ Alternatively, Yang *et al.* developed a magnetic silica-based PL to separate copper and lead ions from a water phase.¹⁴ Because of their low volatility and their high porosity, they are considered promising candidates to substitute organic phases in liquid-liquid extraction (LLE) processes. Among the hydrometallurgical processes, LLE plays an important role in metal extraction. It is used as a separation/purification technique where metals are transferred from an aqueous to an organic phase.¹⁵ While effective, LLE faces sustainability challenges, including reducing emissions and optimizing solvent use.¹⁶ Envisaged as alternatives to the organic phases, PLs could address these challenges and reduce the environmental footprint of LLE processes by minimizing the use of hazardous organic solvents and by improving extraction efficiency.

Lead is a heavy metal with high toxicity and bioaccumulation properties, implying that decontamination treatments must be achieved with an excellent performance. Adsorption, membrane filtration, and ion-exchange are currently the most widely studied systems for water treatment.¹⁷ Among adsorption techniques, activated carbon¹⁸ and porous silica¹¹ are widely used materials because of their high porosity, their good biocompatibility, and their low cost. Besides, materials in liquid or gel form are usually preferred for skin decontamination.^{19,20} Hence, silica-based PLs could combine the performances of the porous silica with the advantages of a fluid behavior.

In this study, a silica-based PL was used as a solvent-free extracting agent for the extraction of lead from an aqueous solution. As illustrated in **Figure A31**, we followed the synthesis methodology proposed by Zhang *et al.*² and applied an optimized characterization⁶ to synthesize PLs based on silica hollow spheres (HS) grafted with organic coronas. The PL was primarily functionalized with thiols to enhance lead capture in the silica shells.

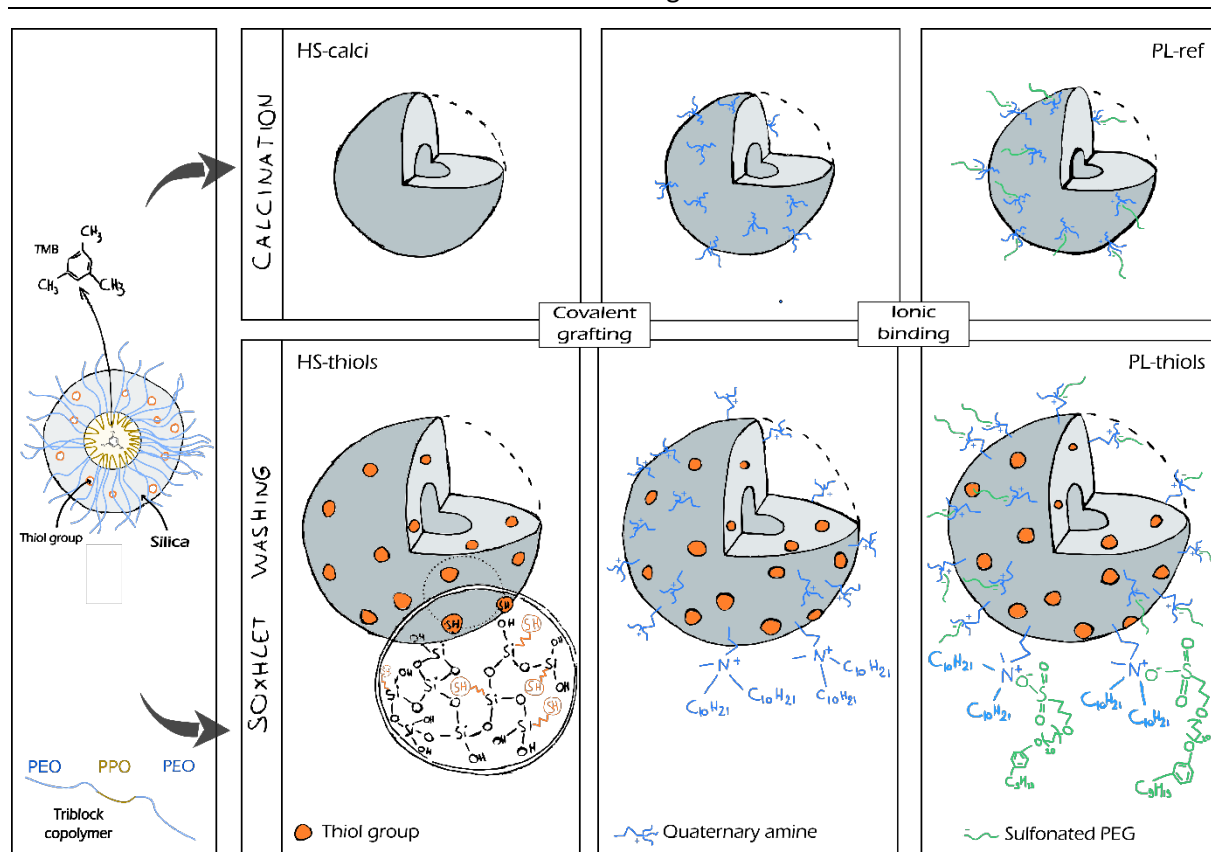


Figure A31. Scheme of PL-ref and PL-thiols syntheses.

After its complete characterization, the accessibility of the PL's porous network to polar liquids was assessed thanks to an original small-angle neutron scattering (SANS) experiment. Finally, extraction tests were performed, and the material was analyzed after the extraction to provide insights on the extraction mechanism.

Materials & Methods

Materials

1,3,5-trimethylbenzene (TMB, 98%), Pluronic F127, potassium sulfate (K_2SO_4), tetramethyl orthosilicate (TMOS, 98%), mercaptopropyl trimethoxysilane (MPTMS, 95%), poly(ethylene glycol) 4-nonylphenyl 3-sulfopropyl ether potassium salt (with an average 20 ethoxy units), acetone, and cysteine hydrochloride hydrate (99%) were purchased from Sigma-Aldrich, France. Toluene (pure) and ethanol (96%) were purchased from Carlo-Erba, France. *N,N*-didecyl-*N*-methyl-*N*-(3-trimethoxysilylpropyl) ammonium chloride (42% in methanol) was supplied by ABCR-Roth Sochiel, France. A standard solution of lead (1003 ppm) in 3-4% nitric acid was purchased from SCP Science, Canada and diluted 2.5 times (400 ppm) with water prior to use. 5,5'-Dithiobis(2-nitrobenzoic acid) (DNTB, 99%) was purchased from Alfa-Aesar, Massachusetts.

For thiol titration, a phosphate buffer at pH = 8 was made with 5.34 g of dibasic potassium phosphate (Sigma-Aldrich, 99%) and 222 mg of monobasic potassium phosphate (Sigma-Aldrich, 99%) in 200 mL of water.

Methods

Thiol-functionalized silica HSs were synthesized as described in a previous study.⁶ Their fabrication is based on the formation of a soft template made of an oily swelling agent (TMB) and a triblock copolymer (Pluronic F127). TMOS and MPTMS were used as silica precursors in the presence of K_2SO_4 , with MPTMS being employed to add thiol groups inside the silica gel. The organic molecules were then removed by a Soxhlet washing with ethanol with varying time durations (from 1 to 5 days) in order to maintain the thiol integrity. These spheres are referred to as HS-thiols. As a reference for extraction tests, nonfunctionalized HSs were also synthesized in the same way. Instead of the Soxhlet washing, they underwent a calcination step at 550 °C under air for 10 h after the sol-gel process to remove both the template and the thiol groups. They are named HS-calci.

Afterward, the PL was obtained as described previously,⁶ thanks to the grafting of a cationic organosilicon [*N,N*-didecyl-*N*-methyl-*N*-(3-trimethoxysilylpropyl) ammonium] at the surface of the HS in a first step, followed by the addition of a sulfonated polyethylene glycol derivative to form a canopy through ionic interactions with the organosilicon layer (**Figure A31**). This last step led to a liquid at room temperature after washing with hot toluene and drying. To avoid any loss, the material was then collected by dissolving it again in acetone and drying in a small flask under vacuum for 1 hour. The functionalized PL was obtained by grafting HS-thiols, and it was labelled PL-thiols. The nonfunctionalized PL was obtained by grafting HS-calci, and it was labelled PL-ref.

The extraction of lead was achieved by contacting the PL-thiols (100 mg) with 5 mL of an aqueous phase containing lead at 400 ppm. The separation was performed with membrane filter containing tubes (from Vivaspin, 30 kDa MWCO) that could go inside the centrifuge to overcome the issue that the PL was hydrophilic. For the sake of comparison, the extraction was also done with the nonfunctionalized PL (PL-ref, 133 mg), as well as with HSs (25 mg) with or without thiols inside their shells. The concentration of lead in the aqueous phases was measured by inductively coupled plasma (ICP) analysis.

Characterization

Thiol titration in HS-thiols was performed by chemically reacting the spheres with the DNTB reagent,²¹ and quantification was made by UV-visible spectroscopy on a Varian Cary 50 Bio (Agilent Technologies) spectrometer, with the software Varian UV Scan 3.00. The sample was prepared as follows: a phosphate buffer at pH8 was prepared and outgassed under argon atmosphere for 30 min. Then, 5.0 mg of HS-thiol powder was crushed and dispersed in 25 mL of buffer. Three milliliters of this solution were then mixed with 5 mL of water and 2 mL of buffer. Separately, 40 mg of DNTB was dissolved in 5 mL of a buffer. All compounds were deoxygenized under argon for 10 min before use. Finally, 20 μ L of the reactive solution (containing DNTB) was added to the preheated mixture containing HS-thiols at 40 °C. After 40 min of reaction, the absorbance was measured at 409 nm (see **Figure A39**). To quantify the thiol concentration, an etalon curve was also done with a cysteine solution (8.0 mg in 25 mL of buffer) (**Figure S6**, Supporting Information).

The accessibility of the internal cavities of the PLs was assessed by using SANS measurements. SANS measurements were performed at the Institut Laue-Langevin (ILL, The European Neutron Source, Grenoble, France) on the instrument D11 (lowest momentum transfer small-angle diffractometer) operated with a monochromatic beam (relative fwhm 10%) and with ^3He detectors. Configurations with a wavelength of 4.6 Å and a sample-to-detector distance of 1.7 and 16.5 m were used to cover

a total q -range from 0.002 to 0.4 \AA^{-1} where q is the magnitude of the wavevector [$q = (4\pi/\lambda) \sin(\vartheta/2)$, ϑ being the scattering angle]. All measurements were performed under atmospheric pressure and at room temperature. Samples were contained in quartz cuvettes type 120-QS of 1 mm pathway (Hellma, Müllheim, Germany). Standard corrections for sample volume, neutron beam transmission, empty cell signal subtraction, and detector efficiency were applied to obtain the scattered intensities. The absolute scale (cm^{-1}) was calculated by normalization with the incident neutron beam. Data reduction was performed with Grasp 9.25b,²² accounting for the detector background (measured with $^{10}\text{B}_4\text{C}$), transmission, sample pathway, parallax, scattering by D_2O , and dividing by the scattering of 1 mm of H_2O as a flat field correction. The intensity of 1 mm of H_2O was used as a secondary standard to obtain the absolute scale. Data are available on demand (DOI 10.5291/ILL-DATA.9-10-1628). Data modeling was performed with Sasview 5.0.4. As described in the following, core-shell models were taken into account to reproduce the experimental data, with a Baxter sticky hard sphere structure factor. Instrumental resolution was not taken into account.

Aqueous phases of extraction tests were collected and analyzed by ICP optical emission spectroscopy measurements. The device was an iCAP 7400 Duo Full MFC from Thermo Scientific equipped with Thermo Scientific Qtegra Intelligent Scientific Data Solution version 2.10 software. Calibration was carried out with standard solutions (1000 mg/L, SCP Science), and samples were diluted 100 times in HNO_3 (1%) prior to the analysis. The extraction capacity was defined as

$$Q_e = \frac{\frac{C_{Moth}}{MW} - \frac{C_{MA}}{MW}}{\frac{m_{mat}}{V_{sol}}}$$

where Q_e is the extraction capacity (mmol.g^{-1}) of the porous material, C_{Moth} is the massic concentration of the mother solution, C_{MA} is the massic concentration of the aqueous phase after extraction, MW is the molecular weight of the metal, m_{mat} is the mass of the porous material, and V_{sol} is the volume of the aqueous phase.

Further characterizations of the materials before and after extraction were obtained by transmission electronic microscopy (TEM), energy-dispersive X-ray spectroscopy (EDS), thermogravimetric analysis (TGA), Fourier-transform infrared spectroscopy (FTIRS), and nitrogen sorption with Brunauer–Emmett–Teller (BET) and density functional theories (DFT).

TEM was performed on a JEOL 1400+ apparatus with an emission gun operating at 120 kV, equipped with a LaB6 filament and a sCMOS JEOL Matataki Flash camera. Samples were first dissolved in EtOH before their deposition on a 400 mesh carbon-coated copper grid.

Additionally, imaging of HS-thiols after extraction and corresponding EDS analyses were achieved on a high resolution JEOL 2200 FS microscope (HRTEM) at 200 kV. EDS signals were accumulated at different positions by a silicon drift EDX detector (SDD Oxford Instrument XMaxN 100 TLE) combined with an STEM setup.

A Mettler-Toledo (Greifensee, Switzerland) TG device (with STARe Software) was used to characterize the chemical composition of the materials. The samples were put in alumina crucibles, and they were heated under air from 25 to 800 ° C at a rate of 5 ° C/min.

Nitrogen sorption analysis was carried out at 77 K with a Micromeritics (Norcross, GA, USA) ASAP-2020 instrument. Powders were outgassed for 48 h at 80 ° C prior to measurement, and PL-thiols were outgassed under nitrogen at 80 ° C for 96 h. Specific surface areas were computed by following the BET model in the P/P_0 region [0.01; 0.25]. The diameters of the micropores were obtained thanks to DFT

calculation using the ASAP 2020 V3 software and a model based on cylindrical pores and an oxide surface.

FTIR analysis was achieved on a PerkinElmer (Wellesley, MA, USA) Spectrum 100 spectrometer in transmission mode in the range 380-4000 cm^{-1} , with a resolution of 4 cm^{-1} . Scans were repeated four times.

Results & Discussion

Synthesis of thiol-functionalized porous liquids

Thiol-functionalized PLs (PL-thiols) were obtained by following the method described previously by Dai and coworkers.² As illustrated in **Figure A31**, silica HSs (HS-thiols) are prepared through a sol-gel process, templated with F127 surfactants. The PL is further obtained by a surface modification of HS-thiols with a large cationic organosilicon [*N,N*-didecyl-*N*-methyl-*N*-(3-trimethoxysilylpropyl) ammonium], followed by the addition of a second ionically bound layer of a sulfonated PEG derivative. In the present study, the calcination of the HS was replaced with a Soxhlet washing in ethanol to remove the template without destroying the thiols introduced during the silica condensation step. A nonfunctionalized PL (PL-ref) starting from calcined HS (HS-calci) was also synthesized for comparison.

In **Figure A32a**, the TEM image of HS-thiols shows monodisperse spherical particles with a total diameter of 37.8 ± 1.8 nm containing a hollow cavity (22.8 ± 1.7 nm of diameter). Similarly, the TEM image of the PL-thiols shows that the grafting process does not alter the HSs (**Figure A32a**). SANS experiments of HS-thiols and PL-thiols (**Figure A32b**) show oscillations in the range $0.01 - 0.1 \text{ \AA}^{-1}$, followed by a plateau at angles below 0.01 \AA^{-1} . Parameters used to calculate fitting curves of the experimental signals are listed in **Table S1** in Supporting Information. In particular, a spherical core-shell form factor and a sticky hard sphere structure factor were used, confirming the spherical shape of the nanospheres. Diameters obtained with this model were in excellent agreement with the ones determined by TEM (23 and 37 nm of internal and external diameters, respectively). The discrepancy between experiment and calculation in the 0.002-0.015 Q -range for the PL-thiols sample can easily be assigned to the aggregation of the nanospheres, which cannot be accounted with a simple model.

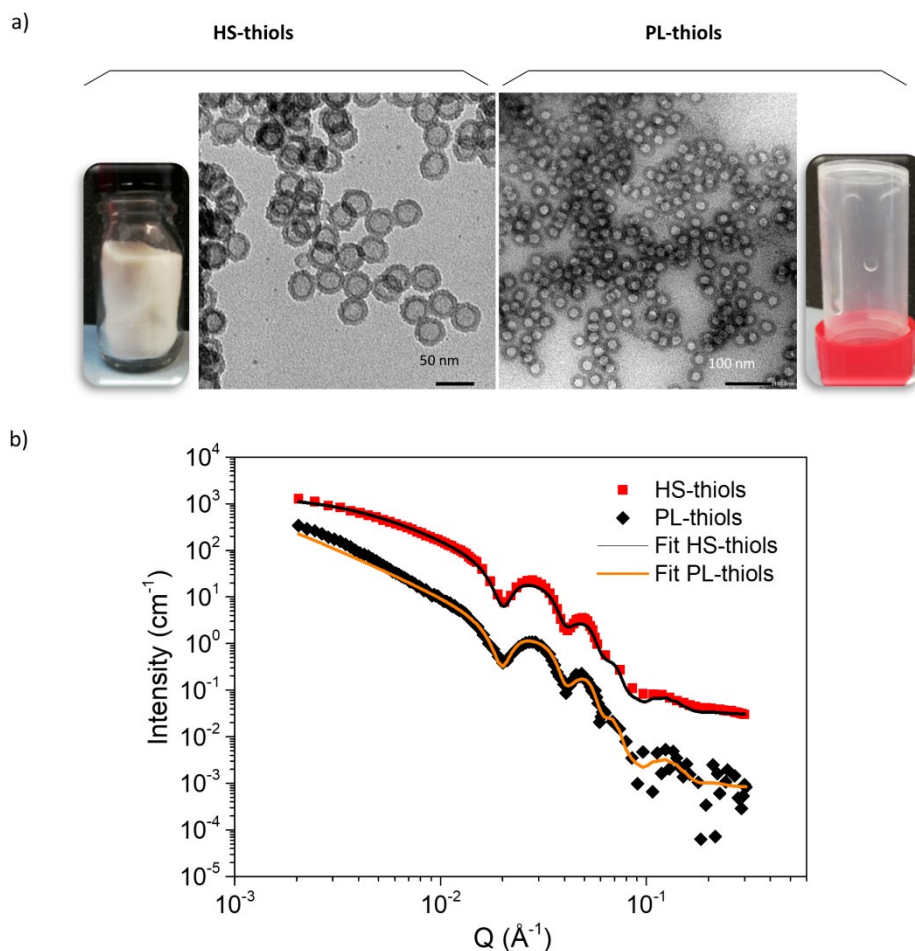


Figure A32. a) Pictures and TEM images and b) SANS signals of HS-thiols and PL-thiols. For TEM, magnification is, respectively, x100k and x60k. For SANS, scatters and lines correspond to the experimental data and fit, respectively.

As mentioned above, the functionalized PL (PL-thiols) was synthesized by a surface modification of the HS-thiols (**Figure A31**). The efficiency of this double-step organic grafting on HS-calci was already assessed in previous studies,^{2,6} and the results were similar for HS-thiols. In particular, the TGA trace (**Figure A33a**) suggested the presence of 88% of organic grafting (including thiol groups) and 7% of silica constituting the residual mass. This slightly lower silica content compared to PL-ref (8% of silica) is explained by the presence of thiols and the variability of the synthesis method. Two weight losses were visible for the organic parts: the main loss between 200 and 400 °C was attributed to the polymeric canopy whereas the smaller decrease between 500 and 600 °C was due to the covalently bonded organosilicon. In PL-thiols, this latter weight loss was switched slightly toward higher temperatures (600 – 700 °C) compared to PL-ref, probably because of the degradation of thiols occurring at the same time. The last 5% of the total mass were lost between 100 and 200 °C, and they were attributed to residual acetone from the synthesis (trapped inside the silica spheres). Besides, the FTIR spectra of PL-ref and PL-thiols were similar (**Figure A33b**), and they were consistent with previous published studies.^{2,6} In particular, the presence of organosilicon was verified by the adsorption band of the C-N bond at 1243 cm^{-1} . The intense bands at 1096 and 2868 cm^{-1} characteristic of C-O-C and CH_2 stretching, respectively, along with the broad band at 3422 cm^{-1} and the weak peak at 1350 cm^{-1} owing to the OH stretching of the hydrogen bonds and S=O stretching of the sulfonate group, respectively,

confirmed the presence of the sulfonated PEG. In **Figure S1** (Supporting Information), the FTIR spectra of HS-calci and HS-thiols clearly show the presence of the organic moieties, with the stretching peak at 2912 cm^{-1} corresponding to the CH_2 backbone of the silica co-precursor (MPTMS). The silica network itself displayed a strong signal with the Si-O-Si antisymmetric stretching at 1045 and 1186 cm^{-1} (TO and LO mode, respectively) and the symmetric stretching at 804 cm^{-1} .²³ The weak S-H stretching peak expected in the $2600\text{--}2550\text{ cm}^{-1}$ region was unfortunately not visible because of the proportionally too strong signal of the silica.

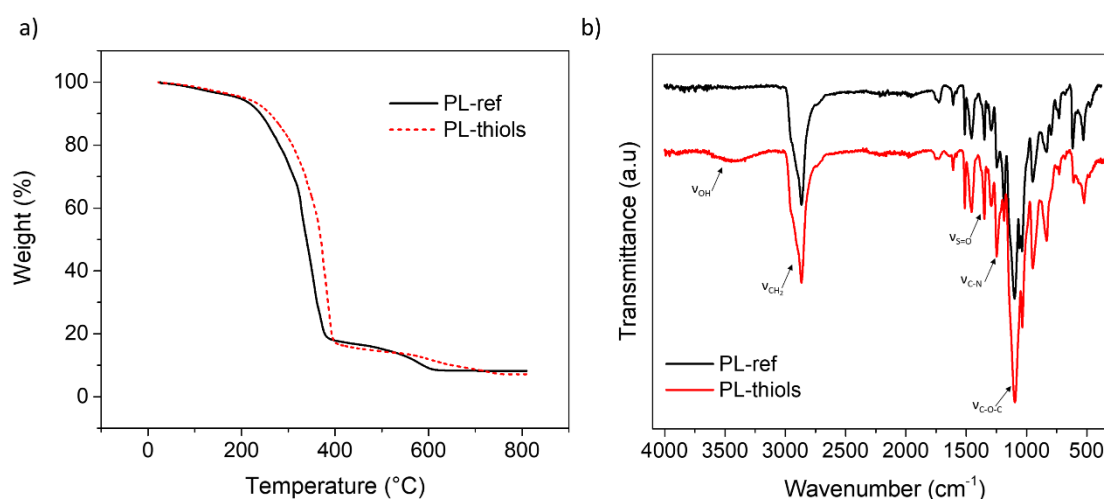


Figure A33. a) TGA traces of PL-ref and PL-thiols under air at 5 °C/min , b) FTIR spectra of PL-ref and PL-thiols.

Optimization of the template removal

To remove the surfactant and TMB from the cavity of the HS, without degrading the thiol groups, a Soxhlet washing with ethanol was performed. In order to optimize it, the porosity of HS-thiols was followed by nitrogen sorption measurements when varying the time of washing (24 h and 120 h), and it was compared to the porosity of HS-calci (**Figure A34a**). HS-calci displayed a type IV + type I hybrid isotherm disclosing the presence of micropores and a hysteresis at relative pressures between 0.4 and 0.9 typical of the large mesoporous cavities.^{2,6} According to the BET model, a specific surface area of $323 \pm 5\text{ m}^2\text{ g}^{-1}$ was obtained for this sample, and DFT calculations revealed the presence of a high proportion (71%) of 1.4 nm-large micropores inside the silica shell. In comparison, HS-thiols washed for only 24 h showed less porosity with a specific surface area of $199 \pm 5\text{ m}^2\text{ g}^{-1}$. In particular, the cavity was not completely empty given that the hysteresis loop was not visible in this signal. In addition, a comparatively less significant increase in the adsorbed gas volume at low relative pressures was observed, indicating that the micropores were also partially obstructed. Therefore, HS-thiols underwent an extensive washing for 5 days (120 h) to determine whether all the template could be extracted totally. Indeed, the nitrogen sorption measurement after 120 h displayed a high porosity, with a specific surface area similar to the one of HS-calci ($308 \pm 2\text{ m}^2\text{ g}^{-1}$), and a substantial increase in the adsorbed volume in the micropore region was visible. Indeed, DFT calculations showed 75% of 1.4 nm-large micropores. Finally, the presence of the hysteresis in the region $0.4\text{--}0.9 P/P_0$ suggests the presence of an empty cavity that is accessible to the gas and supports the conclusion that the removal of the template was effective. Furthermore, the porous volume of the micropores could be directly

read on the curve at $0.09 P/P_0$ (after applying a correction factor specific for nitrogen), and it was $0.095 \text{ cm}^3 \text{ g}^{-1}$. Based on these results, the porosity of the silica shell of HS-thiols (volume of micropores in the volume of the silica shell) was estimated to 12%, and this value was used to refine the fit of SANS measurements.

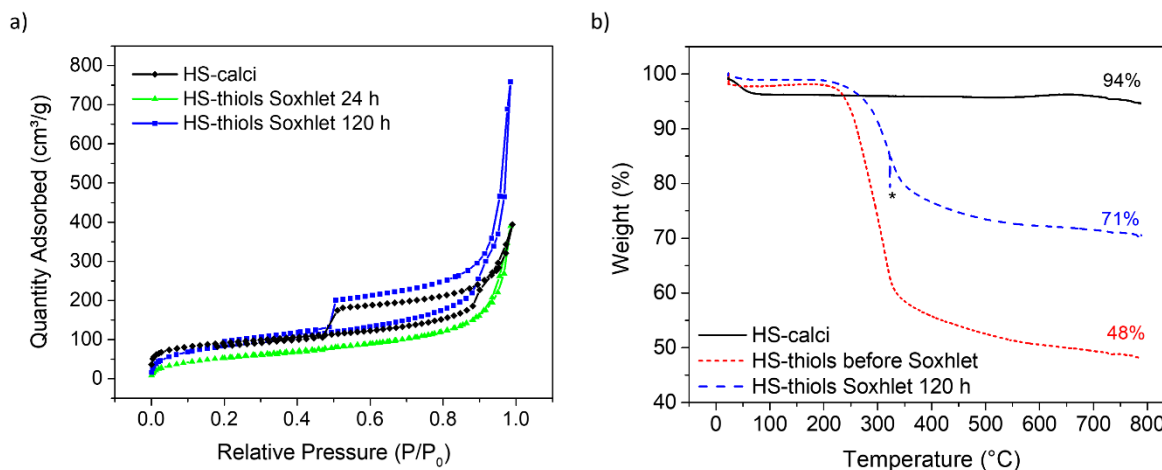


Figure A34. **a)** Nitrogen sorption isotherms of HS-calci (black), HS-thiols washed by Soxhlet after $t_1 = 24 \text{ h}$ (green), and HS-thiols washed by Soxhlet after $t_2 = 120 \text{ h}$ (blue), **b)** TGA of HS after calcination (HS-calci, black), and before (red) and after (blue) Soxhlet washing for 120 h (HS-thiols). The star indicates an artefact from the device.

In the TGA traces (**Figure A34b**), the silica content of HS-calci was 94%, mainly because of the presence of water, given that the silica network is highly hygroscopic. In contrast, the silica content of HS-thiols after and before the Soxhlet washing (120 h) were 71 and 48% respectively. Hence, the thiol part accounted for near to 30% of the total weight of the materials, and this number was consistent with the literature.¹³ The organic template represented about 20%.

Porous liquid porosity measurement

To assess the porosity of PL-thiols, a nitrogen sorption analysis was performed after an extensive outgassing under nitrogen for 4 days at $80 \text{ }^\circ\text{C}$. However, no signal was obtained under these conditions (**Figure A35**). This suggested that the porosity of HS-thiols was either completely obstructed or that the pores were filled with a solvent from the last steps of the synthesis. Because of confinement, this solvent may be too hard to remove under normal outgassing conditions. Since the organosilicon was carefully chosen not to penetrate the pores, the hypothesis of a residual solvent was more likely to be considered. To verify this, a study of the permeability of PL-ref and PL-thiols to liquids was conducted by using SANS analysis.

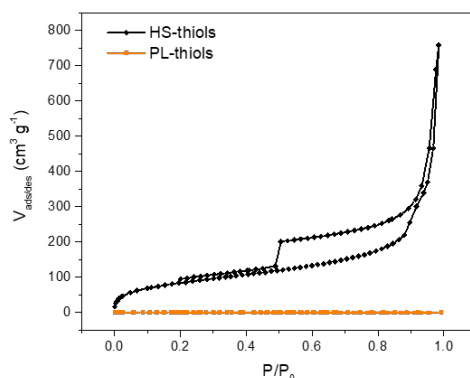


Figure A35. Nitrogen sorption isotherms of HS-thiols and PL-thiols.

Permeability of the porous liquids to liquids

It is of high importance to evaluate the pore accessibility to polar liquids before considering PLs for metal extraction. SANS measurements were therefore performed on the PL-ref after its immersion in aqueous solutions of various volume fractions of D_2O : $x_{D_2O} = V(D_2O)/(V(H_2O)+V(D_2O))$. Neutron scattering experiments indeed present the unique property of allowing measuring a sample structure with a gradual contrast by immersing it in solutions with various ratios of hydrogenated and deuterated compounds.²⁴ If the scattering signal collapses at some ratio, such a so-called contrast matching experiment allows determining the scattering length density (*sl/d*) of the material (which is related to its density). For porous materials, it is necessary that the liquid solution penetrates the whole porosity to match the contrast. In the case of complete matching (*i.e.*, scattering extinction), such an experiment therefore demonstrates that the liquid fully penetrates the internal cavities of the material. If some signal remains visible at the maximum contrast matching, it may be due to unfilled pores or to unmatched parts of the material (*e.g.*, for hybrid materials). In case of the residual signal at the maximum contrast matching, a fit is necessary to conclude on the solvent accessibility to the PL's porous network.

Figure A36 presents a SANS contrast variation experiment with PL-ref immersed in various H_2O/D_2O solutions. A constant was further subtracted to account for an incoherent background mainly due to hydrogen atoms (**Figure A36b**).

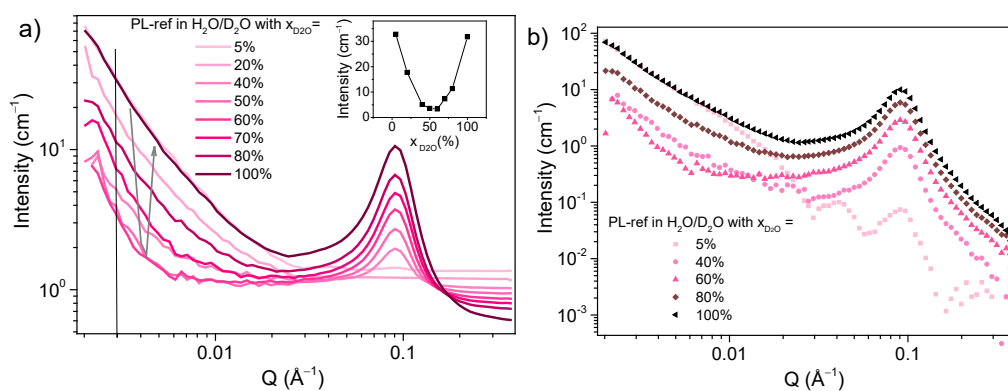


Figure A36. SANS spectra of PL-ref immersed in H_2O/D_2O mixtures with various ratios x_{D_2O} **a)** before and **b)** after incoherent signal subtraction. The rotating arrow indicates the trend of evolution in

intensity at 0.003 \AA^{-1} from $x_{D_2O} = 5\%$ to $x_{D_2O} = 100\%$. The top inset of Figure 6a displays the variation of intensity at 0.003 \AA^{-1} . For sake of clarity, some ratios were not plotted in Figure 6b.

As plotted in the top inset of **Figure A36a**, the scattering intensity at small angles (arbitrarily measured at 0.003 \AA^{-1}) shows a strong variation with the ratio x_{D_2O} . The maximum contrast matching (*i.e.*, the signal with the minimum intensity) occurs at $x_{D_2O} = 52\%$, corresponding to an *sl**d* of the $\text{H}_2\text{O}/\text{D}_2\text{O}$ mixture of $3.06 \cdot 10^{-6} \text{ \AA}^{-2}$. This value is consistent with a matching of the PL made up of silica and organics ($sl_{dense\ silica} = 3.46 \cdot 10^{-6} \text{ \AA}^{-2}$ and $sl_{OS+PEG} = 0.24 \cdot 10^{-6} \text{ \AA}^{-2}$, see details in Supporting Information).

Moreover, a strong structural peak is visible at 0.09 \AA^{-1} and its intensity increases gradually when increasing x_{D_2O} ratios. Even after subtracting the incoherent signal (**Figure A36b**), this peak hides the residual signal of the PL and prevents performing a proper fit at x_{D_2O} ratios close to the matching contrast. Since this peak was not visible in the case of the dry PL (**Figure S2**, Supporting Information), it was attributed to the structural organization of the amphiphilic organic shell in the presence of water.²⁵ To confirm this hypothesis, water was replaced with a simple hydrotrope as ethanol, which is expected to prevent the formation of such nanodomains.

The contrast variation experiment was therefore performed with PL-ref and PL-thiols in the presence of mixtures of hydrogenated and deuterated ethanol (EtOH/EtOD). Results obtained with PL-ref and PL-thiols are, respectively, presented in **Figure S3** (Supporting Information) and **Figure A37**.

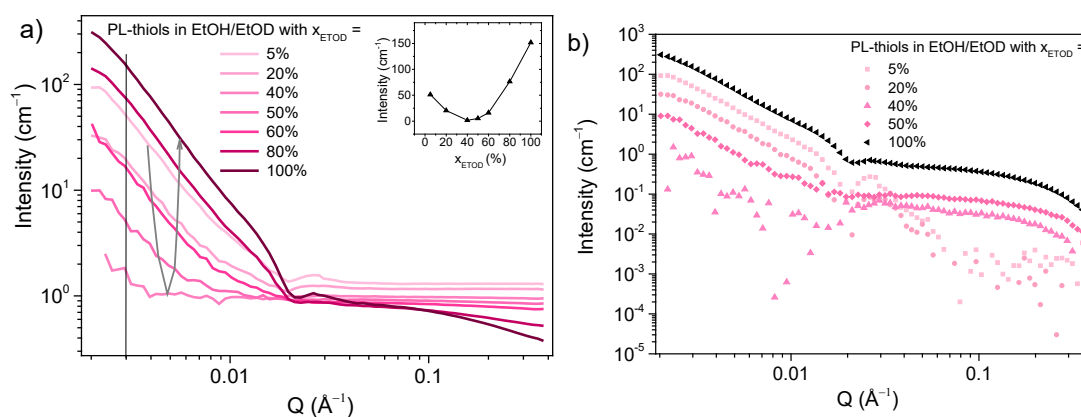


Figure A37. SANS spectra of PL-thiols immersed in EtOH/EtOD mixtures with various ratios x_{EtOD} **a)** before and **b)** after incoherent signal subtraction. The rotating arrow indicates the trend of evolution in intensity at 0.003 \AA^{-1} from $x_{D_2O} = 5\%$ to $x_{D_2O} = 100\%$. The top inset of Figure 7a displays the variation of intensity at 0.003 \AA^{-1} . For sake of clarity, some ratios were not plotted in Figure 7b.

The strong structural peak present in the case of water disappeared in the case of ethanol, confirming that it was due to a structuration of the organic shell of the PLs in the presence of water. It is also interesting to notice that the ratio of maximum contrast matching occurs at $x_{EtOD} = 43\%$ for PL-thiols, corresponding to an *sl**d* value of $2.42 \cdot 10^{-6} \text{ \AA}^{-2}$. The lower *sl**d* value for PL-thiols than for PL-ref is consistent with a higher content of organics in this PL due to its functionalization with thiols. In order to verify if the PL is fully permeable to ethanol, it remains necessary to investigate the origin of the residual scattering signal at this ratio of maximum contrast matching.

SANS data measured with $x_{EtOD} = 40\%$ was therefore compared with three calculated curves corresponding to the three scenarios illustrated in **Figure A38**: *i)* the solution enters the organic shell but not the micropores of the HS; *ii)* the solution fills all the micropores of the HS but the internal cavity is not accessible; *iii)* the PL is fully penetrated by the solution. At higher angles, a residual signal of the organic chains in ethanol was calculated thanks to an Ornstein-Zernike model. The parameters used for calculation are listed in **Table S2** (Supporting Information).

It appears clearly that case *iii)* provided the best fit with the experimental data, with a dramatic decrease in the signal intensity. This experiment therefore demonstrated that both micropores and internal cavities contained in the PL are fully accessible to polar liquids, which confirms that this material can be considered as a candidate for metal extraction by LLE or surface decontamination.

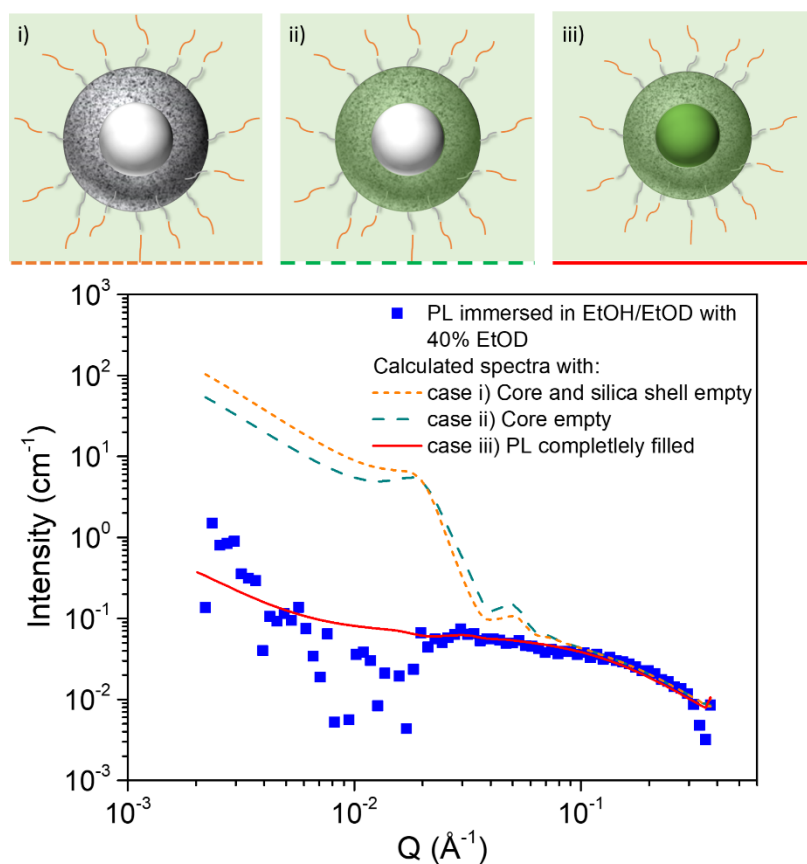


Figure A38. SANS data of PL-thiols immersed in EtOH/EtOD with $x_{EtOD} = 40\%$ and SANS spectra calculated with models corresponding to the three scenarios illustrated on the top of the figure: *i)* solution enters the organic shell but not the micropores of the HS; *ii)* solution fills all the micropores of the HS but the internal cavity is not accessible; *iii)* PL is fully penetrated by the solution.

Extraction tests

PLs are promising candidates for metal extraction because of the high surface area of the nanoitems they contain. In particular, their fluid behavior could be interesting for metal extraction. A functionalization of these tunable materials is expected to be important for the extraction of a targeted metal. Herein, extraction tests on an aqueous solution of lead were performed either with the HS or with the PL, both with and without thiols functionalization. After mixing the porous materials (25 mg of HS and 100-130 mg of PL) with an aqueous solution containing 400 ppm of lead, the separation was

performed by centrifugation with membrane filter containing tubes (from Vivaspin). The results of extraction after 24 h of contact at room temperature are gathered in **Table A3**. For HS-thiols, the highest extraction yield was $43.9 \pm 1.1\%$, corresponding to an extraction capacity of $0.079 \pm 0.003 \text{ mmol}_{\text{Pb}} \text{ g}_{\text{mat}}^{-1}$. Regarding PL-thiols, the extraction yield was higher (58.3%), corresponding to an extraction capacity of $0.058 \pm 0.002 \text{ mmol}_{\text{Pb}} \text{ g}_{\text{mat}}^{-1}$. According to the TGA of HS-thiols and PL-thiols (**Figure A33a** and **Figure A34b**), only 10% of the weight of the PL is attributed to the thiol-containing HSs. Hence, a theoretical extraction capacity would only amount to $0.008 \text{ mmol}_{\text{Pb}} \text{ g}_{\text{mat}}^{-1}$ based on the results obtained for solid HS-thiols. Therefore, the capacity was largely increased (7 times) by the presence of the organic moieties. Furthermore, HS-calci and PL-ref containing no thiols showed no performance in lead extraction. These results show that not only are the thiol groups accessible but also that their presence is essential for the success of the extraction, and that no extraction can be attributed to the organic corona alone.

This extraction capacity is lower than the one observed by Yang *et al.* with their magnetic PL,¹⁴ despite the absence of functionalization of the silica shell in their material. Indeed, they observe a surprisingly high adsorption capacity of around 1 mmol g^{-1} , but it is worthy of note that the hybrid liquid with no pores they used as a comparison also displayed a significant adsorption capacity of 0.6 mmol g^{-1} . It is not clear in this case to what extent the presence of the HSs played an important role in the total extraction of the metal. Besides, the extraction capacities observed for similar systems in solid-liquid extraction are also higher.^{26–28} For instance, Wu *et al.*²⁷ reported a capacity of 0.5 mmol g^{-1} for a thiol-functionalized mesoporous silica. However, if their material were dispersed at 10% in an organic matrix, it would be expected to decrease to about 0.05 mmol/g that is slightly lower than the capacity displayed by the PL-thiols.

Table A3. Extraction yields and extraction capacities of HSs and PLs with and without thiols.

	Hollow silica spheres		Porous Liquid	
	Without thiols (HS-calci)	With thiols (HS-thiols)	Without thiols (PL-ref)	With thiols (PL-thiols)
Extraction (%)	No extraction	43.9 ± 1.1	6.3 ± 2	58.3 ± 1.3
Extraction capacity ($\text{mmol}_{\text{Pb}}/\text{g}_{\text{mat}}$)	No extraction	0.079 ± 0.003	$(5 \pm 40) \times 10^{-6}$	0.058 ± 0.002
Extraction capacity ($\text{mmol}_{\text{Pb}}/\text{g}_{\text{SiO}_2}$)	No extraction	0.079 ± 0.003	$(6.3 \pm 50) \times 10^{-5}$	0.58 ± 0.02

Lead extraction mechanisms

The mechanism of extraction of lead was studied by TEM and EDX analyses. TEM images of HS-thiols after extraction (**Figure S4**, Supporting Information) did not allow observation of lead inside the cavities and around the spheres. As a result, one can assume that lead did not precipitate and was located in a cation form inside the silica shell. Moreover, the EDX cartography (**Figure S5**, Supporting Information) suggested that the lead and the sulfur signals were located on the silica HSs; however, the resolution of the analysis was too poor to conclude whether lead was effectively linked to the thiol groups inside the silica shells.

To quantify the ratio of metal over chelating groups, it was necessary to titrate the thiol groups in HS-thiols. Even though TGA gives an estimation of the total number of thiols, it was expected that not all thiols would be accessible. Indeed, the use of the co-condensation method implies that functional groups are well dispersed in the silica network, so they are not necessarily close to an open pore surface. In order to further quantify the accessible thiols in HS-thiols, a titration method using the Ellman's reagent has been applied.²¹ Briefly, it consisted of contacting the powder of HS-thiols with a mixture of water and phosphate buffer (pH8) containing the DTNB reagent (Ellman's reagent) at a known concentration (**Figure A39**). The absorbance was measured at 409 nm, and the concentration was deduced from an etalon curve obtained by using cysteine as a standard (**Figure S6**, Supporting Information). In this manner, a concentration of 0.31 mmol g⁻¹ of accessible thiols was found for HS-thiols (corresponding to about 3.4% of the total thiol groups).

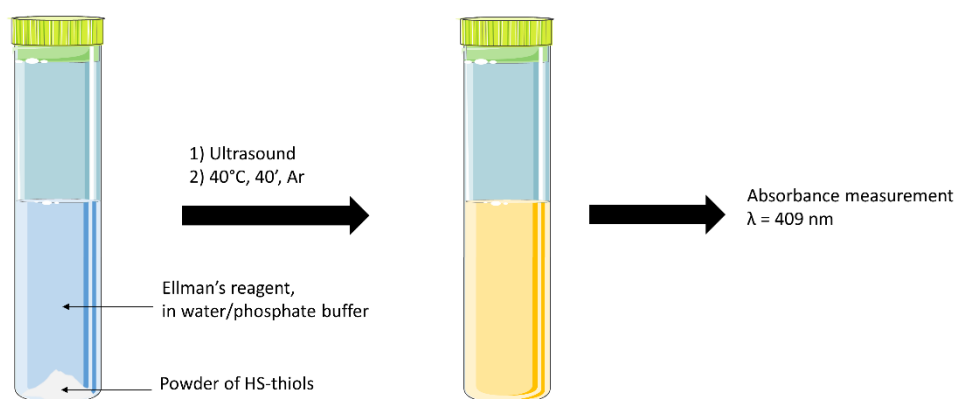


Figure A39. Illustration of the thiol titration in HS-thiols by reaction with DTNB (Ellman's reagent) under an argon atmosphere. The concentration was deduced from an etalon curve obtained using cysteine as a standard. The figure was partly generated using Servier Medical Art, provided by Servier, licensed under a Creative Commons Attribution 3.0 unported license.

Considering this number of accessible thiol groups of 0.31 mmol g⁻¹, one can conclude that there was one lead atom for three thiols. According to the literature, the coordination number of lead with thiols is usually 1,^{29,30} meaning that about one-third of the thiols may contribute to the complexation of lead. Because the thiols are introduced in the silica network by co-condensation, it is likely that two-thirds of the accessible thiols are located in too highly sterically hindered pores, preventing a good complexation.

Conclusion

In this study, a silica-based PLs was functionalized with thiol groups to evaluate its potential application for lead extraction, which is essential for applications such as LLE, water, or skin decontamination. A complete characterization of the obtained materials (HSs and PL) allowed validating the synthesis methodology and revealed that the porous network of the PL requires extensive drying to be fully empty. As the accessibility of this porous network to aqueous solutions and metals is essential to applying PLs for LLE, an original SANS experiment was proposed to verify that PLs are permeable to liquids. By immersing PLs in various solutions and performing a so-called contrast variation experiment, we successfully demonstrated that both the micropores of the silica coronas and the internal cavities of the silica hollow nanospheres were accessible to liquids. The PLs were further tested for the LLE of

lead. The functionalization of the PL with thiols led to a good extraction capacity, whereas the absence of thiols implied no extraction. Interestingly, the presence of the organic corona induced an enhanced extraction since the extraction capacity of the PL was more than 7 times higher than that of pure spheres (when taking into account the lower mass fraction of spheres in the PL). It was finally estimated that around 32% of the accessible thiols were occupied by a lead ion. This study therefore provides a proof-of-concept for using silica-based PLs for LLE of metals and reveals the important parameters for optimizing an efficient extraction. PLs need to be functionalized with a chelating agent to improve metal extraction, revealing that extraction occurs primarily in the micropores of silica coronas and that the internal mesocavity may not be necessary for such applications. Lead extraction could therefore be improved both by a higher density of accessible grafted thiols and thicker silica coronas.

Supporting Information

The Supporting Information is available free of charge at:
<https://pubs.acs.org/doi/10.1021/acs.jpcc.3c08295>.

Acknowledgement

The authors greatly acknowledge Xavier Le Goff for TEM/HRTEM and EDS analyses and Dianath Dine Moreira for her contribution to the metal extraction experiments. Fabrice Giusti is also greatly thanked for his support, advice, and contribution to the thiol titration experiment. The authors express their gratitude to Gwenaëlle Ginot Seux for her help in drawing the schemes of this publication. This research was supported financially by CEA fundings. This work benefited from the use of the SasView application, originally developed under NSF award DMR-0520547. SasView contains code developed with funding from the European Union's Horizon 2020 research and innovation program under the SINE2020 project, grant agreement No 654000.

References

- (1) O'Reilly, N.; Giri, N.; James, S. L. Porous Liquids. *Chem. - Eur. J.* **2007**, *13* (11), 3020–3025. <https://doi.org/10.1002/chem.200700090>.
- (2) Zhang, J.; Chai, S.; Qiao, Z.; Mahurin, S. M.; Chen, J.; Fang, Y.; Wan, S.; Nelson, K.; Zhang, P.; Dai, S. Porous Liquids: A Promising Class of Media for Gas Separation. *Angew. Chem.* **2015**, *127* (3), 946–950. <https://doi.org/10.1002/ange.201409420>.
- (3) Li, P.; Schott, J. A.; Zhang, J.; Mahurin, S. M.; Sheng, Y.; Qiao, Z.; Hu, X.; Cui, G.; Yao, D.; Brown, S. *et al.* Electrostatic-Assisted Liquefaction of Porous Carbons. *Angew. Chem. Int. Ed.* **2017**, *56* (47), 14958–14962. <https://doi.org/10.1002/anie.201708843>.
- (4) Liu, Y.; Bai, Y.; Tian, T. Preparation of Porous Liquid Based on Silicalite-1. *Materials* **2019**, *12* (23), 3984. <https://doi.org/10.3390/ma12233984>.
- (5) Kumar, R.; Dhasaiyan, P.; Naveenkumar, P. M.; Sharma, K. P. A Solvent-Free Porous Liquid Comprising Hollow Nanorod–Polymer Surfactant Conjugates. *Nanoscale Adv.* **2019**, *1* (10), 4067–4075. <https://doi.org/10.1039/C9NA00353C>.
- (6) Ben Ghazi-Bouvrande, J.; Pellet-Rostaing, S.; Dourdain, S. Key Parameters to Tailor Hollow Silica Nanospheres for a Type I Porous Liquid Synthesis: Optimized Structure and Accessibility. *Nanomaterials* **2021**, *11* (9), 2307. <https://doi.org/10.3390/nano11092307>.
- (7) Sheng, L.; Lei, J.; Chen, Z.; Wang, Y. Solvent-Free Porous Liquids for CO₂ Capture Based on Silica Nanoparticles with Different Core Structures. *Colloids Surf. Physicochem. Eng. Asp.* **2022**, *634*, 128016. <https://doi.org/10.1016/j.colsurfa.2021.128016>.
- (8) Costa Gomes, M.; Pison, L.; Červinka, C.; Padua, A. Porous Ionic Liquids or Liquid Metal–Organic Frameworks? *Angew. Chem. Int. Ed.* **2018**, *57* (37), 11909–11912. <https://doi.org/10.1002/anie.201805495>.
- (9) Giri, N.; Del Pópolo, M. G.; Melaugh, G.; Greenaway, R. L.; Rätzke, K.; Koschine, T.; Pison, L.; Gomes, M. F. C.; Cooper, A. I.; James, S. L. Liquids with Permanent Porosity. *Nature* **2015**, *527* (7577), 216–220. <https://doi.org/10.1038/nature16072>.
- (10) Nedelec, T. L. Synthèse et évaluation de silices hybrides fonctionnalisées pour la récupération de l'uranium en milieu sulfurique. phdthesis, Université Montpellier, 2019. <https://theses.hal.science/tel-02931584> (accessed 2023-09-04).
- (11) Shao, P.; Liang, D.; Yang, L.; Shi, H.; Xiong, Z.; Ding, L.; Yin, X.; Zhang, K.; Luo, X. Evaluating the Adsorptivity of Organo-Functionalized Silica Nanoparticles towards Heavy Metals: Quantitative Comparison and Mechanistic Insight. *J. Hazard. Mater.* **2020**, *387*, 121676. <https://doi.org/10.1016/j.jhazmat.2019.121676>.
- (12) Wang, D.; Ying, Y.; Xin, Y.; Li, P.; Yang, Z.; Zheng, Y. Porous Liquids Open New Horizons: Synthesis, Applications, and Prospects. *Acc. Mater. Res.* **2023**, *4*, 10, 854–866. <https://doi.org/10.1021/accountsmr.3c00106>.
- (13) Hemming, E. B.; Masters, A. F.; Maschmeyer, T. The Encapsulation of Metal Nanoparticles within Porous Liquids. *Chem. Commun.* **2019**, *55* (75), 11179–11182. <https://doi.org/10.1039/C9CC03546J>.
- (14) Yang, R.; Zhang, Q.; Shi, J.; Zheng, Y.; Wang, D.; Zhang, J.; Liu, S.; Fu, Z. A Novel Magnetic Loading Porous Liquid Absorbent for Removal of Cu(II) and Pb(II) from the Aqueous Solution. *Sep. Purif. Technol.* **2023**, *314*, 123605. <https://doi.org/10.1016/j.seppur.2023.123605>.
- (15) El-Nadi, Y. A. Solvent Extraction and Its Applications on Ore Processing and Recovery of Metals: Classical Approach. *Sep. Purif. Rev.* **2017**, *46* (3), 195–215. <https://doi.org/10.1080/15422119.2016.1240085>.
- (16) Reck, B. K.; Graedel, T. E. Challenges in Metal Recycling. *Science* **2012**, *337* (6095), 690–695. <https://doi.org/10.1126/science.1217501>.
- (17) Fu, F.; Wang, Q. Removal of Heavy Metal Ions from Wastewaters: A Review. *J. Environ. Manage.* **2011**, *92* (3), 407–418. <https://doi.org/10.1016/j.jenvman.2010.11.011>.
- (18) Brasquet, C.; Le Cloirec, P. Adsorption onto Activated Carbon Fibers: Application to Water and Air Treatments. *Carbon* **1997**, *35* (9), 1307–1313. [https://doi.org/10.1016/S0008-6223\(97\)00079-1](https://doi.org/10.1016/S0008-6223(97)00079-1).
- (19) Esswein, E. J.; Boeniger, M. F.; Ashley, K. Handwipe Method for Removing Lead from Skin.
- (20) Filon, F. L.; Boeniger, M.; Maina, G.; Adami, G.; Spinelli, P.; Damian, A. Skin Absorption of Inorganic Lead (PbO) and the Effect of Skin Cleansers. *J. Occup. Environ. Med.* **2006**, *48* (7), 692–699.
- (21) Ellman, G. L. Tissue Sulfhydryl Groups. *Arch. Biochem. Biophys.* **1959**, *82* (1), 70–77. [https://doi.org/10.1016/0003-9861\(59\)90090-6](https://doi.org/10.1016/0003-9861(59)90090-6).
- (22) Dewhurst, C. D. Graphical Reduction and Analysis Small-Angle Neutron Scattering Program: GRASP. *J. Appl. Crystallogr.* **2023**, *56* (5), 1595–1609. <https://doi.org/10.1107/S1600576723007379>.

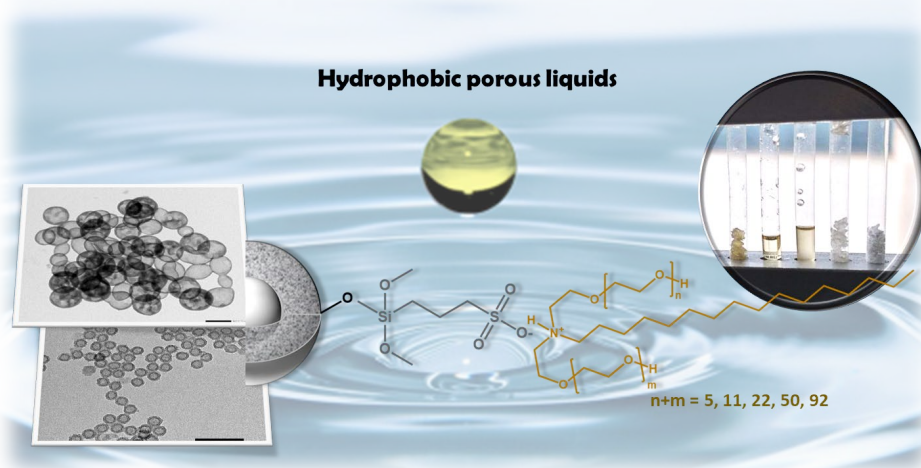
Appendix H
Publications during the PhD

- (23) Musić, S.; Filipović-Vinceković, N.; Sekovanić, L. Precipitation of Amorphous SiO₂ Particles and Their Properties. *Braz. J. Chem. Eng.* **2011**, *28*, 89–94. <https://doi.org/10.1590/S0104-66322011000100011>.
- (24) Morineau, D.; Xia, Y.; Alba-Simionesco, C. Finite-Size and Surface Effects on the Glass Transition of Liquid Toluene Confined in Cylindrical Mesopores. *J. Chem. Phys.* **2002**, *117* (19), 8966–8972. <https://doi.org/10.1063/1.1514664>.
- (25) Ben Ghazi-Bouvrande, J. B. Les liquides poreux : un nouveau concept pour la séparation chimique. phdthesis, Montpellier, Ecole nationale supérieure de chimie, 2022. <https://theses.hal.science/tel-03880557> (accessed 2023-03-14).
- (26) Gunathilake, C.; Kadanapitiye, M. S.; Dudarko, O.; Huang, S. D.; Jaroniec, M. Adsorption of Lead Ions from Aqueous Phase on Mesoporous Silica with P-Containing Pendant Groups. *ACS Appl. Mater. Interfaces* **2015**, *7* (41), 23144–23152. <https://doi.org/10.1021/acsami.5b06951>.
- (27) Wu, S.; Li, F.; Xu, R.; Wei, S.; Li, G. Synthesis of Thiol-Functionalized MCM-41 Mesoporous Silicas and Its Application in Cu(II), Pb(II), Ag(I), and Cr(III) Removal. *J. Nanoparticle Res.* **2010**, *12* (6), 2111–2124. <https://doi.org/10.1007/s11051-009-9770-3>.
- (28) Heidari, A.; Younesi, H.; Mehraban, Z. Removal of Ni(II), Cd(II), and Pb(II) from a Ternary Aqueous Solution by Amino Functionalized Mesoporous and Nano Mesoporous Silica. *Chem. Eng. J.* **2009**, *153* (1), 70–79. <https://doi.org/10.1016/j.cej.2009.06.016>.
- (29) Quirarte-Escalante, C. A.; Soto, V.; de la Cruz, W.; Porras, G. R.; Manríquez, R.; Gomez-Salazar, S. Synthesis of Hybrid Adsorbents Combining Sol–Gel Processing and Molecular Imprinting Applied to Lead Removal from Aqueous Streams. *Chem. Mater.* **2009**, *21* (8), 1439–1450. <https://doi.org/10.1021/cm801480v>.
- (30) Bjørklund, G.; Crisponi, G.; Nurchi, V. M.; Cappai, R.; Buha Djordjevic, A.; Aaseth, J. A Review on Coordination Properties of Thiol-Containing Chelating Agents Towards Mercury, Cadmium, and Lead. *Molecules* **2019**, *24* (18), 3247. <https://doi.org/10.3390/molecules24183247>.

Hydrophobic Porous Liquids with Controlled Cavity Size and Physico-Chemical Properties

Lorianne Ginot, Amal Ben Boubker, Fabrice Giusti, Sandrine Dourdain* and Stéphane Pellet-Rostaing
ICSM, Univ Montpellier, CEA, CNRS, ENSCM, 30207 Marcoule, France

Email: sandrine.dourdain@cea.fr



To cite this: L. Ginot, A. El Bakkouche, F. Giusti, S. Dourdain, S. Pellet-Rostaing, Hydrophobic Porous Liquids with Controlled Cavity Size and Physico-Chemical Properties. *Adv. Sci.* 2024, 11, 2305906. <https://doi.org/10.1002/adv.202305906>

Abstract

Developing greener hydrometallurgical processes implies offering alternatives to conventional solvents used for liquid-liquid extraction (LLE) of metals. In this context, it is proposed to substitute the organic phase by a hydrophobic silica-based porous liquid (PL). Two different sulfonated hollow silica particles (HSPs) are modified with various polyethoxylated fatty amines (EthA) forming a canopy that provides both the targeted hydrophobicity and liquefying properties. This study shows that these properties can be tuned by varying the number of ethylene oxide units in the EthA: middle-range molecular weight EthAs allow obtaining a liquid at room temperature, while too short or too long EthA leads to solid particles. Viscosity is also impacted by the density and size of the silica spheres: less viscous PLs are obtained with small low-density spheres, while for larger spheres (*c.a.* 200 nm) the density has a less significant impact on viscosity. According to this approach, hydrophobic PLs are successfully synthesized. When contacted with an aqueous phase, the most hydrophobic PLs obtained allow a subsequent phase separation. Preliminary extraction tests on three rare earth elements have further shown that functionalization of the PL is necessary to observe metal extraction.

Keywords

Porous liquids, silica hollow spheres, nanoscale ionic materials, hydrophobicity, solvent extraction.

Introduction

Liquid-liquid extraction (LLE) is a widely used separation technique for many applications, ranging from analytical methods to water treatment or industrial hydrometallurgical processes.¹ In this latter case, LLE is the most common technique applied since it can handle large amounts of metals, by generally employing low-cost compounds. For instance, it is largely applied in the recycling chemistry of critical metals such as rare earth elements from permanent magnets.² Besides, liquids are far simpler to manipulate and store than gas or solids. LLE unfortunately implies the use of huge amounts of solvents and diluents, thus having a high environmental cost,^{1,2} and it also faces the well-known drawback of the formation of a third phase.³ Therefore, alternatives are required, and a number of studies are focusing on new eco-friendly formulations^{1,4} or non-volatile organic phases like ionic liquids or deep-eutectic solvents.⁵⁻⁷ Flotation is also considered to develop new routes of separation.⁸ Solid-liquid extraction is usually proposed as an alternative to replace the solvent phase by a porous solid capable of extracting the elements of interest generally with excellent capacity and selectivity.^{3,9-11} Despite these good performances, the use of solids requires to change infrastructure with respect to already existing ones. Given that they combine the properties of porous solids with the easiness of manipulating liquids, porous liquids might be good candidates as an alternative to the solvent phase in LLE.

Porous liquids (PLs) have been a fast-growing field of research since their concept was first introduced by O'Reilly *et al.*¹² in 2007. They describe liquid materials at room temperature or below 100 °C that have an intrinsic porosity, due to the presence of host cage molecules, particles or networks, either dispersed in a hindered solvent, chemically modified, or physically treated to ensure a liquid behavior through weak interactions. This intrinsic porosity is sustainable and significant enough to consider these materials as carriers for many species. Despite their high potential, the application of PLs is consistently restricted to gas sorption so far.¹³⁻¹⁶ In fact, among the different kinds of PLs that exist, most of them contain cavities less than 1 or 2 nanometers large, implying that the pores would be too small to welcome larger species like metal ions or metalorganic particles. In contrast, silica-based PLs are promising materials for metal extraction or catalysis because of their low cost, tunable and relatively easy synthesis, and the nanometric size of their cavities.^{14,17} Hence, Hemming *et al.*¹⁸ recently demonstrated the possibility of encapsulating nanoparticles of gold, platinum and palladium inside the silica hollow cores during their synthesis, without significantly affecting the grafting steps forming the PL afterward. Furthermore, Yang *et al.* successfully separated heavy metals like lead and copper from a water phase by using a magnetic silica-based PL to make the collection possible.^{1957575757[1]} In addition, at variance with LLE requiring the use of high amount of toxic volatile solvents, solvent-free silica-based PLs account for a process with low impacts on the environment.

Silica-based PLs were synthesized for the first time by Zhang *et al.*¹⁴ in 2015. This synthesis consists in grafting a cationic organosilicon to the surface of hollow silica particles (HSPs), then adding a second layer of a sulfonated polyethylene glycol (PEG) derivative bound by ionic interactions. This last step is responsible for the liquid behavior of the porous material, along with its hydrophilicity, and no additional solvent is required. Many of the latest studies reported in the literature are restricted to systems based on Zhang's method,^{15,20-23} and only few knowledge has been gathered about their synthesis and their tunable properties up to now. Very recently, Ben Ghazi Bouvrande *et al.*²³ assessed various experimental conditions for the synthesis of silica-based PLs and highlighted the impact of different parameters (such as temperature and emulsion formulation) on PLs final properties.

Meanwhile, Lai *et al.*²⁴ investigated the impact of the grafting density and the molecular weight of the tethered groups on the permeability and the viscosity of the PL.

Considering the numerous applications involving HSPs described in the literature, it would be worthy to consider their extension to silica-based PLs. Hence, the fabrication of stable antibacterial coatings,²⁵ functional superhydrophobic surfaces,^{26–28} smart inks and paints,^{29,30} and functional glasses, as well as catalysis in hydrophilic or hydrophobic media,^{18,31} cosmetics,³² and LLE are all applications that could fit to these innovative liquid materials, along with gas sorption and separation. To broaden the applications of PLs, it is necessary to adapt the synthesis to tune their structural and physicochemical properties. For instance, LLE requires a hydrophobic PL, as well as adjustable and functionalizable silica cores. In particular, the cavities of the HSPs used by Zhang *et al.* are small (14 nm of internal diameter) whereas syntheses of bigger HSPs with larger pores inside the shell are largely described in literature (with internal diameters over 100 nm).^{27,33–35} Forming a porous liquid with such big cavities could lead to an even broader range of applications. In particular for LLE, a bigger cavity could mean more room for a possible metallic nucleation, while larger pores could facilitate the diffusion of metallic ions inside the shell.

This study proposes a new route to synthesize hydrophobic PLs with adjustable size of cavities. As illustrated in **Figure AA1a**, PLs with various particles size, density and porosity were prepared: small non-porous silica nanoparticles (SiNPs) and porous HSPs with two different sizes (“small” HSPs, which are few tens of nanometers large, referred to as sHSPs, and “big” HSPs, which are few hundreds of nanometers large, referred to as bHSPs) were compared. Inspired from the work of Rodriguez *et al.*³⁶, the particles were then covalently grafted by a sulfonated organosilicon. These modified silica spheres were further liquefied by the neutralization of the sulfonated surfaces with commercially available *N,N*-polyethoxylated fatty amines (EthAs) forming the organic canopy (**Figure AA1b**). The length of the hydrocarbon tail of these amphiphilic amines derivatives was considered as sufficiently hydrophobic and was fixed (mixture of C₁₆ to C₁₈ alkyl chains) whereas the length of the two PEG substituents was varying with a total number of ethylene oxide units (n+m) ranging from 5 to 92, allowing to tune the hydrophobicity of the final material.

Before achieving the synthesis of the corresponding PLs, the silica spheres were synthesized and characterized in terms of shape, size, density and porosity. The physico-chemical properties of PLs were also determined (physical state, melting temperature, viscosity, and molecular structure). Given that hydrophobicity is a key parameter for an application in LLE, it has also been assessed for two PLs by evaluating their behavior when contacted with water. Finally, preliminary extraction tests on three rare earth elements (neodymium, praseodymium, dysprosium) generally found in permanent magnets were conducted on PLs after their functionalization with a specific chelating ligand.

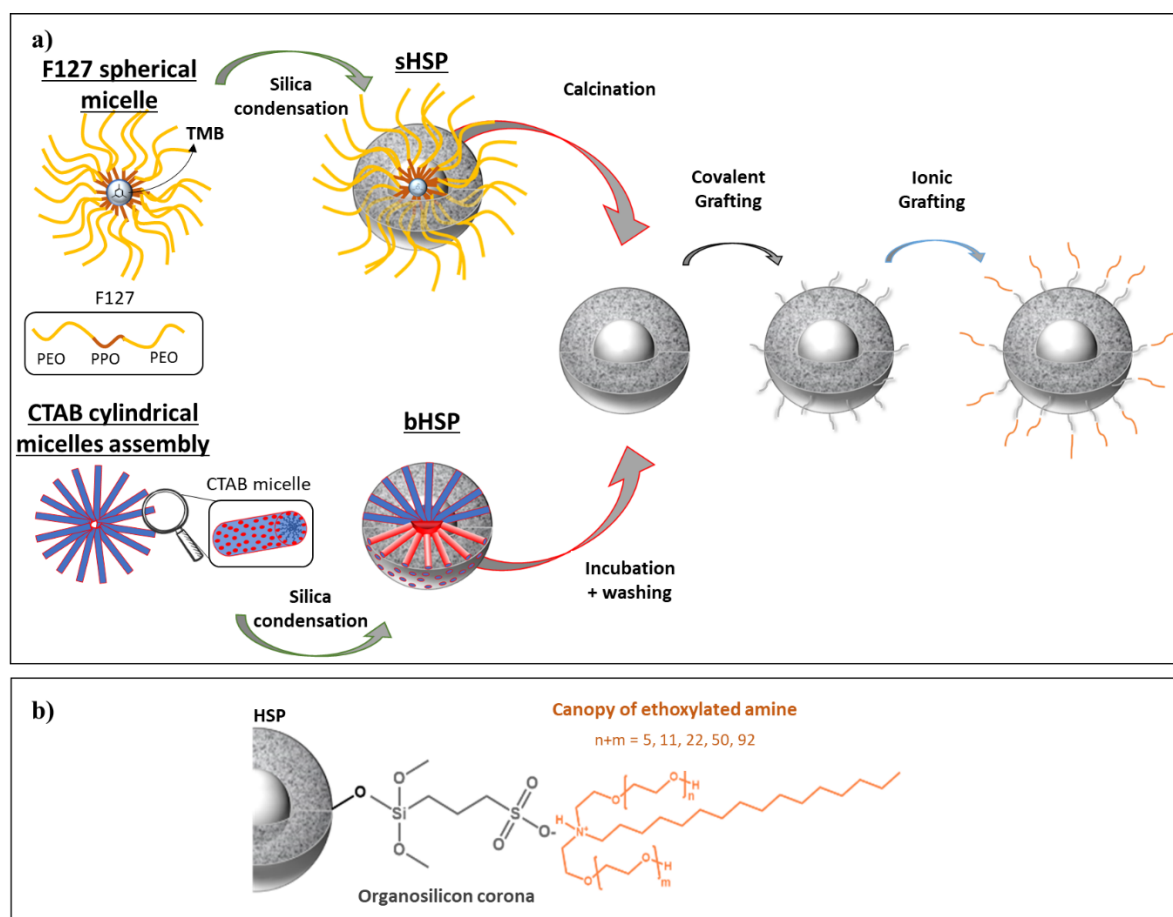


Figure AA1. Synthesis of the porous liquids. **a)** The main four steps of the synthesis: HSP formation, calcination, covalent grafting of the sulfonated organosilicon, and ionic binding with the ethoxylated fatty amine. **b)** Scheme of the final grafting at the HSP surface. For the sake of simplification, a generic structure of commercially available modified tallow amines was given as polyethoxylated derivatives of hexadecylamine. The overall number of ethylene oxide units ($n+m$) was varied from 5 to 92.

Results and discussion

Synthesis and characterization of the hollow silica particles

The basic building blocks of the PLs are the HSPs, whose size, cavity diameter, and shell porosity can be tuned by using different synthesis methods. In this study, three kinds of silica cores were investigated. Small hollow particles, sHSPs were synthesized with the use of the oily 1,3,5-tetramethylbenzene (TMB) and the amphiphilic F127 as templating agents.¹⁴ Calcination of the resulting material provided the expected sHSPs in quantitative yield. Big hollow particles, bHSPs were obtained by following a procedure derived from the Stöber method³³ with an additional incubation step in water leading to the formation of the hollow cavities of bHSPs (**Figure AA1a**). Besides, commercially available SiNPs were used as a non-porous reference. Transmission electron microscopy (TEM) imaging allowed to observe the cavity of the HSPs and to distinguish them from the SiNPs that showed no contrast difference between their core and their surface (**Figure AA2**).

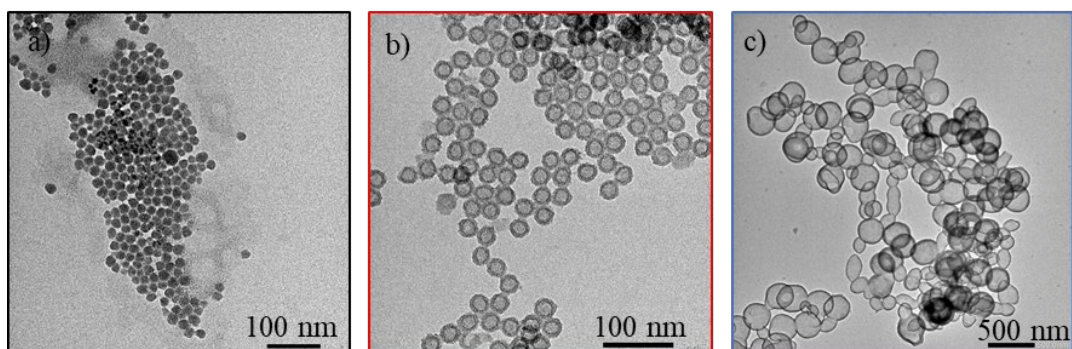


Figure AA2. TEM images of **a)** SiNPs (x80k) **b)** sHSPs (x80k), and **c)** bHSPs (x10k).

It can be noticed that some of the bHSPs present a non-perfect spherical shape. This can be assigned to the use of a soft template for such big particles.²⁷ The internal and external diameters could be extracted from the images. SiNPs have a diameter of 17.4 ± 2.8 nm, sHSPs are in the same size range with an external diameter of 25.4 ± 1.4 nm, and an internal diameter of 14.8 ± 1.3 nm, while bHSPs are one order of magnitude bigger with mean external and internal diameters of 236.0 ± 64.4 nm and 203.6 ± 58.8 nm respectively (**Figure S2**, Supporting Information). These results are gathered in **Table AA1** and **Table S1** (Supporting Information). TEM results were correlated with those deduced from SAXS and USAXS (**Figure AA3**). The three powders provide an increase in scattering intensity at low angles, which is characteristic of nanospheres. Oscillations were fitted with SasView software for SiNPs and sHSPs. They correspond to monodisperse nanospheres and nanoshells respectively, with diameters consistent with the ones obtained from TEM images (**Table S1**, **S2** and **Figure S3**, Supporting Information). The less pronounced oscillations observable for SiNPs are consistent with a higher polydispersity for these particles. bHSPs are found to be too big and polydisperse to provide any proper fit in this Q range.

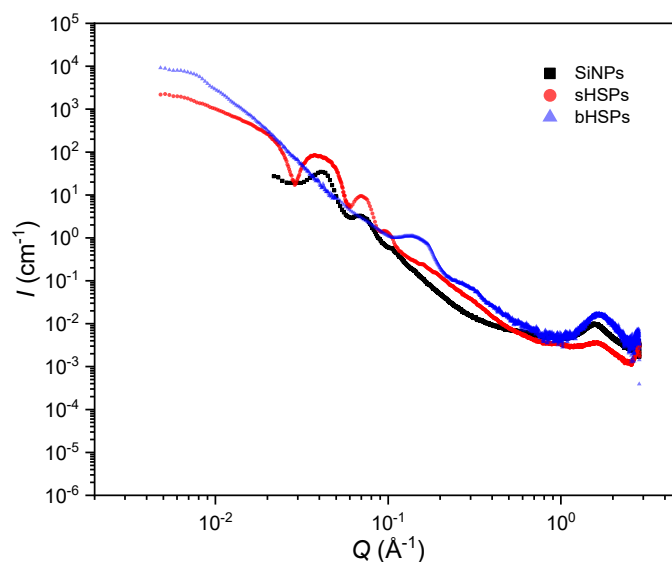


Figure AA3. Comparison of the structural organization of SiNPs (black squares), sHSPs (red circles), and bHSPs (blue triangles) powders by SAXS-USAXS.

Additionally to the size of the particles, their density and their porosity are expected to play a role on the dynamics and on the viscosity of the final PL. The packing densities of the three powders were measured by packing a calibrated mass of the materials in a graduated container and measuring their volume (**Table AA1**). SiNPs are the densest particles (1.02 ± 0.06) because of their smallest size and insignificant porosity. In the same manner, sHSPs are denser than bHSPs (0.56 ± 0.06 and 0.12 ± 0.06 respectively) because they are smaller and less porous.

Table AA1. Relationship between the size, packing density and porous properties of the powders for the three silica cores used to synthesize hybrid liquids.

	External diameter (TEM) [nm]	Internal diameter (TEM) [nm]	Packing density [g/cm ³]	S _{BET} [m ² /g]	Porous volume ^{b)} [cm ³ /g]	Pores size ^{c)} [nm]
SiNPs	17.4 ± 2.8	-	1.02 ± 0.06	175	0.42	-
sHSPs	25.4 ± 1.4	14.8 ± 1.3	0.56 ± 0.06	691 ^{a)}	0.66	1.4
bHSPs	236.0 ± 64.4	203.6 ± 58.8	0.12 ± 0.06	981	0.78	1.5/ <u>3.7</u>

^{a)}The presence of a high content of microporosity in sHSPs induces an artificial increase in the BET specific surface area; ^{b)}Porous volume recorded at $P/P_0 = 0.87$ to exclude the interparticle void; ^{c)}Pores size in the silica shell for sHSPs and bHSPs, the underlined value corresponds to the most represented.

To correlate the density with the porosity of the spheres, N₂ sorption measurements were also performed (**Figure AA4**) and the main characteristics are gathered in **Table AA1**. For the SiNPs, a Type IV isotherm (named according to the IUPAC classification) was obtained, with a low volume of adsorbed gas (0.42 cm³/g), suggesting the presence of a few mesopores. Similarly, sHSPs displayed a Type I + Type IV hybrid isotherm, with an H1 hysteresis at relative pressures between 0.5 and 0.87, revealing a large distribution of mesopores (the cavities) and the presence of a microporosity in the shell. The porous volume is estimated at 0.66 cm³/g (see details in Section S2, Supporting Information), and the diameter of the pores is 1.4 nm based on density functional theory (DFT) calculations (**Figure AA4**, insert). The signal of bHSPs approaches a hybrid Type II + Type IV curve typical of a macroporous solid containing micro- and mesopores. In this case, the cavity inside the particle is considered as a macropore because its diameter overcomes 50 nm. Moreover, the presence of two steps (for relative pressures ≈ 0.005 and 0.3) instead of one indicates two different populations of micro- or mesopores in the shell. The porous volume is 0.78 cm³/g (see Section S2, Supporting Information) and this high porosity is consistent with the lowest density discussed previously. The distribution obtained by DFT confirms that the major part of the pores has a diameter of 3.7 nm and the minor part has a diameter of 1.5 nm. The presence of mesopores is encouraging for application in LLE.

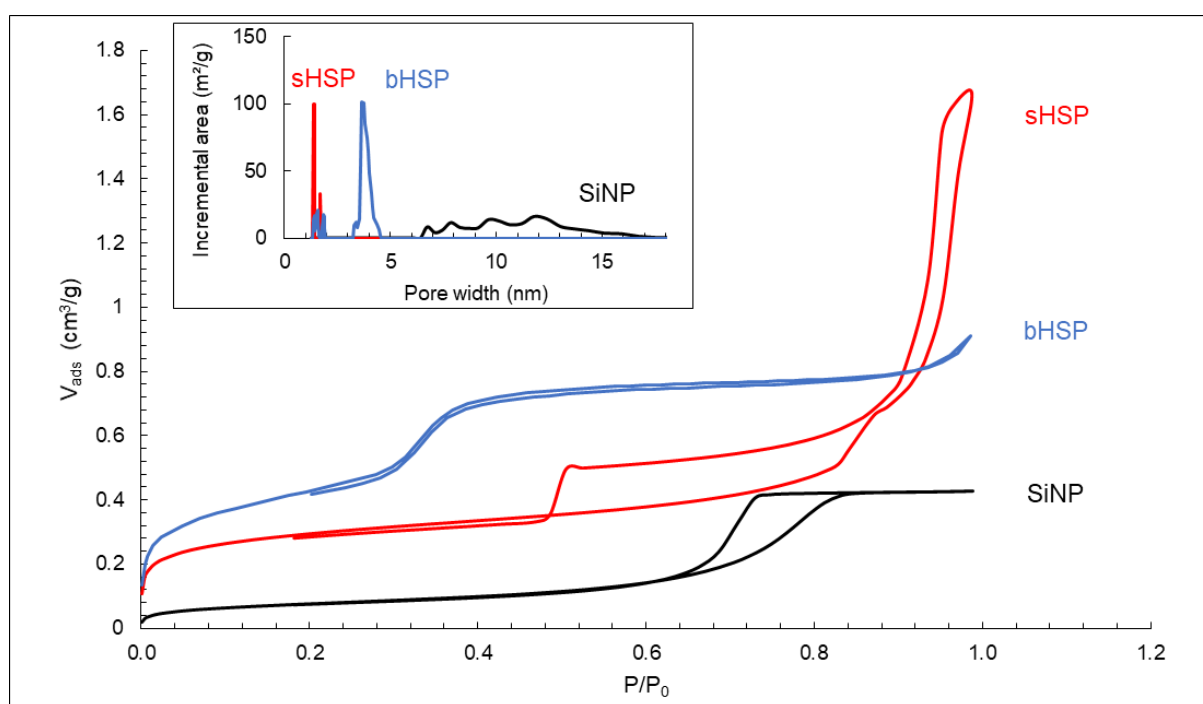


Figure AA4. Adsorption/desorption isotherms of N₂ sorption at 77K in SiNPs (black), sHSPs (red), and bHSPs (blue). Insert: pore size distribution expressed by surface area (DFT).

Synthesis and characterization of the porous liquids

Synthesis of porous liquids

The PLs synthesis involved the modification of silica spheres with surrounding amphiphilic brushes whose chain mobility, ionic interaction strength, and hydrophilic/lipophilic balance (HLB) were expected as some of the main key parameters ruling the properties of the modified materials. This modification consisted first in the covalent grafting of a sulfonated organosilicon, namely the 3-(trihydroxysilyl)-1-propane sulfonic acid (SIT), onto the surface of the silica particles achieved in heated lightly acidic (adjustment at pH 5-6 with NaOH 1M) aqueous solutions (**Figure AA1**).³⁶ It was then followed by the protonation of the tethered sulfonate groups by using a cation-exchanger column. Finally, the recovered high sulfonic acid-containing material was allowed to establish an ionic interaction with stoichiometric amount (neutralization monitored by pH-meter) of a fatty ethoxylated amine (EthA) carrying two PEG arms containing a tunable number of ethylene oxide units (n and m with $n+m = 5, 11, 22, 50, 92$; labelled EthA-5 to EthA-92). These amines were all commercially available, except for EthA-92 that was synthesized in the laboratory according to the procedure described by Atta *et al.*³⁷ by ethoxylation of the stearylamine with the corresponding PEG (see section S1, Supporting Information). All modified materials were distinguished according to the nature of the silica sphere precursor and the $n+m$ value of the associated EthA (*e.g.*, PL-sHSPs-22 was made with sHSPs and EthA-22). For liquids based on SiNPs, they were labeled PL-SiNPs even though these materials are non-porous. Their physico-chemical properties have been summarized in **Table AA2**.

Size and shape analysis of PLs

In **Figure AA5**, TEM images show that the particles' shapes and sizes are not altered by the chemical modification. Additionally, the particles appear less aggregated on the copper grid than in **Figure AA2**, suggesting the presence of the organic molecules between the particles. However, the PEG length

seemed to have only little impact on the distance between particles (**Figure S4** and **Table S4**, Supporting Information) and was ≈ 30 nm in all cases.

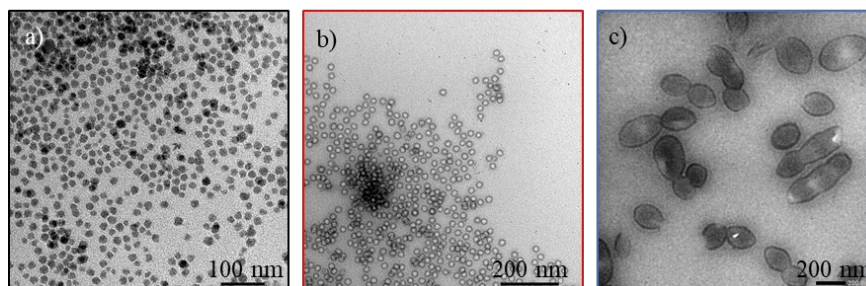


Figure AA5. TEM images of PLs **a)** PL-SiNPs-11 (x60k), **b)** PL-sHSPs-11 (x40k), **c)** PL-bHSPs-11 (x20k).

Structural analyses of PLs with SAXS and USAXS measurements (**Figure S5**, Supporting Information) corroborated these results. The remaining oscillations are characteristic of the silica cores integrity. A structural peak is moreover present for all the PLs, corresponding to a correlation distance of 3.9 to 4.0 nm (except for PL-sHSPs-92 in **Figure S5b**). This peak reflects a structural contribution of the amorphous amine since it is also present in the signals of the pristine amines in **Figure S5d** (except for EthA-50 and EthA-92). As observed previously,³⁸ this peak was attributed to nanostructuring of the PEG chains induced by water.

Assessment of the grafting efficiency

The grafting efficiency was primarily evaluated by TGA and FTIR spectroscopy. **Figure AA6a** shows the thermal decomposition of pure EthA-22 and PL-sHSPs-22 under air, at a rate of 5 °C/min.

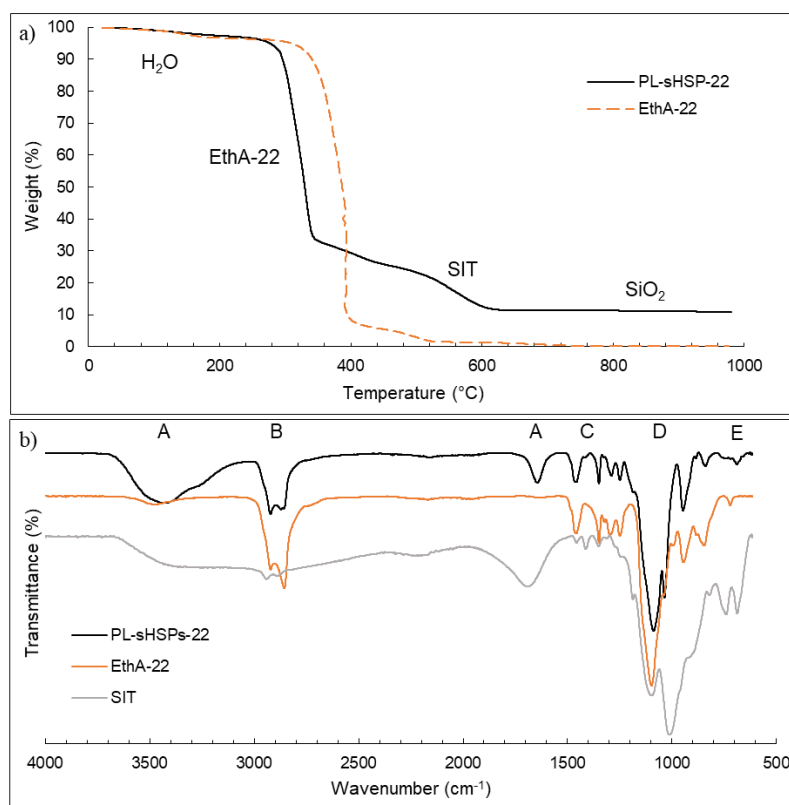


Figure AA6. Grafting efficiency of sHSPs in PL-sHSPs-22 proved by **a)** thermal decomposition of PL-sHSPs-22 and EthA-22, **b)** FTIR spectra of PL-sHSPs-22, EthA-22 and SiO₂.

A large fall in weight (68%) was observed at 325 °C, which is attributed to the deterioration of the canopy. Also, a small percentage of the weight loss ($\approx 6\%$) was visible at ≈ 380 °C, which may be due to a molecular weight dispersion of the commercial EthA. Indeed, this dispersion was also visible in the decomposition of the pure amine. Furthermore, the weight loss in the signal of EthA-22 occurred at higher temperatures, indicating that the presence of silica nanoparticles lowers its thermal stability.³⁹ A second major weight loss at 550 °C (12.4%) was caused by the deterioration of the SIT corona, and the residual weight percentage finally gave the silica content of the PL (10.9% in this case). In addition, at temperatures ≈ 100 °C, a small weight loss of 2.6% was revealed, corresponding to residual water contained in the PL. Repetitions of the same measurement led to water contents varying between 1% and 5%, suggesting that the material is highly hygroscopic. The measurements were performed for all the PLs (**Figure S6**, Supporting Information), and two histograms are represented in **Figure S7** (Supporting Information) to summarize these results (**Figure S7a** considers the impact of the chains lengths whereas **Figure S7b** shows the impact of the core nature). When the amine length was varied from $n+m = 5$ to 92 (**Figures S6a, S7a**), the weight content corresponding to the canopy was consistently increased. Details on the molar ratios of Amine/SiO₂ and Amine/SIT are provided in **Tables S5, S6** (Supporting Information).

FTIR spectroscopy confirmed the efficient grafting of the organosilicon and of the polyethoxylated canopy (**Figure AA6b**). Two small absorption bands at 1413 cm⁻¹ (C) and 687 cm⁻¹ (E) appear after the addition of the SIT onto the silica spheres, which are respectively assigned to the S = O stretching of the sulfonate and to the vibration of the CH₂ groups of the propyl chain. Two other peaks at 2918 and 2857 cm⁻¹ (B) correspond to the stretching of CH₂ groups and an increase in intensity of these peaks was observed after the addition of the amine due to its long alkyl chain. The very intense band at 1066 cm⁻¹ (D) includes both the Si-O-Si and the CH₂-CH₂-O stretching.^{23,40} The two broad bands at 3433 and 1645 cm⁻¹ (A) are reported to be characteristic of OH bonds in water molecules.^{23,41} In **Figure S8** (Supporting Information), the FTIR signals of all the PL-sHSPs normalized according to the peak (E) were consistent with an increase in the number of ethoxy groups when varying the amines from 5 to 92.

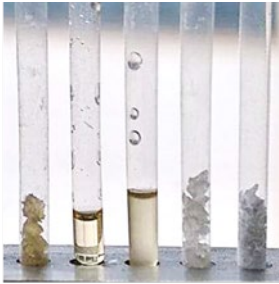
Physical properties of porous liquids

PLs were further characterized to investigate their macroscopic properties, and how they are influenced by the nature of the silica core and of the canopy. For comparison, it is worthy to note that pure amines EthA-50 and EthA-92 are in a solid state whereas the three low molecular weight amines (EthA-5, EthA-11, and EthA-22) are in a liquid state at room temperature. **Table Aa2** gathers the physical states of PLs obtained at room temperature while varying the number of ethoxylated groups of the canopy from 5 to 92, onto three types of silica spheres: SiNPs, sHSPs and bHSPs.

Among all the PLs based on sHSPs, only PL-sHSPs-11 and PL-sHSPs-22 display a liquid behavior at room temperature. PL-sHSPs-5 becomes solid because of a too-high ratio of silica content over organic molecules. On the other hand, PL-sHSPs-50 and PL-sHSPs-92 are also solid at room temperature. This behavior is assumed to be caused by crystalline domains in longer ethoxylated chains with hydrogen bonding occurring and leading to less mobility.²⁴ Additionally, a longer ethoxylated chain is more likely to interact with a neighboring silica particle, creating a network-like structure.⁴² DSC measurements allowed to compare the melting temperatures of all the PLs (**Table AA2**; **Figure S9**, Supporting Information). They are consistent with the previous observations.

Table AA2. Physical state of PLs at room temperature, along with their melting temperature (T_m) in °C and the viscosity (η) in Pa.s at 50°C and $\dot{\gamma} = 10 \text{ s}^{-1}$ (*italic*). The picture shows all the PL-sHSPs at room temperature.

		Hydrophobicity ←				
n+m	5	11	22	50	92	
PL-SiNPs		liquid	liquid		solid	
			14.2°C		54.8°C	
			<i>10.8 ± 0.5 Pa.s</i>			
PL-sHSPs	solid	liquid	liquid	solid	solid	
	no melting	10°C	2.8°C	40.6°C	54.8°C	
		<i>28.6 ± 2.0 Pa.s</i>	<i>3.1 ± 0.5 Pa.s</i>	<i>17.9 ± 6.0 Pa.s</i>		
PL-bHSPs	solid	liquid	liquid			
	50.5°C		15.3°C			
			<i>36.1 ± 0.5 Pa.s</i>			



Furthermore, the viscosities of the PLs were measured at different temperatures, and **Figures S10, S11** (Supporting Information) show the results for PL-sHSPs-22. Note that condensation occurred at 15 °C, leading to a significant decrease in viscosity, therefore the corresponding value has not been reported on **Figure S10**. At 20 °C, the viscosity of PL-sHSPs-22 is very high (10^4 Pa.s), but it exponentially decreases when increasing the temperature: at 50 °C, the viscosity is $\approx 10^0$ Pa.s. This value is comparable to the ones reported in literature for similar PLs.^{43,44}

The impact of the PEG length of the EthAs on the viscosity was studied at 50 °C. The viscosity of the PLs-sHSPs at a flow shear rate ($\dot{\gamma}$) of 10 s^{-1} are reported in **Table AA2**. A minimum of viscosity was found for PL-sHSPs-22, in accordance with the physical states and the melting points that were discussed previously. However, the viscosity of PL-sHSPs-92 was measured at 57 °C, just above its melting point (55 °C), and it happened to be lower than other PLs, with a value of 2.0 ± 0.5 Pa.s. This result suggests that at high molecular weights, PEGylated amines are playing a role of plasticizer and decrease the viscosity, even if the melting point remains relatively high.

The influence of the silica core was also studied by measuring the viscosity of PL-SiNPs-22, PL-sHSPs-22 and PL-bHSPs-22 at 50 °C and 10 s^{-1} (**Table AA2**). The lowest viscosity was obtained for PL-sHSPs-22 (3.1 ± 0.5 Pa.s) because of i) the small size of sHSPs with respect to bHSPs, and ii) the small density of sHSPs with respect to SiNPs. An intermediate viscosity of 10.8 ± 0.5 Pa.s was found for PL-SiNPs-22. By contrast, PL-bHSPs-22 displayed a higher viscosity (36.1 ± 0.5 Pa.s), suggesting that the large diameter of bHSPs contributes to a decrease in molecular mobility, even though the density of these spheres is very low (**Table AA1**). However, it is worthy to note that when it comes to lightest amines, the trend is different. In fact, a liquid behavior was observed for PL-bHSPs-5 above 50 °C, while PL-sHSPs-5 was a solid at any temperature. Thus, in this latter case, the density of the spheres has a more significant impact than their diameter. In conclusion, the obtained results illustrate a balance between the

particles sizes and densities in the contribution to the viscosity of the final PL, that is intrinsically linked to the size of the organic canopy.

Hydrophobicity and stability in water

By varying the number of ethoxylated units in the lateral PEG chains of the amine in the canopy of PLs, it was possible to obtain either hydrophilic or hydrophobic materials.

A simple test was first conducted by mixing a small quantity of PL-sHSPs-11 and PL-sHSPs-22 with water (1:3 w/w and 1:1 w/w respectively). After centrifugation, PL-sHSPs-11 separated well from the aqueous phase (**Figure AA7a**) whereas PL-sHSPs-22 and water were forming one viscous phase (**Figure AA7b**). When adding more water (1:20 w/w, **Figure AA7c**), PL-sHSPs-22 was totally solubilized in the aqueous phase and the centrifugation just allowed to observe a small fraction of silica in the bottom of the tube. Therefore, it can be assumed that the amine was solubilized in water, leading to the deterioration of the canopy of the PL in this latter case.

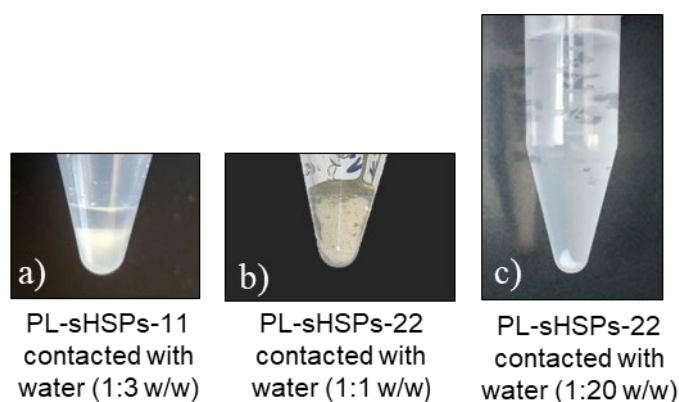


Figure AA7. Impact of contacting water with PL-sHSPs-11 and PL-sHSPs-22.

In order to confirm these results, SAXS measurements have been achieved on the different phases of the samples (**Figure AA8**). In **Figure AA8a** concerning PL-sHSPs-11, the oscillations and the structural peak at 0.16 \AA^{-1} characteristic of the PLs is maintained after contact with water, suggesting that the structure of the PL was not altered by the water. However, some water entered the PL, as indicated by the large “solvent” peak at $\approx 1.5 \text{ \AA}^{-1}$ that indicates the presence of both silica and water. In the aqueous phase, the oscillations disappeared but the increase in intensity at small angles can be attributed to the presence of silica shells and organic molecules. Hence, a small amount of PL is expected to be solubilized in water. In the case of PL-sHSPs-22 (**Figure AA8b**), a small amount of water does not significantly change the structure of the PL whereas a higher dilution leads to a signal really similar to the amine EthA-22 in water (cyan curve). This corroborates the previous observation of a precipitate in **Figure AA7c**: the solid corresponds to the sHSPs grafted with the sulfonated organosilicon derivative while the amine EthA-22 is solubilized in water. These results suggest that there is a threshold in the number of ethoxylated units that can be present without making the PL hydrophilic.

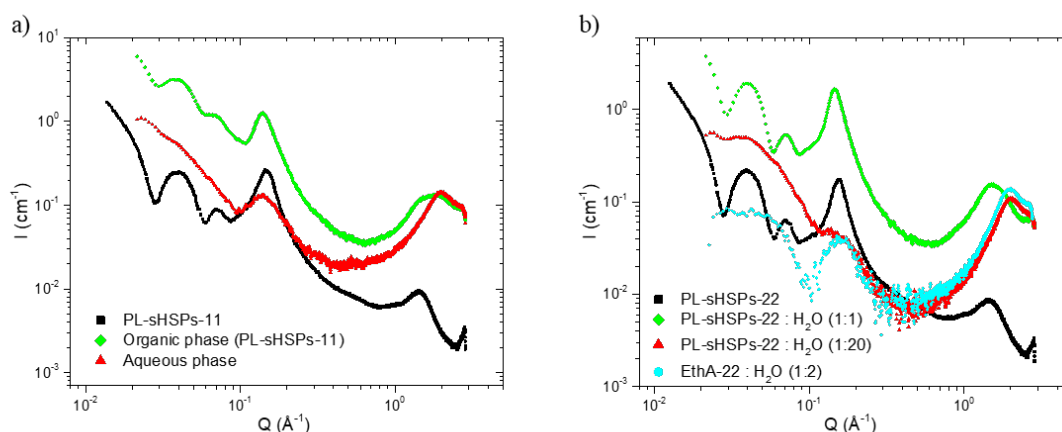


Figure AA8. Effect of the water on the structure of **a)** PL-sHSPs-11 measured by SAXS. Black: PL-sHSPs-11 before contact, green: PL-sHSPs-11 after contact, and red: the aqueous phase of the contact test, **b)** PL-sHSPs-22. Black: pure PL-sHSPs-22, green: PL-sHSPs-22 and a small amount of water (1:1 w/w), red: PL-sHSPs-22 and a huge amount of water (1:20 w/w), cyan: EthA-22 solubilized in water (1:2 w/w).

TGA and total organic carbon (TOC) analyses were also performed to quantitatively support these results. In the case of PL-sHSPs-11 contacted with water, the organic phase contained 51% of water, but it dried spontaneously at room temperature in few hours. It is assumed that this water was trapped inside the silica particle and the first hydrophilic corona. After drying, the TGA signal totally overlapped the one of PL-sHSPs-11 before contact, confirming the SAXS data concerning the stability of this PL against water (**Figure S12a**, Supporting Information). Furthermore, 10% of the PL-sHSPs-11 was lost in the aqueous phase, according to the TOC analysis. This small fraction confirms the hydrophobicity of the PL conferred by the amine EthA-11. In the case of PL-sHSPs-22, TGA showed that after aqueous contact, 6.4% of organic molecules were present in water, along with 0.7% of silica (**Figure S12b**, Supporting Information). These values led to a 100% of the initial weight of PL-sHSPs-22 that had been dissolved in water (except for a negligible weight of silica that has precipitated).

At this point, it is interesting to note that because EthAs with $n+m$ up to 50 were industrial amphiphilic compounds derived from tallow mixtures, the length of the alkyl chain could not be accurate and lay between 16 to 18 carbon atoms. In the case of EthA-92 that was synthesized in the laboratory, the number of carbon atoms was set to 18 as the starting material was the octadecylamine. In all cases, these carbon chains were considered to provide a sufficient hydrophobic character to the overall material. Therefore, this study concerned only the influence of PEGs length, and no peculiar attention was paid to that of the alkyl tail.

Functionalization and application in rare earth extraction

To apply PLs in LLE, not only have they to be hydrophobic and contain large pores, but a functionalization is also expected to ensure an enhanced and specific extraction of the targeted metal. In this study, functionalization of the sHSPs by co-condensation of tetramethyl orthosilicate (TMOS) with silanized ethylenediaminetetraacetic acid (Si-EDTA) was performed at 16:1 TMOS:Si-EDTA molar ratio, and rather than calcination, a further step of washing with EtOH and HCl (pH1) for 24h was implemented. Preliminary tests of LLE on three rare earth elements (neodymium, praseodymium, dysprosium) were performed. To simulate a magnet lixiviate, they were dissolved in nitric acid at pH 2 at initial concentrations of 500 ppm, 68 ppm and 50 ppm for Nd, Pr, and Dy respectively. This solution

was contacted with either PL-sHSPs-11 or PL-sHSPs-SiEDTA-11 during 24h at room temperature. The metal concentrations in the aqueous phases were measured by Inductively Coupled Plasma (ICP) analysis and the resulting extraction yields and extraction capacities are given in **Table AA3**. The PL-sHSPs-11 with no functional groups did not show any extraction of rare earth elements, whereas PL-sHSPs-SiEDTA-11 displayed measurable extraction yields and significant loading capacities (Q_e) for the three metals. This proof of concept therefore shows that the presence of functional groups is necessary to perform efficient LLE with such PLs.

Table AA3. Extraction yield and capacity of Nd, Pr and Dy by PL-sHSPs-11 and PL-sHSPs-SiEDTA-11.

	PL-sHSPs-11		PL-sHSPs-SiEDTA-11	
	$E\%$ (%)	Q_e (mmol/g)	$E\%$ (%)	Q_e (μ mol/g)
Nd	Traces	-	2.3	71.9
Pr	Traces	-	6.0	26.7
Dy	Traces	-	4.3	11.5

Conclusion

A range of new silica-based porous liquids (PLs) based on modified silica spheres reversibly surrounded by an amphiphilic canopy has been developed by successfully varying the nature of both silica cores and canopies. For the sake of comparison, small non-porous silica nanoparticles (SiNPs) and porous hollow silica particles (HSPs) of two different sizes were first designed as starting silica cores before their surface modification with sulfonic acid groups. Acido-basic reaction between these functional groups and an ethoxylated fatty amine (EthA) led to the formation of the canopy. Liquefying properties and hydrophobicity were also both tuned for the first time according to the number of ethoxylated units ($n+m$) born by the EthA, which was varied from 5 to 92. Only six synthesized materials were observed to display a liquid behavior at room temperature. Considering the effect of the silica particle nature, it was evidenced that the density and the diameter of the silica spheres both played a role on the physical properties of the final PLs. Comparing SiNPs and sHSPs, the lower density of sHSPs implied a decrease in viscosity of the final PL. Besides, PLs obtained with these latter silica cores were less viscous than the one obtained by using bHSPs, even though they are much less dense. Regarding the effect of the organic grafting, it has been shown that the physical state of the final material also strongly depends on the number of ethylene oxide units in the EthA that forms the canopy. Hence, intermediate-range molecular weight amines ($n+m = 11$ and 22) led to liquids at room temperature, whereas high molecular weight amines led to solids that melted at low temperature ($40-55$ °C). The lightest amine did not allow to obtain a liquid at any temperature when grafted on sHSPs. In addition, using EthA-11 led to hydrophobic PLs whereas EthA-22 made the PLs hydrophilic. In order to test the hydrophobicity of the obtained PLs, PL-sHSPs-11, and PL-sHSPs-22 were contacted to pure water. A solubilization in water was observed for the less hydrophobic PL-sHSPs-22, while a clear phase separation could be obtained with the more hydrophobic PL-sHSPs-11. This unprecedented result is an essential prerequisite for considering applying PLs to liquid-liquid extraction (LLE). Preliminary LLE tests have been performed on three rare earth elements (Nd, Pr, Dy). It was shown that metal

extraction is possible with such hydrophobic PLs and that it requires their previous functionalization with a chelating ligand (EDTA). Further studies will include an optimization of the ratio chelating ligand:silica as well as the evaluation of other chelating groups like diglycolamide to enhance the intra-lanthanide selectivity of extraction. Finally, since the use of a short organosilicon could lead to a blockage of the microporosity in the silica shell, therefore decreasing the accessibility to the empty cavities, optimization of the synthesis should include the use of a bigger organosilicon, or an efficient removal of the template after the organosilicon grafting.

Materials & Methods

Materials

Ludox HS40, tetramethyl orthosilicate (TMOS), (3-mercaptopropyl)trimethoxysilane (MPTMS), potassium sulfate (K_2SO_4), tetraethyl orthosilicate (TEOS), cetyltrimethylammonium bromide (CTAB), PluronicF127, and 1,3,5-trimethylbenzene (TMB) were purchased from Sigma-Aldrich. Aqueous ammonia (NH_4OH , 25%) was purchased from Fisher. 3-(trihydroxysilyl)-1-propane sulfonic acid (SIT, 30-35%) was purchased from Gelest. Ethanol (EtOH) and sodium hydroxide (NaOH) were purchased from Carlo Erba. Silanized ethylenediaminetetraacetic acid (Si-EDTA, 45%) was purchased from ABCR. Ethoxylated amines (EthAs) came from three different sources: Rokamin SR5 (EthA-5), Rokamin SR11 (EthA-11), and Rokamin SR22 (EthA-22) were supplied by PCC Group, Ethox SAM50 (EthA-50) was supplied by Ethox Chemicals, and EthA-92 was synthesized according to the method reported by Atta *et al.*³⁷ The detailed procedure as well as NMR spectra of EthA-22, EthA-50, and EthA-92 are included in the Supporting Information (see section S1). Deionized water with a resistivity of 18.2 M Ω .cm and a TOC value below 5 ppb was provided by a Milli-Q direct 8 water purifier device (Merck, France).

Synthesis

Hollow silica particles syntheses

sHSPs were synthesized according to the method described by Zhang *et al.*¹⁴ as follows: 8.33 g (0.66 mmol) of F127, 8.33 g (69.3 mmol) of TMB, and 7.25 g (41.6 mmol) of K_2SO_4 were mixed together with 500 mL of water in a 1L-round bottom flask maintained at 13.5 °C, and stirred during 4 h. Then, 20.25 g (133.0 mmol) of TMOS and 6.5 g (33.1 mmol) of MPTMS were added and the mixture was let at 13.5 °C during 24 h then aged at 100 °C under stirring during 24 h. The product was then filtered on a 5-13 μ m paper and washed three times with water. It was then calcined during 10 h at 450 °C and the solid (*c.a.* 10 g) was grinded before being used.

bHSPs synthesis was inspired from the method of Teng *et al.*³³ that was derived from the Stöber method.⁴⁵ It consisted in dissolving 0.450 g (1.23 mmol) of CTAB in a solution containing 52.5 mL of EtOH, 150 mL of deionized H_2O , and 3 mL (40.2 mmol) of a 25% aqueous NH_3 solution. 3 mL (13.4 mmol) of TEOS was added quickly and the suspension was let under stirring during 24 h at room temperature to make the condensation of TEOS. The product was washed three times with EtOH by centrifugation, before being incubated in 1.2 L of water and heated at 70 °C during 20 h. The bHSPs were washed three times with EtOH. To remove the CTAB template, 360 mL of a EtOH:HCl 10^{-3} N mixture was heated at 60 °C, and the spheres were suspended overnight in this medium. The spheres were recovered after centrifugation and they were then washed three times in EtOH prior to a further extraction performed in a EtOH:HCl 10^{-2} N mixture heated at 60 °C during 3 h. The final product (*c.a.* 400 mg) was obtained after washing three times in EtOH and drying under vacuum.

Porous liquids syntheses

PL-SiNPs synthesis

PL-SiNPs synthesis was inspired by the work of Rodriguez *et al.*^{36,46} concerning Nanoscale Ionic Materials (NIMs): 2.860 g (19.0 mmol) of Ludox HS40 solution were diluted in 25 mL of deionized water (from Milli-Q). 6.4 g (10.1 mmol) of SIT solution were diluted in 25 mL of deionized water, in a 100 mL-round bottom flask. The silica suspension was added dropwise to the SIT solution under vigorous stirring. The pH was adjusted at pH 5-6 with NaOH 1 M, then the solution was heated at 70 °C to start the hydrolysis and it was left at 70 °C during 24 h. It was then dialyzed with a 6000-8000 kDa membrane to remove the excess of NaOH and unreacted SIT prior to elution through an ion-exchange column (Dowex 50W-X8) to protonate the sulfonate salts. The Total Organic Carbon (TOC) analysis of the dialysis external water baths allowed determining the amount of unreacted SIT ($\approx 76\%$). Hence, 2.4 mmol of SIT were grafted upon 1.14 g (19.0 mmol) of silica spheres. Finally, a v:v 100 times diluted aqueous solution of EthA was prepared (the dilution was only ten times for EthA-92) and added dropwise to the solution of grafted nanospheres. The addition, which was followed by pH measurement, could be stopped just after the equivalence point. It was useful to highlight that this equivalence point led to only 0.09 mmol of SIT, meaning that either the protonation in the column was not total, or the column retained some product inside. The product was dried under vacuum at 35 °C before yielding the expected material, namely PL-SiNPs-n+m, where n+m is the global number of the ethylene oxide units in the EthA (*e.g.* PL-SiNPs-22 when n+m = 22). As an example, the overall yield of PL-SiNPs-11 was 3%, mainly due to a poor dispersion of the silica spheres in water (see details in **Table S3**, Supporting Information). This point might be improved by an ultrasonic-assisted reaction between the spheres and the SIT.

PL-sHSPs synthesis

2 g of sHSPs was dispersed in 325 mL of deionized water and mixed at 15,000 rpm with an Ultra-turrax rotor during 5'. After 1 min of sonication (30 W), the dispersion was added dropwise to a solution containing 14.3 g (22.6 mmol) of SIT solution and 325 mL of deionized water under vigorous stirring. The following steps (pH adjustment, dialysis, protonation of tethered sulfonate groups, and subsequent neutralization by the EthA) were performed according to similar procedures to those described for PL-SiNPs but with two slight adaptations. First, the solution recovered after the reaction with the SIT was concentrated by evaporation under reduced pressure to 100 mL before pouring it into dialysis tubes. Second, the solution recovered after the dialysis was centrifuged at 4000 g for 10' in order to eliminate some precipitated aggregates. PL-sHSPs-11 was obtained with an overall yield of 4% (**Table S3**, Supporting Information).

PL-bHSPs synthesis

PL-bHSPs synthesis was achieved following a similar procedure to that described above. 300 mg of bHSPs were dispersed in 50 mL of deionized water and the resulting solution was then added dropwise to a solution containing 3 g (4.75 mmol) of SIT solution and 50 mL of deionized water under vigorous stirring. Subsequent treatments and procedures were applied using the same method as described for PL-sHSPs. PL-bHSPs-11 was obtained in 1% overall yield (**Table S3**, Supporting Information).

Synthesis of porous a liquid functionalized with EDTA (PL-sHSPs-SiEDTA-11)

PL-sHSPs-SiEDTA-11 was synthesized according to a similar method to that described for sHSPs synthesis. F127 (1 g), K₂SO₄ (0.72 g), TMB (1.2 mL) were dissolved in 60 mL of deionized water and left

for 4 h at 13.5 °C under stirring. Then, 2.48 g (16.0 mmol) of TMOS and 0.87 g (1.0 mmol) of SiEDTA were added to the solution. After 24 h, the temperature was set to 100 °C for another 24 h. Afterward, the mixture was filtered on 5-13 µm paper and washed three times with water to obtain a wet white gel. The material was dissolved in 50 mL of deionized water and dispersed with an Ultra-turrax rotor (5') then sonicated for 1'. A solution of SIT (3.58 g) in 50 mL of deionized water was prepared, and the suspension of silica spheres was added dropwise under vigorous stirring. The pH was adjusted to 5-6 with NaOH 1 M and the mixture was heated for 24 h at 70 °C. After 5 days of dialysis with deionized water (8 batches), the suspension was centrifuged to eliminate non-grafted spheres. The supernatant was dried and dispersed again in an EtOH/HCl solution (pH 1). The dispersion was heated to reflux under stirring for 24 h to extract the template. After a filtration and three washing with ethanol, the solid was dried and dispersed again in water, before elution through an ion-exchange column to protonate the sulfonate salts and obtain sHSPs-SiEDTA@SIT. Finally, it was grafted with EthA-11 by following the previous procedure and the functionalized PL (PL-sHSPs-SiEDTA-11) was collected after drying under vacuum.

Characterization methods

Total organic carbon (TOC) measurements were performed with a Shimadzu TOC-VCSH analyzer calibrated with potassium phthalate solution.

Pure SiNPs, HSPs and PLs were imaged by Transmission Electron Microscopy (TEM) on a JEOL (Tokyo, Japan) 1400+ at 100 kV, equipped with a sCMOS JEOL Matataki Flash camera and a LaB6 filament. The solid samples were first dissolved in EtOH before their deposition on a carbon-coated grid whereas those which were liquid at room temperature were not diluted in solvent (except for PL-bHSPs-11 that was dissolved in EtOH to increase the contrast). Sizes were measured with ImageJ software, on a minimum of 200 spheres (core, shell, total) to get a representative panel of the sample.

Structural information about HSPs and PLs were obtained thanks to Small Angle X-Ray Scattering (SAXS) and Ultra-Small Angle X-Ray Scattering (USAXS) measurements. The SAXS device was a home-built one at the ICSM (Marcoule, France) using a bench built by Xenocs with a molybdenum anode as X-ray Source (0.71 Å) and a MAR Research 345 detector at 770 mm from the sample. The USAXS device was a homemade instrument located at the SWACS-Lab platform (CEA, Saclay, France), equipped with a X-ray source (8 keV) that produced a collimated beam and a flux of 0.8x0.8 mm and 108 photons/s on the sample respectively. The detector (Dectris Pilatus 200K) was located at 114 cm from the sample and calibration was achieved by using tetradecanol. Samples (powders and liquids) were put inside 2 mm-thick capillaries. PL-bHSPs-11 was too viscous to enter a capillary, therefore a Kapton adhesive tape was used instead. The exposition time was 1800 s except for sHSPs (600 s). Calibration was done using a polyethylene standard. Data treatment was done with PySAXS 3.26 and modeling was performed with SasView 5.0.4.

The specific surface area of HSPs was deduced from N₂ sorption experiments coupled to a Brunauer-Emmett-Teller (BET) analysis. The pore size distribution was computed thanks to the Barrett-Joyner-Halenda (BJH) model and the Density Functional Theory (DFT). The device was a Micromeritics TriStar II 3020 (Georgia, USA). HSPs and SiNPs were previously outgassed with a Micromeritics VacProp 061 at 80 °C for 48 h.

Thermogravimetric Analyses (TGA) gave access to the composition of PLs. The measurements were performed on a Mettler Toledo (Greifensee, Swiss) device with the STARE Software V13.00, under air

atmosphere, from 25 °C to 1000 °C at a rate of 5 °C/min. The samples (\approx 10-20 mg) were kept in a 70 μ L alumina's crucible.

Differential Scanning Calorimetry (DSC) was used to determine the melting temperature of PLs and EthAs. The measurements were conducted on a Mettler Toledo DSC1 located in the University of Montpellier, France, under N₂ atmosphere. First, the samples were cooled down to -100 °C at 5 °C/min. After an isotherm lasting 5 min, a heating rate of 4 °C/min was applied to reach 150 °C. The melting temperature is taken at the melting peak maximum.

Fourier Transform Infrared Spectroscopy (FTIR) was carried out on Perkin Elmer (Wellesley, MA, USA) Spectrum 100 spectrometer in Attenuated Total Reflectance (ATR) transmission mode. A small amount of powder or net liquid was homogeneously dispersed on the beam path. The wavenumber range was from 615 to 4000 cm⁻¹. The beam resolution was 4 cm⁻¹. Each measurement was repeated four times.

The viscosity of PLs was analyzed at different temperatures on a RM200 CP-4000 cone-plate rheometer from Lamy Rheology (Limonest, France), equipped with a MK-CP2020 cone (angle 2°, diameter 20 mm) and a Peltier plate able to set a temperature between 15 and 60 °C. The gap was set to 50 μ m. The curves could be modeled by a Bingham fitting (with an exception for the viscosity at 20 °C that did not follow the same behavior) directly on the Rheomatic-P V2.1.0.4 software. The values of viscosities obtained with this model were close to the one obtained at 10 s⁻¹ flow shear rate for each PL (corresponding to a shear rate at the beginning of the zone of Newtonian behavior).

Hydrophobicity of PL-sHSPs-11 and PL-sHSPs-22 was determined by contacting a certain amount of PL with water at various water:PL weight ratios, and the phase separation was assessed after, depending on the involved PL, 5 to 20 min of centrifugation at 4000 to 15500 g. The TOC analysis of the aqueous phase was used to determine the quantity of organic molecules that were transferred into the aqueous phase.

Metal concentrations in the aqueous phase before and after extraction were analyzed by Inductively Coupled Plasma Optical Emission Spectroscopy (ICP-OES) on an iCAP 7400 Duo Full MFC from Thermo Scientifi (Waltham, Massachusetts). The software was Thermo Scientifi Qtegra Intelligent Scientific Data Solution Version 2.10. Samples were first diluted 100 times in HNO₃ 1%. A calibration line was obtained from standard solutions (1000 mg/L, SCP Science).

Metal extraction

An aqueous solution containing 500 ppm of Nd, 68 ppm of Pr, and 50 ppm of Dy in nitric acid at pH 2.2 was prepared. 5.0 mL of this solution was contacted with either 30 mg of PL-sHSPs-11 or 50 mg of PL-sHSPs-SiEDTA-11 and it was let under stirring at room temperature for 24 h. The two phases were separated immediately and the aqueous phase was analyzed by ICP. The extraction efficiency $E_{\%}$ was defined as:

$$E_{\%} = \left(1 - \frac{C_{MA}}{C_{Moth}}\right) \times 100 \quad (1)$$

With C_{Moth} the massic concentration of the metal cation M into the mother solution and C_{MA} its massic concentration into the aqueous phase after extraction.

The loading capacity Q_e (mmol.g⁻¹) was computed according to the following equation:

$$Q_e = \frac{\frac{C_{\text{Moth}}}{MW} - \frac{C_{\text{MA}}}{MW}}{\frac{m_{\text{mat}}}{V_{\text{sol}}}} \quad (2)$$

With MW the molecular weight of the metal, m_{mat} the mass of the porous material, and V_{sol} the volume of the aqueous phase.

Supporting Information

Supporting Information is available from the Wiley Online Library or from the author.

Acknowledgements

The authors greatly acknowledge Amine Geneste for his contribution to the DSC measurements, Xavier Legoff and Joseph Lautru for their help with the TEM analyses, and Olivier Taché for his guidance through the USAXS experiments. The authors also greatly thank Guilhem Arrachart for his support and his advices related to the synthesis of the porous liquids. Finally, Justine Ben Ghozi-Bouvrande is acknowledged for the synthesis of the amine EthA-92.

References

- [1] Z. Li, K. H. Smith, G. W. Stevens, **2015**, DOI 10.1016/j.cjche.2015.07.021.
- [2] M. K. Jha, A. Kumari, R. Panda, J. Rajesh Kumar, K. Yoo, J. Y. Lee, *Hydrometallurgy* **2016**, *165*, 2.
- [3] N. N. Hidayah, S. Z. Abidin, *Miner. Eng.* **2017**, *112*, 103.
- [4] J. Płotka-Wasyłka, M. Rutkowska, K. Owczarek, M. Tobiszewski, J. Namieśnik, *TrAC Trends Anal. Chem.* **2017**, *91*, 12.
- [5] R. Rogers, K. Seddon, *Science* **2003**, *302*, 792.
- [6] K. R. Seddon, *J. Chem. Technol. Biotechnol.* **1997**, *68*, 351.
- [7] D. J. G. P. van Osch, L. F. Zubeir, A. van den Bruinhorst, M. A. A. Rocha, M. C. Kroon, *Green Chem.* **2015**, *17*, 4518.
- [8] C. Micheau, O. Diat, P. Bauduin, *J. Mol. Liq.* **2018**, *253*, 217.
- [9] J. Florek, D. Larivière, H. Kählig, S. L. Fiorilli, B. Onida, F.-G. Fontaine, F. Kleitz, *ACS Appl. Mater. Interfaces* **2020**, *12*, 57003.
- [10] A. A. Atia, *Hydrometallurgy* **2005**, *80*, 13.
- [11] M. A. Tadda, A. Ahsan, A. Shitu, M. Elsergany, A. Thirugnanasambantham, B. Jose, M. Razzaque, N. Norsyahariati, **2016**, *2*, 7.
- [12] N. O'Reilly, N. Giri, S. L. James, *Chem. - Eur. J.* **2007**, *13*, 3020.
- [13] M. Costa Gomes, L. Pison, C. Červinka, A. Padua, *Angew. Chem. Int. Ed.* **2018**, *57*, 11909.
- [14] J. Zhang, S. Chai, Z. Qiao, S. M. Mahurin, J. Chen, Y. Fang, S. Wan, K. Nelson, P. Zhang, S. Dai, *Angew. Chem.* **2015**, *127*, 946.
- [15] L. Sheng, J. Lei, Z. Chen, Y. Wang, *Colloids Surf. Physicochem. Eng. Asp.* **2022**, *634*, 128016.
- [16] N. Giri, M. G. Del Pópolo, G. Melaugh, R. L. Greenaway, K. Rätzke, T. Koschine, L. Pison, M. F. C. Gomes, A. I. Cooper, S. L. James, *Nature* **2015**, *527*, 216.
- [17] D. Wang, Y. Ying, Y. Xin, P. Li, Z. Yang, Y. Zheng, *Acc. Mater. Res.* **2023**, DOI 10.1021/accountsmr.3c00106.
- [18] E. B. Hemming, A. F. Masters, T. Maschmeyer, *Chem. Commun.* **2019**, *55*, 11179.
- [19] R. Yang, Q. Zhang, J. Shi, Y. Zheng, D. Wang, J. Zhang, S. Liu, Z. Fu, *Sep. Purif. Technol.* **2023**, *314*, 123605.
- [20] P. Li, J. A. Schott, J. Zhang, S. M. Mahurin, Y. Sheng, Z. Qiao, X. Hu, G. Cui, D. Yao, S. Brown, Y. Zheng, S. Dai, *Angew. Chem. Int. Ed.* **2017**, *56*, 14958.
- [21] Y. Liu, Y. Bai, T. Tian, *Materials* **2019**, *12*, 3984.
- [22] R. Kumar, P. Dhasaiyan, P. M. Naveenkumar, K. P. Sharma, *Nanoscale Adv.* **2019**, *1*, 4067.
- [23] J. Ben Ghozi-Bouvrande, S. Pellet-Rostaing, S. Dourdain, *Nanomaterials* **2021**, *11*, 2307.
- [24] Y. Lai, J. Yang, L. Cai, M. Zhang, X. He, H. Yu, M. Li, G.-H. Ning, P. Yin, *Adv. Funct. Mater.* **n.d.**, *n/a*, 2210122.
- [25] X. Li, Z. Shi, Z. Cui, S. Zhu, *Chem. Res. Chin. Univ.* **2018**, *34*, 495.
- [26] T. Gao, B. P. Jelle, L. I. C. Sandberg, A. Gustavsen, *ACS Appl. Mater. Interfaces* **2013**, *5*, 761.

Appendix H
Publications during the PhD

- [27] J. Sharma, G. Polizos, *Nanomaterials* **2020**, *10*, 1599.
- [28] L. Xu, J. He, *Langmuir* **2012**, *28*, 7512.
- [29] W. Li, Z. Qiu, M. Tebyetekkerwa, J. Zhang, Y. Wang, T. Gao, J. Wang, Y. Ding, Y. Xie, *Prog. Org. Coat.* **2019**, *127*, 8.
- [30] E. Carretti, M. Bonini, L. Dei, B. H. Berrie, L. V. Angelova, P. Baglioni, R. G. Weiss, *Acc. Chem. Res.* **2010**, *43*, 751.
- [31] S. Ikeda, Y. Ikoma, H. Kobayashi, T. Harada, T. Torimoto, B. Ohtani, M. Matsumura, *Chem. Commun.* **2007**, 3753.
- [32] A. Belostozky, S. Bretler, M. Kolitz-Domb, I. Grinberg, S. Margel, *Mater. Sci. Eng. C* **2019**, *97*, 760.
- [33] Z. Teng, X. Su, Y. Zheng, J. Sun, G. Chen, C. Tian, J. Wang, H. Li, Y. Zhao, G. Lu, *Chem. Mater.* **2013**, *25*, 98.
- [34] H. Chen, Z. Yan, B. Li, Y. Li, Q.-H. Wu, *Mater. Lett.* **2013**, *112*, 78.
- [35] M. N. Gorsd, L. R. Pizzio, M. N. Blanco, *Procedia Mater. Sci.* **2015**, *8*, 567.
- [36] R. Rodriguez, R. Herrera, L. A. Archer, E. P. Giannelis, *Adv. Mater.* **2008**, *20*, 4353.
- [37] A. Atta, G. EL-Mahdy, H. Al-Lohedan, M. Abdullah, *Int. J. Electrochem. Sci.* **2016**, *11*, 882.
- [38] J. B. Ben Ghazi-Bouvrande, Les liquides poreux : un nouveau concept pour la séparation chimique, phdthesis, Montpellier, Ecole nationale supérieure de chimie, **2022**.
- [39] S. S. Devangamath, B. Lobo, S. P. Masti, S. Narasagoudr, *J. Mater. Sci. Mater. Electron.* **2020**, *31*, 2904.
- [40] E. D. Pereira, R. Cerruti, E. Fernandes, L. Peña, V. Saez, J. C. Pinto, J. A. Ramón, G. E. Oliveira, F. G. de Souza Júnior, *Polímeros* **2016**, *26*, 137.
- [41] J.-J. Max, C. Chapados, *Appl. Spectrosc.* **1999**, *53*, 1045.
- [42] S. Y. Kim, H. W. Meyer, K. Saalwächter, C. F. Zukoski, *Macromolecules* **2012**, *45*, 4225.
- [43] D. Wang, Y. Xin, X. Li, F. Wang, Y. Wang, W. Zhang, Y. Zheng, D. Yao, Z. Yang, X. Lei, *Chem. Eng. J.* **2021**, *416*, 127625.
- [44] D. Wang, Y. Xin, X. Li, H. Ning, Y. Wang, D. Yao, Y. Zheng, Z. Meng, Z. Yang, Y. Pan, P. Li, H. Wang, Z. He, W. Fan, *ACS Appl. Mater. Interfaces* **2021**, *13*, 2600.
- [45] W. Stöber, A. Fink, E. Bohn, *J. Colloid Interface Sci.* **1968**, *26*, 62.
- [46] R. Rodriguez, R. Herrera, A. B. Bourlinos, R. Li, A. Amassian, L. A. Archer, E. P. Giannelis, *Appl. Organomet. Chem.* **2010**, *24*, 581.

References

- (1) Egleston, B. D.; Mroz, A.; Jelfs, K. E.; Greenaway, R. L. Porous Liquids – the Future Is Looking Emptier. *Chem. Sci.* **2022**, *13* (18), 5042–5054. <https://doi.org/10.1039/D2SC00087C>.
- (2) Li, Y. Research Progress of Porous Liquids. *ChemistrySelect* **2020**, *5* (43), 13664–13672. <https://doi.org/10.1002/slct.202003957>.
- (3) O'Reilly, N.; Giri, N.; James, S. L. Porous Liquids. *Chem. - Eur. J.* **2007**, *13* (11), 3020–3025. <https://doi.org/10.1002/chem.200700090>.
- (4) Bennett, T. D.; Coudert, F.-X.; James, S. L.; Cooper, A. I. The Changing State of Porous Materials. *Nat. Mater.* **2021**, *20* (9), 1179–1187. <https://doi.org/10.1038/s41563-021-00957-w>.
- (5) Li, Z.; Smith, K. H.; Stevens, G. W. The Use of Environmentally Sustainable Bio-Derived Solvents in Solvent Extraction Applications—A Review | Elsevier Enhanced Reader. **2015**. <https://doi.org/10.1016/j.cjche.2015.07.021>.
- (6) Hidayah, N. N.; Abidin, S. Z. The Evolution of Mineral Processing in Extraction of Rare Earth Elements Using Solid-Liquid Extraction over Liquid-Liquid Extraction: A Review. *Miner. Eng.* **2017**, *112*, 103–113. <https://doi.org/10.1016/j.mineng.2017.07.014>.
- (7) Cram, D. J.; Tanner, M. E.; Knobler, C. B. Host-Guest Complexation. 58. Guest Release and Capture by Hemicarcerands Introduces the Phenomenon of Constrictive Binding. *J. Am. Chem. Soc.* **1991**, *113* (20), 7717–7727. <https://doi.org/10.1021/ja00020a039>.
- (8) Robbins, T. A.; Knobler, C. B.; Bellew, D. R.; Cram, D. J. Host-Guest Complexation. 67. A Highly Adaptive and Strongly Binding Hemicarcerand. *J. Am. Chem. Soc.* **1994**, *116* (1), 111–122. <https://doi.org/10.1021/ja00080a014>.
- (9) Maitra, P.; Wunder, S. L. Oligomeric Poly(Ethylene Oxide)-Functionalized Silsesquioxanes: Interfacial Effects on T_g , T_m , and ΔH_m . *Chem. Mater.* **2002**, *14* (11), 4494–4497. <https://doi.org/10.1021/cm0203518>.
- (10) Cardoen, G.; Coughlin, E. B. Hemi-Telechelic Polystyrene-POSS Copolymers as Model Systems for the Study of Well-Defined Inorganic/Organic Hybrid Materials. *Macromolecules* **2004**, *37* (13), 5123–5126. <https://doi.org/10.1021/ma049769c>.
- (11) Pyun, J.; Matyjaszewski, K.; Wu, J.; Kim, G.-M.; Chun, S. B.; Mather, P. T. ABA Triblock Copolymers Containing Polyhedral Oligomeric Silsesquioxane Pendant Groups: Synthesis and Unique Properties. *Polymer* **2003**, *44* (9), 2739–2750. [https://doi.org/10.1016/S0032-3861\(03\)00027-2](https://doi.org/10.1016/S0032-3861(03)00027-2).
- (12) Randriamahefa, S.; Lorthioir, C.; Guégan, P.; Penelle, J. Synthesis and Bulk Organization of Polymer Nanocomposites Based on Hemi/Ditelechelic Poly(Propylene Oxide) End-Functionalized with POSS Cages. *Polymer* **2009**, *50* (16), 3887–3894. <https://doi.org/10.1016/j.polymer.2009.06.031>.
- (13) Hsu, S. C. N.; Ramesh, M.; Espenson, J. H.; Rauchfuss, T. B. Membership Rules for a Molecular Box: The Admission Process and Protection Provided to Guest Molecules. *Angew. Chem. Int. Ed.* **2003**, *42* (23), 2663–2666. <https://doi.org/10.1002/anie.200219562>.
- (14) Chaffee, K. E.; Fogarty, H. A.; Brotin, T.; Goodson, B. M.; Dutasta, J.-P. Encapsulation of Small Gas Molecules by Cryptophane-111 in Organic Solution. 1. Size- and Shape-Selective Complexation of Simple Hydrocarbons. *J. Phys. Chem. A* **2009**, *113* (49), 13675–13684. <https://doi.org/10.1021/jp903452k>.
- (15) Giri, N.; Davidson, C. E.; Melaugh, G.; Del Pópolo, M. G.; Jones, J. T. A.; Hasell, T.; Cooper, A. I.; Horton, P. N.; Hursthouse, M. B.; James, S. L. Alkylated Organic Cages: From Porous Crystals to Neat Liquids. *Chem. Sci.* **2012**, *3* (6), 2153. <https://doi.org/10.1039/c2sc01007k>.
- (16) Melaugh, G.; Giri, N.; Davidson, C. E.; James, S. L.; Pópolo, M. G. D. Designing and Understanding Permanent Microporosity in Liquids. *Phys. Chem. Chem. Phys.* **2014**, *16* (20), 9422–9431. <https://doi.org/10.1039/C4CP00582A>.
- (17) Zhang, J.; Chai, S.; Qiao, Z.; Mahurin, S. M.; Chen, J.; Fang, Y.; Wan, S.; Nelson, K.; Zhang, P.; Dai, S. Porous Liquids: A Promising Class of Media for Gas Separation. *Angew. Chem.* **2015**, *127* (3), 946–950. <https://doi.org/10.1002/ange.201409420>.
- (18) Giri, N.; Del Pópolo, M. G.; Melaugh, G.; Greenaway, R. L.; Rätzke, K.; Koschine, T.; Pison, L.; Gomes, M. F. C.; Cooper, A. I.; James, S. L. Liquids with Permanent Porosity. *Nature* **2015**, *527* (7577), 216–220. <https://doi.org/10.1038/nature16072>.

- (19) Akutagawa, T.; Jin, R.; Tunashima, R.; Noro, S.; Cronin, L.; Nakamura, T. Nanoscale Assemblies of Gigantic Molecular $\{\text{Mo}_{154}\}$ -Rings: (Dimethyldioctadecylammonium)₂₀ $[\text{Mo}_{154}\text{O}_{462}\text{H}_8(\text{H}_2\text{O})_{70}]$. *Langmuir* **2008**, *24* (1), 231–238. <https://doi.org/10.1021/la701364k>.
- (20) Moro, S.; Parneix, C.; Cabane, B.; Sanson, N.; d'Espinose De Lacaillerie, J.-B. Hydrophobization of Silica Nanoparticles in Water: Nanostructure and Response to Drying Stress. *Langmuir* **2017**, *33* (19), 4709–4719. <https://doi.org/10.1021/acs.langmuir.6b04505>.
- (21) Eliášová, P.; Opanasenko, M.; Wheatley, P. S.; Shamzhy, M.; Mazur, M.; Nachtigall, P.; Roth, W. J.; Morris, R. E.; Čejka, J. The ADOR Mechanism for the Synthesis of New Zeolites. *Chem. Soc. Rev.* **2015**, *44* (20), 7177–7206. <https://doi.org/10.1039/C5CS00045A>.
- (22) Jie, K.; Onishi, N.; Schott, J. A.; Popovs, I.; Jiang, D.; Mahurin, S.; Dai, S. Transforming Porous Organic Cages into Porous Ionic Liquids via a Supramolecular Complexation Strategy. *Angew. Chem. Int. Ed.* **2020**, *59* (6), 2268–2272. <https://doi.org/10.1002/anie.201912068>.
- (23) Kearsey, R. J.; Alston, B. M.; Briggs, M. E.; Greenaway, R. L.; Cooper, A. I. Accelerated Robotic Discovery of Type II Porous Liquids. *Chem. Sci.* **2019**, *10* (41), 9454–9465. <https://doi.org/10.1039/C9SC03316E>.
- (24) Ben, T.; Ren, H.; Ma, S.; Cao, D.; Lan, J.; Jing, X.; Wang, W.; Xu, J.; Deng, F.; Simmons, J. M.; Qiu, S.; Zhu, G. Targeted Synthesis of a Porous Aromatic Framework with High Stability and Exceptionally High Surface Area. *Angew. Chem. Int. Ed.* **2009**, *48* (50), 9457–9460. <https://doi.org/10.1002/anie.200904637>.
- (25) Cahir, J.; Tsang, M. Y.; Lai, B.; Hughes, D.; Alam, M. A.; Jacquemin, J.; Rooney, D.; James, S. L. Type 3 Porous Liquids Based on Non-Ionic Liquid Phases – a Broad and Tailorable Platform of Selective, Fluid Gas Sorbents. *Chem. Sci.* **2020**, *11* (8), 2077–2084. <https://doi.org/10.1039/C9SC05770F>.
- (26) Mastalerz, M.; Oppel, I. M. Rational Construction of an Extrinsic Porous Molecular Crystal with an Extraordinary High Specific Surface Area. *Angew. Chem. Int. Ed.* **2012**, *51* (21), 5252–5255. <https://doi.org/10.1002/anie.201201174>.
- (27) Ma, L.; Haynes, C. J. E.; Grommet, A. B.; Walczak, A.; Parkins, C. C.; Doherty, C. M.; Longley, L.; Tron, A.; Stefankiewicz, A. R.; Bennett, T. D.; Nitschke, J. R. Coordination Cages as Permanently Porous Ionic Liquids. *Nat. Chem.* **2020**, *12* (3), 270–275. <https://doi.org/10.1038/s41557-020-0419-2>.
- (28) Deng, Z.; Ying, W.; Gong, K.; Zeng, Y.-J.; Yan, Y.; Peng, X. Facilitate Gas Transport through Metal-Organic Polyhedra Constructed Porous Liquid Membrane. *Small* **2020**, *16* (11), 1907016. <https://doi.org/10.1002/smll.201907016>.
- (29) Liu, H.; Liu, B.; Lin, L.-C.; Chen, G.; Wu, Y.; Wang, J.; Gao, X.; Lv, Y.; Pan, Y.; Zhang, X.; Zhang, X.; Yang, L.; Sun, C.; Smit, B.; Wang, W. A Hybrid Absorption–Adsorption Method to Efficiently Capture Carbon. *Nat. Commun.* **2014**, *5* (1), 5147. <https://doi.org/10.1038/ncomms6147>.
- (30) Gaillac, R.; Pullumbi, P.; Beyer, K. A.; Chapman, K. W.; Keen, D. A.; Bennett, T. D.; Coudert, F.-X. Liquid Metal–Organic Frameworks. *Nat. Mater.* **2017**, *16* (11), 1149–1154. <https://doi.org/10.1038/nmat4998>.
- (31) Costa Gomes, M.; Pison, L.; Červinka, C.; Padua, A. Porous Ionic Liquids or Liquid Metal–Organic Frameworks? *Angew. Chem. Int. Ed.* **2018**, *57* (37), 11909–11912. <https://doi.org/10.1002/anie.201805495>.
- (32) Shan, W.; Fulvio, P. F.; Kong, L.; Schott, J. A.; Do-Thanh, C.-L.; Tian, T.; Hu, X.; Mahurin, S. M.; Xing, H.; Dai, S. New Class of Type III Porous Liquids: A Promising Platform for Rational Adjustment of Gas Sorption Behavior. *ACS Appl. Mater. Interfaces* **2018**, *10* (1), 32–36. <https://doi.org/10.1021/acsami.7b15873>.
- (33) Liu, S.; Liu, J.; Hou, X.; Xu, T.; Tong, J.; Zhang, J.; Ye, B.; Liu, B. Porous Liquid: A Stable ZIF-8 Colloid in Ionic Liquid with Permanent Porosity. *Langmuir* **2018**, *34* (12), 3654–3660. <https://doi.org/10.1021/acs.langmuir.7b04212>.
- (34) Li, P.; Chen, H.; Schott, J. A.; Li, B.; Zheng, Y.; Mahurin, S. M.; Jiang, D.; Cui, G.; Hu, X.; Wang, Y.; Li, L.; Dai, S. Porous Liquid Zeolites: Hydrogen Bonding-Stabilized H-ZSM-5 in Branched Ionic Liquids. *Nanoscale* **2019**, *11* (4), 1515–1519. <https://doi.org/10.1039/C8NR07337F>.
- (35) He, S.; Chen, L.; Cui, J.; Yuan, B.; Wang, H.; Wang, F.; Yu, Y.; Lee, Y.; Li, T. General Way To Construct Micro- and Mesoporous Metal–Organic Framework-Based Porous Liquids. *J. Am. Chem. Soc.* **2019**, *141* (50), 19708–19714. <https://doi.org/10.1021/jacs.9b08458>.
- (36) Corsini, C.; M. Correa, C.; Scaglione, N.; Costa Gomes, M.; Padua, A. How Do Deep Eutectic Solvents Form Porous Liquids? The Example of Methyltriphenylphosphonium Bromide: Glycerol and ZIF-8. *J. Phys. Chem. B* **2024**, *128* (10), 2481–2489. <https://doi.org/10.1021/acs.jpcc.3c08490>.
- (37) Avila, J.; Corsini, C.; Correa, C. M.; Rosenthal, M.; Padua, A.; Costa Gomes, M. Porous Ionic Liquids Go Green. *ACS Nano* **2023**, *17* (20), 19508–19513. <https://doi.org/10.1021/acsnano.3c06343>.
- (38) Dai, D.; Luo, L.; Zhu, Q.; Wang, D.; Li, T. Preserving Macroporosity in Type III Porous Liquids. *Angew. Chem.* **2023**, *135* (25), e202303102. <https://doi.org/10.1002/ange.202303102>.

- (39) Notman, N. A Fluid Idea, with Holes., 2018. <https://eic.rsc.org/feature/a-fluid-idea-with-holes/3008369.article>.
- (40) Jie, K.; Zhou, Y.; Ryan, H. P.; Dai, S.; Nitschke, J. R. Engineering Permanent Porosity into Liquids. *Adv. Mater.* **2021**, *33* (18), 2005745. <https://doi.org/10.1002/adma.202005745>.
- (41) Caira, M. R.; Bourne, S. A.; Mhlongo, W. T.; Dean, P. M. New Crystalline Forms of Permethylated β -Cyclodextrin. *Chem. Commun.* **2004**, No. 19, 2216–2217. <https://doi.org/10.1039/B408660K>.
- (42) Lai, Y.; Yang, J.; Cai, L.; Zhang, M.; He, X.; Yu, H.; Li, M.; Ning, G.-H.; Yin, P. Precise Modulation of Surface Layer Dynamics for Tunable Flowability and Gas Absorption Properties of Molecular Porous Liquids. *Adv. Funct. Mater.* **2023**, *33* (12), 2210122. <https://doi.org/10.1002/adfm.202210122>.
- (43) Liu, Y.; Bai, Y.; Tian, T. Preparation of Porous Liquid Based on Silicalite-1. *Materials* **2019**, *12* (23), 3984. <https://doi.org/10.3390/ma12233984>.
- (44) Kumar, R.; Dhasaiyan, P.; Naveenkumar, P. M.; Sharma, K. P. A Solvent-Free Porous Liquid Comprising Hollow Nanorod–Polymer Surfactant Conjugates. *Nanoscale Adv.* **2019**, *1* (10), 4067–4075. <https://doi.org/10.1039/C9NA00353C>.
- (45) Shi, T.; Zheng, Y.; Wang, T.; Li, P.; Wang, Y.; Yao, D. Effect of Pore Size on the Carbon Dioxide Adsorption Behavior of Porous Liquids Based on Hollow Silica. *ChemPhysChem* **2018**, *19* (1), 130–137. <https://doi.org/10.1002/cphc.201700842>.
- (46) Sheng, L.; Lei, J.; Chen, Z.; Wang, Y. Solvent-Free Porous Liquids for CO₂ Capture Based on Silica Nanoparticles with Different Core Structures. *Colloids Surf. Physicochem. Eng. Asp.* **2022**, *634*, 128016. <https://doi.org/10.1016/j.colsurfa.2021.128016>.
- (47) Li, P.; Schott, J. A.; Zhang, J.; Mahurin, S. M.; Sheng, Y.; Qiao, Z.; Hu, X.; Cui, G.; Yao, D.; Brown, S.; Zheng, Y.; Dai, S. Electrostatic-Assisted Liquefaction of Porous Carbons. *Angew. Chem. Int. Ed.* **2017**, *56* (47), 14958–14962. <https://doi.org/10.1002/anie.201708843>.
- (48) Dinker, M. K.; Li, M.-M.; Zhao, K.; Zuo, M.; Ding, L.; Liu, X.-Q.; Sun, L.-B. Transformation of Type III to Type II Porous Liquids by Tuning Surface Rigidity of Rhodium(II)-Based Metal-Organic Polyhedra for CO₂ Cycloaddition. *Angew. Chem. Int. Ed.* **2023**, *62* (31), e202306495. <https://doi.org/10.1002/anie.202306495>.
- (49) Sheng, L.; Chen, Z.; Xu, B.; Shi, J. Molecular Dynamics Study of the Dispersion Stability and Fluidity of Porous Liquids with Different Canopy Structures. *J. Phys. Chem. B* **2021**, *125* (20), 5387–5396. <https://doi.org/10.1021/acs.jpcc.1c02450>.
- (50) Li, P.; Wang, D.; Zhang, L.; Liu, C.; Wu, F.; Wang, Y.; Wang, Z.; Zhao, Z.; Wu, W.; Liang, Y.; Li, Z.; Wang, W.; Zheng, Y. An In Situ Coupling Strategy toward Porous Carbon Liquid with Permanent Porosity. *Small* **2021**, *17* (10), 2006687. <https://doi.org/10.1002/smll.202006687>.
- (51) Paul, D. R.; Kemp, D. R. The Diffusion Time Lag in Polymer Membranes Containing Adsorptive Fillers. *J. Polym. Sci. Polym. Symp.* **1973**, *41* (1), 79–93. <https://doi.org/10.1002/polc.5070410109>.
- (52) Carné-Sánchez, A.; Craig, G. A.; Larpent, P.; Hirose, T.; Higuchi, M.; Kitagawa, S.; Matsuda, K.; Urayama, K.; Furukawa, S. Self-Assembly of Metal–Organic Polyhedra into Supramolecular Polymers with Intrinsic Microporosity. *Nat. Commun.* **2018**, *9* (1), 2506. <https://doi.org/10.1038/s41467-018-04834-0>.
- (53) Wang, D.; Xin, Y.; Li, X.; Ning, H.; Wang, Y.; Yao, D.; Zheng, Y.; Meng, Z.; Yang, Z.; Pan, Y.; Li, P.; Wang, H.; He, Z.; Fan, W. Transforming Metal–Organic Frameworks into Porous Liquids via a Covalent Linkage Strategy for CO₂ Capture. *ACS Appl. Mater. Interfaces* **2021**, *13* (2), 2600–2609. <https://doi.org/10.1021/acsami.0c18707>.
- (54) Ben Ghazi-Bouvrande, J.; Pellet-Rostaing, S.; Dourdain, S. Key Parameters to Tailor Hollow Silica Nanospheres for a Type I Porous Liquid Synthesis: Optimized Structure and Accessibility. *Nanomaterials* **2021**, *11* (9), 2307. <https://doi.org/10.3390/nano11092307>.
- (55) Wang, D.; Xin, Y.; Li, X.; Wang, F.; Wang, Y.; Zhang, W.; Zheng, Y.; Yao, D.; Yang, Z.; Lei, X. A Universal Approach to Turn UiO-66 into Type 1 Porous Liquids via Post-Synthetic Modification with Corona-Canopy Species for CO₂ Capture. *Chem. Eng. J.* **2021**, *416*, 127625. <https://doi.org/10.1016/j.cej.2020.127625>.
- (56) Li, M.-M.; Dinker, M. K.; Liu, Y.; Zuo, M.; Ding, L.; Liu, X.-Q.; Sun, L.-B. Role of Cavities Created by Azobenzene-Modified UiO-66 in Bulky Ionic Liquid for High Photoresponsive CO₂ Uptake Behavior. *J. Mater. Chem. A* **2023**, *11* (39), 21058–21065. <https://doi.org/10.1039/D3TA04786E>.
- (57) Yang, R.; Zhang, Q.; Shi, J.; Zheng, Y.; Wang, D.; Zhang, J.; Liu, S.; Fu, Z. A Novel Magnetic Loading Porous Liquid Absorbent for Removal of Cu(II) and Pb(II) from the Aqueous Solution. *Sep. Purif. Technol.* **2023**, *314*, 123605. <https://doi.org/10.1016/j.seppur.2023.123605>.
- (58) Xin, Y.; Ning, H.; Wang, D.; Li, X.; Fan, W.; Ju, X.; Wang, H.; Zhang, Y.; Yang, Z.; Yao, D.; Zheng, Y. A Generalizable Strategy Based on the Rule of “like Dissolves like” to Construct Porous Liquids with Low

- Viscosity for CO₂ Capture. *Nano Res.* **2023**, *16* (7), 10369–10380. <https://doi.org/10.1007/s12274-023-5516-2>.
- (59) Ginot, L.; El Bakkouche, A.; Giusti, F.; Dourdain, S.; Pellet-Rostaing, S. Hydrophobic Porous Liquids with Controlled Cavity Size and Physico-Chemical Properties. *Adv. Sci.* **2024**, *11* (4), 2305906. <https://doi.org/10.1002/advs.202305906>.
- (60) Ginot, L.; Ben Ghazi-Bouvrande, J.; Prévost, S.; Pellet-Rostaing, S.; Dourdain, S. Lead Extraction in a Functionalized and Permeable Silica-Based Porous Liquid. *J. Phys. Chem. B* **2024**, *128* (10), 2550–2558. <https://doi.org/10.1021/acs.jpcc.3c08295>.
- (61) Rouquerol, J.; Rouquerol, F.; Llewellyn, P.; Maurin, G.; Sing, K. *Adsorption by Powders and Porous Solids: Principles, Methodology and Applications*; Academic Press, 2013.
- (62) Pratt, L. R.; Pohorille, A. Theory of Hydrophobicity: Transient Cavities in Molecular Liquids. *Proc. Natl. Acad. Sci. U. S. A.* **1992**, *89* (7), 2995–2999.
- (63) Avila, J.; Červinka, C.; Dugas, P.; Pádua, A. A. H.; Costa Gomes, M. Porous Ionic Liquids: Structure, Stability, and Gas Absorption Mechanisms. *Adv. Mater. Interfaces* **2021**, *8* (9), 2001982. <https://doi.org/10.1002/admi.202001982>.
- (64) Taylor, S. F. R.; McCrellis, C.; McStay, C.; Jacquemin, J.; Hardacre, C.; Mercy, M.; Bell, R. G.; de Leeuw, N. H. CO₂ Capture in Wet and Dry Superbase Ionic Liquids. *J. Solut. Chem.* **2015**, *44* (3), 511–527. <https://doi.org/10.1007/s10953-015-0319-z>.
- (65) Bourlinos, A. B.; Giannelis, E. P.; Zhang, Q.; Archer, L. A.; Floudas, G.; Fytas, G. Surface-Functionalized Nanoparticles with Liquid-like Behavior: The Role of the Constituent Components. *Eur. Phys. J. E* **2006**, *20* (1), 109–117. <https://doi.org/10.1140/epje/i2006-10007-3>.
- (66) Li, X.; Wang, D.; He, Z.; Su, F.; Zhang, J.; Wang, Y.; Xin, Y.; Wang, H.; Yao, D.; Li, M.; Zheng, Y. Dual Stimuli-Responsive Porous Ionic Liquids with Reversible Phase Transition Behavior Based on Ionic Liquid Crystals for CO₂ and C₂H₄ Adsorption. *J. Mater. Chem. A* **2022**, *10* (25), 13333–13344. <https://doi.org/10.1039/D2TA01341J>.
- (67) Sheng, L.; Chen, Z.; Wang, Y. Molecular Dynamics Simulations of Stability and Fluidity of Porous Liquids. *Appl. Surf. Sci.* **2021**, *536*, 147951. <https://doi.org/10.1016/j.apsusc.2020.147951>.
- (68) Dukes, D.; Li, Y.; Lewis, S.; Benicewicz, B.; Schadler, L.; Kumar, S. K. Conformational Transitions of Spherical Polymer Brushes: Synthesis, Characterization, and Theory. *Macromolecules* **2010**, *43* (3), 1564–1570. <https://doi.org/10.1021/ma901228t>.
- (69) Sheng, L.; Chen, Z. Molecular Dynamics Study of Dispersion and Fluidity of Porous Liquids with Different Pore Sizes. *J. Mol. Liq.* **2021**, *333*, 115890. <https://doi.org/10.1016/j.molliq.2021.115890>.
- (70) Ma, J.; He, L.; Yang, R.; Wang, D.; Qu, D.; Su, C.; Pang, H.; Wu, W.; Li, P.; Zhang, L.; Liu, X. Porous Liquid Metal-Organic Frameworks with Selectively High Gas Solubility. *Fuel* **2023**, *344*, 128051. <https://doi.org/10.1016/j.fuel.2023.128051>.
- (71) Zhang, F.; Yang, F.; Huang, J.; Sumpter, B. G.; Qiao, R. Thermodynamics and Kinetics of Gas Storage in Porous Liquids. *J. Phys. Chem. B* **2016**, *120* (29), 7195–7200. <https://doi.org/10.1021/acs.jpcc.6b04784>.
- (72) Greenaway, R. L.; Holden, D.; Eden, E. G. B.; Stephenson, A.; Yong, C. W.; Bennison, M. J.; Hasell, T.; Briggs, M. E.; James, S. L.; Cooper, A. I. Understanding Gas Capacity, Guest Selectivity, and Diffusion in Porous Liquids. *Chem. Sci.* **2017**, *8* (4), 2640–2651. <https://doi.org/10.1039/C6SC05196K>.
- (73) Knebel, A.; Bavykina, A.; Datta, S. J.; Sundermann, L.; Garzon-Tovar, L.; Lebedev, Y.; Durini, S.; Ahmad, R.; Kozlov, S. M.; Shterk, G.; Karunakaran, M.; Carja, I. D.; Simic, D.; Weilert, I.; Klüppel, M.; Giese, U.; Cavallo, L.; Rueping, M.; Eddaoudi, M.; Caro, J.; Gascon, J. Solution Processable Metal–Organic Frameworks for Mixed Matrix Membranes Using Porous Liquids. *Nat. Mater.* **2020**, *19* (12), 1346–1353. <https://doi.org/10.1038/s41563-020-0764-y>.
- (74) Hemming, E. B.; Masters, A. F.; Maschmeyer, T. The Encapsulation of Metal Nanoparticles within Porous Liquids. *Chem. Commun.* **2019**, *55* (75), 11179–11182. <https://doi.org/10.1039/C9CC03546J>.
- (75) Hemming, E. B.; Masters, A. F.; Maschmeyer, T. Exploring Opportunities for Platinum Nanoparticles Encapsulated in Porous Liquids as Hydrogenation Catalysts. *Chem. – Eur. J.* **2020**, *26* (31), 7059–7064. <https://doi.org/10.1002/chem.201905288>.
- (76) Hemming, E. B.; Masters, A. F.; Maschmeyer, T. Immobilisation of Homogeneous Pd Catalysts within a Type I Porous Liquid*. *Aust. J. Chem.* **2020**, *73* (12), 1296–1300. <https://doi.org/10.1071/CH20256>.
- (77) Yu, G.; Jin, D.; Zhang, F.; Tian, S.; Zhou, Z.; Ren, Z. Extraction-Adsorption Coupled Desulfurization of Fuel Oil by Novel Functionalized Porous Liquids. *Chem. Eng. J.* **2023**, *453*, 139935. <https://doi.org/10.1016/j.cej.2022.139935>.

- (78) Zhang, J.; Yin, J.; Fu, W.; Ran, H.; Jiang, W.; Li, H.; Zhu, W.; Li, H.; Zhang, M. Highly Efficient Extractive Desulfurization by Specific Functionalized Porous Ionic Liquids via C-H $\cdots\pi$ Interactions. *Fuel Process. Technol.* **2023**, *243*, 107687. <https://doi.org/10.1016/j.fuproc.2023.107687>.
- (79) Dinker, M. K.; Zhao, K.; Dai, Z.; Ding, L.; Liu, X.; Sun, L. Porous Liquids Responsive to Light**. *Angew. Chem. Int. Ed.* **2022**, *61* (50), e202212326. <https://doi.org/10.1002/anie.202212326>.
- (80) Whipple, D. T.; Kenis, P. J. A. Prospects of CO₂ Utilization via Direct Heterogeneous Electrochemical Reduction. *J. Phys. Chem. Lett.* **2010**, *1* (24), 3451–3458. <https://doi.org/10.1021/jz1012627>.
- (81) Kim, C.; Yoo, C.-J.; Oh, H.-S.; Min, B. K.; Lee, U. Review of Carbon Dioxide Utilization Technologies and Their Potential for Industrial Application. *J. CO₂ Util.* **2022**, *65*, 102239. <https://doi.org/10.1016/j.jcou.2022.102239>.
- (82) Zou, Y.-H.; Huang, Y.-B.; Si, D.-H.; Yin, Q.; Wu, Q.-J.; Weng, Z.; Cao, R. Porous Metal–Organic Framework Liquids for Enhanced CO₂ Adsorption and Catalytic Conversion. *Angew. Chem.* **2021**, *133* (38), 21083–21088. <https://doi.org/10.1002/ange.202107156>.
- (83) Qiao, Z.-A.; Zhang, P.; Chai, S.-H.; Chi, M.; Veith, G. M.; Gallego, N. C.; Kidder, M.; Dai, S. Lab-in-a-Shell: Encapsulating Metal Clusters for Size Sieving Catalysis. *J. Am. Chem. Soc.* **2014**, *136* (32), 11260–11263. <https://doi.org/10.1021/ja505903r>.
- (84) Gao, T.; Jelle, B. P.; Sandberg, L. I. C.; Gustavsen, A. Monodisperse Hollow Silica Nanospheres for Nano Insulation Materials: Synthesis, Characterization, and Life Cycle Assessment. *ACS Appl. Mater. Interfaces* **2013**, *5* (3), 761–767. <https://doi.org/10.1021/am302303b>.
- (85) Sharma, J.; Polizos, G. Hollow Silica Particles: Recent Progress and Future Perspectives. *Nanomaterials* **2020**, *10* (8), 1599. <https://doi.org/10.3390/nano10081599>.
- (86) Xu, L.; He, J. Fabrication of Highly Transparent Superhydrophobic Coatings from Hollow Silica Nanoparticles. *Langmuir* **2012**, *28* (19), 7512–7518. <https://doi.org/10.1021/la301420p>.
- (87) Li, X.; Shi, Z.; Cui, Z.; Zhu, S. Silver Chloride Loaded Hollow Mesoporous Silica Particles and Their Application in the Antibacterial Coatings on Denture Base. *Chem. Res. Chin. Univ.* **2018**, *34* (3), 495–499. <https://doi.org/10.1007/s40242-018-7376-y>.
- (88) Li, W.; Qiu, Z.; Tebyetekerwa, M.; Zhang, J.; Wang, Y.; Gao, T.; Wang, J.; Ding, Y.; Xie, Y. Preparation of Silica/Polymer Nanocomposites with Aggregation-Induced Emission Properties as Fluorescent Responsive Coatings. *Prog. Org. Coat.* **2019**, *127*, 8–15. <https://doi.org/10.1016/j.porgcoat.2018.11.001>.
- (89) Carretti, E.; Bonini, M.; Dei, L.; Berrie, B. H.; Angelova, L. V.; Baglioni, P.; Weiss, R. G. New Frontiers in Materials Science for Art Conservation: Responsive Gels and Beyond. *Acc. Chem. Res.* **2010**, *43* (6), 751–760. <https://doi.org/10.1021/ar900282h>.
- (90) Belostozky, A.; Bretler, S.; Kolitz-Domb, M.; Grinberg, I.; Margel, S. Solidification of Oil Liquids by Encapsulation within Porous Hollow Silica Microspheres of Narrow Size Distribution for Pharmaceutical and Cosmetic Applications. *Mater. Sci. Eng. C* **2019**, *97*, 760–767. <https://doi.org/10.1016/j.msec.2018.12.093>.
- (91) Ikeda, S.; Ikoma, Y.; Kobayashi, H.; Harada, T.; Torimoto, T.; Ohtani, B.; Matsumura, M. Encapsulation of Titanium(IV) Oxide Particles in Hollow Silica for Size-Selective Photocatalytic Reactions. *Chem. Commun.* **2007**, No. 36, 3753. <https://doi.org/10.1039/b704468b>.
- (92) Dusselier, M.; Davis, M. E. Small-Pore Zeolites: Synthesis and Catalysis. *Chem. Rev.* **2018**, *118* (11), 5265–5329. <https://doi.org/10.1021/acs.chemrev.7b00738>.
- (93) Wang, L.; Han, Y.; Feng, X.; Zhou, J.; Qi, P.; Wang, B. Metal–Organic Frameworks for Energy Storage: Batteries and Supercapacitors. *Coord. Chem. Rev.* **2016**, *307*, 361–381. <https://doi.org/10.1016/j.ccr.2015.09.002>.
- (94) U.S. Geological Survey. *Mineral Commodity Summaries 2022*; 2022. <https://doi.org/10.3133/mcs2022>.
- (95) Yoon, H.-S.; Kim, C.-J.; Chung, K.-W.; Kim, S.-D.; Lee, J.-Y.; Kumar, J. R. Solvent Extraction, Separation and Recovery of Dysprosium (Dy) and Neodymium (Nd) from Aqueous Solutions: Waste Recycling Strategies for Permanent Magnet Processing. *Hydrometallurgy* **2016**, *165*, 27–43. <https://doi.org/10.1016/j.hydromet.2016.01.028>.
- (96) Xie, F.; Zhang, T. A.; Dreisinger, D.; Doyle, F. A Critical Review on Solvent Extraction of Rare Earths from Aqueous Solutions. *Miner. Eng.* **2014**, *56*, 10–28. <https://doi.org/10.1016/j.mineng.2013.10.021>.
- (97) Vlassopoulos, D.; Fytas, G.; Pispas, S.; Hadjichristidis, N. Spherical Polymeric Brushes Viewed as Soft Colloidal Particles: Zero-Shear Viscosity. *Phys. B Condens. Matter* **2001**, *296* (1), 184–189. [https://doi.org/10.1016/S0921-4526\(00\)00798-5](https://doi.org/10.1016/S0921-4526(00)00798-5).
- (98) Bourlinos, A. B.; Herrera, R.; Chalkias, N.; Jiang, D. D.; Zhang, Q.; Archer, L. A.; Giannelis, E. P. Surface-Functionalized Nanoparticles with Liquid-Like Behavior. *Adv. Mater.* **2005**, *17* (2), 234–237. <https://doi.org/10.1002/adma.200401060>.

- (99) Rodriguez, R.; Herrera, R.; Archer, L. A.; Giannelis, E. P. Nanoscale Ionic Materials. *Adv. Mater.* **2008**, *20* (22), 4353–4358. <https://doi.org/10.1002/adma.200801975>.
- (100) Rodriguez, R.; Herrera, R.; Bourlinos, A. B.; Li, R.; Amassian, A.; Archer, L. A.; Giannelis, E. P. The Synthesis and Properties of Nanoscale Ionic Materials. *Appl. Organomet. Chem.* **2010**, *24* (8), 581–589. <https://doi.org/10.1002/aoc.1625>.
- (101) Li, X.; Liu, X.; Ma, Y.; Li, M.; Zhao, J.; Xin, H.; Zhang, L.; Yang, Y.; Li, C.; Yang, Q. Engineering the Formation of Secondary Building Blocks within Hollow Interiors. *Adv. Mater.* **2012**, *24* (11), 1424–1428. <https://doi.org/10.1002/adma.201104167>.
- (102) Liu, J.; Yang, Q.; Zhang, L.; Yang, H.; Gao, J.; Li, C. Organic–Inorganic Hybrid Hollow Nanospheres with Microwindows on the Shell. *Chem. Mater.* **2008**, *20* (13), 4268–4273. <https://doi.org/10.1021/cm800192f>.
- (103) Teng, Z.; Han, Y.; Li, J.; Yan, F.; Yang, W. Preparation of Hollow Mesoporous Silica Spheres by a Sol–Gel/Emulsion Approach. *Microporous Mesoporous Mater.* **2010**, *127* (1–2), 67–72. <https://doi.org/10.1016/j.micromeso.2009.06.028>.
- (104) Teng, Z.; Su, X.; Zheng, Y.; Sun, J.; Chen, G.; Tian, C.; Wang, J.; Li, H.; Zhao, Y.; Lu, G. Mesoporous Silica Hollow Spheres with Ordered Radial Mesochannels by a Spontaneous Self-Transformation Approach. *Chem. Mater.* **2013**, *25* (1), 98–105. <https://doi.org/10.1021/cm303338v>.
- (105) Stöber, W.; Fink, A.; Bohn, E. Controlled Growth of Monodisperse Silica Spheres in the Micron Size Range. *J. Colloid Interface Sci.* **1968**, *26* (1), 62–69. [https://doi.org/10.1016/0021-9797\(68\)90272-5](https://doi.org/10.1016/0021-9797(68)90272-5).
- (106) Karstedt, B. Platinum Complexes of Unsaturated Siloxanes and Platinum Containing Organopolysiloxanes. US3775452A, November 27, 1973.
- (107) Devangamath, S. S.; Lobo, B.; Masti, S. P.; Narasagoudr, S. Thermal, Mechanical, and AC Electrical Studies of PVA–PEG–Ag₂S Polymer Hybrid Material. *J. Mater. Sci. Mater. Electron.* **2020**, *31* (4), 2904–2917. <https://doi.org/10.1007/s10854-019-02835-3>.
- (108) Pereira, E. D.; Cerruti, R.; Fernandes, E.; Peña, L.; Saez, V.; Pinto, J. C.; Ramón, J. A.; Oliveira, G. E.; Souza Júnior, F. G. de. Influence of PLGA and PLGA-PEG on the Dissolution Profile of Oxaliplatin. *Polímeros* **2016**, *26*, 137–143. <https://doi.org/10.1590/0104-1428.2323>.
- (109) Max, J.-J.; Chapados, C. Influence of Anomalous Dispersion on the ATR Spectra of Aqueous Solutions. *Appl. Spectrosc.* **1999**, *53*, 1045–1053. <https://doi.org/10.1366/0003702991948044>.
- (110) Gallas, J.-P.; Goupil, J.-M.; Vimont, A.; Lavalley, J.-C.; Gil, B.; Gilson, J.-P.; Miserque, O. Quantification of Water and Silanol Species on Various Silicas by Coupling IR Spectroscopy and In-Situ Thermogravimetry. *Langmuir* **2009**, *25* (10), 5825–5834. <https://doi.org/10.1021/la802688w>.
- (111) Brilmayer, R.; Kübelbeck, S.; Khalil, A.; Brodrecht, M.; Kunz, U.; Kleebe, H.-J.; Buntkowsky, G.; Baier, G.; Andrieu-Brunsen, A. Influence of Nanoconfinement on the pKa of Polyelectrolyte Functionalized Silica Mesopores. *Adv. Mater. Interfaces* **2020**, *7* (7), 1901914. <https://doi.org/10.1002/admi.201901914>.
- (112) Cao, C.; Fadeev, A. Y.; McCarthy, T. J. Reactions of Organosilanes with Silica Surfaces in Carbon Dioxide. *Langmuir* **2001**, *17* (3), 757–761. <https://doi.org/10.1021/la000849t>.
- (113) Aytimur, A.; Koçyiğit, S.; Uslu, İ.; Gökmeşe, F. Preparation and Characterization of Polyvinyl Alcohol Based Copolymers as Wound Dressing Fibers. *Int. J. Polym. Mater. Polym. Biomater.* **2015**, *64* (3), 111–116. <https://doi.org/10.1080/00914037.2014.891118>.
- (114) Université Mohammed V - Agdal/Faculté des Sciences/SMC5/SPECTROSCOPIE. Tables IR, 2016.
- (115) Riyahi, S.; Haghgoo, S.; Gorji, E.; riyahi alam, N. Size Reproducibility of Gadolinium Oxide Based Nanomagnetic Particles for Cellular Magnetic Resonance Imaging: Effects of Functionalization, Chemisorption and Reaction Conditions. *Iran. J. Pharm. Res. IJPR* **2015**, *14*, 3–14.
- (116) Launer, P. J.; Arkles, B.; Silicon Compounds: Silanes&Silicones, Gelest, Inc Morrisville, PA. Infrared Analysis of Organosilicon Compounds: Spectra-Structure Correlations, 2013.
- (117) Su, M.; Hongjiu, S.; Du, B.; Li, X.; Ren, G.; Wang, S. Mesoporous Silica with Monodispersed Pores Synthesized from the Controlled Self-Assembly of Silica Nanoparticles. *Korean J. Chem. Eng.* **2015**, *32*. <https://doi.org/10.1007/s11814-014-0270-5>.
- (118) Lin, J. Radiation-Induced Alterations in Mesoporous Silicas : The Effect of Electronic Processes Involving Ions and Electrons. phdthesis, Montpellier, Ecole nationale supérieure de chimie, 2022. <https://theses.hal.science/tel-03880560> (accessed 2024-07-02).
- (119) Ben Ghazi-Bouvrande, J. B. Les liquides poreux : un nouveau concept pour la séparation chimique. phdthesis, Montpellier, Ecole nationale supérieure de chimie, 2022. <https://theses.hal.science/tel-03880557> (accessed 2023-03-14).
- (120) Guerinoni, E.; Dourdain, S.; Lu, Z.; Giusti, F.; Arrachart, G.; Couturier, J.; Hartmann, D.; Pellet-Rostaing, S. Highly Efficient Diluent-Free Solvent Extraction of Uranium Using Mixtures of Protonated Trioctylamine

- and Quaternary Ammonium Salts. Comparative Life Cycle Assessment with the Conventional Extractant. *Hydrometallurgy* **2024**, *224*, 106257. <https://doi.org/10.1016/j.hydromet.2023.106257>.
- (121) Lin, K.-Y. Design, Synthesis and Evaluation of Liquid-like Nanoparticle Organic Hybrid Materials for Carbon Dioxide Capture, Columbia University, 2012. <https://doi.org/10.7916/D8Q2467C>.
- (122) Seeton, C. J. Viscosity–Temperature Correlation for Liquids. *Tribol. Lett.* **2006**, *22* (1), 67–78. <https://doi.org/10.1007/s11249-006-9071-2>.
- (123) Jha, M. K.; Kumari, A.; Panda, R.; Rajesh Kumar, J.; Yoo, K.; Lee, J. Y. Review on Hydrometallurgical Recovery of Rare Earth Metals. *Hydrometallurgy* **2016**, *165*, 2–26. <https://doi.org/10.1016/j.hydromet.2016.01.035>.
- (124) Cheisson, T.; Schelter, E. J. Rare Earth Elements: Mendeleev’s Bane, Modern Marvels. *Science* **2019**, *363* (6426), 489–493. <https://doi.org/10.1126/science.aau7628>.
- (125) Vidal, O.; Goffé, B.; Arndt, N. Metals for a Low-Carbon Society. *Nat. Geosci.* **2013**, *6* (11), 894–896. <https://doi.org/10.1038/ngeo1993>.
- (126) Vidal, O.; Rostom, F.; François, C.; Giraud, G. Global Trends in Metal Consumption and Supply: The Raw Material–Energy Nexus. *Elements* **2017**, *13* (5), 319–324. <https://doi.org/10.2138/gselements.13.5.319>.
- (127) Florek, J.; Larivière, D.; Kählig, H.; Fiorilli, S. L.; Onida, B.; Fontaine, F.-G.; Kleitz, F. Understanding Selectivity of Mesoporous Silica-Grafted Diglycolamide-Type Ligands in the Solid-Phase Extraction of Rare Earths. *ACS Appl. Mater. Interfaces* **2020**, *12* (51), 57003–57016. <https://doi.org/10.1021/acsami.0c16282>.
- (128) Hu, Y.; Misal Castro, L. C.; Drouin, E.; Florek, J.; Kählig, H.; Larivière, D.; Kleitz, F.; Fontaine, F.-G. Size-Selective Separation of Rare Earth Elements Using Functionalized Mesoporous Silica Materials. *ACS Appl. Mater. Interfaces* **2019**, *11* (26), 23681–23691. <https://doi.org/10.1021/acsami.9b04183>.
- (129) Ogata, T.; Narita, H.; Tanaka, M. Adsorption Mechanism of Rare Earth Elements by Adsorbents with Diglycolamic Acid Ligands. *Hydrometallurgy* **2016**, *163*, 156–160. <https://doi.org/10.1016/j.hydromet.2016.04.002>.
- (130) Tunsu, C.; Petranikova, M.; Gergorić, M.; Ekberg, C.; Retegan, T. Reclaiming Rare Earth Elements from End-of-Life Products: A Review of the Perspectives for Urban Mining Using Hydrometallurgical Unit Operations. *Hydrometallurgy* **2015**, *156*, 239–258. <https://doi.org/10.1016/j.hydromet.2015.06.007>.
- (131) Belfqueh, S.; Chapron, S.; Giusti, F.; Pellet-Rostaing, S.; Seron, A.; Menad, N.; Arrachart, G. Selective Recovery of Rare Earth Elements from Acetic Leachate of NdFeB Magnet by Solvent Extraction. *Sep. Purif. Technol.* **2024**, *339*, 126701. <https://doi.org/10.1016/j.seppur.2024.126701>.
- (132) Liu, Y.; Zhao, C.; Liu, Z.; Liu, S.; Zhou, Y.; Jiao, C.; Zhang, M.; Gao, Y.; He, H.; Zhang, S. Study on the Extraction of Lanthanides by Isomeric Diglycolamide Extractants: An Experimental and Theoretical Study. *RSC Adv.* **2022**, *12* (2), 790–797. <https://doi.org/10.1039/D1RA07020G>.
- (133) El Ouardi, Y.; Virolainen, S.; Massima Mouele, E. S.; Laatikainen, M.; Repo, E.; Laatikainen, K. The Recent Progress of Ion Exchange for the Separation of Rare Earths from Secondary Resources – A Review. *Hydrometallurgy* **2023**, *218*, 106047. <https://doi.org/10.1016/j.hydromet.2023.106047>.
- (134) Spedding, F. H.; Powell, J. E.; Wheelwright, E. J. The Stability of the Rare Earth Complexes with N-Hydroxyethylethylenediaminetriacetic Acid. *J. Am. Chem. Soc.* **1956**, *78* (1), 34–37. <https://doi.org/10.1021/ja01582a007>.
- (135) Zaheri, P.; Abolghasemi, H.; Mohammadi, T.; Maraghe, M. G. Synergistic Extraction and Separation of Dysprosium and Europium by Supported Liquid Membrane. *Korean J. Chem. Eng.* **2015**, *32* (8), 1642–1648. <https://doi.org/10.1007/s11814-014-0350-6>.
- (136) Turanov, A. N.; Karandashev, V. K.; Boltoeva, M. Solvent Extraction of Intra-Lanthanides Using a Mixture of TBP and TODGA in Ionic Liquid. *Hydrometallurgy* **2020**, *195*, 105367. <https://doi.org/10.1016/j.hydromet.2020.105367>.
- (137) Wang, K.; Adidharma, H.; Radosz, M.; Wan, P.; Xu, X.; Russell, C. K.; Tian, H.; Fan, M.; Yu, J. Recovery of Rare Earth Elements with Ionic Liquids. *Green Chem.* **2017**, *19* (19), 4469–4493. <https://doi.org/10.1039/C7GC02141K>.
- (138) Arrachart, G.; Couturier, J.; Dourdain, S.; Levard, C.; Pellet-Rostaing, S. Recovery of Rare Earth Elements (REEs) Using Ionic Solvents. *Processes* **2021**, *9* (7), 1202. <https://doi.org/10.3390/pr9071202>.
- (139) Rout, A.; Kotlarska, J.; Dehaen, W.; Binnemans, K. Liquid–Liquid Extraction of Neodymium(III) by Dialkylphosphate Ionic Liquids from Acidic Medium: The Importance of the Ionic Liquid Cation. *Phys. Chem. Chem. Phys.* **2013**, *15* (39), 16533–16541. <https://doi.org/10.1039/C3CP52218K>.
- (140) Smith, E. L.; Abbott, A. P.; Ryder, K. S. Deep Eutectic Solvents (DESs) and Their Applications. *Chem. Rev.* **2014**, *114* (21), 11060–11082. <https://doi.org/10.1021/cr300162p>.

- (141) Florindo, C.; Branco, L. C.; Marrucho, I. M. Quest for Green-Solvent Design: From Hydrophilic to Hydrophobic (Deep) Eutectic Solvents. *ChemSusChem* **2019**, *12* (8), 1549–1559. <https://doi.org/10.1002/cssc.201900147>.
- (142) Schaeffer, N.; Conceição, J. H. F.; Martins, M. A. R.; Neves, M. C.; Pérez-Sánchez, G.; Gomes, J. R. B.; Papaiconomou, N.; Coutinho, J. A. P. Non-Ionic Hydrophobic Eutectics – Versatile Solvents for Tailored Metal Separation and Valorisation. *Green Chem.* **2020**, *22* (9), 2810–2820. <https://doi.org/10.1039/D0GC00793E>.
- (143) Zante, G.; Boltoeva, M. Review on Hydrometallurgical Recovery of Metals with Deep Eutectic Solvents. *Sustain. Chem.* **2020**, *1* (3), 238–255. <https://doi.org/10.3390/suschem1030016>.
- (144) Favero, U. G.; Schaeffer, N.; Passos, H.; Cruz, K. A. M. L.; Ananias, D.; Dourdain, S.; Hespanhol, M. C. Solvent Extraction in Non-Ideal Eutectic Solvents – Application towards Lanthanide Separation. *Sep. Purif. Technol.* **2023**, *314*, 123592. <https://doi.org/10.1016/j.seppur.2023.123592>.
- (145) Sebba, F. Concentration by Ion Flotation. *Nature* **1959**, *184* (4692), 1062–1063. <https://doi.org/10.1038/1841062a0>.
- (146) Micheau, C.; Diat, O.; Bauduin, P. Ion Foam Flotation of Neodymium: From Speciation to Extraction. *J. Mol. Liq.* **2018**, *253*, 217–227. <https://doi.org/10.1016/j.molliq.2018.01.022>.
- (147) Skorzevska, K.; Jonchère, A.; Pasquier, C.; Girard, L.; Bauduin, P. Superchaotropic Ion Flotation: A New Concept for the Extraction and Separation of Nanometer-Sized Ions by Non-Ionic Surfactant-Based Foams. *Sep. Purif. Technol.* **2023**, *323*, 124284. <https://doi.org/10.1016/j.seppur.2023.124284>.
- (148) Brinker, C. J.; Scherer, G. W. *Sol-Gel Science: The Physics and Chemistry of Sol-Gel Processing*; Gulf Professional Publishing, 1990.
- (149) Kobler, J.; Möller, K.; Bein, T. Colloidal Suspensions of Functionalized Mesoporous Silica Nanoparticles. *ACS Nano* **2008**, *2* (4), 791–799. <https://doi.org/10.1021/nn700008s>.
- (150) Hu, J.; Du, P.; Xu, R.; Deng, W. Supersmall Dendritic Mesoporous Silica Nanospheres as Antioxidant Nanocarriers for Pickering Emulsifiers. *J. Agric. Food Chem.* **2021**, *69* (49), 14893–14905. <https://doi.org/10.1021/acs.jafc.1c03016>.
- (151) Dupont, D.; Brullot, W.; Bloemen, M.; Verbiest, T.; Binnemans, K. Selective Uptake of Rare Earths from Aqueous Solutions by EDTA-Functionalized Magnetic and Nonmagnetic Nanoparticles. *ACS Appl. Mater. Interfaces* **2014**, *6* (7), 4980–4988. <https://doi.org/10.1021/am406027y>.
- (152) Sukhbaatar, T.; Piton, R.; Giusti, F.; Arrachart, G.; Duvail, M.; Kumari, A.; Daware, S.; Gupta, S.; Goverapet, S.; Sahu, S. K.; Rai, B.; Pellet-Rostaing, S. Lipophilic Edta-Based Ligands for the Extraction of Rare Earths. Preprint 2024. <https://doi.org/10.2139/ssrn.4804995>.
- (153) Sorin, A.; Favre-Réguillon, A.; Pellet-Rostaing, S.; Sbaï, M.; Szymczyk, A.; Fievet, P.; Lemaire, M. Rejection of Gd(III) by Nanofiltration Assisted by Complexation on Charged Organic Membrane: Influences of pH, Pressure, Flux, Ionic Strength and Temperature. *J. Membr. Sci.* **2005**, *267* (1), 41–49. <https://doi.org/10.1016/j.memsci.2005.05.022>.
- (154) Atta, A.; EL-Mahdy, G.; Al-Lohedan, H.; Abdullah, M. Adsorption Characteristics and Corrosion Inhibition Efficiency of Ethoxylated Octadecylamine Ionic Liquid in Aqueous Acid Solution. *Int. J. Electrochem. Sci.* **2016**, *11*, 882–898.
- (155) Bernadó, P.; Svergun, D. I. Structural Analysis of Intrinsically Disordered Proteins by Small-Angle X-Ray Scattering. *Mol. Biosyst.* **2012**, *8* (1), 151–167. <https://doi.org/10.1039/c1mb05275f>.
- (156) Khodadadi, H.; Aghakhani, S.; Majd, H.; Kalbasi, R.; Wongwises, S.; Afrand, M. A Comprehensive Review on Rheological Behavior of Mono and Hybrid Nanofluids: Effective Parameters and Predictive Correlations. *Int. J. Heat Mass Transfer.* **2018**, *127* (B), 997–1012. <https://doi.org/10.1016/j.ijheatmasstransfer.2018.07.103>